Automatised Constraints on New Physics at the LHC and Beyond

Dissertation
zur
Erlangung des Doktorgrades (Dr. rer. nat.)
der
Mathematisch-Naturwissenschaftlichen Fakultät
der
Rheinischen Friedrich-Wilhelms-Universität Bonn

von
Daniel Schmeier
aus
Köln

Bonn, 06.06.2016

Dieser Forschungsbericht wurde als Dissertation von der
Mathematisch-Naturwissenschaftlichen Fakultät der Universität Bonn angenommen und ist
auf dem Hochschulschriftenserver der ULB Bonn
http://hss.ulb.uni-bonn.de/diss_online elektronisch publiziert.

1. Gutachter:	Prof. Herbert K. Dreiner, Ph.D.
2. Gutachter:	Prof. Dr. Manuel Drees
Tag der Promotion:	25.08.2016
Erscheinungsjahr:	2016

Summary

In this thesis, we discuss the development and use cases of the public software `CheckMATE` which is designed to allow for easy tests of theories beyond the Standard Model against current results from the Large Hadron Collider (LHC). We illustrate the general functionality of this tool and provide hands-on examples to explain how it can be used to test results from the ATLAS and CMS experiments. In addition, we explain how new analyses can be conveniently added to the existing framework. This tool is then used to project a search for monojet final states to a high luminosity LHC with a centre-of-mass energy of 14 TeV. Here, our prospective analysis is used to determine the expected sensitivity to a Higgs Portal scenario which couples the Standard Model to a hidden sector via an invisibly decaying second heavy scalar. We show that complementary bounds to those derived from Higgs boson searches in 8 TeV LHC data can be set, however only if a significant reduction of the current systematic uncertainties for the background estimates of such a search can be achieved. Furthermore, we use `CheckMATE` and its large set of implemented searches for natural Supersymmetry to show how an extension of the Minimal Supersymmetric Standard Model by an additional chiral gauge singlet typically reduces the LHC sensitivity. In the context of R-parity violating Supersymmetry, we go beyond `CheckMATE` and the LHC and derive how the expected sensitivity of the proposed fixed-target experiment SHiP to observe long-lived neutralinos produced via rare Standard Model meson decays can significantly improve existing bounds from low energy observations.

Acknowledgements

There are a lot of people which supported me in various aspects within the last few years and to whom I owe at least some words of gratitude at this stage.

First and foremost I am very thankful to Herbi for taking me as his PhD student and for having given me such an exceptionally large amount of freedom in choosing my own research path. I also feel honoured of having deserved staying in his group until the very end, despite my unusual place of residence and my severe lack of interest in sports of any kind.

My thanks also go to the remaining assessors of this dissertation, to Manuel Drees for his interesting and instructive contributions to our discussions during lunch breaks, Journal Clubs and the like, to Philip Bechtle for exhaustively testing the performance of `CheckMATE` in the high statistics limit and to Martin Langer for spending the time and effort of refereeing this thesis.

I can hardly express the amount of respect and thankfulness I owe to Jamie who always supported me from the beginning of my first Master's project until the final revision of this document and who encouraged me to take the risk and work on `CheckMATE` — the most successful project of my scientific carreer so far.

I am extremely lucky to have experienced the luxury of wonderful colleagues in the last few years. For the great athmosphere which has always made me enjoy coming to the BCTP I want to thank my original 'PhD-Rangers' Kilian, Tim, Toby and Stefano, our youngest 'Desperate Gradstudent' Annika, my new protégé Sebastian, 'the elder' Florian, Lorenzo, Martin and Manuel as well as 'the supporters' Dagmar, Petra, Patricia, Christa and Leni. I also want to thank my long-term remote colleague Jong Soo for all the fruitful collaborations until now and my former competitor Sabine for her hospitality in Grenoble where a sizable fraction of this work was written. The old and new co-`CheckMATE`-ers also deserve my appreciation for their contribution to the tool's success.

For the great amount of active and passive support outside of Academia I want to thank both my family and my future family in-law. The ladies of our annual Thursday night meetings, in particular Sonja, also deserve my words of thanks for the wonderful dishes they served, the gossip they provided me with and for the countless hours of fun I had.

I want to close with a big thank you to you, Elena. I am grateful for all your love, support and understanding in the past years. You are the most important person in my life and each day I am happy to have you around. I love you.

List of Publications

The projects presented within this thesis contain results published in the following journals and preprint archives:

Jordy de Vries, Herbert Dreiner, Daniel Schmeier
"R-Parity Violation and Light Neutralinos at SHiP and the LHC"
arXiv:1511.07436 [hep-ph] *(Submitted to Phys.Rev)*

Jong Soo Kim, Daniel Schmeier, Jamie Tattersall
"Naughty or Nice? The Role of the 'N' in the Natural NMSSM for the LHC"
arXiv:1510.04871 [hep-ph], *Phys.Rev.* **D93** (2016) No.5, 055018

Jong Soo Kim, Oleg Lebedev, Daniel Schmeier
"Higgsophilic gauge bosons and monojets at the LHC"
arXiv:1507.08673 [hep-ph], *J.High Energ.Phys.* **11** (2015) 128

Sergey Alekhin *et al.*
"A facility to Search for Hidden Particles at the CERN SPS: the SHiP physics case"
arXiv:1504.04855 [hep-ph] *(Accepted in Rep.Prog.Phys.)*

Jong Soo Kim, Daniel Schmeier, Jamie Tattersall, Krzysztof Rolbiecki
"A framework to create customised LHC analyses within CheckMATE"
arXiv:1503.01123 [hep-ph], *Comput.Phys.Commun.* **196** (2015) 535-562

Manuel Drees, Herbert Dreiner, Jong Soo Kim, Daniel Schmeier, Jamie Tattersall
"CheckMATE: Confronting your Favourite New Physics Model with LHC Data"
arXiv:1312.2591 [hep-ph], *Comput.Phys.Commun.* **187** (2014) 227-265

Contents

CHAPTER 1

Introduction

> *A scientist, whether theorist or experimenter, puts forward statements or systems of statements, and tests them step by step. In the field of the empirical sciences, more particularly, he constructs hypotheses, or systems of theories, and tests them against experience by observation and experiment.*
>
> — Karl R. Popper, The Logic of Scientific Discovery [1], p. 3

With these sentences, Popper starts his famous book on the logic of science in which he proclaims the concept of *falsifiability* to identify scientifically valid theories. It only values those hypotheses with predictions which can be experimentally violated and prefers those theories with the simultaneously largest predictability and smallest amount of conflicts with observation. With this idea, he gives an answer to the long existing *problem of induction* raised by David Hume in the 18^{th} century which states the logical flaw of generalising a finite set of positive observations to a universally valid law of Nature [2].

Popper advertises falsification not only as a philosophical but also as a highly practical guidance principle for theoretical sciences as it has historically proven to have resulted in the formulation of the two most groundbreaking and fundamental theories of Nature:

> *What compels the theorist to search for a better theory [...] is almost always the experimental falsification of a theory, so far accepted and corroborated: it is, again, the outcome of tests guided by theory. Famous examples are the Michelson-Morley experiment which led to the theory of relativity, and the falsification, by Lummer and Pringsheim, of the radiation formula of Rayleigh and Jeans, and of that of Wien, which led to the quantum theory.*
>
> — Karl R. Popper, The Logic of Scientific Discovery [1], p. 90

It is by this scientific process of consequent experimental falsification and improved predictability how we discovered e.g. the first constituents of the atom [3] and the proof that it is not as "indivisible" as its original Greek name implied, that there exist elementary particles beyond the constituents of ordinary matter [4], how the plethora of observed particles can be organised and new states predicted by the notion of internal symmetries [5], and how our combined knowledge of particles and symmetries in the 1960s and 1970s could be formulated within a concise *Standard Model of particle physics* [6–8]. This theory was able to provide quantitative predictions for many experimental observables that were subsequently measured, for example by relating the elementary charges of weak and electromagnetic interactions to the masses of the associated force mediator particles [9, 10]. It also successfully predicted the existence of new particles, most importantly the Higgs boson which was finally discovered in 2012 by the two multipurpose experiments ATLAS [11] and CMS [12] at the Large Hadron Collider (LHC). Interestingly, the principle of falsifiability was especially important for the discovery of this

particle, as the construction of the LHC could be strongly motivated by the realisation that the non-observation of a Higgs-boson with sub-TeV mass would yield a non-unitary Standard Model [13], i.e. a theory with an ill-defined notion of interaction probability. Such a theoretical inconsistency would have falsified the underlying explanation for the masses of the mediator particles.

Unfortunately, it is also the same process which gives us certainty today that the Standard Model is *not* the true theory of Nature. Not only is the fundamental gravitational interaction manifestly not incorporated but there are also various experimental observations from subatomic up to cosmological scales — we discuss some of them in more detail later in this thesis — which experimentally violate the quantitiative predictions of this theory. In our quest for the ultimate description of the Universe, we sooner or later necessarily require an extension of the Standard Model. This new theory *Beyond the Standard Model*, or BSM, clearly should be able to explain these experimental discrepancies while not violating the past correct predictions of the Standard Model. It should do so at a comparable level of predictability though, as it is trivial to extend a theory by sufficiently many theoretical degrees of freedom to fit all experimental facts. Or alternatively, using Popper's words:

> *Simple statements, if knowledge is our object, are to be prized more highly than less simple ones because they tell us more; because their empirical content is greater; and because they are better testable.*
>
> — Karl R. Popper, The Logic of Scientific Discovery [1], p. 142

By now, no BSM theory could be formulated which according to this measure could be considered as the successor of the Standard Model. We therefore still consider this theory as the most correct description of Nature we currently have. Still, we are seeking for as many experimental tests as possible to explore the Standard Model's full region of validity but also to hopefully find more hints for the physics which lies beyond.

Before the construction of the LHC, many theories beyond the Standard Model had been invented in order to solve its known experimental and theoretical inconsistencies. These models often predicted significant deviations from Standard Model expectations which were hoped to be seen within the LHC's first period of data taking. Unfortuntely, no such significant BSM signal has been observed so far which puts tight constraints on the viable parameter regions of these new physics models.

One famous example for the LHC falsification of a BSM theory is the so-called *constrained Minimal Supersymmetric Standard Model* [14] which would have been a very good candidate to solve various problems of the Standard Model, see e.g. Ref. [15], which predicted distinct signals to be seen in early LHC data, see e.g. Ref. [16], but whose prefered parameter regions could practically be excluded by the incompatibility of the null results from the $\sqrt{s} = 8\,\text{TeV}$ run with observations from other experiments, see e.g. Refs. [17, 18].

In principle, each additional analysis performed by ATLAS and CMS which agrees with Standard Model predictions gives us more information where we should preferably move within the space of proposed BSM theories. Practically, however, it becomes increasingly more laborious for a new model to be tested against all existing results as the number of measurements we need to compare against multiplies. This might tempt theorists and phenomenologists to only analyse a small subset of existing collider limits and potentially miss important ones. Also, each individual person spends a tremendous, redundant amount of workload into the technicalities of translating a theory model into an LHC prediction even though — as we show in this work

— the process of translation is typically universal for a very large set of possible models. A single calculation setup, if properly generalised, could be re-used by many people and could be continuously extended to new LHC results.

In this thesis we focus on the computer tool `CheckMATE` (Check Models At Terascale Energies) which is designed with the purpose to solve the above illustrated problem of wasted research labour. This program provides a convenient framework to test a given BSM theory against current LHC results via simple and straightforward input and output routines. It also allows for the results of upcoming future LHC analyses to be added to the existing framework without much effort and to perform projective studies for the high luminosity LHC. The two main aspects of this work are to describe the general features of the program as a public phenomenology tool and to apply it to put constraints on specific BSM theories.

The content of this thesis is outlined as follows. In Chapter 2 we start with a brief summary of the mathematical formulation of the Standard Model. We define its field and symmetry content and the resulting terms and parameters of the Lagrangian. After pointing out some of its experimental and theoretical problems we propose BSM extensions designed to solve these issues and we discuss the models' respective main features which are of interest for the studies pursued in this thesis.

The connection between model building and collider analysis is illustrated in Chapter 3. Here, we explain the general tools and methods to perform a prediction for LHC results in a particular search channel given any possible BSM theory and how this prediction can be quantitatively compared to the experimental observation. Along the way, we always put particular emphases on the automation of this task by making use of publicly available software.

This general explanation greatly aids understanding the inner workings of `CheckMATE` which we introduce in Chapter 4. After explaining the modules and functionalities of the tool in general we provide two detailed example runs which illustrate how `CheckMATE` can be used to test a given model against existing implemented LHC results and how new analyses from ATLAS or CMS can easily be added to the framework in the future.

In Chapter 5, we use `CheckMATE` to estimate the future sensitivity of the LHC at a centre-of-mass energy of 14 TeV to a *Higgs Portal* scenario. Here, the Standard Model is coupled to an invisible sector via the two Higgs-like fields which is expected to produce new distinctive final state signatures with a single hard jet and large amount of missing transverse energy. The expected results are compared to current limits from Higgs measurements performed at 8 TeV to show which regions of parameter space could be covered with large integrated luminosities.

Another physics case study is provided in Chapter 6 in which we use the full set of 8 TeV analyses to test the distinct signatures of a *natural NMSSM*. This model is designed to solve the hierarchy problem of the Standard Model without introducing fine-tuned parameter combinations. It predicts various possible decay chains with respectively different final states which however typically all involve third generation quarks. We illustrate how the large amount of implemented ATLAS and CMS results in `CheckMATE` tests this large set of possible signatures without much additional effort and show which regions of parameter space are covered.

Lastly — in accordance with the title of this thesis — we go beyond `CheckMATE` and the LHC by discussing the sensitivity of the proposed fixed-target experiment SHiP (Search for Hidden Particles) in Chapter 7. This experiment is designed to look for long-lived neutral particles, for example the lightest neutralino in the R-parity violating supersymmetric Standard Model. We determine the expected sensitivity of this experiment for some benchmark scenarios of this model and show how they could largely improve existing constraints on R-parity violating couplings derived from current precision experiments and the LHC.

Notation and Conventions

Throughout this thesis we make use of natural units and set the constants $\hbar = c = 1$. Four-vector products are defined as $A^\mu B_\mu \equiv g_{\mu\nu} A^\mu B^\nu$ with $g_{\mu\nu} = \mathrm{diag}(1, -1, -1, -1)$ and using the Einstein summation convention for greek indices. Spinor objects ψ are always defined in four-component notation and we make use of the following definitions:

Dirac matrices $\boldsymbol{\gamma^\mu}$: Defined by $\gamma^\mu\gamma^\nu + \gamma^\nu\gamma^\mu = 2g^{\mu\nu}$

Dirac adjoint spinor: $\overline{\psi} \equiv \psi^\dagger\gamma^0$

chiral gamma matrix: $\gamma^5 \equiv i\gamma^0\gamma^1\gamma^2\gamma^3$

chiral projection operators: $P_{L/R} \equiv \frac{1}{2}\left(1 \mp \gamma^5\right)$

chiral spinor components: $\psi_L \equiv P_L\psi, \psi_R \equiv P_R\psi$

charge conjugation matrix $\boldsymbol{C}$: Defined by $C^{-1}\gamma^\mu C = -(\gamma^\mu)^T$ and $C^T = -C$

charge conjugated spinor: $\psi^c \equiv C\overline{\psi}^T$

Rules to convert between the above four-component notation and the completely equivalent two-component notation often used in chiral theories can be found in Ref. [19].

CHAPTER 2

Theories of Nature — The Standard Model and Beyond

The Standard Model of particle physics is one of the most successful theories of Nature. It is able to explain countless experimental observations in the context of weak, strong and electromagnetic interactions in an appealing theoretical framework. However, there exists compelling evidence from both theory and experiment which provides strong motivation that the Standard Model is not the ultimate theory of Nature. Curiously, the very same evidence predicts signs of new physics to appear at current experiments.

Within this thesis it is hence not the Standard Model but various possible extensions which we study with respect to both existing and future experiments. In this chapter we motivate and explain the main properties of each of these models which are analysed in the subsequent chapters of this thesis.

In Section 2.1 we begin with a short summary of the Standard Model of particle physics. We define its particle content, the corresponding Lagrangian and discuss the mechanism of spontaneous electroweak symmetry breaking. We then focus on two important drawbacks which motivate the Standard Model extensions discussed within this thesis. These two deficiencies are the lack of a dark matter candidate and the so-called hierarchy problem.

The first extended model which we discuss in Section 2.2 is a *Higgs Portal* setup. In that section we show how the Higgs sector is changed by the presence of an additonal scalar gauge singlet. This singlet can be linked to a dark matter candidate in order to solve the first of the two problems of the Standard Model.

The second problem is typically solved within *Supersymmetry* and we provide a small summary of general supersymmetric model building in Section 2.3. This will aid us to discuss the general features of the minimal and next-to-minimal supersymmetric versions of the Standard Model in Sections 2.4 and 2.5, respectively.

In general, we attempt to achieve a good balance between providing a self-contained document on the one hand while trying to focus the discussion to the subjects relevant for this thesis on the other hand. References pertaining to more detailed and/or complete studies are given at the appropriate locations. Finally, we have endevoured to follow common naming conventions found in the literature, however some deviations were necessary for consistency and unambiguity within this thesis.

2.1 Introduction to the Standard Model

The Standard Model of particle physics is a relativistic quantum field theory which applies the concept of a gauge symmetry to describe electroweak [6] and strong [8] interactions between

Field	Lorentz repr.	$SU(3)_C$ repr.	$SU(2)_L$ repr.	$U(1)_Y$ charge
H	scalar	singlet	doublet	1
Q_i	left-chiral	triplet	doublet	1/3
U_i	right-chiral	triplet	singlet	4/3
D_i	right-chiral	triplet	singlet	−2/3
L_i	left-chiral	singlet	doublet	−1
E_i	right-chiral	singlet	singlet	−2
G^a_μ	vector	octet	singlet	0
W^A_μ	vector	singlet	triplet	0
B_μ	vector	singlet	singlet	0

Table 2.1: Field content of the Standard Model, their representations under the Lorentz group and the Standard Model gauge groups.

particles. Fields are categorised according to their transformation behaviour under the gauge group $SU(3)_C \otimes SU(2)_L \otimes U(1)_Y$ where only gauge invariant combinations of these fields are allowed. Fermions, i.e. particles with half-integer spin which follow Dirac-Fermi statictics, are split into so-called *left-chiral* and *right-chiral* components. These transform differently under the overall Lorentz-group of special relativity. A *chiral* theory of fermions arises as left- and right-chiral components are in general allowed to transform differently under the gauge symmetry groups. Such a theory manifestly breaks parity symmetry, i.e. the symmetry of spatial inversions, which has been known to be violated by weak interactions [20, 21]. For each chiral fermion field there exist three copies with identical quantum numbers typically referred to as *generations*. The appearance of complete fermion generations is important in order to avoid gauge anomalies which can spoil the underlying gauge symmetry [22]. Assuming the gauge symmetry to be local requires spin 1 particles called *vector bosons* to be added in addition. These fields mediate interactions between particles which are both charged underneath the same gauge group. Lastly, one adds a scalar field to the theory which is charged under $SU(2)_L \otimes U(1)_Y$ and whose vacuum state manifestly breaks this symmetry at low energies. The resulting full set of fields including their transformation behaviour under the mentioned symmetry groups are listed in Table 2.1.

2.1.1 Standard Model Lagrangian

The full Lorentz, gauge invariant and renormalisable[1] Lagrangian which can be constructed using fields in Table 2.1 contains the following parts:

- Kinetic terms of the fermions do not only describe the propagation of the free fermion fields but also contain their interactions with the gauge bosons through the gauge covariant

[1] To allow for a predictable theory which is valid at all physical scales, *renormalisability* forbids all interactions with coupling constants of negative mass dimension.

derivative D_μ:

$$\mathcal{L}_{\text{fermions}} = \sum_{i=1}^{3} \sum_{\psi_i} i\overline{\psi_i}\gamma^\mu \mathrm{D}_\mu \psi_i, \tag{2.1}$$

$$\mathrm{D}_\mu \equiv \partial_\mu + ig_C \sum_{a=1}^{8} G_\mu^a \frac{\hat{t}^a}{2} + ig_L \sum_{A=1}^{3} W_\mu^A \frac{\hat{\sigma}^A}{2} + ig_Y B_\mu \frac{\hat{Y}}{2}. \tag{2.2}$$

Here, $i \in \{1,2,3\}$ iterates through all three generations while the sum over ψ_i runs over the set $\{Q_i, U_i, D_i, L_i, E_i\}$, which contains all Standard Model fermions of a given generation. The prefactors g_Y, g_L and g_C in the covariant derivative correspond to the gauge couplings of $U(1)_Y, SU(2)_L$ and $SU(3)_C$, respectively. The generators $\hat{t}^a$ acting on an $SU(3)$ triplet field correspond to the eight Gell-Mann matrices and yield 0 otherwise. Similarly, $\hat{\sigma}^A$ are represented by the Pauli-matrices if acting on an $SU(2)$ doublet and 0 otherwise. Finally, $\hat{Y}\psi = Y_\psi \psi$ with Y_ψ being the $U(1)_Y$ charge as listed in Table 2.1.

- Gauge kinetic terms describe the vector bosons' propagation and, in the case of a non-Abelian group, also their self-interaction.

$$\mathcal{L}_{\text{gauge bosons}} = -\frac{1}{4}\sum_{a=1}^{8} G_{\mu\nu}^a G^{\mu\nu,a} - \frac{1}{4}\sum_{A=1}^{3} W_{\mu\nu}^A W^{\mu\nu,A} - \frac{1}{4} B_{\mu\nu} B^{\mu\nu}, \tag{2.3}$$

$$W_{\mu\nu}^A \equiv \partial_\mu W_\nu^A - \partial_\nu W_\mu^A - g_L \sum_{B,C=1}^{3} \epsilon^{ABC} W_\mu^B W_\nu^C, \tag{2.4}$$

$$G_{\mu\nu}^a \equiv \partial_\mu G_\nu^a - \partial_\nu G_\mu^a - g_C \sum_{b,c=1}^{8} f^{abc} G_\mu^b G_\nu^c, \tag{2.5}$$

$$B_{\mu\nu} \equiv \partial_\mu B_\nu - \partial_\nu B_\mu. \tag{2.6}$$

Here, ϵ^{ABC} and f^{abc} denote the structure constants of the non-Abelian gauge groups $SU(2)$ and $SU(3)$ respectively. They are determined by commutators of the respective generators, e.g. $[\hat{t}^a, \hat{t}^b] \equiv 2i \sum_c f^{abc} \hat{t}^c$.

- The non-Abelian, non-chiral nature of $SU(3)$ allows for an additional $\mathcal{CP}$-violating term

$$\mathcal{L}_{\text{CPV}} = -\theta \frac{g_C^2}{64\pi^2} \epsilon^{\mu\nu\rho\sigma} \sum_{a=1}^{8} G_{\mu\nu}^a G_{\rho\sigma}^a. \tag{2.7}$$

Experimentally, it has been deduced to be very small due to the non-observation of an electric dipole moment of the neutron, see e.g. Ref. [23]. As a result it plays no role in our subsequent, collider focussed discussions and is only mentioned here for completeness.

- The kinetic term of the $SU(2)_L \otimes U(1)_Y$-charged Higgs field H also involves covariant derivatives and hence couples the Higgs field to the gauge bosons. Furthermore, the Higgs potential allows for a mass parameter and a Higgs self-interaction which are necessary so

that the Higgs field acquires a non-trivial vacuum, see Section 2.1.2.

$$\mathcal{L}_{\text{Higgs}} = (\mathrm{D}_\mu H)^\dagger (\mathrm{D}^\mu H) - \mu_H^2 H^\dagger H - \frac{\lambda_H}{4}(H^\dagger H)^2. \tag{2.8}$$

- Lastly, the assigned quantum numbers of the fermions and the Higgs field allow for the following gauge invariant Yukawa couplings:

$$\mathcal{L}_{\text{Yukawa}} = -\sum_{i,j=1}^{3} \left(Y_e^{ij} (\overline{L_i} H) E_j + Y_d^{ij} (\overline{Q_i} H) D_j + Y_u^{ij} (\overline{Q_i} H^c) U_j \right) + \text{h.c.} \ . \tag{2.9}$$

  In this notation, we make use of the $SU(2)$ conjugate field $H^c \equiv i\sigma_2 H^*$. Throughout this thesis, when encountering products of $SU(2)$ doublets $A = (A_1, A_2), B = (B_1, B_2)$ they must be read as the gauge invariant combinations $(A^\dagger B) \equiv A_1^\dagger B_1 + A_2^\dagger B_2$ and $(A \cdot B) \equiv A_1 B_2 - B_1 A_2$.

2.1.2 Higgs Mechanism

The gauge symmetries and the associated quantum numbers have important consequences regarding the masses of the Standard Model particles. First of all, a gauge symmetry generally forbids mass terms $\frac{1}{2} m_V^2 V_\mu V^\mu$ for the associated gauge bosons. Additionally, assigning different quantum numbers to the chiral components f_L, f_R of a fermion f automatically forbids Dirac mass terms of the form

$$m_f^D \overline{f_L} f_R + \text{h.c.} \ . \tag{2.10}$$

Furthermore, a gauge invariant Majorana mass term

$$m_f^M \overline{f_L} f_L^c + \text{h.c} \quad \text{or} \quad m_f^M \overline{f_R} f_R^c + \text{h.c} \tag{2.11}$$

would require at least one of the two chiral components to be a complete gauge singlet, a condition which none of the fermions in Table 2.1 fulfills. Hence, no valid mass terms can be written down for any of the Standard Model fermions and hence under unbroken Standard Model symmetries are also predicted to be massless.

The masslessness of all fermions and vector bosons however is in clear disagreement with experimental observations e.g. from the measured mass of the top quark [24] and the Z boson [25]. For that reason, this symmetry must be broken at low energy scales. However, in order to not spoil the advantageous theoretical features of a gauge symmetric theory, a situation where the symmetry is restored in the ultraviolet limit would be highly appreciated.

In the Standard Model, this is achieved by adding the scalar field H to the theory [7]: Assuming $\mu_H^2 < 0, \lambda_H > 0$ for the parameters in $\mathcal{L}_{\text{Higgs}}$, a potential as depicted in Fig. 2.1 emerges. Here, the full potential is invariant under the considered gauge symmetry group, however the state $H = 0$ does not correspond to a state of minimum energy. Thus, the Higgs field chooses one of the degenerate vacuum states with $\langle H \rangle \neq 0$. For low energies and small fluctuations of the field around this vacuum state, the symmetry appears to be broken even though the full theory is still gauge invariant. Such a *spontaneosly broken gauge symmetry* allows for massive vector bosons while still keeping the theory renormalisable at all orders [26].

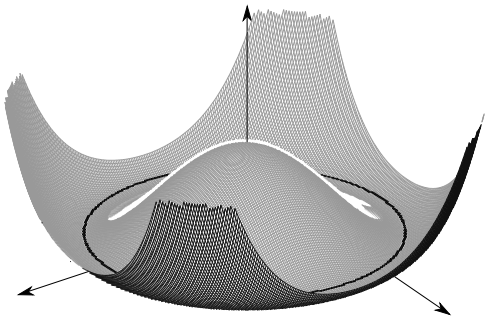

Figure 2.1: Sketch of the Standard Model Higgs potential. Shown are two orthogonal directions of the complex Higgs field, e.g. $\mathrm{Re}(H)$ and $\mathrm{Im}(H)$, and the resulting value of the potential in Eq. (2.8) for $\mu_H^2 < 0, \lambda_H > 0$. The set of possible vacuum states, i.e. the states with the lowest energy, are depicted as the black circle.

Let us discuss the consequences of this in more detail. First of all we define the *vacuum expecation value* (vev) $v \equiv \langle H \rangle$ of the Higgs field. For v to indeed be the minimum of the potential, the following *minimisation condition* has to be fulfilled by the parameters in Eq. (2.8):

$$2\mu_H^2 + \lambda_H v^2 = 0. \tag{2.12}$$

We can use this condition to trade the parameter μ_H^2 in the Standard Model Lagrangian for the more physical parameter v.

The $\mathcal{CP}$-even scalar Higgs particle $h(x)$ can be written as the fluctuation of the Higgs field around its vacuum expecation value[2]

$$H(x) = \begin{pmatrix} 0 \\ v + \frac{1}{\sqrt{2}} h(x) \end{pmatrix} \tag{2.13}$$

with real-valued v. In this notation we have used the gauge degrees of freedom[3] in our theory to specifically set the vacuum state to have the form depicted in Eq. (2.13).

By choosing this vacuum state we must not spoil the $U(1)_{\mathrm{EM}}$ symmetry of electromagnetism. Otherwise the photon as the associated vector boson of that group would gain mass in contradiction to experimental observations, see e.g. Ref. [29]. Hence, breaking the symmetry should yield an unbroken $U(1)_{\mathrm{EM}}$ generator $\hat{Q}$ such that the choice of the vacuum in Eq. (2.13) is invariant under the transformation $H \to e^{-ie\hat{Q}} H$. It can be derived that

$$\hat{Q} = \hat{T}^3 + \frac{\hat{Y}}{2} \tag{2.14}$$

is the correct choice for this unbroken generator[4]. Here, $\hat{T}^3$ returns $\pm\frac{1}{2}$ for the upper/lower

[2] Here and in the following, we occasionally write fields like $h(x)$ with explicit spacetime argument to distinguish these from parameters like v. We typically do this during discussions of vacuum expectation values and mass terms. It is however always assumed that fields are spacetime-dependent objects even if not explicitly written.

[3] The gauge in which H takes the form of Eq. (2.13) is called *unitary gauge* [27]. It has the advantage that no Goldstone bosons [28] have to be considered within calculations as these are fully absorbed in the definition of the gauge bosons.

[4] In fact, the vacuum in Eq. (2.13) has been chosen on purpose in order for the generators $\hat{Q}, \hat{T}^3$ and $\hat{Y}$ to reproduce the Gell-Mann-Nishijima formula [30], known from early baryon spectroscopy, in Eq. (2.14).

component of an $SU(2)_L$ doublet and 0 for a singlet.

With this choice of the $U(1)_{\text{EM}}$ generator, the corresponding decomposition of the other fermion multiplets after electroweak symmetry breaking results in

$$Q_i = \begin{pmatrix} u_{L,i} \\ d_{L,i} \end{pmatrix}, \quad L_i = \begin{pmatrix} \nu_{L,i} \\ e_{L,i} \end{pmatrix}, \quad U_i = u_{R,i}, \quad D_i = d_{R,i}, \quad E_i = e_{R,i}. \tag{2.15}$$

In the four-component notation we use throughout this thesis, the chiral components $u_{L,i}, u_{R,i}$ are related to the full Dirac spinor u_i via $u_{L,i} \equiv P_L u_i$ and $u_{R,i} \equiv P_R$.

2.1.3 Masses and Mixings

Due to the vev v, mass terms for gauge bosons, fermions and the Higgs particle itself emerge through the respective Higgs couplings in Eq. (2.8) and Eq. (2.9). The relevant terms read

$$\begin{aligned} \mathcal{L}_{\text{mass terms}} =& \frac{1}{4} g_Y^2 v^2 B_\mu B^\mu + \frac{1}{4} g_L^2 v^2 W_\mu^3 W^{3\mu} - \frac{1}{2} g_L g_Y v^2 W_\mu^3 B^\mu + \frac{1}{2} g_L^2 v^2 W_\mu^+ W^{-\mu} \\ & - \frac{1}{2} \lambda_H v^2 h^2 - \sum_{i,j=1}^{3} \left(Y_e^{ij} v \bar{e}_{L,i} e_{R,j} + Y_u^{ij} v \bar{u}_{L,i} u_{R,j} + Y_d^{ij} v \bar{d}_{L,i} d_{R,j} + \text{h.c.} \right), \end{aligned} \tag{2.16}$$

where we have defined $W_\mu^\pm \equiv (W_\mu^1 \pm i W_\mu^2)/\sqrt{2}$ as eigenstates of the charge operator with eigenvalues ± 1, respectively.

First of all we can immediately read off the Higgs boson mass as $m_h^2 = \lambda_H v^2$ and the mass of the charged W boson as $m_W^2 = \frac{1}{2} g_L^2 v^2$. The remaining two vector fields W_μ^3 and B_μ however mix due to the presence of a bilinear $W_\mu^3 B^\mu$ term. Diagonalising the resulting mass matrix yields a massive eigenstate $Z_\mu = \cos\theta_W W_\mu^3 - \sin\theta_W B_\mu$ with mass $m_Z^2 = \frac{1}{2}(g_L^2 + g_Y^2) v^2$ and a massless orthogonal photon A_μ. The associated *Weinberg angle* θ_W is given by the relation $\cos\theta_W \equiv m_W / m_Z$.

In the Yukawa sector of Eq. (2.16) one finds that expanding H around its vev yields Dirac mass terms for the fermions. We use bi-unitary transformations to redefine the left- and right-chiral fermion fields in family space in order to diagonalise the Yukawa matrices $Y_d^{ij}, Y_u^{ij}, Y_e^{ij}$. This yields nine eigenvalues $y_d^i = \{y_d, y_s, y_b\}, y_u^i = \{y_u, y_c, y_t\}$ and $y_e^i = \{y_e, y_\mu, y_\tau\}$ and a diagnoal fermion mass sector

$$\mathcal{L}_{\text{fermion masses}} = -\sum_{i=1}^{3} \left(y_u^i v \overline{u_i} u_i + y_d^i v \overline{d_i} d_i + y_e^i v \overline{e_i} e_i \right) \tag{2.17}$$

with fermion masses $m_f = y_f v$ for $f \in \{e, \mu, \tau, d, u, c, s, b, t\}$. Since the Standard Model contains no $\nu_{R,i}$ field, neutrinos are predicted to be massless and thus $m_f = 0$ for $f \in \{\nu_e, \nu_\mu, \nu_\tau\}$

The above bi-unitary rotations into mass eigenstates do not affect the family diagonality of the neutral interactions in Eq. (2.1). Those contain terms of type $Z_\mu \sum_i (A \overline{f_{L,i}} \gamma^\mu f_{L,i} + B \overline{f_{R,i}} \gamma^\mu f_{R,i}$ with family-independent prefactors A and B which only depend on the gauge quantum numbers of f. Thus, the interaction stays diagonal under basis rotations of $f_{L,i}$ and $f_{R,i}$. This *GIM-mechanism* [31] is another appealing consequence of the family structure of the Standard Model as it strongly suppresses flavour-changing neutral currents in accordance to experiment, see e.g. Ref. [32].

However, this does not necessarily hold for the charged gauge interactions. These couple

to fermion currents $\sum_i \overline{f'_{L,i}}\gamma^\mu f_{L,i}$ with different fermions $f'_{L,i}$ and $f_{L,i}$ which typically undergo different rotations in the Yukawa sector. For leptons it is still possible to simultaneously diagonalise both mass and gauge sector. This is thanks to the massless neutrino sector which provides sufficient degrees of freedom to choose the neutrino basis $\nu_{L,i}$ to diagonalise the charged current. In the quark sector, however, a simultaneous redefinition of the up- and down-type quark fields to diagonalise the mass sector fixes the basis and leads to a family-nondiagonality in the charged gauge sector. Thus we find

$$\mathcal{L}_{\text{charged current}} = W^\pm_\mu \Big(\sum_{i=1}^{3} g_L \overline{e_{L,i}}\gamma^\mu \nu_{L,i} + \sum_{i,j=1}^{3} g_L V^{ij}_{\text{CKM}} \overline{u_{L,i}}\gamma^\mu d_{L,j} \Big). \tag{2.18}$$

The resulting *Cabbibo-Kobayashi-Maskawa* (CKM [33]) *matrix* V^{ij}_{CKM} contains the last four physically observable parameters of the Standard Model, namely three mixing angles and a CP-violating phase.

After rotating all fields in Eqs. (2.1), (2.8) and (2.9) into the above derived mass eigenstates all possible couplings of these states can be determined. We do not provide a full list of all these interactions here but refer to Ref. [34] where an exhaustive list of all Standard Model Feynman rules can be found. For the upcoming discussion of possible extensions of the Higgs sector in Section 2.2, let us however list the coupling of the Standard Model Higgs boson to all other Standard Model particles here:

$$\mathcal{L}_{h(\text{SM})(\text{SM})} = \frac{\sqrt{2}m_W^2}{v} h W^+_\mu W^{\mu,-} + \frac{m_Z^2}{\sqrt{2}v} h Z_\mu Z^\mu - \sum_f \frac{m_f}{\sqrt{2}v} h \bar{f} f. \tag{2.19}$$

2.1.4 Accidental Symmetries

The above described gauge symmetry is a fundamental symmetry of the theory which is respected by quantum effects due to the absence of anomalies. We defined the Standard Model field content and the corresponding quantum numbers in Table 2.1 in such a way that the resulting interactions in the Lagrangian reproduce experimentally observed features like e.g. fermion masses and parity violating weak interactions.

The allowed terms in the Standard Model Lagrangian however show additional Abelian symmetries which result from imposing renormalisability in conjunction with the field content and their associated quantum numbers. These *accidental symmetries* are *baryon number* $U(1)_B$ which associates $1/3$ to Q_i, U_i, D_i for $i = 1,2,3$ and 0 to the rest and *lepton family number* $U(1)_{L_i}$ which associates -1 to L_i, E_i and 0 to the rest. Note that the latter is conserved family wise due to the massless neutrino and the resulting complete diagonalisability of the lepton sector. It is trivially related to the family-independent *lepton number* defined as $L \equiv L_1 + L_2 + L_3$.

A phenomenological consequence of baryon number conservation is the stability of the lightest baryon, i.e. the proton. This is in agreement with experimental lower limits on the proton lifetime, e.g. $\tau_{p\to e^+X} > 8\times 10^{32}$ yrs [35]. Also, lepton flavour violating processes in the Standard Model like $\mu \to e\gamma$ are both expected [36] and observed [37] to occur very rarely and thus favour a family-wise conservation of lepton.

Due to anomalies, these global symmetries are however not protected from quantum effects and are in fact violated by higher order effective operators [38]. As an example, the Weinberg

operator

$$\mathcal{L}_{\text{Weinberg}} = \frac{c_{ij}}{\Lambda}(\overline{L_i}H^c)(H^\dagger L_j^c) \tag{2.20}$$

is a dimension 5 operator which violates $U(1)_{L_{i/j}}$ by one unit each and could give a Majorana mass term to neutrinos after electroweak symmetry breaking. Alternatively, the dimension 6 operator [39]

$$\mathcal{L}_{\text{proton decay}} = \frac{c'_{ijkl}}{\Lambda^2}\overline{U_i^c}U_j\overline{D_k^c}E_k \tag{2.21}$$

would allow proton decay. However, these *effective operators* are suppressed by a heavy scale Λ and thus if this scale is sufficiently high, at the Planck scale of 10^{18} GeV for instance, they would not lead to any observable effects.

Since these accidental symmetries are a byproduct of the symmetries and field content of the Standard Model, they can easily be violated as soon as one or both are changed. This typically allows for tree level proton decay operators which then have to be suppressed by other means in order to not be in conclict with experimental results. We encounter such a scenario later in the discussion of R-parity violating supersymmetry in Section 2.4.3.

2.1.5 Hints for Physics Beyond

Even though the Standard Model is very successful in explaining various experimental observations, we have reason to believe that it is just an effective version of a more complete theory of Nature. Those reasons originate from e.g. the mismatch of a predicted massless neutrino sector and observed neutrino oscillations [40], discrepancies of predicted [41] and observed [42] anomalous magnetic moment of the muon, the absence of sufficiently large $\mathcal{CP}$ violation in order to explain our Universe's observed baryon asymmetry [43] and conceptual problems of adding gravity to the quantum field theoretical framework [44]. Two more of these issues which serve as an important motivation for the models analysed within this thesis are discussed in slightly more detail in the following.

Lack of Dark Matter Candidate

Various measurements of the total matter density in our Universe, from velocity distributions of stars observed by J. Oort in the early 1930's [45] to precice modern measurements of cosmic microwave background fluctuations by the Planck sattelite [46], suggest that the total matter density of our Universe is significantly larger than what can be explained by only baryonic contributions from Standard Model particles. We write Ω_X as the ratio of the mass density of X normalised to the *critical density* which would lead to a Universe with no global curvature. The most recent fit of the Planck collaboration results in the following values for the total matter density Ω_m and its contribution from baryonic matter Ω_b:

$$\Omega_m = 0.3089 \pm 0.0062, \tag{2.22}$$

$$\Omega_b = 0.0486 \pm 0.0003. \tag{2.23}$$

The surplus of matter responsible for the difference $\Omega_c \equiv \Omega_m - \Omega_b$ is usually associated to *cold dark matter*. The typical explanation, see e.g. Ref. [47] for a short review, involves the

postulation of one or more new massive particles which only interact weakly with the Standard Model and which hence are often refered to as *WIMPs* (Weakly Interacting Massive Particles). Since Ω_c typically decreases for larger dark matter annhilation rates, see e.g. Ref. [48], a rather weak interaction strength is required as otherwise the resulting reduction of Ω_c would be too large to account for the observed value.

An astonoishing coincidence, commonly refered to as the *WIMP miracle*, is that the annihilation cross section of the order of the Standard Model electroweak interaction is approximately of the correct scale for a dark matter candidate to yield the correct value for Ω_c. In that specific case, the dark matter candidate must not be lighter than 2 GeV as otherwise the contribution from Ω_c would lead to a total value of Ω which exceed the critical value and lead to an unobserved closed Universe [49]. This *Lee-Weinberg bound* on the mass of a cold dark matter candidate, i.e. a particle with typically at least GeV scale mass, is typically model-dependent. The exact rates of WIMP-Standard Model interactions have to be calculated to determine the proper bound for a given model, see e.g. Ref. [48]. Possible candidates for such a particle are introduced in upcoming Sections 2.2 and 2.3 and in the second case we also discuss the corresponding Lee-Weinberg-bound.

Note that we assume the dark matter candidate to be cold, i.e. it is non-relativistic by the time the expansion rate of the Universe overcomes the interaction rate of WIMPs with the Standard Model bath. Any new particle species which is very light and thus relativistic is called *hot dark matter*. These additional relativistic particles would play an important role for the thermal evolution of our Universe and experimental observation, e.g. from Big Bang nucleosynthesis [50] and structure formation [51, 52], put strong upper *Cowski-McClelland bounds* [53] of the mass of such particles at the eV level. Such a light dark matter candidate typically cannot account for the full value of Ω_c and thus additional cold dark matter would be necessary to solve the dark matter puzzle.

Hierarchy Problem

The Higgs boson is the first, and so far only, fundamental scalar particle which has been experimentally observed. Its mass has been determined with relatively good precision to be close to 125 GeV [54] and hence to be close to the electroweak symmetry breaking scale, represented by the size of m_W and m_Z.

However, on theoretical grounds such a value for the Higgs mass appears somewhat unexpected. This is due to the fact that we know that the Standard Model does not account for gravitational effects and hence has to be replaced by a more complete theory of Nature at the scale $M_{\text{Planck}} = \mathcal{O}(10^{18}\,\text{GeV})$ at the latest. The expectation of a physics scale Λ much larger than the electroweak symmetry breaking scale is in strong disaccord with a small Higgs mass [55, 56]. To illustrate this, let us consider a toy model taken from Ref. [57] which contains the Standard Model Higgs field plus a heavy scalar S with mass m_S and/or heavy chiral fermion $F_{L/R}$ with mass m_F. Possible interactions with the Higgs field H then read

$$-\mathcal{L}_{\text{heavy}} = \lambda_{SH}|S|^2|H|^2 + \left(\lambda_{FH}\overline{F_L}F_R H + \text{h.c.}\right) \tag{2.24}$$

$$= \lambda_{SH}v^2|S|^2 + \sqrt{2}v\lambda_{SH}|S|^2 h + \frac{1}{2}\lambda_{SH}|S|^2h^2 + \lambda_{FH}v\overline{F}F + \frac{1}{\sqrt{2}}\lambda_{FH}\overline{F}Fh, \tag{2.25}$$

where we expanded the Higgs field around its vev in step 2 and assumed that all couplings are real. The resulting 1-loop effects to the Higgs boson mass m_h^2 are illustrated in Fig. 2.2. The

correction δm_h^2 to the Higgs mass is then approximately given by the corresponding amplitudes $\Pi_{hh}(q)$ in the limit of vanishing external momentum[5]

$$i\Pi_{hh}^F(0) = -2\lambda_{HF}^2 \int \frac{d^4k}{(2\pi)^4} \left(\frac{1}{k^2 - m_F^2} + \frac{2m_F^2}{(k^2 - m_F^2)^2} \right), \tag{2.26}$$

$$i\Pi_{hh}^S(0) = \lambda_{SH} \int \frac{d^4k}{(2\pi)^4} \Big(\frac{1}{k^2 - m_S^2} + 2\lambda_{SH} v^2 \frac{1}{(k^2 - m_S^2)^2} \Big). \tag{2.27}$$

As it often occurs in quantum field theory, these amplitudes diverge if the full phase space integral d^4k is considered. In a proper renormalisation procedure, these divergencies are first extracted by using a well-defined regulator and afterwards absorbed by unobservable counter terms. In the commonly used *dimensional regularisation* approach [58], the above 4-dimensional integrals are analytically continued into $4-\epsilon$ dimensions with $\epsilon > 0$. To keep the physical mass dimension of the above integrals, d^4k is replaced with $d^dk\ \mu^\epsilon$, with μ being a dimensionful, auxiliary *renormalisation scale*. The above results can then conveniently be written as

$$i\Pi_{hh}^F(0) = -\frac{i\lambda_{HF}^2}{8\pi^2} \Big(A_0(m_F^2) + 2m_F^2 B_0(0, m_F^2, m_F^2) \Big), \tag{2.28}$$

$$i\Pi_{hh}^S(0) = \frac{i\lambda_{HS}}{16\pi^2} \Big(A_0(m_S^2) + 2\lambda_{HS} v^2 B_0(0, m_S^2, m_S^2) \Big), \tag{2.29}$$

using the *Passarino-Veltman* functions [59]

$$A_0(m^2) \equiv \frac{(2\pi\mu)^\epsilon}{i\pi^2} \int d^dk \frac{1}{k^2 - m^2}, \tag{2.30}$$

$$B_0(q^2, m_1^2, m_2^2) \equiv \frac{(2\pi\mu)^\epsilon}{i\pi^2} \int d^dk \frac{1}{k^2 - m_1^2} \frac{1}{(k+q)^2 - m_2^2}. \tag{2.31}$$

These functions contain terms which diverge in the $\epsilon \to 0$ limit but which are removed from physical observables during the renormalisation procedure. The resulting finite terms depend on the exact used renormalisation scheme. In the *dimensional reduction* ($\overline{\text{DR}}$) scheme [60], for instance, the renormalised result is given by [61]

$$A_0(m^2)_{\overline{\text{DR}}\text{ ren.}} = m^2 \Big(1 - \log \frac{m^2}{\mu^2} \Big), \tag{2.32}$$

$$B_0(0, m^2, m^2)_{\overline{\text{DR}}\text{ ren.}} = -\log \frac{m^2}{\mu^2}, \tag{2.33}$$

and thus the renormalised amplitudes become

$$i\Pi_{hh}^F(0)_{\overline{\text{DR}}\text{ ren.}} = -\frac{i\lambda_{HF}^2}{8\pi^2} \Big(m_F^2 - 3\log \frac{m_F^2}{\mu^2} \Big), \tag{2.34}$$

[5] The precise mass correction would have to be determined by finding the root of $q^2 - m_h^2 - \Pi_{hh}(q^2)$. However, for the discussion of arising divergencies we pursue here, the leading term $\Pi_{hh}(q^2) = \Pi_{hh}(0) + \mathcal{O}(q^2)$ is sufficient to look at.

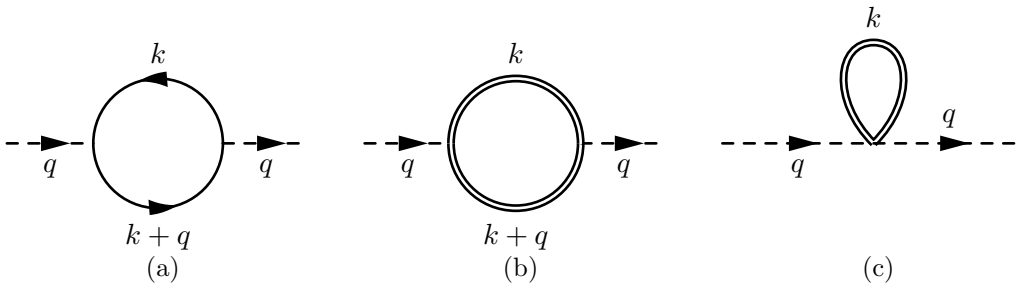

Figure 2.2: Next-to-leading order corrections to the Higgs mass from the fermion F in (a) and the heavy scalar S in (b) and (c) for the toy model discussed in Section 2.1.5.

$$i\Pi^S_{hh}(0)_{\overline{\text{DR}}\text{ ren.}} = \frac{i\lambda_{HS}}{16\pi^2}\left(m_S^2 - (m_S^2 + 2\lambda_{HS}v^2)\log\frac{m_F^2}{\mu^2}\right). \tag{2.35}$$

One finds that both the scalar and the fermion leads to quadratic corrections to the Higgs mass of the order $\delta m_h^2 = \mathcal{O}(m_S^2, m_F^2)$. Since m_S or m_F are physical scales of particles associated to some high scale physics, we would expect any kind of new physics appearing at scale Λ to drive the Higgs mass to order Λ itself. Even though we do not know the actual high scale physics yet, we would expect it at a scale $M_{\text{GUT}} = \mathcal{O}(10^{15})$ GeV or even $M_{\text{Planck}} = \mathcal{O}(10^{18})$ GeV. It seems very unlikely that, despite the large corrections this would imply on m_h^2, the resulting observed value for the Higgs boson mass would be $\mathcal{O}(10^2)$ GeV. This *hierarchy problem* can only be solved if there exists a mechanism which ensures that these corrections are small. We discuss such a mechanism in Section 2.3.

2.2 Higgs Portal Extension

As explained in Section 2.1.5, a reasonable extension of the Standard Model which is supposed to explain WIMP dark matter should contain particles which only interact weakly with the Standard Model. Since matter within the Standard Model mostly couples via gauge interactions mediated by the $W^\pm, Z$ and γ bosons, one easy way to ensure a naturally small interaction rate is to only add particles to the field content which are uncharged under the Standard Model gauge group. We call this set of particles, and possible additional mechanisms that come along with them, the *hidden sector*.

This hidden sector might contain interesting physics beyond the Standard Model in order to explain the value of Ω_c. One of the earliest discussions of such a model can be found in Ref. [62], where the hidden sector only contained a scalar field S being the dark matter candidate. Since then, countless studies with various manifestations and implications of the dark sector have been performed. Two summaries of hidden sector models can be found in Ref. [63] and we provide more detailed references which are relevant to our work at the appropriate places in Chapter 5. The results of the following discussion regarding the particle content and interaction pattern of such a setup is rather universal and can hence be found in any of the references.

In our case, we consider a hidden sector which contains a scalar Standard Model singlet S which is charged under a *hidden gauge group* $U(1)_X$ with a massive gauge boson Z'_μ being the dark matter candidate. This gauge boson gains its mass by spontaneously breaking the hidden

Field	Lorentz repr.	$SU(3)_C$ repr.	$SU(2)_L$ repr.	$U(1)_Y$ charge	$U(1)_X$ charge
H	scalar	singlet	doublet	1	0
S	scalar	singlet	singlet	0	1
Q_i	left-chiral	triplet	doublet	1/3	0
U_i	right-chiral	triplet	singlet	4/3	0
D_i	right-chiral	triplet	singlet	$-2/3$	0
L_i	left-chiral	singlet	doublet	-1	0
E_i	right-chiral	singlet	singlet	-2	0
G^a_μ	vector	octet	singlet	0	0
W^A_μ	vector	singlet	triplet	0	0
B_μ	vector	singlet	singlet	0	0
Z'_μ	vector	singlet	singlet	0	0

Table 2.2: Field content of the Higgs Portal, their representations under the Lorentz group, the Standard Model and the dark gauge group.

symmetry by assigning a vev to S. The Lagrangian of this theory is given by

$$\mathcal{L}_{\text{hidden}} = (\mathrm{D}'_\mu S^\dagger)(\mathrm{D}'^\mu S) - \mu_S^2 S^\dagger S - \frac{\lambda_S}{4}(S^\dagger S)^2 - \frac{1}{4}F'_{\mu\nu}F'^{\mu\nu}, \tag{2.36}$$

$$\mathrm{D}'_\mu \equiv \partial_\mu + i\tilde{g}q_X Z'_\mu, \tag{2.37}$$

$$F'_{\mu\nu} \equiv \partial_\mu Z'_\nu - \partial_\nu Z'_\mu, \tag{2.38}$$

where q_X is the $U(1)_X$ charge of S. If S aquires the vev $\langle S\rangle = z$ the covariant derivative yields a mass term $m^2_{Z'} = 2\tilde{g}^2 q_X^2 z^2$ for Z'_μ in close analogy to the W boson in the Standard Model. Note that all observables we discuss in the following depend only on the product $\tilde{g}q_X$, which is why we can choose q_X to be 1 without loss of generality. In Table 2.2 we list all fields of our model and their respective quantum numbers.

As the Lagrangian in Eq. (2.36) is invariant under $Z'_\mu \to -Z'_\mu$, it can be understood that no interactions with single Z' fields exists. As such it is by construction stable and hence renders a valid dark matter candidate. To explain the observed value of Ω_c there must exist some interaction between the hidden sector and the Standard Model. By constrution, the gauge singlet S does not interact with the Standard Model fields via gauge interactions. Moreover, the quantum numbers of the Standard Model fermions are such that no renormalisable Yukawa-like interaction terms with S is allowed by gauge and Lorentz symmetries. Therefore, such a setup automatically renders the hidden sector decoupled from the Standard Model fermion sector.

However, there exists a gauge invariant combination $H^\dagger H$ of the scalar Higgs field of the Standard Model which allows for one renormalisable interaction term[6] with the hidden Higgs

[6] For completeness, it should be noted that in the above setup another interaction between the two decoupled sectors would be allowed, namely gauge kinetic mixing $\tilde{\epsilon}F'_{\mu\nu}B^{\mu\nu}$ between the gauge bosons of the dark $U(1)_X$ and the Standard Model $U(1)_Y$ [64]. In general, if this term is set to zero as a boundary condition at any chosen scale, quantum corrections reintroduce it at any other scale. However, since none of our fields is charged under both gauge groups, see Table 2.2, no 1-loop corrections are expected, see e.g. Ref. [65]. Even if fermions were present in our dark sector, a correction to $F'_{\mu\nu}B^{\mu\nu}$ would not happen before three-loop order in perturbation

field S:

$$\mathcal{L}_{\text{mix}} = -\lambda_{HS} H^\dagger H S^\dagger S. \tag{2.39}$$

From the Lagrangians in Eqs. (2.8), (2.36) and (2.39), the combined scalar potential of S and H can be determined to be

$$V_{\text{scalar}} = \mu_H^2 H^\dagger H + \mu_S^2 S^\dagger S + \frac{\lambda_H}{4}(H^\dagger H)^2 + \frac{\lambda_S}{4}(S^\dagger S)^2 + \lambda_{HS} H^\dagger H S^\dagger S, \tag{2.40}$$

where all products of fields are Hermitean which implies that all parameters are real by construction. Choosing the vevs as $\langle H \rangle = v, \langle S \rangle = z$, it follows that if both $2\lambda_{HS}\mu_S^2 - \lambda_S \mu_H^2$ and $2\lambda_{HS}\mu_H^2 - \lambda_H \mu_S^2$ are positive the following two minimisation conditions for $v, z \neq 0$ emerge:

$$2\mu_H^2 + \lambda_H v^2 + 2\lambda_{HS} z^2 = 0, \tag{2.41}$$

$$2\mu_S^2 + \lambda_S z^2 + 2\lambda_{HS} v^2 = 0. \tag{2.42}$$

Again, these conditions can be used to replace μ_H^2, μ_S^2 by v, z in the following discussion.

After expanding[7] the two scalar fields

$$S(x) = z + \frac{1}{\sqrt{2}} s^0(x), \tag{2.43}$$

$$H(x) = \begin{pmatrix} 0 \\ v + \frac{1}{\sqrt{2}} h^0(x) \end{pmatrix}, \tag{2.44}$$

we find that Eq. (2.39) induces a non-diagonal bilinear mixing term $2\lambda_{HS} z v s^0(x) h^0(x)$. Thus, to obtain the mass eigenstates of our model we have to diagonalise the mass matrix

$$\mathcal{M}_{h^0(x), s^0(x)} = \begin{pmatrix} \lambda_H v^2 & 2\lambda_{HS} v z \\ 2\lambda_{HS} v z & \lambda_S z^2 \end{pmatrix}, \tag{2.45}$$

which yields 2 $\mathcal{CP}$-even mass eigenstates $h(x), H(x)$. These are admixtures of the two scalar fields $h^0(x), s^0(x)$

$$\begin{pmatrix} h(x) \\ H(x) \end{pmatrix} = \begin{pmatrix} \cos\alpha & -\sin\alpha \\ \sin\alpha & \cos\alpha \end{pmatrix} \begin{pmatrix} h^0(x) \\ s^0(x) \end{pmatrix} \tag{2.46}$$

with respective masses

$$m_{h/H}^2 = \frac{1}{2}\left[(\lambda_H v^2 + \lambda_S z^2) \mp \sqrt{(\lambda_S z^2 - \lambda_H v^2)^2 + 16\lambda_{HS}^2 z^2 v^2} \right] \tag{2.47}$$

theory. It would thus be sufficiently suppressed and still be negligible for our present study. For an analysis of dark matter interaction via explicit kinetic mixing of a hidden vector boson with the Standard Model $U(1)$ we refer to Ref. [66].

[7] We also assume unitary gauge in the $U(1)_X$ sector and fully absorb the Goldstone boson of S in the longitudinal mode of the Z'.

while the mixing angle α is given as

$$\tan(2\alpha) = \frac{4\lambda_{HS} v z}{\lambda_H v^2 - \lambda_S z^2}. \tag{2.48}$$

In the decoupling limit $\lambda_{HS} = 0$ in this definition, $h(x)$ corresponds to the Standard Model Higgs field $h^0(x)$ where we retain the previous result $m_h^2 = \lambda_H v^2$ of Section 2.1. Thus if we assume small mixing angles, the lighter of the two mass eigenstates behaves mostly Standard Model like.

The parameter $v \approx 174\,\text{GeV}$ [67] is fixed e.g. by the observed gauge boson masses m_W, m_Z, whose predicted values are identical to the Standard Model. $m_h \approx 125\,\text{GeV}$ [54] is the measured mass of the Standard Model like Higgs boson. Since $m_{Z'} = \sqrt{2}\tilde{g}z$ fixes the hidden vev z for a given gauge coupling and gauge boson mass, the four free parameters of this model can be chosen to be $m_H, \sin\alpha, \tilde{g}$ and $m_{Z'}$. The original fundamental parameters $\lambda_H, \lambda_S, \lambda_{HS}, \mu_H, \mu_S$ and z of the model are then fixed by

$$\lambda_H = \frac{1}{2v^2}\Big(m_h^2 + m_H^2 + (m_H^2 - m_h^2)\cos(2\alpha)\Big), \tag{2.49}$$

$$\lambda_S = \frac{\tilde{g}^2}{m_{Z'}^2}\Big(m_h^2 + m_H^2 - (m_H^2 - m_h^2)\cos(2\alpha)\Big), \tag{2.50}$$

$$\lambda_{HS} = \frac{\tilde{g}\sqrt{2}}{4 m_{Z'} v}(m_H^2 - m_h^2)\sin(2\alpha) \tag{2.51}$$

plus the above heavy gauge boson mass formula and the minimisation conditions in Eqs. (2.41) and (2.42).

One important consequence of this mixing in the scalar sector is the emergence of two particles which are coupled both to the Standard Model and the hidden sector. As only the Higgs sector mediates between these two otherwise decoupled regions, this feature motivates the commonly used name *Higgs Portal* for this model. After rotating to the mass eigenbasis, the scalar interactions of Eq. (2.19) in the Standard Model become

$$\mathcal{L}_{h/H(\text{SM})(\text{SM})} = \Big(h\cos\alpha + H\sin\alpha\Big)\left(\frac{\sqrt{2}m_W^2}{v} W_\mu^+ W^{\mu,-} + \frac{m_Z^2}{\sqrt{2}v} Z_\mu Z^\mu - \sum_f \frac{m_f}{\sqrt{2}v}\bar{f}f\right), \tag{2.52}$$

whereas the couplings to the hidden gauge boson Z' are given as

$$\mathcal{L}_{h/HZ'Z'} = \Big(h\sin\alpha - H\cos\alpha\Big)\tilde{g} m_{Z'} Z'_\mu Z'^\mu. \tag{2.53}$$

Another relevant operator for the upcoming discussion is the coupling which mediates decay of the heavy scalar into two light scalars, i.e.

$$\mathcal{L}_{Hhh} = \frac{2m_h^2 + m_H^2}{2\sqrt{2}v}\sin(2\alpha)\left(\cos\alpha + \sqrt{2}\tilde{g}\frac{v\sin\alpha}{m_{Z'}}\right) H h^2. \tag{2.54}$$

We analyse the phenomenology of this model in Chapter 5.

2.3 Introduction to General Supersymmetric Models

In Section 2.1.5 we derived the corrections to the Higgs mass m_h^2 via a heavy scalar with mass m_S and coupling $\kappa_S(S^\dagger S)(H^\dagger H)$ as well as a heavy Dirac fermion F with interaction $\kappa_F \overline{F_L} F_R H + \text{h.c.}$

$$i\Pi_{hh}^F(0) = -\frac{i\lambda_{HF}^2}{8\pi^2}\left(m_F^2 - 3\log\frac{m_F^2}{\mu^2}\right), \tag{2.55}$$

$$i\Pi_{hh}^S(0) = \frac{i\lambda_{HS}}{16\pi^2}\left(m_S^2 - (m_S^2 + \lambda_{HS}v^2)\log\frac{m_S^2}{\mu^2}\right). \tag{2.56}$$

We argued how this is problematic as it requires a dangerous fine tuning between the observed low scale value of m_h and the expected high scale correction via S or F.

However, the above example suggests that the dangerous quadratic corrections cancel exactly in the special case $m_S = m_F$, $\lambda_{HF}^2 = \lambda_{HS}$ and if there exist two mass degenerate complex scalar fields S. Even though this might look like an artifically fine-tuned setup, it can fundamentally related to a new symmetry called *Supersymmetry* [68, 69], or SUSY. The corresponding symmetry transformation rotates bosonic into fermionic states and vice versa such that the total action stays invariant. This requires the number of bosonic and fermionic degrees in any supersymmetric theory to be equal and thus explains why, as required in the example above, each massive Dirac fermion is associated with two complex scalars. Furthermore it requires all associated masses and coupling constants for S and F to be equal in order to create a supersymmetric Lagrangian. From this it is easy to understand why $m_S = m_F$, $\lambda_{HF}^2 = \lambda_{HS}$ and therefore the desired automatic cancelation of all quadratic Higgs mass corrections follows.

In the following, we provide a very brief summary of the most important steps to create a supersymmetric Lagrangian. We follow the very good reviews in Refs. [57, 70], however will consistently use four-component spinor notation as mentioned in Chapter 1.

2.3.1 Structure of General Supersymmetric Theories

Since bosonic and fermionic degrees of freedom cannot be distinguished in a fully supersymmetric theory, they are only allowed to appear within full *supermultiplets*. One generally distinguishes between two main classes of supermultiplets:

- *Chiral Supermultiplets* $\widehat{\Phi}(x)$ contain a complex scalar field $\phi(x)$, a left-chiral Weyl-spinor $\psi(x)$ and an auxiliary scalar field $F(x)$. They are typically used to describe chiral fermions and/or complex scalar fields within a supersymmetric theory. The requirement of an auxiliary field F can be understood if one counts the number of bosonic (2 for a complex scalar ϕ) and fermonic (4 for a Weyl-fermion ψ) off-shell degrees of freedom, which need to be equal in a supersymmetric framework. The field F however has a trivial kinetic term and thus can be easily integrated out from the Lagrangian. In the results we show below, this integration step is already performed and thus we only show the resulting interaction terms for the physical fields ϕ, ψ.

- *Vector Supermultiplets* $\widehat{V}(x)$ contain a real vector field $V_\mu(x)$, a Majorana fermion $\lambda(x)$ with $\lambda^c = \lambda$ and another auxiliary scalar field $D(x)$. As this multiplet contains real fields, it is used to accomodate for gauge bosons which arise from real, adjoint representations of gauge groups. The field $D(x)$, just as $F(x)$, can easily well be integrated out from the spectrum which has also already been done in the following discussion.

Supersymmetry Conserving Lagrangian

The Lagrangian of a supersymmetric theory can be constructed from the given set of supermultiplets by following a particular set of rules. These can be derived from a more profound mathematical description of supersymmetric fields and ensure gauge invariance, renormalisablity and invariance under supersymmetric transformations.

A few words about notation: whenever we write $\sum_{\widehat{\Phi}} f(\psi, \phi)$, it is to be understood that we sum over all chiral superfields $\widehat{\Phi}$ in a given model and insert its constituents ψ and ϕ into f. Analogously, we understand $\sum_{\widehat{V}^a} g_V f(V_\mu^a, \lambda^a)$ as the sum over all vector superfields $\widehat{V}^a$ associated to the gauge groups of a model with coupling constants g_V and generator index a, respectively. Lastly, in $\sum_{\widehat{V}^a} \widehat{t}^a \psi$ the matrix $\widehat{t}^a$ corresponds to the ath generator of the group associated to $\widehat{V}$ and corresponds to the representation of ψ in that group.

- Kinetic terms including gauge covariant derivatives for all superfields are given as (see for comparison Eqs. (2.1), (2.3) and (2.8))

$$\mathcal{L}_{\text{kin}} = \sum_{\widehat{\Phi}} \Big(i\overline{\psi}\gamma^\mu \mathrm{D}_\mu \psi + (\mathrm{D}_\mu \phi)^\dagger (\mathrm{D}^\mu \phi) \Big) + \sum_{\widehat{V}^a} \Big(\frac{1}{4} V^a_{\mu\nu} V^{\mu\nu,a} + \frac{1}{2} \overline{\lambda^a} i \gamma^\mu \mathrm{D}_\mu \lambda^a \Big), \tag{2.57}$$

$$V^a_{\mu\nu} \equiv \partial_\mu V^a_\nu - \partial_\nu V^a_\mu - g_V \sum_{b,c} f^{abc} V^b_\mu V^c_\nu, \tag{2.58}$$

$$\mathrm{D}_\mu \psi \equiv \Big(\partial_\mu + \sum_{\widehat{V}^a} i g_V V^a_\mu \widehat{t}^a \Big) \psi, \tag{2.59}$$

$$\mathrm{D}_\mu \phi \equiv \Big(\partial_\mu + \sum_{\widehat{V}^a} i g_V V^a_\mu \widehat{t}^a \Big) \phi, \tag{2.60}$$

$$\mathrm{D}_\mu \lambda^a \equiv \partial_\mu \lambda^a - g_V \sum_{b,c} f^{abc} \lambda^b V^c_\mu. \tag{2.61}$$

  Herea, f^{abc} are the structure constants of the group which is associated to $\widehat{V}$.

- Supersymmetric gauge theories require more interaction terms than those hidden in the covariant derivatives of the kinetic terms, namely

$$\mathcal{L}_{\text{gauge}} = \sum_{\widehat{V}^a} \sum_{\widehat{\Phi}} \Big(-2 g_V \overline{\lambda^a} (\phi \widehat{t}^a \psi) + \text{h.c.} \Big) - \frac{1}{2} \sum_{\widehat{V}^a} g_V^2 \Big(\sum_{\Phi} \phi^\dagger \widehat{t}^a \phi \Big)^2. \tag{2.62}$$

- Renormalisable, gauge invariant interactions between scalars and fermions are formulated by constructing a *superpotential* $\mathcal{W}$. This object contains all gauge-invariant products of at most three chiral superfields, and can hence be generally written as

$$\mathcal{W} = \sum_{i,j,k} y_{ijk} \widehat{\Phi}_i \widehat{\Phi}_j \widehat{\Phi}_k + \sum_{i,j} M_{ij} \widehat{\Phi}_i \widehat{\Phi}_j + \sum_i L_i \widehat{\Phi}_i, \tag{2.63}$$

  with y_{ijk} and M_{ij} being symmetric in all their respective indices.

Given this superpotential, the Lagrangian can be constructed as follows:

$$\mathcal{L}_{\mathcal{W}} = -\frac{1}{2}\left(\sum_{i,j}\overline{\psi_i^c}\psi_j\frac{\partial^2\mathcal{W}}{\partial\widehat{\Phi}_i\partial\widehat{\Phi}_j}\bigg|_{\widehat{\Phi}\to\phi} + \text{h.c.}\right) - \sum_i\left|\frac{\partial\mathcal{W}}{\partial\widehat{\Phi}_i}\right|^2_{\widehat{\Phi}\to\phi}. \tag{2.64}$$

Here, i, j iterate over all chiral superfields and the derivative terms should be understood as first taking the derivative of $\mathcal{W}$ with respect to the superfield(s) $\widehat{\Phi}_{i/j}$ and then, in the result, replacing all superfields with the scalar component of the respective field.

Soft Supersymmetry Breaking Part

With the terms listed above, a fully supersymmetric Lagrangian can be constructed. From e.g. investigating Eq. (2.64), one immediately finds that all particles in the same superfield have identical masses. Unfortunately, this is in strong tension with experimental results as no scalar particles with masses equal to those of the known quarks and leptons have been seen so far. We therefore conclude that Supersymmetry, if realised in Nature, must be a broken symmetry.

There are various different ways to break Supersymmetry, see e.g. the review in Ref. [71]. The breaking mechanism should not spoil the features of Supersymmetry, most importantly its solution to the hierarchy problem. As can be understood from our toy model in Section 2.1.5, it is the appearance of operators with dimensionless couplings which leads to quadratically divergent behaviour. Hence, we should only allow for so–called *soft Supersymmetry breaking terms* i.e. additional terms to those in the previous section which explicitly distinguish between components in a supermultiplet but which require dimensionful coupling constants. In general, this would allow for the following additional terms in the Lagrangian[8]:

- The scalar components of all chiral superfields can have independent mass terms:

$$\mathcal{L}_{\text{scalar mass}} = -\sum_{\widehat{\Phi}_i,\widehat{\Phi}_j} m^2_{\phi_i\phi_j}\phi_i^\dagger\phi_j. \tag{2.65}$$

  Note that only combinations Φ_i, Φ_j with the same gauge quantum numbers are allowed to have off-diagonal $m^2_{\phi_i\phi_j}$ contributions as otherwise Eq. (2.65) would violate gauge invariance.

- The fermionic components of each vector supermultiplet, typically referred to as *gauginos*, can also have an independent, complex Majorana mass term

$$\mathcal{L}_{\text{gaugino mass}} = -\sum_{\widehat{V}^a}\left(\frac{1}{2}m_\lambda\overline{\lambda^a}P_L\lambda^a + \text{h.c.}\right). \tag{2.66}$$

- Each allowed product of superfields in the superpotential yields an analogous product of

[8] By pure dimensional arguments, additional allowed terms would be a mixed trilinear scalar term $\phi_i^*\phi_j\phi_k$ and — in case of an Abelian symmetry — a gaugino-fermion bilinear term $\lambda\psi_i$. However, even though they fulfill our qualitative dimensionality argument, it can be shown that these typically do allow for quadratically divergent corrections [72] and hence should not be included.

the respective scalar field components with a dimensionful prefactor:

$$\mathcal{L}_{\text{scalar interaction}} = \sum_{i,j,k} A_{ijk} y_{ijk} \phi_i \phi_j \phi_k - \sum_{i,j} B_{ij} M_{ij} \phi_i \phi_j + \sum_i C_i L_i \phi_i + \text{h.c.} \ , \tag{2.67}$$

where y_{ijk}, M_{ij} and L_i are the corresponding non-vanishing terms in Eq. (2.64) and thus A_{ijk} and B_{ij} are also required to be fully symmetric in all their indices.

Note that within a specific model for Supersymmetry breaking, e.g. via giving vevs to the auxiliary F– [73] or D–terms [74], the above terms would be strongly correlated through the respective underlying mechanism. However, if we are ignorant about the exact details of SUSY breaking we should consider each possible of the above terms as a free parameter.

2.4 Minimal Supersymmetric Standard Model

To promote the Standard Model as defined in Section 2.1 to a supersymmetric theory, we have to arrange the fields listed in Table 2.1 into full supermultiplets as described in the previous section. This necessarily introduces one chiral supermultiplet for each Standard Model fermion field. As an example, the $SU(2)_L$ fermion doublet $Q_L = (u_L, d_L)$ is now accompanied by a scalar $SU(2)_L$ doublet $\widetilde{Q}_L = (\widetilde{u}_L, \widetilde{d}_L)$ and forms a chiral superfield $\widehat{Q}_L$. Since the rules in Section 2.3.1 require chiral supermultiplets to contain left-chiral Weyl fermions only, Standard Model fermion fields in Table 2.1 which were originially defined in the right-chiral representation of the Lorentz group have to be conjugated before being promoted to a chiral supermultiplet. As an example, the right-chiral $SU(2)_L$ singlet d_R is translated into a superfield $\widehat{D}^c$ which contains the charge conjugated fermion field $D^c = (d_R^c)$ and a corresponding conjugated scalar field $\widetilde{d}_R^*$.

An important subtlety arises when trying to promote the scalar Standard Model Higgs field H to a chiral supermultiplet: In Section 2.1, we shortly mentioned the anomaly freedom of the Standard Model fermion sector. However, a chiral supermultiplet for H would introduce a chiral fermion $\widetilde{H}$ to the field content which is charged under the gauge groups and which would spoil the gauge anomaly cancellation. To avoid this, the contribution to the anomalous amplitude has to be cancelled. This can be achieved by adding a second chiral Higgs superfield with same $SU(2)_L$ representation but opposite hypercharge to the field content. These two fields will be called $\widehat{H}_u$ and $\widehat{H}_d$ from now on, for reasons which become apparent below.

The resulting supermultiplet content of this *Minimal Supersymmetric Standard Model* (MSSM) is listed in Table 2.4. A valid superpotential which reproduces the Yukawa- and Higgs-sector from the Standard Model is given as:

$$\mathcal{W}_{\text{MSSM}} = \mu\Big(\widehat{H}_u \cdot \widehat{H}_d\Big) + \sum_{i,j=1}^{3} \Big[\Upsilon_e^{ij}\Big(\widehat{L}_i \cdot \widehat{H}_d\Big)\widehat{E}_j^c + \Upsilon_d^{ij}\Big(\widehat{Q}_i \cdot \widehat{H}_d\Big)\widehat{D}_j^c + \Upsilon_u^{ij}\Big(\widehat{H}_u \cdot \widehat{Q}_i\Big)\widehat{U}_j^c\Big] \tag{2.68}$$

Note the definition of $SU(2)_L$ products given in Section 2.1.1. With the prescription from Section 2.3, it is straightforward to show that $\mathcal{W}_{\text{MSSM}}$ indeed reproduces the Yukawa terms of the Standard Model in Eq. (2.9). The necessity of adding a second chiral Higgs superfield with opposite hypercharge becomes also apparent here: without either $\widehat{H}_u$ or $\widehat{H}_d$, it would not be possible to construct Yukawa terms for both up- and down-type quarks. This is a consequence of the rules for supersymmetric Lagrangians which do not allow for the usage of $H^c = i\sigma_2 H^*$

Superfield	Type	$SU(3)_C$	$SU(2)_L$	$U(1)_Y$
$\widehat{H}_u$	chiral	singlet	doublet	1
$\widehat{H}_d$	chiral	singlet	doublet	-1
$\widehat{Q}_i$	chiral	triplet	doublet	$1/3$
$\widehat{U}_i^c$	chiral	anti-triplet	singlet	$-4/3$
$\widehat{D}_i^c$	chiral	anti-triplet	singlet	$2/3$
$\widehat{L}_i$	chiral	singlet	doublet	-1
$\widehat{E}_i^c$	chiral	singlet	singlet	2
$\widehat{G}_\mu^a$	vector	octet	singlet	0
$\widehat{W}_\mu^A$	vector	singlet	triplet	0
$\widehat{B}_\mu$	vector	singlet	singlet	0

Table 2.3: Superfield content of the Minimal Supersymmetric Standard Model and the respective transformation properties under the Standard Model gauge groups.

as we did in the Standard Model. The MSSM hence shows the feature of a Two-Higgs Doublet Model of type II [75].

Note that since the two scalar components of the Higgs fields generally acquire different vevs v_u and v_d, we deliberately renamed the prefactors of the Yukawa couplings compared to the Standard Model analogon in Eq. (2.9). The relation $m_f = y_f v$ shown in Eq. (2.17) has to be replaced with $m_{f_u} = h_{f_u} v_u$ and $m_{f_d} = h_{f_d} v_d$ with $f_u \in \{u, c, t\}$, $f_d \in \{d, s, b, e, \mu, \tau\}$ and h_{f_u}, h_{f_d} being the corresponding eigenvalues of the above Υ matrices. Neutrinos, as in the Standard Model, are massless.

In addition to all the terms which can be derived from the superpotential, the MSSM comes along with a long list of SUSY conserving terms from the gauge covariant kinetic terms of all fields in Table 2.4 and soft Supersymmetry breaking terms via $\mathcal{L}_{\text{scalar mass}}$, $\mathcal{L}_{\text{gaugino mass}}$ and $\mathcal{L}_{\text{scalar interaction}}$. As we only require a handful of these in the later discussions we will not give a full list here but mention those we need at the appropriate places. An exhaustive list of all terms, before and after electroweak symmetry breaking, can be found in Ref. [76]. In the following we concentrate on a few important aspects which will be of relevance in the remainder of this work.

2.4.1 The MSSM Higgs Sector and its Problems

Similarly to the Higgs Portal scenario, the MSSM contains two scalar fields with a combined scalar potential. However, the facts that both fields are charged under the gauge group and that we have to consider a general softly broken supersymmetric model renders the calculation slightly more complicated. For a very detailed discussion, see Ref. [77].

Following the rules of supersymmetric Lagrangians given in Section 2.3.1, this potential can be found to contain the following terms

$$V(H_u, H_d) = |\mu|^2(|H_u|^2 + |H_d|^2) \qquad \text{from } \mathcal{L}_{\mathcal{W}} \tag{2.69}$$

$$+ \frac{g_L^2 + g_Y^2}{8}\left(|H_u|^2 - |H_d|^2\right)^2 + \frac{g_L^2}{2}\left|H_u^\dagger H_d\right|^2 \qquad \text{from } \mathcal{L}_{\text{gauge}} \tag{2.70}$$

$$+ m_{H_u}^2 |H_u|^2 + m_{H_d}^2 |H_d|^2 \qquad \text{from } \mathcal{L}_{\text{scalar mass}} \tag{2.71}$$

$$- \Big(B\mu (H_u \cdot H_d) + \text{h.c.} \Big). \qquad \text{from } \mathcal{L}_{\text{scalar interaction}} \tag{2.72}$$

Now both H_u and H_d acquire vacuum expectation values v_u and v_d, respectively. Similarly to Eq. (2.13), we can expand both fields around their vevs. However, since we cannot use our gauge degree of freedom to simultaneously set all Goldstone boson degrees of freedom to zero, we do not fix a gauge yet and start with the more general form

$$H_d(x) = \begin{pmatrix} v_d + \frac{1}{\sqrt{2}}(h_d^0(x) + i\ a_d^0(x)) \\ h_d^-(x) \end{pmatrix}, \quad H_u(x) = \begin{pmatrix} h_u^+(x) \\ v_u + \frac{1}{\sqrt{2}}\Big(h_u^0(x) + i\ a_u^0(x)\Big) \end{pmatrix}. \tag{2.73}$$

To simplify the discussion, we assume that all parameters are real and hence $\mathcal{CP}$ is conserved in the scalar sector. Then, we can identify h_u^+, h_d^- as electrically charged fields, h_u^0, h_d^0 as $\mathcal{CP}$-even and a_u^0, a_d^0 as $\mathcal{CP}$-odd fields.

A similar calculation as done in section Section 2.1 shows that the gauge boson mass formulas $m_Z^2 = \frac{1}{2}(g_L^2 + g_Y^2)v^2$ and $m_W = \frac{1}{2}g_L^2 v^2$ from the Standard Model are kept with the definition $v \equiv v_u^2 + v_d^2$. After inserting the expansions of H_u and H_d around their vevs into Eq. (2.72) we can derive two minimisation conditions which have to be fulfilled to get a minimum with $v_u, v_d \neq 0$:

$$m_{H_u}^2 + |\mu|^2 + \frac{g_L^2 + g_Y^2}{4}(v_u^2 - v_d^2) = B\mu \cot\beta, \tag{2.74}$$

$$m_{H_d}^2 + |\mu|^2 + \frac{g_L^2 + g_Y^2}{4}(v_d^2 - v_u^2) = B\mu \tan\beta, \tag{2.75}$$

where we define $\tan\beta \equiv v_u/v_d$ as the ratio of the two vacuum expectation values. Using these two minimisation conditions we can trade the parameters $m_{H_d}^2$ and $m_{H_d}^2$ for m_Z — an experimentally fixed quantity — and a free parameter $\tan\beta$.

Re-expressing the original Lagrangian in terms of these new parameters and the expanded fields $h_{u/d}^0, h_{u/d}^\pm$ and $a_{u/d}^0$ yields the following mass matrices for the $\mathcal{CP}$-odd and the electrically charged fields

$$\mathcal{M}^2_{a_u^0(x), a_d^0(x)} = B\mu \begin{pmatrix} \cot\beta & 1 \\ 1 & \tan\beta \end{pmatrix}, \tag{2.76}$$

$$\mathcal{M}^2_{h_u^+(x), h_d^+(x)} = \Big(B\mu + \frac{1}{2}m_W^2 \sin 2\beta\Big) \cdot \begin{pmatrix} \cot\beta & 1 \\ 1 & \tan\beta \end{pmatrix}. \tag{2.77}$$

As both of these have vanishing determinant, they each contain one massless Goldstone eigenstate $G^0, G^\pm$ which serve as the longitudinal gauge boson modes. They can be obtained by rotating the respective bases by a β dependent matrix, i.e.

$$\begin{pmatrix} G(x) \\ A(x) \end{pmatrix} = \widehat{\mathcal{R}}(\beta) \begin{pmatrix} a_u^0(x) \\ a_d^0(x) \end{pmatrix}, \tag{2.78}$$

$$\begin{pmatrix} G^\pm(x) \\ H^\pm(x) \end{pmatrix} = \widehat{\mathcal{R}}(\beta) \begin{pmatrix} h_u^+(x) \\ h_d^+(x) \end{pmatrix}, \tag{2.79}$$

$$\text{with } \widehat{\mathcal{R}}(\beta) \equiv \begin{pmatrix} -\sin\beta & \cos\beta \\ \cos\beta & \sin\beta \end{pmatrix}. \tag{2.80}$$

This matrix will prove to be useful in the more complicated NMSSM case in Section 2.5. The eigenstates $A, H^{\pm}$ orthogonal to the Goldstone modes correspond to new particles predicted by the MSSM scalar sector and have tree-level masses

$$m_A^2 \equiv -\frac{2B\mu}{\sin 2\beta}, \tag{2.81}$$

$$m_{H^{\pm}} \equiv m_A^2 + m_W^2. \tag{2.82}$$

Both these additional particles decouple from the spectrum in the limit $m_A \gg m_Z$ which we henceforth call the *decoupling limit* [78].

With this definition of m_A, the mass matrix of the $\mathcal{CP}$-even fields can be written in compact form as follows:

$$\mathcal{M}^2_{h_u^0(x),h_d^0(x)} = \begin{pmatrix} m_Z^2\sin^2\beta + m_A^2\cos^2\beta & -\frac{1}{2}(m_Z^2+m_A^2)\sin 2\beta \\ -\frac{1}{2}(m_Z^2+m_A^2)\sin 2\beta & m_Z^2\cos^2\beta + m_A^2\sin^2\beta \end{pmatrix} \tag{2.83}$$

and its eigenvalues can easily be evaluated as

$$m_{h/H}^2 \equiv \frac{1}{2}\Big(m_A^2 + m_Z^2 \mp \sqrt{(m_A^2+m_Z^2)^2 - 4m_A^2 m_Z^2\cos^2 2\beta}\Big). \tag{2.84}$$

One can show, see e.g. Ref. [78], that the couplings of h to Standard Model particles approaches the Standard Model result in the decoupling limit such that we can indeed identify h with h_{SM} in this limit. Then the masses in Eq. (2.84) simplify to

$$m_h^2 \approx m_Z^2\cos^2 2\beta, \tag{2.85}$$

$$m_H^2 \approx m_A^2 \tag{2.86}$$

and we find the well-known peculiar upper tree level bound of $m_h \leq m_Z = 91\,\text{GeV}$ for the lightest Higgs boson in the MSSM [79]. This bound did not exist in the non-Supersmmetric Standard Model, see Section 2.1.3. The main cause for this is the appearance of a free quartic coupling $\lambda|H^\dagger H|^2$ in the Standard Model which can be used to scale the Higgs boson mass $m_h^2 = \lambda v^2$ arbitrarily within perturbative bounds. In the MSSM, however, this free parameter is not permitted as neither a corresponding gauge invariant term can be formulated for the superpotential $\mathcal{W}$ nor can it be put in $\mathcal{L}_{\text{scalar interaction}}$ as it is not a dimensionful parameter. Instead, the terms in $\mathcal{L}_{\text{gauge}}$ do introduce quartic couplings among the H_u and H_d fields with however gauge-coupling dependent prefactors. As these are experimentally fixed, the above limit arises.

At first sight, this upper bound seems to violate the observation of a Standard Model like Higgs boson with mass 125 GeV at the LHC. However, so far we have only discussed the MSSM Lagrangian at tree level. In a next-to-leading order calculation, the large Yukawa coupling h_t, see the discussion below Eq. (2.68), introduces sizable quantum effects to the above tree level term due to top quarks and their scalar partners. In the limit where both $\tilde{t}_L, \tilde{t}_R$ have equal

mass $m_{\tilde{t}} \gg m_t$, this correction reads[9] [81]

$$\Delta m_h^2 \approx \frac{3m_t^4}{2\pi^2 v^2} \ln\left(\frac{m_{\tilde{t}}}{m_t}\right) \tag{2.87}$$

With $3m_t^4/2\pi^2v^2 \approx (70\,\text{GeV})^2$ it follows that $m_{\tilde{t}}/m_t$ should be approximately 5, or in other words, we require scalar top partners with about TeV masses in order to reach the correct Higgs mass.

2.4.2 The Naturalness Problem of the MSSM

The requirement of sufficiently heavy scalar top partners to explain the experimentally observed Higgs boson unfortunately leads to problems in the theoretical analysis of the Higgs potential. To understand this, we have to go back to our minimisation conditions, Eqs. (2.74) and (2.75). Using the definition of m_Z^2 we use these conditions to write

$$m_Z^2 = \frac{2}{\tan^2(\beta) - 1}\left(m_{H_d}^2 - \tan^2(\beta) m_{H_u}^2\right) - 2|\mu|^2 \tag{2.88}$$

This condition requires the linear combination of three dimensionful parameters predicted by Supersymmetry to yield m_Z, a dimensionful quantity which characterises the electroweak scale $\Lambda_{\text{EW}} \approx 100\,\text{GeV}$. As the respective prefactors of the linear combination are all of order 1, we would expect each individual term itself to be of order Λ_{EW}. Otherwise, miraculous cancellations of large numbers would have to take place in order to result in a small number, a situation which is commonly refered to as *unnatural* for a theory and which we already disfavoured in our discussion of the hierarchy problem in Section 2.1.5.

This condition play an important role for the discussion of heavy scalar tops if we embed higher order corrections into our discussion. We do this again in a qualitative manner and refer to Ref. [82] for more detailled results. Suppose Λ_S is the scale at which Supersymmetry is broken and where the parameters are again chosen such that both $\tilde{t}_L, \tilde{t}_R$ have common mass $m_{\tilde{t}}$. Then, in the leading log approximation[10] the corrections on $m_{H_u}^2$ at the electroweak scale Λ_{EW}, which is the scale at which Eq. (2.88) should be evaluated, is given as

$$\Delta m_{H_u}^2\big|_{\tilde{t}} \approx -\frac{3m_t^2}{4\pi^2 v^2} m_{\tilde{t}}^2 \ln\left(\frac{\Lambda_S}{\Lambda_{\text{EW}}}\right). \tag{2.93}$$

Furthermore, $m_{\tilde{t}}$ receives large corrections to $\mathcal{O}(\alpha_s)$ from heavy gluinos with mass $m_{\tilde{g}}$. This provides another important correction to the parameter $m_{H_u}^2$ which in the leading log approx-

[9] This is a very qualitative result as e.g. typically the scalar top partners will not have the same mass due to large off-diagonal elements in the mass matrix, see upcoming Section 2.5.4. For a review of more sophisticated higher order Higgs mass calculations, see Ref. [80].

[10] In the leading log approximation, the coupled system of renormalisation group equations

$$\mathrm{d}X(Q)/\mathrm{d}(\ln(Q)) = \alpha Y(Q), \tag{2.89}$$
$$\mathrm{d}Y(Q)/\mathrm{d}(\ln(Q)) = \beta X(Q) \tag{2.90}$$

with known boundary values $X(Q_0), Y(Q_0)$ is approximately solved via

$$X(Q_1) \approx X(Q_0) + \alpha Y(Q_0)\ln(Q_1/Q_0), \tag{2.91}$$
$$Y(Q_1) \approx Y(Q_0) + \beta X(Q_0)\ln(Q_1/Q_0) \tag{2.92}$$

instead of solving the exact coupled system of differential equations. The solutions are accurate for small α, β.

imation is given as

$$\Delta m^2_{H_u}\big|_{\tilde{g}} \approx -\frac{2m_t^2}{\pi^3 v^2}\alpha_s m^2_{\tilde{g}}\,\ln\Big(\frac{\Lambda_S}{\Lambda_{\mathrm{EW}}}\Big). \tag{2.94}$$

Naturalness requires these corrections to be at most of order Λ_{EW} themselves. This translates into mass bounds on the relevant particles, typically of order $m_{\tilde{t}} \lesssim m_{\tilde{g}} \lesssim \mathcal{O}(1\text{ TeV})$. In our simplified discussion, when we compare Eq. (2.93) with Eq. (2.87), it seems almost impossible to satisfy both conditions unless absurd values for Λ_S are chosen. A more careful analysis including possible splitting in the stop sector, see e.g. Ref. [82], reveals that it is possible to find natural values which yield the correct mass for m_h, which however yield a significantly fine-tuned scenario often labelled as being subject to the *little hierarchy problem* [83].

Since $m^2_{H_d}$ does not undergo equally large higher order corrections — the corresponding Yukawa coupling h_b is almost two orders of magnitude smaller than h_t — there is typically no naturalness problem associated to this parameter. As a SUSY conserving parameter, however, $|\mu^2|$ is neither related to Λ_{EW} nor to Λ_S and thus a natural *a priori* value for this parameter is even harder to explain.

In Section 2.5, we provide an elegant solution to these two naturalness problems by extending the MSSM in such a way that the $|\mu|$-term is by construction of order electroweak scale and no heavy SUSY partners for the top and gluon are required to get the correct value for m_h.

2.4.3 Light Neutralinos, Dark Matter and RPV

Neutralinos and Charginos In the Standard Model the interaction mediators as spin 1 vector bosons, the matter fields as spin 1/2 fermions and the scalar Higgs field with spin 0 were clearly distinct objects. In Supersymmetry, however, these individual fields with well-defined spin have to be promoted into supermultiplets. This creates overlaps between the originally separated groups of particles and can cause fields with the same quantum numbers to mix.

In the MSSM, the fermionic chiral supermultiplet partners $\widetilde{h}_u, \widetilde{h}_d$ of the neutral higgs fields h_u and h_d mix with the fermionic vector supermultiplet partners $\widetilde{W}^3, \widetilde{B}$ of the neutral gauge bosons W^3_μ, B_μ. They form a set of four fermionic fields with spin 1/2, no colour and no electric charge. After writing down all allowed mass terms in the MSSM, one finds the following nondiagonal Majorana mass matrix in the basis $\mathcal{B}^0 = (\widetilde{B}(x), \widetilde{W}^3(x), \widetilde{h}_u(x), \widetilde{h}_d(x))$:

$$\mathcal{M}_{\mathcal{B}^0} = \begin{pmatrix} M_1 & 0 & -m_Z\cos\beta\sin\theta_W & m_Z\sin\beta\sin\theta_W \\ 0 & M_2 & m_Z\cos\beta\cos\theta_W & -m_Z\sin\beta\cos\theta_W \\ -m_Z\cos\beta\sin\theta_W & m_Z\cos\beta\cos\theta_W & 0 & -\mu \\ m_Z\sin\beta\sin\theta_W & -m_Z\sin\beta\cos\theta_W & -\mu & 0 \end{pmatrix}. \tag{2.95}$$

Here, β and μ are parameters of the Higgs sector as explained in Section 2.4.1. M_1 and M_2 are the soft SUSY breaking masses in $\mathcal{L}_{\text{gaugino mass}}$ of $\widetilde{B}$ and $\widetilde{W}^A$, respectively. Due to the off-diagonal elements, the fields mix to four *neutralinos* $\widetilde{\chi}^0_{1/2/3/4}$, where the indices 1 to 4 label the lightest to heaviest mass eigenstates.

Similarly, the partners of the charged gauge bosons $W^\pm$ and the charged higgs fields h_u^+, h_d^-

form conjugate Dirac fermion pairs $(\widetilde{W}^+, \widetilde{W}^-), (\widetilde{h}_d^+, \widetilde{h}_u^-)$ with a coupled Dirac mass matrix

$$\mathcal{M}_{\widetilde{W}^+(x),\widetilde{h}_d^+(x)} = \begin{pmatrix} M_2 & \sqrt{2} m_W \sin\beta \\ \sqrt{2} m_W \cos\beta & \mu \end{pmatrix}, \tag{2.96}$$

which upon diagonalisation yields two *chargino* mass eigenstates called $\widetilde{\chi}_{1/2}^{\pm}$.

Depending on how the dimensionful parameters M_1, M_2 and μ as well as $\tan\beta$ are chosen, various masses and mixing patterns can be created. If we for example check the determinant of the neutralino mass matrix in Eq. (2.95)

$$\det \mathcal{M}_{\mathcal{B}^0} = \mu \left[m_Z^2 \sin 2\beta \left(M_1 \cos^2\theta_W + M_2 \sin^2\theta_W \right) - M_1 M_2 \mu \right] \tag{2.97}$$

we find that as long as all parameters are real, this determinant and hence the mass of the lightest eigenstate can be chosen arbitrarily small, down to $m_{\widetilde{\chi}_1^0} = 0$ [84]. Such an extremely light neutralinos is very often required to be a mostly $\widetilde{B}^0$ state. Otherwise, a light $\widetilde{W}^0$ or $\widetilde{h}^0$ would often be accompanied by a light $\widetilde{W}^{\pm}$ or $\widetilde{h}^{\pm}$, as they depend on the same parameters μ and M_2, and thus would be excluded by lower chargino mass bounds of $m_{\widetilde{\chi}^{\pm}} \gtrsim 90\,\text{GeV}$ [85]. Interestingly, it can be shown that in such a case there are no universal lower mass bounds on the lightest neutralino [84, 86, 87].

It turns out that in most realistic MSSM scenarios the lightest neutralino is also the *LSP* (lightest supersymmetric particle). To illustrate this, in Ref. [88] several million random parameter configurations in a 19-dimensional constrained MSSM setup were tested against various theoretical and experimental limits from low-energy experiments and results from the LEP electron-positron-collider. Only $\approx 1\,\%$ of the scanned models which passed all the considered constraints contained a non-neutralino LSP. All SUSY-based models within this thesis will hence always have a neutralino LSP.

Neutralino Dark Matter Since the neutralinos are admixtures of Higgs-like and gauge-boson-like fermions, they typically couple to Standard Model particles with electroweak gauge coupling strength. Furthermore, it can be shown — see also the discussion in the next paragraph — that if the superpotential only contains the terms in Eq. (2.68) all interaction vertices contain an even number of SUSY particles [89]. This automatically renders the LSP, which as explained above is often the lightest neutralino, stable. In total, we hence find that $\widetilde{\chi}_1^0$ shows all characteristic properties mentioned in Section 2.1.5 to be a potential candidate to solve the dark matter puzzle. We refer to Ref. [90] for a detailed general review on Supersymmetric dark matter and to Ref. [91] for updated statements on neutralino dark matter considering recent results from the LHC.

As we already discussed in Section 2.1.5, in order to be in agreement with the observation of a flat cosmological metric and results from structure formation, the MSSM parameter space must be chosen such that the resulting mass spectrum and annihilation rates result are respectively in agreement with the Cowskis-McClelland bound if the neutralino is light or the Lee-Weinberg bound if the neutralino is heavy. It can be shown [84, 91–93] that this excludes the following mass region for a light, stable neutralino dark matter candidate

$$0.7\,\text{eV} \leq m_{\widetilde{\chi}_1^0} \leq 24\,\text{GeV}. \tag{2.98}$$

***R*-Parity Violation** We constructed the MSSM superpotential in Eq. (2.68) in such a way that it reproduces the known Standard Model Yukawa and Higgs interactions. As mentioned in the previous paragraph, this automatically ensures that any SUSY interaction involves an even number of SUSY particles which causes the LSP to be stable by construction. This statement can be put in the context of a conserved discrete quantum number called *R-Parity* which can be defined as [89, 94]

$$R_P \equiv (-1)^{3B+L+2s}, \tag{2.99}$$

with L and B denoting lepton and baryon number (see Section 2.1.4) and s being the spin of a given field.

If we followed the general rule of putting all gauge-invariant products of chiral superfields up to order three into the superpotential, a careful investigation of Table 2.4 reveals the following additional terms which would be allowed but which would violate R_P:

$$\begin{aligned}\mathcal{W}_{\text{RPV}} = &\sum_{i=1}^{3} \kappa_i \left(\widehat{H}_u \cdot \widehat{L}_i\right) + \sum_{i,j,k=1}^{3} \lambda_{ijk} \left(\widehat{L}_i \cdot \widehat{L}_j\right) \widehat{E}^c_k \\ &+ \sum_{i,a,b=1}^{3} \lambda'_{iab} \left(\widehat{L}_i \cdot \widehat{Q}_a\right) \widehat{D}^c_b + \sum_{a,b,c=1}^{3} \lambda''_{abc} \widehat{U}^c_a \widehat{D}^c_b \widehat{D}^c_c \end{aligned} \tag{2.100}$$

Note that due to gauge invariance, λ_{ijk} and λ''_{abc} are antisymmetric under $i \leftrightarrow j$ and $b \leftrightarrow c$, respectively. Also, since the two chiral superfields $\widehat{H}_d$ and $\widehat{L}_i$ have identical quantum numbers, see Table 2.4, they can in fact not be distinguished in R-parity violating Supersymmetry and thus the κ_i terms can be rotated away by a proper redefinition of those two fields [95]. We will therefore not consider this bilinear operator in the remaining discussion. In text, we will refer to the remaining operators as LLE, LQD and UDD.

A non-zero value for any of these parameters can severely change the phenomenology of the MSSM. First and foremost, LLE and LQD violate lepton while UDD violates baryon number conservation at tree level. As we discussed already for the Standard Model, see Section 2.1.4, this might lead to inconsistencies with low-energy observables. A summary of bounds on individual and products of the above couplings can be found in Ref. [96]. It turns out that these limits are especially severe if more than one coupling is present at a time. As an example taken from that reference, for a standardised sfermion mass value of 100 GeV[11], individual bounds on $\lambda_{131}, \lambda_{132}$ are of order 10^{-1} from measurements of $\Gamma(\tau \to e\nu\overline{\nu})/\Gamma(\tau \to \mu\nu\overline{\nu})$ while the product $\lambda_{131}\lambda_{132}$ is bound to be less than $\mathcal{O}(10^{-7})$ from measurements of the decay $\mu \to 3e$.

One solution to easily avoid these constraints is to forbid all the above operators by adding R-parity as an unbroken symmetry of the supersymmetric Standard Model. This is however a very *ad-hoc* ansatz as there is no theoretical motivation why the laws of Nature should obey R-parity [94]. Alternative solutions therefore only forbid a subset of the operators in Eq. (2.100) and/or higher order effective operators, c.f. Section 2.1.4, e.g. via baryon triality [97] or proton hexality [98], in order to avoid the strong constraints from proton decay but keep the advantageous features of e.g. a lepton-flavour violating theory to allow for Majorana neutrino masses [99].

[11] This value is hardly viable in light of current LHC limits, but as both compared bounds scale equally with $\tilde{m}$ our statement still holds for TeV sfermion masses.

As soon as R-parity violation is present, the number of SUSY particles entering interaction vertices is not necessarily even any more. An important consequence is that the LSP might not be stable any more but can decay into a set of Standard Model particles. On the one hand, this removes the solution to the dark matter problem and with that an important argument in favour of the MSSM. On the other hand, however, it weakens bounds on long-lived heavy particles as those on the neutralino in Eq. (2.98) and therefore re-opens potentially interesting regions in parameter space. An important example which we investigate further in Chapter 7, is a lightest neutralino which has mass of the same order as the Standard Model mesons, $m_{\widetilde{\chi}_1^0} \approx 1 - 5$ GeV. Then, interesting scenarios with long-lived neutralinos with subsequent mesonic decays can occur which can be identified at long-baseline experiments.

2.5 A Natural Next-To-Minimal Supersymmetric Standard Model

The Higgs sector of the MSSM yielded two apparent problems caused by naturalness arguments:

- A natural setup of the Higgs potential demands relatively light scalar top partners. However, these light particles typically do not raise the Higgs mass significantly enough beyond the upper tree level bound of $m_h^2 \leq m_Z^2$ via higher order correction, see Eq. (2.87), in order to explain the observed mass of 125 GeV for the Standard Model like Higgs boson.

- From naturalness arguments one would furthermore expect the superpotential parameter μ to obey $|\mu|^2 \approx m_Z^2$. However, there is no theoretical reason why a Supersymmetry conserving dimensionful parameter should be of electroweak scale order.

Both of these problems can be solved by extending the MSSM particle content by another chiral superfield $\widehat{S}$. In analogy to the Higgs Portal[12] , this superfield is assumed to be uncharged under the Standard Model gauge groups and its scalar component is assumed to acquire a vacuum expectation value z. Furthermore, all chiral superfields carry charge under an additional discrete[13] $\mathbb{Z}_3$ symmetry which fordbids the appearance of any term in the superpotential with less than three terms.

As will become apparent below, such a model is natural in the sense, see Section 2.4.2, that it can accomodate for light higgsinos, third generation squarks and gluinos. Other sfermions and gauginos, however, have no analogous expectation to be light which is why we consider a setup

[12] Note that a large difference to the considered Higgs Portal model in Section 2.2 is the appearance of an operator S^3. It is needed in our following phenomenological discussion to get the right mass hierarchy and hence $\widehat{S}$ cannot carry an additional $U(1)_X$ charge as in the Higgs Portal case.

[13] Care must be taken if a model obeys a discrete symmetry which is spontaneously broken by a particle which is charged under the discrete group, see e.g. Ref. [100]. During the evolution of the Universe from high to low temperatures, a phase transition should create separated regions in the Universe with different discrete charges of the respective vacua. The resulting *domain walls* between these regions would drastically change the cosmological evolution of the Universe and the observed fluctuations of the cosmic microwave background. For the NMSSM, there exist various possible solutions, with however their own new problems in addition. To give one example, the $\mathbb{Z}_3$ symmetry could be broken at a high scale Λ_{High} close to the gravitational Planck scale via $1/\Lambda_{\text{High}}$ suppressed interactions which would be phenomenologically unobservable at low scales. These would cause domain walls to be washed out very early by the inflationary Universe (for an introduction to inflation, see Ref. [101]). However, it can be shown that such a scenario always introduces dimensionful tadpole interactions for S of order Λ_{High} [102], which re-introduce naturalness and/or hierarchy problems if $\langle S \rangle$ is not of order Λ_{High} but of order Λ_{EW}. For possible solutions, see Refs. [103, 104].

Superfield	type	$SU(3)_C$	$SU(2)_L$	$U(1)_Y$	$\mathbb{Z}_3$
$\widehat{H}_u$	chiral	singlet	doublet	1	$2\pi/3$
$\widehat{H}_d$	chiral	singlet	doublet	-1	$2\pi/3$
$\widehat{S}$	chiral	singlet	singlet	0	$2\pi/3$
$\widehat{Q}_3$	chiral	triplet	doublet	$1/3$	$2\pi/3$
$\widehat{U}_3^c$	chiral	anti-triplet	singlet	$-4/3$	$2\pi/3$
$\widehat{D}_3^c$	chiral	anti-triplet	singlet	$2/3$	$2\pi/3$
$\widehat{G}_\mu^A$	vector	octet	singlet	0	$2\pi/3$

Table 2.4: Superfield content of the natural Next-to-Minimal Supersymmetric Standard Model and the respective transformation properties under the Standard Model gauge groups and the NMSSM $\mathbb{Z}_3$ parity.

where these are decoupled from the experimentally accessible spectrum[14]. We therefore restrict the following discussion of the NMSSM only to the relevant light particles and the respective parameters of interest. Most definitions and relations are taken from Ref. [103] and we refer readers to this source and references therein for more information.

2.5.1 Natural Lagrangian

The above described natural NMSSM scenario can be described by the following reduced superpotential

$$\mathcal{W} = h_t(\widehat{Q}_3 \cdot \widehat{H}_u)\widehat{U}_3^c + h_b(\widehat{Q}_3 \cdot \widehat{H}_u)\widehat{D}_3^c + \lambda(\widehat{H}_u \cdot \widehat{H}_d)\widehat{S} + \frac{\kappa}{3}\widehat{S}^3, \tag{2.101}$$

Here we alredy diagonalised the Yukawa matrices $\Upsilon_u^{ij}, \Upsilon_d^{ij}$ of Eq. (2.68) in family space and only list the relevant eigenvalues h_t, h_b for the top and bottom quarks, respectively. λ and κ are new, NMSSM specific parameters which describe the coupling of the singlet field to the two Higgs doublets and the singlet self interaction.

Note that the assumed additional $\mathbb{Z}_3$ symmetry prohibits the problematic MSSM term $\mu(\widehat{H}_u \cdot \widehat{H}_d)$. A vacuum expectation value of the scalar singlet $\langle S \rangle \equiv z$ reintroduces this term after expanding the scalar field S around its minimum:

$$-\mathcal{L} \supset \lambda z(H_u \cdot H_d) \equiv \mu_{\text{eff}}(H_u \cdot H_d). \tag{2.102}$$

Since H_u, H_d and S share a common scalar potential, see below, the vev z and therefore the effective μ term are naturally of electroweak scale order. Thus the μ–problem of the MSSM as discussed in Section 2.4.2 is solved by the spontaneous generation of μ_{eff}.

In addition to the terms derived from this superpotential, the following dimensionful soft SUSY breaking parameters have to be added to the Lagrangian of the theory:

$$-\mathcal{L}_{\text{soft}} = m_{H_u}^2|H_u|^2 + m_{H_d}^2|H_d|^2 + m_S^2|S|^2 + m_{\widetilde{Q}_3}^2|\widetilde{Q}_3|^2 + m_{\widetilde{U}_3^c}^2|\widetilde{U}_3^c|^2 + m_{\widetilde{D}_3^c}^2|\widetilde{D}_3^c|^2 + \frac{1}{2}M_3\widetilde{\widetilde{G}}^a\widetilde{G}^a$$

[14] This can easily be accomplished by setting the corresponding soft SUSY breaking mass terms to a scale of several TeV.

$$- \left(h_t A_t (\widetilde{Q}_3 \cdot H_u) \widetilde{U}_3^c + h_b A_b (\widetilde{Q}_3 \cdot H_b) \widetilde{D}_3^c + \lambda A_\lambda (H_u \cdot H_d) S + \frac{\kappa}{3} A_\kappa S^3 + \text{h.c.} \right) \tag{2.103}$$

where we already assumed all couplings to be real–valued to simplify the discussion. Here, $\widetilde{G}^a$ denotes the gluino field, i.e. the fermionic part of the vector superfield associated to the SU(3) gauge group. All other fields denote the scalar component of the respective chiral superfield in Table 2.4.

2.5.2 NMSSM Higgs Sector

The discussion of the MSSM Higgs sector in Section 2.4.1 has to be adapted to the appearance of another scalar field S with vev z. In analogy to the Higgs Portal, the singlet nature of the extra scalar field does not change the Standard Model gauge boson mass formulae and we end up with $m_Z^2 = \frac{1}{2}(g_L^2 + g_Y^2)v^2, m_W^2 = \frac{1}{2} g_L^2 v^2, v \equiv v_u^2 + v_d^2$ and $\tan\beta \equiv v_u/v_d$ identically to the MSSM. The combined scalar potential of H_u, H_d and S, however, now takes a slightly different form

$$\begin{aligned} V(H_u, H_d, S) =& |\lambda (H_u \cdot H_d) + \kappa S^2|^2 + \lambda^2 |S|^2 (|H_u|^2 + |H_d|^2) && \text{from } \mathcal{L}_{\mathcal{W}} \\ &+ \frac{g_L^2 + g_Y^2}{8} \left(|H_u|^2 - |H_d|^2 \right)^2 + \frac{g_L^2}{2} \left| H_u^\dagger H_d \right|^2 && \text{from } \mathcal{L}_{\text{gauge}} \\ &+ m_{H_u}^2 |H_u|^2 + m_{H_d}^2 |H_d|^2 + m_S^2 |S|^2 && \text{from } \mathcal{L}_{\text{scalar mass}} \\ &- (\lambda A_\lambda (H_u \cdot H_d) S - \frac{1}{3} \kappa A_\kappa S^3 + \text{h.c.}). && \text{from } \mathcal{L}_{\text{scalar interaction}}. \end{aligned} \tag{2.104}$$

The minimisation conditions for the three vevs v_u, v_d and z then read

$$m_{H_u}^2 + \mu_{\text{eff}}^2 + \lambda^2 v_d^2 + \frac{\left(g_L^2 + g_Y^2\right)}{4} \left(v_u^2 - v_d^2\right) = (A_\lambda - \kappa z) \mu_{\text{eff}} \cot\beta, \tag{2.105}$$

$$m_{H_d}^2 + \mu_{\text{eff}}^2 + \lambda^2 v_u^2 + \frac{\left(g_L^2 + g_Y^2\right)}{4} (v_d^2 - v_u^2) = (A_\lambda - \kappa z) \mu_{\text{eff}} \tan\beta, \tag{2.106}$$

$$m_S^2 + \kappa z (2\kappa z - A_\kappa) + \lambda^2 \left(v_d^2 + v_u^2\right) = (A_\lambda - 2\kappa z) \lambda \frac{v_d v_u}{z}. \tag{2.107}$$

Comparing the first two of these to their MSSM analogues in Eqs. (2.74) and (2.75) it seems reasonable to define $B_{\text{eff}} \equiv (A_\lambda + \kappa z)$ similarly to the effective μ term. Note that even though both of these conditions contain additional contributions $\propto \lambda^2$ compared to the MSSM case, they still can be combined to an almost identical version of Eq. (2.88)

$$m_Z^2 = \frac{2}{\tan\beta^2 - 1} (m_{H_d}^2 - \tan\beta^2 m_{H_u}^2) - 2\mu_{\text{eff}}^2. \tag{2.108}$$

The problematic $|\mu|^2$ contribution in the MSSM is replaced by the effective analogue in the $\mathbb{Z}_3$-symmetric NMSSM and thus, as z can be expected to be of same order as v_u, v_d, a more natural scenario has been created.

As we did for the previous models, we can use the minimisation conditions to substitute $m_{H_u}^2, m_{H_d}^2$ and m_S^2 with m_Z^2, $\tan\beta$, and μ_{eff}. Furthermore, in the remainder of this chaper we will substitute $A_\lambda = B_{\text{eff}} + \kappa z$ and $z = \mu_{\text{eff}}/\lambda$ as it simplifies the comparison with the MSSM, more specifically with its parameters μ and B.

We again start the discussion of mass eigenstates in the $\mathcal{CP}$-odd sector. The combined mass

matrix of all $\mathcal{CP}$–odd components $\{a_u^0, a_d^0, a_s^0\}$ reads

$$\mathcal{M}^2_{a_u^0(x),a_d^0(x),a_s^0(x)} = \left(\begin{array}{cc:c} & & v_d(B_{\text{eff}}\lambda + 3\kappa\mu_{\text{eff}}) \\ & \mathcal{M}^2_{a_u^0(x),a_d^0(x)} & v_u(B_{\text{eff}}\lambda + 3\kappa\mu_{\text{eff}}) \\ \hdashline \dots & \dots & \frac{1}{2}v^2\frac{\lambda}{\mu_{\text{eff}}}(B_{\text{eff}}\lambda - 3\kappa\mu_{\text{eff}})\sin 2\beta + 3A_\kappa\frac{\kappa}{\lambda}\mu_{\text{eff}} \end{array}\right) \tag{2.109}$$

with the 2×2 matrix in the upper left being the MSSM equivalent matrix of the two doublet-like pseudoscalars

$$\mathcal{M}^2_{a_u^0(x),a_d^0(x)} = B_{\text{eff}}\mu_{\text{eff}}\begin{pmatrix} \cot\beta & 1 \\ 1 & \tan\beta \end{pmatrix}. \tag{2.110}$$

We find the same structure as in the MSSM analogue Eq. (2.76). Hence we can apply the rotation in Eq. (2.80) to decouple the massless Goldstone boson mode. The leftover 2×2 submatrix of the MSSM-like pseudoscalar A and the singlet-like pseudoscalar a_s^0 reads

$$\mathcal{M}^2_{A(x),a_s^0(x)} = \begin{pmatrix} m_A^2 & v\left(\frac{1}{2}m_A^2\frac{\lambda}{\mu_{\text{eff}}}\sin 2\beta + 3\kappa\mu_{\text{eff}}\right) \\ \dots & 3A_\kappa\frac{\kappa}{\lambda}\mu_{\text{eff}} + \frac{1}{2}v^2\frac{\lambda}{\mu_{\text{eff}}}\sin 2\beta\left(\frac{1}{2}m_A^2\frac{\lambda}{\mu_{\text{eff}}}\sin 2\beta - 3\kappa\mu_{\text{eff}}\right) \end{pmatrix} \tag{2.111}$$

where we keep the MSSM definition[15] $m_A^2 \equiv 2B_{\text{eff}}\mu_{\text{eff}}/\sin 2\beta$. We therefore not only find an additional mass eigenstate A_2 compared to the MSSM but also a potentially large mixing between the doublet- and singlet-like pseudoscalars determined by the size of the NMSSM couplings λ, κ.

As the singlet field does not add new electrically charged particles, the charged Higgs sector of the NMSSM has the same dimensionality as in the MSSM case. The mass matrix, however, takes a slightly different form compared to Eq. (2.77)

$$\mathcal{M}^2_{h_u^+(x),h_d^+(x)} = \left(B_{\text{eff}}\mu_{\text{eff}} + \frac{1}{2}m_W^2\sin 2\beta - \frac{1}{2}(\lambda v)^2\sin 2\beta\right)\cdot\begin{pmatrix} \cot\beta & 1 \\ 1 & \tan\beta \end{pmatrix} \tag{2.112}$$

and, in addition to the usual massless Goldstone mode, contains a charged scalar particle with mass

$$m_{H^\pm} \equiv m_A^2 + m_W^2 - (\lambda v)^2 \tag{2.113}$$

which is smaller than the corresponding case in the MSSM, see Eq. (2.82).

Lastly, expanding H_u, H_d and S around their minima, one gets the following symmetric mass matrix for their $\mathcal{CP}$–even components $\{h_u, h_d, h_s\}$ at tree level:

$$\left(\begin{array}{cc:c} & & \mu_{\text{eff}}(2\lambda v_u + \kappa v_d) - \frac{1}{2}m_A^2\frac{\lambda}{\mu_{\text{eff}}}v_u\sin 2\beta \\ & \mathcal{M}^2_{h_u(x),h_d(x)} & \mu_{\text{eff}}(2\lambda v_d + \kappa v_u) - \frac{1}{2}m_A^2\frac{\lambda}{\mu_{\text{eff}}}v_d\sin 2\beta \\ \hdashline \dots & \dots & \frac{1}{2}v^2\frac{\lambda}{\mu_{\text{eff}}}\sin 2\beta(\frac{1}{2}m_A^2\frac{\lambda}{\mu_{\text{eff}}}\sin 2\beta + \kappa\mu_{\text{eff}}) + \frac{\kappa}{\lambda}\mu_{\text{eff}}(4\frac{\kappa}{\lambda}\mu_{\text{eff}} - A_\kappa) \end{array}\right) \tag{2.114}$$

[15] Even though this quantity does not correspond to a physical mass any more, we continue to use m_A to simplify the following expressions. Note that in the original "decoupling limit" $m_A \gg m_Z$ in fact only one eigenstate of Eq. (2.111) decouples.

with the upper h_u, h_d submatrix

$$\mathcal{M}^2_{h_u(x),h_d(x)} = \begin{pmatrix} m_Z^2 \sin^2\beta + m_A^2 \cos^2\beta & \left(\lambda^2 v^2 - \frac{1}{2}(m_Z^2 + m_A^2)\right)\sin 2\beta \\ \left(\lambda^2 v^2 - \frac{1}{2}(m_Z^2 + m_A^2)\right)\sin 2\beta & m_Z^2 \cos^2\beta + m_A^2 \sin^2\beta \end{pmatrix}. \quad (2.115)$$

Compared to the MSSM case in Eq. (2.83), we find additional $\mathcal{O}(\lambda^2)$ contributions which affect[16] the lightest eigenvalue in the decoupling limit

$$m_h \approx m_Z^2 \cos^2 2\beta + (\lambda v)^2 \sin^2 2\beta \quad (2.116)$$

The peculiar upper tree level bound of the MSSM is therefore lifted due to the mixing in the singlet sector. In the context of naturalness, this is a very fortunate effect as we do not necessarily require large higher order corrections as in Eq. (2.87) and thus do not need heavy third generation squarks. A full diagonalisation of Eq. (2.114) yields three $\mathcal{CP}$-even mass eigenstates which we refer to as h, H and H_3.

2.5.3 Natural NMSSM Electroweakinos

In the MSSM, we had four neutral and two charged fermionic partners of Higgs and gauge bosons which mixed into neutralinos and charginos, see Section 2.4.3. In the NMSSM, the fermionic partner $\widetilde{S}$ of the new singlet chiral superfields adds an additional neutral fermion to the particle content which mixes with the MSSM neutralino sector due to the λ operator. The resulting 5×5 matrix can therefore result in an even more intertwined neutralino sector for the general NMSSM.

However, as explained in the beginning of this chapter we are interested in a spectrum which only contains particles which are necessarily light due to naturalness arguments. This constraint does not affect the mass scale of the fermionic partners of the $SU(2)_L \otimes U(1)_Y$ gauge bosons such that we can easily decouple them by setting M_1, M_2, the gaugino mass terms in Eq. (2.95), to sufficiently high values.

The mass matrix of the remaining three neutral fermionic partners of the Higgs chiral superfields fields, $\widetilde{h}_u^0$, $\widetilde{h}_d^0$ and $\widetilde{s}^0$, reads

$$\mathcal{M}_{\widetilde{h}_u^0(x),\widetilde{h}_d^0(x),\widetilde{s}^0(x)} = \begin{pmatrix} 0 & -\mu_{\text{eff}} & -\lambda v_u \\ -\mu_{\text{eff}} & 0 & -\lambda v_d \\ -\lambda v_u & -\lambda v_d & 2\frac{\kappa}{\lambda}\mu_{\text{eff}} \end{pmatrix}. \quad (2.117)$$

As a natural μ_{eff} value is of order m_Z, we expect the two higgsino-like neutralinos to have mass close to the electroweak symmetry breaking scale. Furthermore, the stability of the vacuum with non-vanishing vevs for H_u, H_d and S over the cosmological evolution of the Universe typically requires $\kappa \lesssim \lambda$ [106] and thus keeps the singlino-like neutralino mass also at scale μ_{eff}. We thus expect three neutralinos $\widetilde{\chi}^0_{1,2,3}$ with masses of few $\mathcal{O}(100\ \text{GeV})$. As all off-diagonal elements are proportional to the NMSSM coupling λ, some sizable mixing can occur if this parameter is of order 1. Alternatively, for small values of this parameter we end up with two mass-degenerate higgsino-like neutralinos with mass $\approx \mu_{\text{eff}}$ and one singlino-like neutralino with mass $2\kappa/\lambda\mu_{\text{eff}}$.

[16] Clearly the formula in Eq. (2.116) is only to be understood qualitatively as we did not diagonalise the full mass matrix Eq. (2.114) with its nonvanishing off-diagnal entries. However, the given statement regarding the raise in m_h holds also when taking the full matrix into account, see e.g. Ref. [105].

With similar argumentation as above, the chargino matrix in the NMSSM is reduced due to the possibility to decouple the fermionic $\widetilde{W}^{\pm}$ gaugino. Hence, the remaining two charged higgsino components combine to a single Dirac chargino $\widetilde{\chi}_1^{\pm}$ with mass term

$$\mathcal{L}_{\widetilde{\chi}_1^{\pm}} = -\frac{1}{2}\mu_{\text{eff}}\widetilde{h}_u^+\widetilde{h}_d^- + \text{h.c.} \tag{2.118}$$

and thus is expected at the same mass scale as the higgsino-like neutralinos.

To simplify the following discussion, we use the collective term "higgsino" $(\widetilde{h})$ for the two higgsino-like neutralinos and the chargino. Furthermore, for the sake of simplicity, we use "electroweakino" $(\widetilde{\chi})$ collectively for all three neutralinos and the chargino, even though strictly speaking $\widetilde{s}$ does not have any electroweak charge.

2.5.4 Strongly Interacting Particles of the Natural NMSSM

In the definition of our NMSSM superpotential Eq. (2.101) we alread put in the idea of only considering the SUSY partners of gluon, top and bottom quark to be light as only those are bound by naturalness arguments due to their large Yukawa coupling, see Eqs. (2.93) and (2.94). All other gauginos and sfermions are decoupled, e.g. by setting the corresponding soft breaking mass terms in Eq. (2.65) high enough.

The tree level mass of the gluino, which we from now on refer to by its shorter name $\tilde{g}$, is simply given by the soft SUSY breaking parameter M_3 in Eq. (2.103). The relevant matrices for the stop and sbottom tree level masses read

$$\mathcal{M}^2_{\widetilde{t}_L(x),\widetilde{t}_R(x)} = \begin{pmatrix} m^2_{\widetilde{Q}_3} + m_t^2 + \frac{1}{6}(3m_Z^2 - 4m_W^2)\cos 2\beta & m_t(A_t - \mu_{\text{eff}}\cot\beta) \\ m_t(A_t - \mu_{\text{eff}}\cot\beta) & m^2_{\widetilde{U}_3^c} + m_t^2 - \frac{2}{3}m_W^2\cos 2\beta \end{pmatrix}, \tag{2.119}$$

$$\mathcal{M}^2_{\widetilde{b}_L(x),\widetilde{b}_R(x)} = \begin{pmatrix} m^2_{\widetilde{Q}_3} + m_b^2 + \frac{1}{6}(2m_W^2 - 3m_Z^2)\cos 2\beta & m_b(A_b - \mu_{\text{eff}}\tan\beta) \\ m_b(A_b - \mu_{\text{eff}}\tan\beta) & m^2_{\widetilde{D}_3^c} + m_b^2 - \frac{1}{3}m_W^2\cos 2\beta \end{pmatrix}, \tag{2.120}$$

with eigenstates $\widetilde{t}_{1/2}, \widetilde{b}_{1/2}$. Here, $m_t = v_u h_t, m_b = v_d h_b$ are the tree level top and bottom quark masses just as in the MSSM. Due to the scaling of the off-diagonal elements with these masses, the stop sector typically shows a larger mixing with a more apparent splitting between the two mass eigenstates than the sbottom sector. Note that $\widetilde{t}_L, \widetilde{b}_L$ originate from the same $SU(2)$ doublet and hence each scale with the same soft SUSY breaking parameter $m^2_{\widetilde{Q}_3}$ whereas the corresponding right chiral components each come with individual $m^2_{\widetilde{D}_3^c}, m^2_{\widetilde{U}_3^c}$. In fact, from naturalness arguments only, the sbottom mass parameter $m^2_{\widetilde{D}_3^c}$ is not bounded by Eq. (2.93). Often, the particle $\widetilde{b}_R$ is hence considered to be decoupled as well. However, in the analysis pursued within this thesis, we will keep this parameter degenerate with the other soft third generation squark masses $m^2_{\widetilde{U}_3^c}, m^2_{\widetilde{Q}_3}$, as we do not have any *a priori* reason why Supersymmetry should introduce a big hierarchy between the two chiral bottom partners.

2.5.5 Final Remarks

Again, we only pursued a tree-level discussion of the masses and mixings in our simplified, natural NMSSM setup. As we have already seen during the discussion of the naturalness

problem in Section 2.4.2, the large values of the Yukawa coupling h_t and the strong coupling constant α_S lead to sizable one-loop corrections to the tree-level values we listed before. For a proper study, these should therefore be taken into account. As the singlet field S only couples to the Higgs fields the one-loop diagrams for electroweakino, squark and gluino masses are identical in the NMSSM and the MSSM. An exhaustive discussion of the one-loop calculation of the latter can be found in Ref. [107]. However, the scale dependence via the renormalisation group equations does change due to the presence of the parameters $\lambda, \kappa, A_\lambda, A_\kappa$ and can be found for the NMSSM in e.g. Ref. [108].

For the Higgs sector, however, the MSSM result is significantly affected by the singlet contributions already at tree level and therefore clearly have to be taken into account as well in higher order calculations. Here, calculations require two-loop accuracy, see e.g. Ref. [109], in order to reach a precision of $\mathcal{O}$(few GeV). However, differences up to 8 GeV can arise simply due to different approaches in the fixed order calculation, see Ref. [110]. As we discuss in Section 3.1, there are various computer tools which can do the above calculations automatically. We in particular make use of the programm `NMSSMTools` [111] whose features we discuss in more detail in Section 6.3.1.

Note that also in a higher order calculation of the masses and mixings in our natural NMSSM scenario, a given setup is fixed by specifying the parameters $\{\lambda,\ \kappa,\ A_\lambda,\ A_\kappa,\ \mu_{\text{eff}},\ \tan\beta,\ m^2_{\widetilde{Q}_3},\ m^2_{\widetilde{U}^c_3},\ m^2_{\widetilde{D}^c_3},\ A_t,\ A_b,\ M_3\}$.

2.6 Summary

In this chapter, we started with an introduction to the Standard Model of particle physics and reasons why we believe it is not the full theory of Nature. We then briefly motivated and discussed three interesting theories beyond the Standard Model:

1. The *Higgs Portal* model extends the Standard Model field content by a singlet scalar field S which among all Standard Model particles only couples to the Standard Model Higgs boson at the renormalisable level. The field S is connected to a dark sector which we assume to contain the gauge boson Z' associated to a dark gauge group which only S is charged under. If S acquires a vacuum expectation value, the Z' boson gains mass and since it is stable could hence provide the dark matter candidate which is missing in the Standard Model. In such a scenario, the singlet scalar would mix with the Standard Model Higgs field and result in two scalar particles h, H which can both couple to the dark sector and the Standard Model. This model is further discussed in Chapter 5.

2. The *Natural NMSSM* is an extension to the well-known MSSM, the minimal supersymmetric extension of the Standard Model. The Standard Model like scalar boson which results from diagonalising the two MSSM Higgs fields has an upper tree level mass bound which seems inconsistent with the observation of a 125 GeV Standard Model boson at the LHC. Higher order corrections due to heavy third generation squarks can raise the mass to the observed value which however leads to an unnatural Higgs potential. The NMSSM avoids this naturalness problem by adding another chiral superfield S, similarly to the Higgs Portal, which can raise the Higgs boson mass already at the tree level due to mixing effects. This can allow for naturally light third generation squarks and gluinos. In addition, a natural effective μ term leads to three relatively light neutralinos and one chargino. We discuss the collider phenomenology of such a mass hierarchy in Chapter 6.

3. During the supersymmetrisation of the Standard Model, *R-Parity violating* terms appear which can easily violate experimental low-energy constraints as they violate baryon and/or lepton number. However, various possible discrete symmetries can forbid one or more of these terms in such a way that invidiual terms can be non-vanishing while not being in conflict with existing bounds. An important difference to the MSSM is that the lightest supersymmetric particle, typically the lightest neutralino, is not necessarily stable. This allows for neutralino masses of the scale of Standard Model mesons which in the R-Parity conserving MSSM would violate cosmological constraints. The observation of possible phenomenological consequences of such a setup is discussed in Chapter 7.

CHAPTER 3

Principles of Monte-Carlo Based Proton-Proton Collider Phenomenology

One insightful experimental method to test the models we have described in Chapter 2 is to accelerate two elementary or composite particles to high energies and bringing them to collision. This will result in either the same two particles simply moving in a different direction with unchanged kinetic energy (*elastic scattering*) or — the typically more interesting case — in the production of new final state particles (*inelastic scattering*).

According to the principles of quantum mechanics, given a state of fixed energy in the initial state, there usually exists an infinite set of possible final states, each associated with a finite and deterministic probability to be observed if the experiment is performed. By redoing the experiment often enough, these predictable probabilities become measurable via the frequencies with which certain final states are observed.

For a scattering experiment, these frequencies can be measured by counting the number $N^{\text{exp.}}$ of experimentally observed final state configurations (*events*) which pass a well-defined set of constraints (*cuts*). These cuts, as will be explained later within this chapter, typically select events with a specific number of final state objects which pass well-chosen kinematic constraints, usually designed to be sensitive to a particular class of models.

The analogous number $N^{\text{th.}}$ can be derived from the theoretically predicted probabilities of a final state to occur. Hence, comparing the two numbers tests the compatibility of the given theoretical model with experimental facts. This prediction $N^{\text{th.}}$ is always associated with an error $\Delta N^{\text{th.}}$ which combines uncertainties arising from inaccuracies within the experimental setup as well as potential approximations in the theoretical calculation. Therefore, the compatibility test usually returns a continuous p-value which states the probability that the observation can be explained within the uncertainties of the theoretical model. The acceptance range for this probability can in principle be chosen at will, however a commonly used convention is to discard a model if it returns a p-value of less than 5 %.

The calculation of the number of events $N^{\text{th.}}$ can be written in the following factorised form

$$N^{\text{th.}} = \sum_{\text{final states } X} \Big(\sigma_{pp\to X} \times \mathcal{A}(X) \times \epsilon(X) \Big) \times L, \tag{3.1}$$

with the *cross section* σ for a given process X, the *acceptance* $\mathcal{A}$, the *final state efficiency* ϵ and the integrated luminosity L. Except for L, which is a purely experimental quantity that is fixed for a given dataset (for more information see Appendix A.1), the other numbers are highly model-dependent and all need to be evaluated carefully to compare theory to experiment.

Within this chapter, we explain the meaning of these individual contributions and sketch numerical methods based on Monte-Carlo simulations, i.e. simulations of representative finite

event samples, to evaluate them. Since a significant portion of this thesis is related to the creation of a computer tool which seeks to automise parts of this calculation, a particular focus is put on the current status of other publicly available tools which help finding one or more of the ingredients in Eq. (3.1). Afterwards, we illustrate the standard statistical method to compare $N^{\text{th.}}$ to $N^{\text{exp.}}$.

Parts of this chapter are based on excellent summaries of the topic in Refs. [112–115] and we refer to these and references therein for further information.

3.1 Model Building and Interpretation

Finding Particles and Interactions In Chapter 2 we have seen examples for different particle physics models. Such a model is typically defined by a declaration of the symmetries of the physical system, the set of fields the model is supposed to contain and how these fields transform under the given symmetry groups. From that information, the most general, renormalisable Lagrangian can be constructed and all free parameters of the theory can be defined. This sets up the mathematical framework of the theory and all its degrees of freedom.

However, in order to do phenomenological studies, the mathematical language of products of fields within a Lagrangian must be translated into a set of particles with well defined masses and a list of possible interactions with their respectice coupling constants. We already illustrated the basic steps of this conversion within the examples of Chapter 2:

1. Given the field content construct the most general Lagrangian which is renormalisable[1] and invariant under the assumed symmetries.

2. In case of spontaneously broken symmetries, minimise the potential and expand fields around their vacuum expectation values.

3. Identify the mass eigenstates (*particles*) of the resulting theory by redefining fields such that bilinear terms in the Lagrangian are diagonal.

4. Identify the interaction terms (*Feynman rules*) of these redefined particle fields.

`LanHEP` [117], `FeynRules` [118] and `SARAH` [119] are current state-of-the art tools which can do the above calculations for in principle any quantum field theoretical model based on the Lagrangian formulation. By providing a set of symmetries, fields and defining the corresponding terms in the Lagrangian, these tools can determine the respective individual Feynman rules of mass eigenstates in terms of the provided parameters. In the case of supersymmetric models, `SARAH` can also work with the formulation of superfields and do the respective Lagrangian decomposition. Results can be stored in the common *universal file format* (`UFO` [120]) which consists of a set of files containing all necessary analytical information (particles, parameters and vertices) to allow successive tools to calculate particle interactions given the parameters provided. These files can be read by almost all the event generator programs described below, thus enabling the user to choose the combination of tools which suits the given problem best.

[1] The renormalisability constraint can be relaxed in so-called *effective theories*. Here, higher dimensional operators are allowed but by construction suppressed by a mass scale Λ_{extNP} at which new physics is supposed to enter. Within the effective framework, sensible predictions can be made without knowing the actual physics at Λ_{extNP}. A very famous example is Fermi's theory of beta decay [116] via operators of type $\frac{G}{\Lambda^2_{extNP}}(\bar{n}\gamma^\mu P_L p)(\bar{\nu}_e\gamma^\mu P_L e)$. Those gave accurate predictions for energies below the new physics scale $\Lambda_{extNP} \approx M_W$.

```
# Input parameters
BLOCK MODSEL
  3  1   # NMSSM particle content
  1  0   # IMOD
 10  0   # ISCAN
  9  0   # Call micrOmegas
  8  2   # Precision for Higgs masses
 13  1   # Sparticle decays via NMSDECAY
 14  0   # H-> VV,VV*,(V*V*)
BLOCK SMINPUTS
     1     1.27920000E+02   # ALPHA_EM^-1(MZ)
     2     1.16639000E-05   # GF
     3     1.17200000E-01   # ALPHA_S(MZ)
     4     9.11870000E+01   # MZ
     5     4.21400000E+00   # MB(MB)
     6     1.73100000E+02   # MTOP (POLE MASS)
     7     1.77700000E+00   # MTAU
BLOCK MINPAR
     3     2.00000000E+00   # TANBETA(MZ)
BLOCK EXTPAR
     1     9.00000000E+03   # M1
     2     9.00000000E+03   # M2
     3     1.00000000E+03   # M3
    11    -7.30000000E+02   # ATOP
    12    -7.30000000E+02   # ABOTTOM
    13    -7.30000000E+02   # ATAU
    16     0.00000000E+00   # AMUON
    31     5.00000000E+03   # LEFT SELECTRON
    32     5.00000000E+03   # LEFT SMUON
    33     5.00000000E+03   # LEFT STAU
    34     5.00000000E+03   # RIGHT SELECTRON
    35     5.00000000E+03   # RIGHT SMUON
    36     5.00000000E+03   # RIGHT STAU
    41     5.00000000E+03   # LEFT 1ST GEN. SQUARKS
    42     5.00000000E+03   # LEFT 2ND GEN. SQUARKS
    43     1.00000000E+03   # LEFT 3RD GEN. SQUARKS
    44     5.00000000E+03   # RIGHT U-SQUARKS
    45     5.00000000E+03   # RIGHT C-SQUARKS
    46     1.00000000E+03   # RIGHT T-SQUARKS
    47     5.00000000E+03   # RIGHT D-SQUARKS
    48     5.00000000E+03   # RIGHT S-SQUARKS
    49     1.00000000E+03   # RIGHT B-SQUARKS
    61     6.50000000E-01   # LAMBDA
    62     2.60264000E-01   # KAPPA
    63     3.43434000E+02   # ALAMBDA
    64     2.72727000E+01   # AKAPPA
    65     2.46000000E+02   # MUEFF
```

(a) Input

```
[...]
BLOCK MASS   # Mass spectrum
#  PDG Code     mass              particle
        25     1.21688763E+02   # lightest neutral scalar
        35     1.97493947E+02   # second neutral scalar
        45     5.44797841E+02   # third neutral scalar
        36     1.10448059E+02   # lightest pseudoscalar
        46     5.42139501E+02   # second pseudoscalar
        37     5.35378526E+02   # charged Higgs
   1000001     5.05113975E+03   #  ~d_L
   2000001     5.05097751E+03   #  ~d_R
                    [...]
   1000006     4.97617385E+02   #  ~t_1
   2000006     9.44627010E+02   #  ~t_2
                    [...]
   1000021     1.23549746E+03   #  ~g
   1000022     1.99078415E+02   # neutralino(1)
   1000023     2.73162969E+02   # neutralino(2)
   1000025    -2.73695857E+02   # neutralino(3)
                    [...]
BLOCK LOWEN
# Exp. 2 Sigma: 3.04E-4 < BR(b -> s gamma) < 4.06E-4:
     1     3.58336780E-04   # BR(b -> s gamma)
    11     4.01784715E-04   # (BR(b -> s gamma)+Theor.Err.)
    12     2.95480186E-04   # (BR(b -> s gamma)-Theor.Err.)
                    [...]
# 3*3 Higgs mixing
BLOCK NMHMIX
  1  1     4.59645551E-01   # S_(1,1)
  1  2     8.87143833E-01   # S_(1,2)
  1  3     4.12527148E-02   # S_(1,3)
  2  1     1.16411265E-01   # S_(2,1)
  2  2    -1.06234307E-01   # S_(2,2)
  2  3     9.87503260E-01   # S_(2,3)
  3  1     8.80439881E-01   # S_(3,1)
  3  2    -4.49099200E-01   # S_(3,2)
  3  3    -1.52103663E-01   # S_(3,3)
                    [...]
#         PDG            Width
DECAY   1000006     3.56161272E+00   # stop1
#                    stop1 2-body decays
#          BR         NDA      ID1       ID2
     3.39136358E-01    2     1000022     6   # BR(~t_1 -> ~chi_10 t )
     1.24883588E-01    2     1000023     6   # BR(~t_1 -> ~chi_20 t )
     4.41259715E-01    2     1000025     6   # BR(~t_1 -> ~chi_30 t )
     9.47203398E-02    2     1000024     5   # BR(~t_1 -> ~chi_1+ b )
                    [...]
```

(b) Output

Figure 3.1: Exemplary SLHA file for the NMSSM model as used by NMSSMTools. The input parameters can be set by the user by simply editing a text file. Running NMSSMTools on this file produces another file of similar layout which shows results for masses, mixing matrices, low energy observables, high- and low-scale parameters and decay tables for all unstable particles.

In addition to the above mentioned set of UFO files, which carry the analytical information of the underlying model, a *SUSY LesHouches Accord* (SLHA [121]) file is commonly used to store all numerical information; using these file, the user typically fixes the numerical values of the free model input parameters and uses the above mentioned tools to calculate the corresponding masses, mixing matrices, branching ratios etc. which are stored in the same file format. In Fig. 3.1, we show an example input/output combination for the special case of an NMSSM model calculated with NMSSMTools.

As a final note it should be mentioned that, despite their name, SLHA files are also used nowadays to store information of non-supersymmetric models.

Consider Higher Order Effects Note that in the above prescription, free model parameters can be defined at various stages. After the model is fully translated, they can be related to physical observables. However, quantum effects and the resulting renormalisation procedure can complicate these relations significantly. Besides, calculating observables beyond tree

level usually introduces dependencies of the observables on the energy scale of the process. In *Grand Unified Theories*, e.g. $SU(5)$ [122] or minimal Supergravity [123], these scale dependencies are used to define parameter constraints at very high scales. In those cases, additional calculations are required in order to relate the model parameters defined at a high scale to the phenomenologial parameters observable at a low scale by *Renormalisation Group Equations* (RGEs). There exist many tools which are designed to do this numerical calculation for particular models, most importantly Supersymmetry (e.g. `SPheno` [124], `SOFTSUSY` [125], `NMSSMTools` [111], `ISASUSY` [126], `Suspect` [127]). `SARAH` is able to calculate one-loop corrections to tadpole and self energy diagrams as well as the RGEs for any model the user provides up to second order in its parameters. The tool then writes plugins which can be used with the above mentioned spectrum generator `SPHENO` to do the running between high and low scales numerically for specific parameter values.

3.2 Production Cross Section $\sigma_{pp\to X}$ and Monte-Carlo Event Generation

The cross section $\sigma_{pp\to X}$, in simple words, is a measure of the probability for the final state X to be the outcome of a collision of two protons. Depending on the circumstances, X can specify different things. For instance, $pp \to W^+$ could specify the *exclusive* production of a positively charged W-boson, whereas $pp \to W^+ +$ jets would *inclusively* allow for one or more hard jets to be present in the final state[2].

In case X contains particles which are unstable on collider scales, e.g. $c\tau \ll \mathcal{O}(\text{mm})$, it is implicitly assumed that X considers all possible decays of these particles with their respective branching ratios, unless specifically mentioned. In the above example, final states described by $pp \to W^+$ would contain two leptons in approximately a third of all scattering events and hadronic final states for the rest. Alternatively, $pp \to W^+ \to e^+\nu_e$ would only contain the lepton final states.

It is fair to say that in most cases it is $\sigma_{pp\to X}$ which is the most important theoretical contribution to Eq. (3.1). The integrated luminosity L is a fixed experimental quantity and the acceptance and efficiency factors $\mathcal{A} \times \epsilon$ are by construction smaller than 1. Hence it is the cross section which defines the initial scale of the expected event rates and only if it exceeds about $3/L$ a reasonable sensitivity is at all feasible.

Since proton-proton collisions involve strongly interacting particles in the initial and often also in the final state, it becomes practically impossible to evaluate the cross section analytically and one has to rely on numerical methods, usually based on Monte-Carlo integration. Due to the significantly different behaviour of the strong interaction above or below the confinement scale $\Lambda_{QCD} \approx 200\,\text{MeV}$, perturbative methods for the hard interaction and non-perturbative algorithms for soft radiation have to be combined in a systematic way. Therefore, the numerical evaluation of σ consists of various individual parts, graphically represented in the diagram in Fig. 3.2 and outlined step-by-step in the following.

[2] Already from charge conservation it is clear that $pp \to W^+$ does in fact not describe a final state with just a W boson with nothing else but implicitly includes the hadronised remnants of the proton. With X, we merely specify the interesting, high-energetic, model-depdenent part of the final state which is created by the hard scattering of partons.

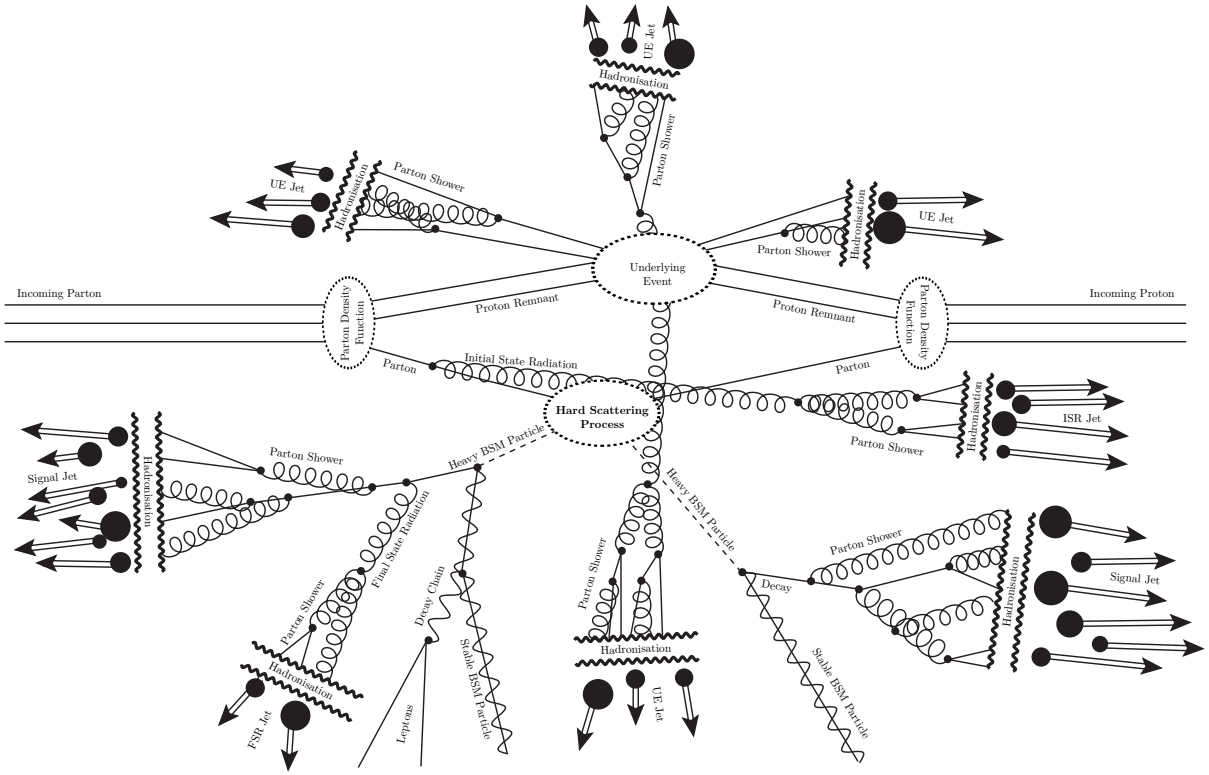

Figure 3.2: Schematical overview about the individual steps of the simulation of a full proton-proton collision. The individual contributions are explained within this chapter. For the sake of clarity, some effects have been neglected or have been represented in a simplified manner. For example, colour reconnection effects would lead to further hadronic activity between the various jet final states.

3.2.1 Parton Interactions and PDFs

Since the proton is a composite object consisting of quarks and gluons, collectively called *partons*, the collision of two protons with centre of mass energy $\sqrt{s}$ can be reformulated as the collision of two partons p_1 and p_2 which carry a fraction $x_{1/2} \equiv 2E_{1/2}/\sqrt{s}$ of the proton's energy [115]:

$$\sigma_{pp\to X} = \sum_{p_1,p_2} \int_0^1 \mathrm{d}x_1 \int_0^1 \mathrm{d}x_2 \; f_{p_1/p}(x_1,\mu_F) f_{p_2/p}(x_2,\mu_F) \hat{\sigma}_{p_1p_2\to X}(x_1,x_2,\mu_F). \tag{3.2}$$

Here, we sum over all possible partons $p_1, p_2 \in \{g, u, \bar{u}, d, \bar{d}, s, \bar{s}, c, \bar{c}, b, \bar{b}, t, \bar{t}\}$ and integrate the *partonic cross section* $\hat{\sigma}_{p_1p_2\to X}$ weighted with the *parton distribution functions* (PDFs) $f_{p_i/p}(x, \mu_F)$, i.e. the probabilities to find a parton p_i with energy $x_i E_i$ inside a proton with energy E_i. The separation of low-energy physics being parameterised by the PDF and high-energy interactions described by the partonic cross section is specified by the *factorisation scale* μ_F. A meaningful result should not largely depend on this artificial scale which is typically achieved by setting it to the energy scale of the scattering process, e.g. the partonic center-of-mass energy $\hat{s}$ in an s-channel process or the momentum transfer Q^2 in a t-channel process [113].

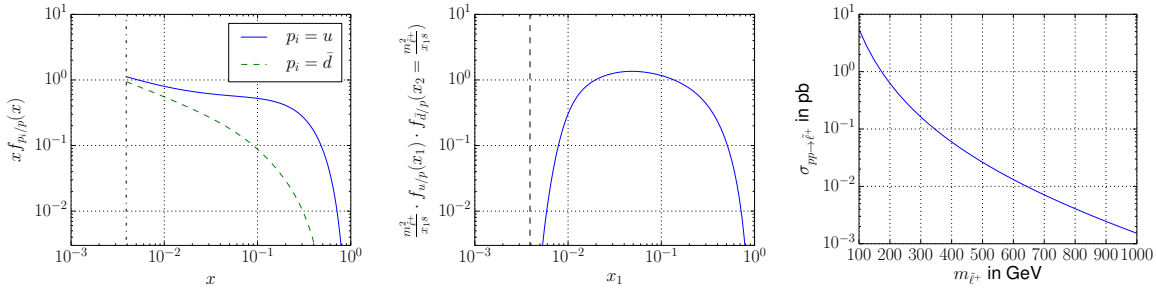

(a) (b) (c)

Figure 3.3: Example distributions for the resonant production of charged sleptons in RPV at the LHC with $\sqrt{s} = 8\,\text{TeV}$ at leading order. (a): Relevant momentum densities $xf(x, \mu_F^2 = m^2_{\tilde{\ell}^+})$ of the proton fitted by the `MSTW` collaboration [128, 129]. (b) PDF product which contributes to resonant production, see Eq. (3.4). Both (a) and (b) use a benchmark value of $m_{\tilde{\ell}^+} = 500\,\text{GeV}$ and dashed-dotted lines denote the lower limit $x \geq m^2_{\tilde{\ell}^2}/s$ for resonant production to be possible. (c): Resulting total proton proton cross section as a function of mass.

The PDFs of the proton are determined by low-energy quantum chromodynamics and are therefore mostly model-independent[3]. They have been experimentally determined by fitting the Dokshitzer-Gribov-Lipatov-Altarelli-Parisi (DGLAP [131]) splitting equations of QCD to various data from deep inelastic scattering (see e.g. [129] and references therein). This set of differential equations describes the evolutions of partons in the low-energy limit via functions $P_{i,jk}$ which represent the probability of the process $i \to j + k$, with i, j, k denoting quarks or gluons. Different fits consider different datasets and different approximations of the functions $P_{i,jk}$. Thus there exists a variety of available PDF implementations (e.g. `CTEQ` [132], MSTW/MRST [129] or `HeraPDF` [133]) which can collectively be used via the `LHAPDF` framework [134]. A selection of these functions are already implemented in the event generators described below and thus the user does not need to take care of the proper folding. However, an analysis of different PDF choices might be advisable to estimate the theory uncertainty caused by different assumptions in the above factorisation ansatz.

To illustrate the process from partonic to hadronic cross section, we show example distributions for the simple case of resonant production process $pp \to \tilde{\ell}_i^+$ in an R-Parity violating scenario with a nonvanishing $\lambda'_{i11} = 0.01$ in Fig. 3.3, see also [135]. The tree-level parton cross section for this process reads [136, 137]

$$\hat{\sigma}_{u\bar{d}\to\ell^+}(x_1, x_2, \mu_F^2) = \hat{\sigma}_0(x_1, x_2)\delta\Big(1 - \frac{m^2_{\tilde{\ell}^+}}{x_1 x_2 s}\Big) \text{ with } \hat{\sigma}_0(x_1, x_2) = \frac{|\lambda'_{i11}|^2\pi}{12 x_1 x_2 s}. \tag{3.3}$$

Note that since this is a tree-level process, there is no dependence of $\hat{\sigma}$ on the factorisation scale and the integral in Eq. (3.2) becomes 1-dimensional due to the on-shell condition $x_1 x_2 s \stackrel{!}{=} m^2_{\tilde{\ell}^+}$, i.e.

$$\sigma_{pp\to\tilde{\ell}^+} = 2\int_r^1 \mathrm{d}x_1 \; \frac{r}{x_1} \; f_{u/p}\Big(x_1, m_{\tilde{\ell}^+}\Big) f_{\bar{d}/p}\Big(\frac{r}{x_1}, m_{\tilde{\ell}^+}\Big)\hat{\sigma}_0\Big(x_1, \frac{r}{x_1}\Big) \text{ with } r \equiv \frac{m^2_{\tilde{\ell}^+}}{s}. \tag{3.4}$$

[3] Models which predict very light, strongly interacting particles can have an impact on the parton density functions. See e.g. Ref. [130] for an example study with very light gluinos in a supersymmetric scenario.

3.2.2 Hard Matrix Element

The calculation of a general partonic cross section can be further factorised into the following form:

$$\hat{\sigma}(p_1 p_2 \to FS) = \frac{1}{2\hat{s}} \int \mathrm{d}\Phi_{FS} \left| \mathcal{M}\Big(p_1 p_2 \to FS\Big) \right|^2 \tag{3.5}$$

with the invariant mass $\hat{s} \equiv x_1 x_2 s$ of the partonic system, the hard partonic matrix element $\mathcal{M}$ and the phase space factor $\mathrm{d}\Phi_{FS}$ over all configurations of final state particle momenta which agree with four-momentum conservation.

The hard matrix element $\mathcal{M}$, typically averaged/summed over unobserved degrees of freedom of incoming/outgoing particles, shows the strongest dependence on the considered model; from the Feynman rules determined in the last step of Section 3.1, all Feynman diagrams for the given process can be constructed and algebraically evaluated according to standard text book formalisms.

Often it is advisable to restrict the phase space integration $\int \mathrm{d}\Phi_{FS}$ to avoid sampling of points which will surely not pass the acceptance and/or efficiency steps described below. The main advantages are the avoidance of dangerous divergent regions of phase space which arise in fixed order QCD calculations and a potential significant speed-up of the overall computational time. However, care must be taken when choosing to cut on phase space since sometimes the effect on the selection efficiency ϵ might not be obvious. As an example, cuts on hadronic objects affect the total hadronic activity of the event which can impact the reconstruction accuracy of missing transverse energy [138] and therefore no strong cut on the final state partons should be set if the low-E_T^{miss} distribution is relevant in the selection.

In the RPV example of the last section we were able to give a completely analytical result for $\hat{\sigma}$. However, since the phase space integration becomes quickly cumbersome for final state multiplicities beyond three, numerical Monte-Carlo integration techniques are used instead. The general approach is to randomly generate on-shell energy-momentum configurations of all final state particles which conserve both energy and momentum of the event. The quantity $|\mathcal{M}|^2$ is then calculated and used as a weight to accept or reject the given configuration. Even though hypothetically easy to achieve, resonances and similarly near-divergent kinematic regions render an efficient practical implementation non-trivial. For more information on this subject, a hands-on introduction to Monte-Carlo event generation can be found in Ref. [139] and the documentation of the tools listed below yields details on the respectively used algorithms.

For the successive steps in the evaluation of $\sigma_{pp\to X} \times \mathcal{A}(X) \times \epsilon(X)$, it will turn out to be useful not just to determine the numerical value of the partonic cross section but also to create a finite sample of events which mimic the kinematic distributions of the assumed underlying model. Such a sample can straightforwardly be created within the considered Monte-Carlo approach by simply storing all accepted phase space configurations in the form of pseudo-data. A common file format for these parton events is the *Les Hoches Event File* (`LHE` or `.lhe`, [141]). It stores global information (e.g. generator settings and total parton cross section) as well as event-wise information (e.g. event weights and four-momenta of each particle) in a human-readable XML-format. In Fig. 3.4, we show and explain the numbers of an example BSM event using this event format.

Publicly available tools which can perform the partonic event generation for any model provided the `UFO` files (see Section 3.1) are `MadGraph5_aMC@NLO` [142], `WHIZARD` [143] and `CalcHep` [144]. Furthermore, `Herwig` [145] and `Sherpa` [146] are also able to read `UFO` files but are unable

```
<event>
4   0  0.4765200E-01  0.9298159E+03  0.7816531E-02  0.9389059E-01
       21   -1    0    0  502  501  0.00000000000E+00  0.00000000000E+00  0.72910386241E+03  0.72910386241E+03  0.00000000000E+00 0. -1.
       21   -1    0    0  504  502  0.00000000000E+00  0.00000000000E+00 -0.16805033323E+04  0.16805033323E+04  0.00000000000E+00 0. -1.
  1000021    1    1    2  503  501 -0.48289281304E+03 -0.51191421184E+03  0.17799846065E+03  0.94670006989E+03  0.60771370000E+03 0. -1.
  1000021    1    1    2  504  503  0.48289281304E+03  0.51191421184E+03 -0.11293979306E+04  0.14629071248E+04  0.60771370000E+03 0. -1.

[...]
</event>
<event>
4   0  0.4765200E-01  0.7468419E+03  0.7816531E-02  0.9640318E-01
       1   -1    0    0  503    0  0.00000000000E+00  0.00000000000E+00  0.34357082340E+03  0.34357082340E+03  0.00000000000E+00 0.  1.
      -1   -1    0    0    0  501  0.00000000000E+00  0.00000000000E+00 -0.17383966309E+04  0.17383966309E+04  0.00000000000E+00 0. -1.
  1000021    1    1    2  502  501 -0.29361372152E+02 -0.43312218784E+03 -0.96508443869E+03  0.12203117777E+04  0.60771370000E+03 0. -1.
  1000021    1    1    2  503  502  0.29361372152E+02  0.43312218784E+03 -0.42974136877E+03  0.86165567657E+03  0.60771370000E+03 0. -1.
[...]
</event>
```

Figure 3.4: Two example `LHE` events for the production of a gluino pair in a supersymmetric theory. For each `<event>` block, the first row lists general event information which can be relevant for subsequent programs. These are, from left to right, the total number of particles in the event, the ID of the process (relevant if a sample contains multiple processes), the event's weight, the PDF factorisation scale in GeV and the used scale-dependent values of α_{QED} and α_{QCD}. The following indented lines show information of each particle, namely the Monte-Carlo particle ID ([140]), a status code (in our case -1 for incoming and 1 for outgoing, can contain more if there are intermediate decay chains or radiation effects), the indices of the first and the last mother (in the above case, both final state particles have the two intial state particles 1 and 2 as mothers, in general this is also used to trace decay chains), flow information of colour and anticolour (colour octet particles are written as colour-anticolour-combinations), the kinematic variables p_x, p_y, p_z, E and mass m of the particle in GeV, proper lifetime $c\tau$ in mm (important for particles with long lifetimes and potentially detached vertices in the detector) and the helicity. Further detailed information on the event can follow after but is ommited here.

to write explicit `LHE` files and instead do the subsequent parton showering and hadronisation effects explained in the upcoming parts of this chapter. At this stage it is also worth mentioning the `Pythia 8` [147] code, which unfortunately is incapable of reading `UFO` files but which comes with a long list of hard matrix elements for many BSM models already implemented, see Ref. [148].

3.2.3 Decays of Heavy BSM Particles

Many collider searches for new physics are based on the assumption that a new, unknown particle is produced during the hard scattering process. For example in Section 3.2.1 we discussed the production of a new charged scalar particle $\tilde{\ell}^+$. These new particles are often unstable and have such small lifetimes that they decay before they hit the very first detector layer, in most cases fast enough for the decay products to be inistinguishable from particles produced in the hard collision. It is therefore only the decay products with sufficiently long lifetimes which are experimentally accessible and thus it is sensible to already take this into account on the event generation level.

Depending on the used tool(s), the calculations discussed in Section 3.1 might have already calculated the branching ratios of all new particles to their various final states and printed those to the used `SLHA` file. Alternatively, the decay width formulae can be provided in the `UFO` files and can immediately be calculated analytically for a given parameter setup. In those cases, the decay step in the event generation is very simple:

1. Loop over all unstable particles p,

2. randomly choose one possible decay mode using the branching ratio as a weight,

3. replace p by its decay products and

4. repeat this step until all final state particles are stable.

Regarding step 3, it is often sufficient to assume the kinematics of the decay products to be uniformly distributed in the mother particle's rest frame. However depending on the used program and how it is linked to the hard matrix element generation (e.g. when using `Herwig++` for both), even the full spin information can be taken into account for the kinematics of the decay.

If however neither the decay table nor the required analytical information to calculate it are known, the partial widths can still be determined numerically by calculating all $1 \to X$ processes using the same methods as described for the hard matrix element calculation above. Unfortunately, this method needs a considerable computational time, since all decay widths have to be calculated one by one numerically before the more important branching ratios can be determined. The numerical effort is especially high if 3- or even 4-body final states are relevant. Another disadvantage is the accuracy of this calculation, which is usually limited to tree level decays whereas analytical calculations of branching ratios often have at least next-to-leading order (NLO) accuracy. Therefore, using the tools mentioned earlier for determining the decay tables is highly encouraged, if possible.

3.2.4 Parton Showering

Let us for the moment switch to an electron-positron collider, the generalisation to hadron colliders is explained later, and suppose the hard process evaluated the cross section $\hat{\sigma}_{e^+e^-\to q\bar{q}}$ of the creation of a quark-antiquark pair[4]. Then the differential cross section for the radiation of an additional gluon with energy $z\sqrt{\hat{s}}$ and angle θ with respect to the final state quark is given as [113]

$$\frac{\mathrm{d}\hat{\sigma}_{e^+e^-\to q\bar{q}g}}{\mathrm{d}z\ \mathrm{d}\cos\theta} \approx \hat{\sigma}_{e^+e^-\to q\bar{q}} C_F \frac{\alpha_S(\hat{s})}{2\pi} \frac{2}{\sin^2\theta} \frac{1+(1-z)^2}{z}. \tag{3.6}$$

Here, $C_F = 4/3$ is a typical number that arises in quark-gluon interactions and which is caused by the underlying group theory. Note that this scenario can be represented in terms of the DGLAP splitting functions encountered above, i.e. $P_{g,qg}(z) = C_F \frac{1+(1-z)^2}{z}$.

The singularities at the poles of Eq. (3.6) for soft ($z \to 0$) or collinear ($\theta \to 0, \pi$) gluons correspond to unresolvable final state radiation and are cancelled by a proper consideration of higher order terms in the perturbative calculation of $\hat{\sigma}$ according to the KLN theorem [149]. They can be avoided by setting proper cuts on resolvable final states, i.e. restrictions on $z, \cos\theta$ which are needed to experimentally distinguish a two-particle from a one-particle final state.

However, the introduction of a lower resolution scale q_0 for the momentum transfer of this extra radiation leads to large logarithmic corrections of order $\alpha_S \log(q_0^2/\hat{s})$ after doing the phase space integral in Eq. (3.6). A logarithm of similar structure arises for the angular integral. In order to get sensible results, it seems necessary to extend the perturbative expansion in α_S of the hard matrix element calculation to take these sizable corrections of order $\alpha_S \log(q_0^2/\hat{s})$and $\alpha_S \log^2(q_0^2/\hat{s})$ into account.

In the Monte-Carlo approach, these extra logarithmic terms can be resummed quite conveniently. The cross section $\sigma_{pp\to q\bar{q}}$ is interpreted as the inclusive probability for the production of

[4] This example does equally well hold in BSM searches, e.g. in the MSSM $e^+e^- \to \tilde{q}\tilde{q}^* \to q\bar{q}\tilde{\chi}\tilde{\chi}$

a quark-antiquark pair, including all possible final state radiation effects. The DGLAP splitting functions are translated into *Sudakov form factors* [113–115]

$$\Delta_i(Q^2, q^2) \equiv \exp\left(-\sum_{jk}\int_{q^2}^{Q^2}\frac{\mathrm{d}k^2}{k^2}\frac{\alpha_S(k^2)}{2\pi}\int_{q_0^2/k^2}^{1-q_0^2/k^2}\mathrm{d}z\ P_{i,jk}(z)\right) \tag{3.7}$$

which denote the probability for a final state particle i produced at energy scale q^2 to not produce radiation within the energy range $[q^2, Q^2]$. With the functions $P_{i,jk}$, calculable from QCD, and the resulting Δ_i at hand, the branching can be recursively performed for a given event returned by the hard matrix element calculation as follows [150]:

1. For each final state parton i, define[5] q_i^2 by the scale of the hard process which created i (similarly to choosing μ_F^2 in Section 3.2.1).
   a) Choose a uniform random number r between 0 and 1.
   b) Solve $\Delta_i(q_i^2, q_{\text{branch}}^2) = r$ for q_{branch}^2. Here, q_i^2 serves as the maximum allowed branching for parton i.
   c) If q_{branch}^2 is smaller than the resolution cutoff q_0^2, usually chosen close to Λ_{QCD}^2, parton i is considered stable down to the hadronisation phase (see below).
   d) Else, branch parton i into two partons j and k at scale q_{branch}^2. Their kinematics are determined randomly according to the splitting kernel $P_{i,jk}$ and q_j^2, q_k^2 are both set to q_{branch}^2.
2. Redo this chain for all new final state partons which were created through branching.

This procedure is an example of a *parton showering* algorithm which uses q^2 as the evolution scale. Other choices (e.g. via p_T or θ) are possible and different approaches are used within the various different event generators available, e.g. `Herwig` and `Herwig++` [145], `Pythia 6` and `Pythia 8` [147], `Sherpa` [146] or `POWHEG BOX` [151]. Ref. [113] shows examples for differences in observable distribution which arise when changing these (and other) assumptions.

Let us now go back to the case of a hadron collider. Here, an analogous procedure can be used for the initial state partons as well. Using a configuration from the hard matrix element calculation, partons can be evolved backwards in time using similar[6] splitting equations, leading to the description of *Initial State Radiation* (ISR).

It is important to note that the hard cross section $\hat{\sigma}(p_1 p_2 \to q\bar{q})$ after all measures the probability for the *overall* process to happen. The above effects merely lead to a further distinction of the events into those which come with extra radiation and those which do not. Therefore, the cross section calculated in the earlier section is not affected by these algorithms but the resulting content of the Monte-Carlo samples are.

[5] In our above description, choosing q_i^2 as the hard scattering scale is a choice which leads to a so–called *wimpy shower*. An alternative choice, $q_i^2 = s$, is usually given the name *power shower*. The latter generally allows for harder radiation and thus might better approximate the appearance of hard jets in an event, which for a wimpy shower would require the full caclulation to next order in α_S. The power shower however comes along with a dangerous double counting issue of being able to generate the same final state configurations by different paths, i.e. the identical configurations soft matrix element + hard radiation and hard matrix element + soft radiation contribute to the total cross section twice.

[6] A change of momentum due to branching of an incoming parton p_i leads to a potentially sizable change in its PDF weight $f_{p_i/p}(x_i, \mu_F)$. To keep the relative event weights uniform, the PDF can be considered by generalising the branching probability to $\Delta_i(Q^2, q^2, x)$ [152].

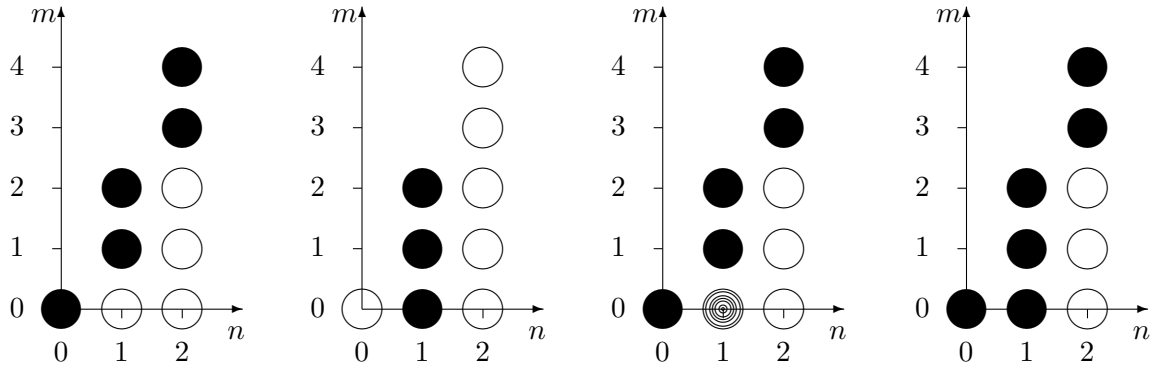

Figure 3.5: Illustration for the considered orders in $\alpha_S^n \log^m(q_0^2/\hat{s})$ in different event generation setups for jet production in e^+e^- collision with a jet resolution scale q_0. Filled dots correspond to correctly considered orders, whereas semi-filled dots correspond to emissions which are only correct above the merging scale. (a) $\bar{q}q$ at tree level plus parton shower. Here, the tree level process is via Z channel exchange and thus at 0^{th} order in α_S. The parton shower adds additional orders of $\alpha_S \log(q_0^2/\hat{s})$ and $\alpha_S \log^2(q_0^2/\hat{s})$ to the tree level diagram. (b) $\bar{q}qg$ at tree level. This includes the full α_S contribution above the resolution scale q_0. (c) $\bar{q}q$ at tree level plus parton shower matched to $\bar{q}qg$ at tree level. This combines the previous two, however the $n = 1, m = 0$ contribution only considers real emissions above the merging scale. (d) $\bar{q}q$ at NLO plus parton shower matched to $\bar{q}qg$ at NLO. Here the full $n = 1, m = 0$ contribution is taken into account. Images and explanations are based on Figs. 5,6 in Ref. [113].

3.2.5 Matching/Merging

Note that the final state $X + j$ created by the parton showering of X could also be counted as an individual final state X' in Eq. (3.1) and calculated independently using the hard matrix element. The former approach is strictly valid only in the soft or collinear limit, whereas the latter ansatz is particularly accurate for hard radiation with large emission angles. Therefore it seems obvious that a consistent combination of the two might be necessary should both be relevant for the final state selection. Careful *matching/merging* procedures (e.g. MLM matching [153], CKKW/CKKW-L [154], `Powheg` [151]) combine Monte-Carlo samples for both X and X' by properly separating the extra partons from the hard matrix element of X' and soft radiation below a certain *merging scale* from X. Going into the details of these algorithms is beyond the scope of this summary and we refer to the given references for more information. Let us just summarise some important key facts:

- The new sample contains events with one hard extra jet (plus eventual further soft jets) taken from the X' sample, and events with only soft (or no) extra jets taken the X sample.
- The cross section evaluated from the matching/merging algorithm should roughly correspond to the cross section of the X sample, as that one should correspond to the inclusive cross section.
- The resulting jet spectrum should be mostly independent of the details of the parton showering algorithm, as differences in the showering of the X sample should only happen in those phase space regions where the matching/merging algorithm prefers the X' sample anway.

- Special care has to be taken to subtract diagrammatic contributions from the X' final state which correspond to decays of an unrelated Y final state. For instance, merging the processes $\tilde{q}\tilde{g}$ and $\tilde{q}\tilde{g}j$ would double count, if considered, the process $\tilde{g}\tilde{g}, \tilde{g} \to \tilde{q}q$ [155].

- All the aforementioned concepts, starting from the PDF folding down to the matching/merging prescription, can be extended to higher-order calculations. Those are needed to consider further corrections which are not accounted for in the matrix element plus parton shower approach. This is illustrated schematically in Fig. 3.5. An important complication of NLO calculations is the proper cancellation of singularities in a numerical approach.

3.2.6 Soft QCD Effects and Hadronisation

With the above steps performed, the model dependent part of the event generation is done, but the generated events still do not yet contain observable information. As an important detail, the final states which we simulated so far mostly contain colour charged objects, whereas only colour neutral objects are stable and observable. It therefore seems obvious that the event generator has to take into account further steps than discussed above.

Fortunately, these additional steps are almost entirely based on low-scale QCD interactions of quarks, gluons and hadrons, and only weakly depend on any possible BSM physics of massive, high-energetic particles. We can therefore restrict this discussion to a short summary of the most important missing steps of the event generation which are needed to obtain realistic events that fully simulate those that could have been produced in an actual collider experiment.

- Besides the hard interaction process which we described above, additional elastic and/or inelastic scattering can happen between the two proton remnants. This is collectively called *Underlying Event* (UE) and can lead to additional hadronic activity in the final state. Usually it is taken into account by phenomenological models based on fits as it mainly occurs in the non-perturbatice soft-QCD limit [113].

- A *hadronisation* phase translates final state partons into physically observable meson and hadron states. According to the theory of *local parton-hadron duality* [156], the kinematics and quantum number distribution of the partonic final state are very close to those of the resulting hadronic final state. However, different tools consider different phenomenological models (e.g. string-based [157] or cluster-based [158]) for how the colour structure of the partonic event determines the colour-neutral meson and baryon distributions.

- Hadrons produced in the previous step with lifetimes smaller than $\mathcal{O}\left(\mathrm{mm}/c\right)$ decay before the detector could observe them. These hadron (and also τ lepton) decays are considered similarly to those of BSM particles explained in Section 3.2.3. Finite lifetimes can be translated into positions of respective *displaced vertices* which, if large enough, can have an impact on the detector reconstruction efficiency.

These effects are taken into account already by the Monte-Carlo generator tools lised above, however with different implementations. Normally the details of these steps do not matter for high-energy BSM phenomenology but they should be kept in mind as a source of theoretical uncertainties in the prediction of the hadronic structure of an event.

3.2.7 Final Output

The tools mentioned in the previous sections usually store their Monte-Carlo events by using the `StdHEP`/`HepEvt` [159] or `HepMC` [160] standards. The former is a binary format written by `Fortran`, which provides a more compact way of storing data but which is not human-readable. In contrast, `.hepmc` files are typically larger but are written in `Ascii` format and hence can be read and written more comfortably. Both formats store the properties of each individual particle, similarly to the above mentioned `.lhe` file. In addition they usually[7] also store the entire history of the event, i.e. one can unambiguously trace back the radiation and decay pattern of each final state object down the hard process. This particle history can be of assistance to improve the accuracy of a fast detector simulation, as explained below.

3.2.8 Higher Order Cross Sections and K-Factors

The aforementioned techniques already require a large computational effort even if the matrix elements are only determined at leading order. It is especially the parton showering and final state hadronisation steps which take a long time to simulate and which typically dominate the overall computing time in a fully automatised collider phenomenology study. Unfortunately, as soon as the final state contains strongly coloured particles, for example the production of scalar quarks in Supersymmetry [163], sizable corrections in next-to-leading-order QCD can be expected.

There exists a strong effort to create a fully automated, model independent event generator with NLO accuracy. The formulation of proper numerical factorisation, regularisation and renormalisation techniques which work independently of any model specification is an extremely challeging task. The `MadGraph5_aMC@NLO` tool officially advertises to only being able to consider NLO QCD corrections for Standard Model processes. In their most recent publication, see Ref. [142], they however discuss how the NLO calculations for any BSM model can in principle already be performed by the current version of the tool. They wish to perform further validation before publishing this as a generally working feature. The `FeynRules` collaboration also lists a handful of models with explicit NLO-compatible `UFO` files on their webpage, see Ref. [161], and provides validation material for some. These can be used by `MadGraph5_aMC@NLO` to perform NLO event generation. Therefore, the era of fully automated NLO calculations as a standard can therefore be expected to start very soon.

Until then, a possible alternative approach is to calculate the total cross section for a given partonic process analytically and independently from the Monte Carlo event generation. Then, the cross section σ in Eq. (3.1) is taken from this analytic calculation while the Monte-Carlo events, simulated at tree level, are used to find $\mathcal{A}(X) \times \epsilon(X)$ as described below in Section 3.3.

Alternatively we can define the *K-factor* $K \equiv \sigma_{\text{NLO}}/\sigma_{LO}$, with σ_{NLO} being the above calculated higher order cross section and the σ_{LO} denoting the tree-level cross section from the same analytic calculation with only leading order accuracy. We then multiply the cross section $\sigma_{\text{LO}}^{\text{MC}}$ determined during the Monte-Carlo event generation process with K in order to get an estimate for the next-to-leading order cross section. Note that to avoid divergencies the full higher order calculation usually has to be performed over the full final state phase space while the Monte Carlo generation often cuts phenomenologically inaccessible phase space regions. By using the K-factor, we get an estimate for the NLO cross section in this finite simulated phase space region.

[7] `Sherpa`, for instance, has an option to not store intermediate particles which can reduce the file size significantly.

Strictly speaking, using a tree-level Monte-Carlo sample combined with an NLO cross section is only valid if kinematic distributions do not change in a higher order calculation. This is generally not the case, however the difference typically only mildly affects $\mathcal{A}(X) \times \epsilon(X)$ and thus the K-factor approximation is often accurate enough. Still, one should ensure that there are no potentially dangerous phase space regions in the simulated sample where a sizable difference between LO and NLO calculation could happen. In general, the more the Monte-Carlo determination differs from the analytical calculation of σ_{LO}, the greater amount of care is required.

Unfortunately, no tool for model-independent automatised NLO cross sections calculations exists either yet — if we ignore the yet unvalidated status of `MadGraph5_aMC@NLO`. In the special case of Supersymmetry, however, the `Prospino` [162] tool can calculate cross sections for the pair production of squarks, sleptons, neutralinos, charginos and gluinos at next-to-leading order in the strong coupling constant. For the even more special case of only strongly interacting particles in the final states, simple to use cross section grids have been established and can be used via the `NLLfast` [163] tool. As this program only interpolates between pre-calculated cross section values, it can determine the NLO cross section for a 2 body final state with only strongly interacting SUSY particles practically instantaneously. This makes it an invaluable tool for collider phenomenology of SUSY models involving squarks or gluinos.

3.3 Acceptance $\mathcal{A}(X)$ and Final State Efficiency $\epsilon(X)$

With the above prescription we can find a finite sample of Monte-Carlo events predicted by theory which represent the total number of produced events of type X during the collision process. Not all of these events will however make it into the final number $N^{\text{th.}}$. Some events are involuntarily lost since the eye of the experiment, the detector, only has a finite accuracy and will unfortunately fail in recording some. This determines the geometrical acceptance $\mathcal{A}(X)$. In addition, some events are actively removed, as we aim to find discriminible features of the new model compared to the Standard Model as the alternative hypothesis. For that purpose, we will choose a number of constraints and remove events from our sample which fail those. From that we can deduce the final state efficiency $\epsilon(X)$ for a detected event to be counted as signal.

Since detector effects can influence $\epsilon(X)$ indirectly, it is not trivial to distinguish between the two factors. As an example, noise in the calorimeter cells can impact reconstructed jet energies and hence affect the result of an often appearing cut on the energy of the hardest jets. This is why one often quotes the product $\mathcal{A} \times \epsilon$[8].

In the following we want to illustrate how this combined factor can be derived in the Monte-Carlo approach as we have used before within this chapter.

3.3.1 Detector Effects and Detector Simulations

So far, our computed Monte-Carlo samples contain a representative set of events as they would be produced in a collision of two protons. If these were produced in an actual experiment, real

[8] It should be noted here that even though complicated, it is possible to apply *unfolding* procedures to carefully factor our the effects from the event selection process and the inaccuracies of the detector. The resulting acceptance factor $\mathcal{A}$ is then purely based on geometrical properties of the final states and defines the so–called *fiducial cross section* $\sigma_{\text{fid}} \equiv \sigma \times \mathcal{A}$. Within this approach, which we will not further discuss within this thesis, it is this value rather than N which is used to compare data and experiment.

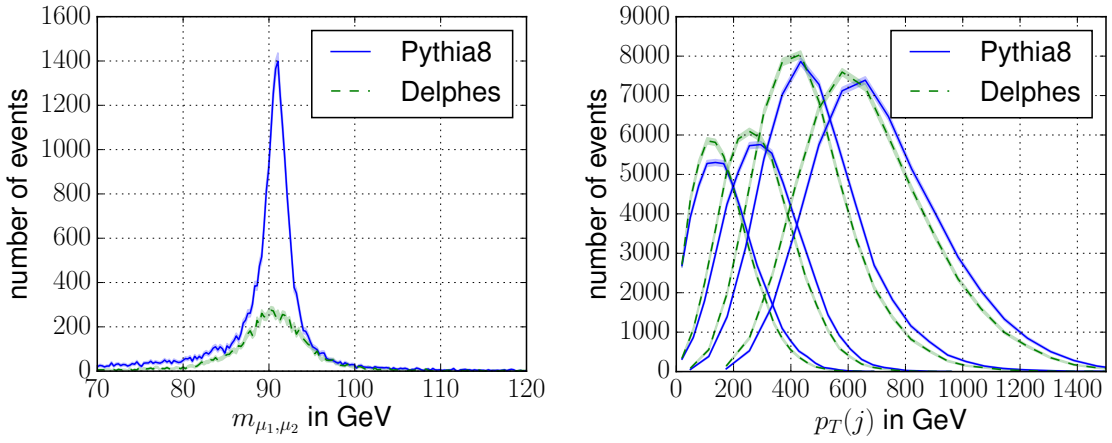

(a) Muon pair invariant mass for $Z \to \mu^+\mu^-$ events

(b) Transverse momentum of the leading four jets in $\tilde{g}\tilde{g}, \tilde{g} \to q\bar{q}\widetilde{\chi}_1^0$ SUSY events

Figure 3.6: Comparison of distributions on generator level and on detector level. 50,000 events were respectively simulated with `Pythia 8` and subsequently passed through `Delphes 3.3.2` with its standard ATLAS setup. Coloured bands denote statistical uncertainties due to finite Monte Carlo samples. For (a), note that not only is the invariant mass distribution significantly smeared but there are is also an overall reduction of reconstructed events due to finite identification efficiencies for muons of order 90 %.

detectors like ATLAS or CMS would not record the same set of objects with exactly identical properties as they are predicted during the collision process. As an example, some particles, like the Standard Model neutrinos ν_i or the many electrically neutral particles in BSM theories, simply leave the detector unseen and hence should be removed from the event. Furthermore, the real detector only covers a finite region around the collision point and thus will not register those events whose final state particles of interest miss the detector region. Finally, detector noise leads to reconstruction errors of the observed properties of a final state.

As the observable kinematics of an event are those which determine the result of the final event selection procedure, it seems to be an important intermediate step on our quest for $N^{\text{th.}}$ to translate from theoretically generated events to physically observable events. This us usually done by applying a *Detector Simulation*.

Given an event in the generated Monte-Carlo sample of the previous section, there are in principle two approaches to consider the effects of a detector:

1. Simulate the propagation of each final state particle through the individual detector components to obtain a set of detector signals similar to what one would obtain from an actual running detector. The same object reconstruction algorithms which are used for the real LHC detector can then be applied to the simulated signals in order to construct the observable event. A standard tool for this *full detector simulation* approach is the `GEANT4` [164] framework, which is often used by experiments to get a reliable simulation of their detector. An extremely big disadvantage is the enormous runtime (see below) which makes this approach pracically impossible to use for a higher dimensional model scan. However, it can be used to provide a basis for the second approach.

2. Apply phenomenological functions taken from measurements and/or full simulation studies to all final state particles in the generated event sample which

- remove particles which are invisible to the detector,
- change the energy and position of a particle according to the resolution of the detector components and
- change the way a particle is recorded according to the efficiencies of the algorithms which reconstruct electrons, muons, photons etc. from the detector signals.

This *fast detector simulation* approach is obviously only an approximaton. It assumes that all relevant detector effects can be parametrised within a universal set of functions. Also, these functions must be independent of the underlying physics model and must be applicable on individual objects regardless of the remaining activity of the event. These statements are in fact not 100 % correct, however this approach still gives accurace enough results to be applicable by phenomenologists. It also comes with a sizable speed boost, e.g. $\mathcal{O}$(ms) in `Delphes` compared to $\mathcal{O}$(min) in the full `GEANT4`-based CMS detector simulation for a full $t\bar{t}$ event in the CMS detector [165, 166].

The two main public tools used by the community are `Delphes` [165] and `PGS` [167]. In contrast to `Delphes`, which is under ongoing improvement to implement new features anticipated by the community, the `PGS` code has not been updated since 2012 and thus can be considered 'outdated'[9]. This is why we focus on `Delphes` in the remainder of this thesis. As it is one of the components of the later discussed tool `CheckMATE`, we postpone the discussion of its features to later. For now it is sufficient to say that it mostly applies phenomenological functions as explained above. However, it also to some extent considers the workflow of an actual detector, e.g. by simulating discrete detector cells of hadronic and electromagnetic calorimeter into which each particle deposits its energy and out of which in the end jet objects are reconstructed by applying the `FastJet` clustering algorithm [168]. The effect of such a fast detector simulation on two example distibutions are shown in Fig. 3.6.

Depending on the desired accuracy, it might not even be necessary to use these tools at all. Simple geometrical and kinematical cuts can already be applied on the event generation level and a Gaussian smearing of energies can easily be done by hand. However, as these tools already take many effects into account and only take a fraction of the computational time of the much more involved event generation, there is no real disadvantage in using them anyway.

`Delphes` stores its output events in so–called `.root` files which can easily be read and analysed within the `ROOT` analysis framework [169].

3.3.2 Data Analysis and Final State Selection

After all the steps described above, we have finally reached the stage where our generated Monte-Carlo sample, to a certain degree of accuracy, is on the same level as real data taken at an actual experiment. If we simply compared the total number of events at this stage, we would hardly be sensitive to any new physics; The total proton-proton cross section is of the order (size of proton)$^2 \approx 10^{-30}\,\mathrm{m}^2 = 10^{-2}\,\mathrm{b}$, whereas the cross section for a typical SUSY process is merely of the order pb and below. Using the total integrated luminosity of $20\,\mathrm{fb}^{-1}$ during the 8 TeV run, it would be impossible to distinguish the $\mathcal{O}(100)$ events of the latter from the Poisson fluctuation of $\mathcal{O}(\sqrt{10^{13}})$ of the former.

[9] It is however still implemented in `MadGraph5_aMC@NLO` and thus often used for a "quick-and-dirty" approximation.

We can drastically improve the situation by finding and applying a set of constraints on our simulated or real data, which remove as many events as possible from Standard Model processes while leaving a potential signal of new physics unspoilt. For that purpose, the features of a potentially interesting new physics model should be analysed and the best set of variables to discriminate against Standard Model events be found. Typically, this step has already been performed by the collaborations before the data is analysed to not be biased by the actual experimental outcome. The allegedly best discriminators are determined from exhaustive simulations of Standard Model backgrounds and interesting new physics signals. Then, the resulting optimal cut prescription is applied on the data and — after some internal cross checks — the results published in combination with the Standard Model expectation.

There is no ultimate set of variables which yields perfect discrimination for all models. However, it is fair to say that most searches for new physics at the LHC rely on one or more of the following features which often occur in BSM physics:

- New particles which decay into a set of visible Standard Model particles can be identified by a characteristic peak in the invariant mass spectrum. A very recent example for such an analysis is the invariant mass measurement of 2-photon final states which have been performed by both ATLAS and CMS on 13 TeV data and which shows some interesting excess over the expected Standard Model background [170].

- Decay chains of heavy into light new particles, which often appear in models with a highly enlarged particle spectrum, yield characteristic peaks or edges in the invariant masses of the visible decay products even if not all decay products are visible. Also, large mass splittings produce harder particles as found in typical Standard Model processes.

- By looking at events with a large amount of missing transverse energy, one is sensitive to physics with new invisible, stable particles. This is a standard method to look for R-Parity conserving Supersymmetry due to its stable neutralino, c.f. Section 2.4.3, or other models with dark matter candidates like our Higgs Portal setup in Section 2.2.

- Furthermore, the observation of single hard objects (so–called *mono-X* final states) can be a hint for invisible particles which were produced in association with the single object. This is one way to identify the production of new particles which decay invisibly into *dark sector* particles.

- Models with new, heavy coloured particles often predict a larger amount of hadronic activity, i.e. a larger number of high energy jets, compared to the pure Standard Model case. This is the avenue to find Supersymmetry with light squarks and/or gluinos.

- Models with broken lepton number symmetry can be identified by lepton number violating final states, typically pairs of leptons with same flavour and same charge. Note that it is not easily possible for baryon number violating models due to the generally large hadronic activity.

- Third generation Standard Model fermions (excluding the neutrino) lead to characteristic jet structures in the final state, which can be tagged experimentally to a good precision. New particles with large couplings to these particles can therefore be identified by looking for a surplus o f these objects in the final state.

Applied Cut	N_{cut}	ϵ_{cut}	ϵ_{tot}
Initial number of events ($\sigma \times \mathcal{L}$)	897	100 %	100.0 %
3 isolated $e^{\pm}, \mu^{\pm}$	148	16 %	16.0 %
1 SFOS pair, $m_{\text{SFOS}} \in [60\,\text{GeV}, 81.2\,\text{GeV}]$	78	53 %	8.7 %
No jet with b-tag	75	96 %	8.3 %
$E_T^{\text{miss}} \in [50\,\text{GeV}, 75\,\text{GeV}]$	20	65 %	2.2 %
$m_T \in [0\,\text{GeV}, 80\,\text{GeV}]$	13	27 %	1.4 %
$\lvert m_{3\ell} - m_Z \rvert \geq 10\,\text{GeV}$	10	77 %	1.1 %

Table 3.1: Example cutflow taken from Ref. [171] applied on a simulated sample based on a supersymmetric model. The target production mode is $pp \to \chi_1^{\pm}\chi_2^0, \chi_1^{\pm} \to W^{\pm}\chi_1^0, \chi_2^0 \to Z\chi_1^0$ with the gauge bosons decaying leptonically. N_{cut} describes the physical number of events that are expected after all cuts up to that point have been applied. ϵ_{cut} is the efficiency of a single cut, i.e. the ratio of N_{cut} values after and before the cut was applied. ϵ_{tot} is the total cut efficiency of applying all cuts up to that point, i.e. the ratio of N_{cut} to N_{cut}(Initial number of events). The last value of ϵ_{tot} corresponds to the overall acceptance times efficiency factor $\mathcal{A} \times \epsilon$ in Eq. (3.1). The Standard Model, in comparison, predicts 22 events after the same set of cuts is applied, mostly originating from direct WZ production.

- BSM particles with lifetimes of order cm/c can lead to decay vertices with a significant spatial distance from the initial collision point. These can be identified by reconstructing the tracks which originate from such a displaced vertex. We discuss a modified version of this signature in our analysis of long-lived neutralinos in R-parity violating supersymmetry in Chapter 7.

Typically, one first defines the final state(s) which are characteristic for one or more target BSM models, finds all Standard Model processes which have similar final states, and identifies the kinematical variables which allows for the distinction of the two. This procedure leads to a set of *cuts*, and in the publications of the experimental collaborations, one usually finds an explicit definition of all these cuts and the resulting number of events N from data and from Standard Model predictions.

In Table 3.1 we show an example cutflow from a particular ATLAS-analysis [171], which is designed to find events with three charged leptons and missing energy as they would appear in a supersymmetric model via the production mode $pp \to \chi_1^{\pm}\chi_2^0, \chi_1^{\pm} \to W^{\pm}\chi_1^0, \chi_2^0 \to Z\chi_1^0$ with the gauge bosons decaying leptonically. The cuts of this analysis are designed to identify the leptons coming from the Z via the invariant mass of two leptons and the neutralinos via a large missing momentum vector. The W boson is identified by making use of the *transverse mass* m_T. This is a kinematic variable generally defined using the transverse projection p_T and the azimuthal angle $\phi[p]$ of two vectors $p^{(1)}$ and $p^{(2)}$ via

$$m_T \equiv \sqrt{2p_T^{(1)}p_T^{(2)}\Big(1 - \cos(\phi[p^{(1)}] - \phi[p^{(2)}])\Big)}. \tag{3.8}$$

$p^{(1)}$ is typically the missing transverse momentum vector and $p^{(2)}$ corresponds to the reconstructed momentum of one visible object. In our case, it corresponds the third lepton which does not belong to the same-flavour opposite-sign (SFOS) pair and which is expected to originate

from the leptonc W decay. Then, $t\bar{t}$ SM processes are vetoed by rejecting events which include a jet which most likely originated from a decaying B-hadron. Lastly, by removing events with a 3-lepton invariant mass too close to the Z boson mass one rejects processes of $Z \to \ell\ell\gamma$ origin, where a photon from final state radiation could have converted to an electron-positron-pair in the detector.

The by construction highly model dependent probability of events from a final state X to pass these constraints is quantified by the final state efficiency $\epsilon(X)$:

$$\epsilon(X) \equiv \frac{\text{Number of recorded } X \text{ events which pass all cuts}}{\text{Number of recorded } X \text{ events}} \tag{3.9}$$

If our generated Monte-Carlo sample covers the kinematic features of the underlying model sufficiently well, we can estimate the efficiency straightforwardly from applying the constraints on the sample. Practically, one sets up a computer analysis program which reads in the `Delphes` output file, loops over all events and checks the given sets of cuts for each individual event. The efficiency is then estimated via

$$\epsilon(X) \approx \frac{\text{Number of MC } X \text{ events after detector simulation which pass all cuts}}{\text{Number of MC } X \text{ events after detector simulation}} \tag{3.10}$$

In principle, analysis programs can be written in any programming language. However, the `ROOT` format in which the `Delphes` output is written must be processed by using the `ROOT` analysis framework which can be used as library extensions for `C++` and `Python`. There also exist backends which allow the construction of an analysis directly within `Delphes`.

Many event generators (e.g. `Pythia` and `MadGraph5_aMC@NLO`) allow for the analysis of the simulated data on-the-fly. Furthermore, the `Rivet` [172] analysis framework offers a comfortable environment to code typical final state selections. However, these approaches skip the detector simulation step and hence are only useful for either first studies of the kinematics of a new model or for comparing unfolded data, c.f. Footnote 8.

Compound recasting tools for LHC results combine an analysis framework with the detector simulation and even with the event simulation parts of the phenomenology chain in order to provide a convenient environment which does as many automatised things at once as possible. The yet unpublished `ATOM` [173] tool extends the `Rivet` analysis framework by a set of identification efficiencies and smearing effects which take into account the most important detector inaccuracies. An alternative approach is followed by the `MadAnalysis5`-collaboration [174] which is strongly connected to the `MadGraph5_aMC@NLO` event generator and uses `Delphes` for the detector parametrisation. These tools already have many published results from CMS and ATLAS implemented and just require the user to provide the generated events for the models to be tested in order to find the efficiency and acceptance factors. If in additon the cross section is also known, they can determine the p-value of the given model by using Eq. (3.1) and applying the methods described in the next section.

In Chapter 4, we present another tool, `CheckMATE`, which provides a very convenient framework to embed analyses and automatically link these to an event generator, a detector simulation and an automatic statistical evaluation. Its main strengths compared to above quoted tools are its self-containement and its user-friendliness.

3.3.3 Statistical Evaluation

With all the individual contributions known, we can finally evaluate $N^{\text{th.}}$ with the help of Eq. (3.1). Let us call this number predicted by our signal model S from now on. In many cases, the new physics model predicts events *in addition to* those $N^{\text{th.}}$ predicted from the Standard Model, called B. In that case, S can simply be added to B and the the total prediction of the BSM hypothesis is to observe $S + B$ events in a given search region[10]. From analysing real data, we know the corresponding experimental number $N^{\text{exp.}}$, or short N. The all-embracing question which we would like to answer is whether the two numbers N and $S+B$ are compatible or if the theory prediction violates the observation.

The standard LHC hypothesis test is the CL_S prescription paired with a likelihood ratio discriminator [175]. We illustrate this method in a simplified scenario in this section, namely a scenario where there are no uncertainties ΔB, ΔS associated to B and S. We explain the advanced methodology including these uncertainties within Appendix A.2.

All LHC results discussed within this thesis show agreement of the data N with the Standard-Model only hypothesis B. It is therefore reasonable to choose the Standard Model (B) as the alternative hypothesis and the BSM model ($S+B$) as the null hypothesis which can be rejected if its predicted S is too large.

The likelihood of observing N events if $S + B$ are theoretically expected is given by the Poisson distribution

$$\mathcal{L}(N|S) = \text{Poiss}(N|S+B) \equiv \frac{(S+B)^N}{N!} e^{-(S+B)}. \tag{3.11}$$

To test the null hypothesis, we use the *Maximum Likelihood Ratio* as the test statistic

$$q_S(N) \equiv -2 \log \left(\frac{\mathcal{L}(N|S)}{\mathcal{L}(N|\hat{S})} \right). \tag{3.12}$$

Here, $\hat{S}$ is the value of S' in the range[11] $[0, S]$ which maximises $\mathcal{L}(N|S')$. $q_S(N)$ becomes larger for smaller likelihoods, that is for less compatibility of observation and null hypothesis. According to Wilk's theorem [176], the maximum likelihood ratio test has the convenient property to equal the χ^2-test in the limit of large event numbers[12], which can help in doing approximate significance tests in scenarios where the likelihood function is very complicated.

In our simple toy case, we can evalute the test statistics analytically:

$$q_S(N) = \begin{cases} 0 & \text{if } N > S+B, \\ -2N \log\left(\frac{S+B}{B}\right) + 2S & \text{if } N < B, \\ -2N \log\left(\frac{S+B}{N}\right) + 2(S+B-N) & \text{else.} \end{cases} \tag{3.13}$$

[10] This statement is correct as long as the BSM model and the Standard Model do not share a common final state. If that is the case, interference effects have to be taken into account and thus S and B do not add incoherently any more.

[11] The lower limit $S' \geq 0$ is caused by the physical assumption of having no negative signal events. The upper limit $S' \leq S$ ensures a one-sided limit.

[12] This can be seen easily for the given example: For large event numbers, the Poissonian distribution resembles a Gaussian distribution $\mathcal{L}(N|S) \propto \exp(-{}^{(S+B-N)^2}/_{2(S+B)})$ and the test statistics becomes $q_S = {}^{(S+B-N)^2}/_{S+B}$, in other words a χ^2 test with one degree of freedom.

In general, however, q_S cannot be given in fully analytic form — see for example Appendix A.2.

From the test statistics we can derive the p-value of our null hypothesis S after the observation of N by calculating

$$\mathrm{CL}_{S+B} \equiv \sum_{N'=0}^{\infty} \mathrm{Poiss}(N'|S+B) \cdot \Theta\Big(q_S(N') - q_S(N)\Big) \tag{3.14}$$

here, $\Theta(x) = 1$ if $x \geq 0$ and 0 else. The motivation behind this formula is the following: If we repeated the experiment infinitely many times and if the hypothesis S was true, we would expect to observe different values N' distributed according to the Poissonian distribution with mean value $S+B$. The relative amount of observations N' which result in a test statistics $q_\mu(N')$ at least as incompatible as the observed $q_\mu(N)$ is described by $\mathrm{CL}_{S+B}(N)$. If this number is small, typically smaller than 0.05, we deduce that it would be very unlikely to observe N if $S+B$ was expected and thus reject the S-hypothesis.

This approach however has a peculiar property: If N happens to be much smaller than B, which statistically can happen in a small fraction of experiments even if B describes Nature accurately, CL_{S+B} will always turn out to be small, regardless of S. Therefore, the above interpretation will always claim a tension with the signal hypothesis and could even conclude that a model with $S \ll 1$ is excluded even though this event number is clearly to small for the experiment to ever be sensitive to it.

A commonly used approach to avoid such false exclusion is to, in addition to CL_{S+B}, determine the p-value for the observation to be compatible with the background-only hypothesis, i.e.

$$1 - \mathrm{CL}_B = \sum_{N'=0}^{\infty} \mathrm{Poiss}(N'|B) \cdot \Theta\Big(q_S(N') - q_S(N)\Big) \tag{3.15}$$

The confidence in the signal hypothesis is then calculated by the CL_S value

$$\mathrm{CL}_S \equiv \frac{\mathrm{CL}_{S+B}}{1 - \mathrm{CL}_B} \tag{3.16}$$

and a model is excluded if it produces a too small CL_S value. For experiments which are in tension with the background-only hypothesis, $1 - \mathrm{CL}_B$ becomes smaller, CL_S increases and thus the limit weakens.

In Fig. 3.8 we show example values for CL_{S+B} and CL_S for N much larger, equal and smaller than B and the resulting 0.05 limits on S. If N is equal to B, the CL_S prescription only multiplies the CL_{S+B} value by 2, and therefore hardly affects the limit. However, for $N \ll B$, as explained above, the CL_{S+B} value would yield a very strong limit on S which could lead to a false exclusion. The CL_S prescription weakens the limit significantly. In fact, it can be shown that no matter how far N and B differ, a value of S smaller than ≈ 3 will never be excluded by CL_S, which corresponds to the typical upper limit of a zero event observation. In the other extreme, $N \gg B$, the upper limit on S is equal in both approaches. However, in this scenario the CL_S prescription cures a peculiar lower limit[13].

[13] It should be noted that the lower limit is only peculiar in the context of the initial assumption that the alternative hypothesis, B describes the observation accurately. Obviously this assumption is false if N is much larger than B and in that case one should rather start rejecting the background-only hypothesis with S as the alternative hypothesis.

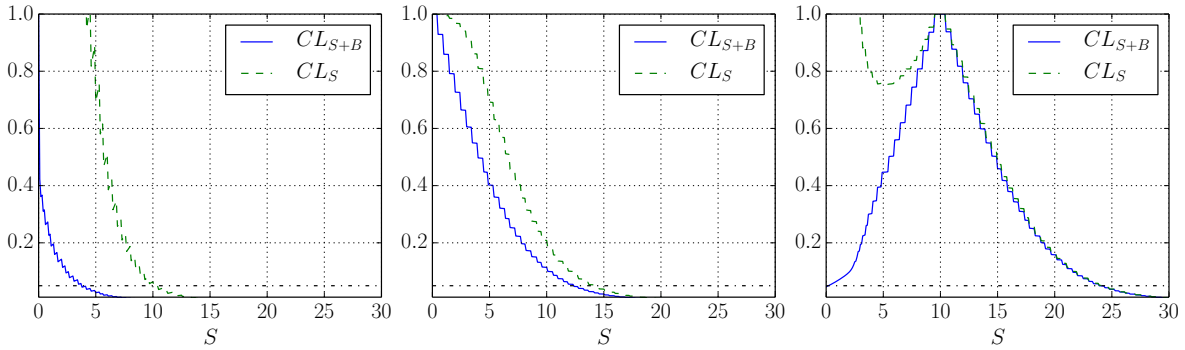

(a) $N = 20, B = 30$ (b) $N = 30, B = 30$ (c) $N = 40, B = 30$

Figure 3.8: CL_{S+B} and CL_S values for increasing S in scenarios with $N \ll, =, \gg B$. An exclusion test based on CL_{S+B} or CL_S would claim that all values for S with CL value smaller than 0.05, shown as a dashed-dotted line, are excluded. The zig-zag shape of the lines is caused by the discreteness of the underlying Poisson statistics. A proper calculation including continuous nuisance parameters, see Appendix A.2, would yield smooth lines.

These standard statistical calculations can easily be done in standalone codes. In advanced situations with for example multiple bins and/or multiple systematic error sources, the statistics framework `RooStats` [177] might be advisable. It is based on the above mentioned `ROOT` framework and provides an environment to define various types of parameters and probability density functions to calculate statistical quantities like q_S, CL_S and other.

3.4 Choosing X

So far we have explained how for a given final state X we can use various tools to find $N^{\mathrm{th.}}$. Eq. (3.1) simply states that the sum over all final states X has to be taken, or in other words: All contributions for a given model have to be added for the final predicted number of signal events.

However, this objective is impossible to pursue. In principle there exists an infinite number of final states which cannot be evaluated in a finite amount of computational time. It will also turn out that almost all final states will not yield a noteworthy contribution to $N^{\mathrm{th.}}$ as one or more factors in Eq. (3.1) turn out to be close to 0. Unfortunately there is no simple rule to filter all relevant out of the many irrelevant final states for a general BSM model. However, there are some easy to check properties which can help reducing the number of necessary-to-test final states significantly:

Estimating the cross section: Due to Poissonian statistics, expected signal rates far below 1 event will hardly make a relevant contribution to whatever statistical hypothesis test we are pursuing. Since the integrated luminosity L is a constant, given a particular data set, and since $\mathcal{A} \times \epsilon$ is by construction a number smaller than 1, we can safely neglect processes which have cross sections far below L^{-1}. Trivial examples are the production of particles with masses beyond the proton-proton centre of mass energy, which always yield $\sigma = 0$, or interactions with heavy intermediate particles of mass M from which $\sigma = \mathcal{O}(1/M^2)$ provides an estimate based on dimensional arguments. Also, the higher the final state mupltiplicity the smaller the cross section due to an increasing phase space suppression.

An alternative to the "educated guess" would be to only simulate the hard process and to performe the PDF folding, i.e. to ignore the computationally intense parton showering and hadronisation simulations. The resulting cross section estimates can be sufficient to filter out irrelevant processes.

Constructing the final state: The selection process which yields the final state efficiency ϵ is designed to largely filter out contributions from processes which do not look like the class of models the analysis was designed for. Therefore, one should focus on those final states which share similarities to these base models. One important property is the number of leptons and the number of jets produced in the hard process which should be compatible[14] with the cuts applied in the event selection. As another example, many LHC analyses are designed to find R-Parity conserving Supersymmetry with an invisible, stable neutralino taking momentum from each event. These analyses are only sensitive to other models if these predict a similar invisible stable particle in the final state.

3.5 Summary

In this chapter, we discussed the necessary steps to test a given particle physics model against observed data from ATLAS or CMS and which public tools are available to automatise individual tasks. Let us bring these together for a short recipe of collider phenomenology:

1. Use a model building tool and/or a spectrum generator to translate model parameters into physical masses and couplings,
2. run one (or more) event generator(s) to simulate the collison process and obtain a Monte-Carlo sample which includes a finite sample of representative final state configurations,
3. apply a detector simulation to consider experimental uncertainties in the final state reconstruction,
4. quantify the content of the simulated data by a well-defined cut-prescription to find a prediction S of signal events with certain properties,
5. combine this predicted number with the respective observed and Standard Model expected numbers to calculate a statistical p-value and
6. discard a model if the p-value is too small.

Even though the possibility to delegate the tricky calculations to external tools simplifies the effort tremendously, it is still not a trivial task. Along the way, we have seen that different approximations have to be made and thus for each task there are many available tools which each come with individual stengths, weaknesses and various tuning parameters. One of the most challenging parts is therefore to understand these and carefully choose the tools and settings which suits the given problem best. The respective tools' documentations might help for this choice and in case of doubts, the impact of different settings or even different tools on the results should be analysed and compared to real data and/or results from sophisticated experimental studies. Still, in the upcoming chapter we present a tool which combines all but the first step in a fully automatised form.

[14] It shouldn't be ignored that extra jets can appear via initial or final state radiation and jets, as well as leptons, might not all be reconstructed in the detector.

CHAPTER 4

Automatised LHC Tests with CheckMATE

In the previous chapter we discussed the general Monte Carlo approach to test a given particle physics model against experimental results. We encountered various tools which had to be connected in order to successively translate a theoretical model into a p-value which states its compatibility with observation. This was done by simulating pseudo-collision events, passing them through a detector simulation, analysing the simulated data in close analogy to real data and apply a well-defined statistical measure to the final number.

With the many independent searches which have been performed by ATLAS and CMS on LHC data taken at $\sqrt{s} = 7,8\,\text{TeV}$, the above task quickly becomes very tedious to perform. Depending on the model of interest, the respective potentially relevant analyses have to be identified and translated into program code which fits in the above tool framework. Before the actual model can be analysed, the implemented code first has to be validated against benchmark models that are also tested within the experimental publications to check that these results can be reproduced. Not only is this very time consuming but also a repetitive task, especially if many people need to make use of the same analysis and each performs the above task independently of one another. Moreover, the remaining links of the above tool chain hardly change and are to certain degrees universally applicable to any model. It is therefore feasible and very valuable if a public tool could be provided which not only combines the individual steps discussed in the previous chapter but which also provides the framework to embed analyses in such a way that — if implemented and validated once — they can be universally applied to any model.

`CheckMATE` (Check Models at Terascale Energies) is a tool which we developed with the above motivation in mind and which we discuss in detail within this chapter. We start with a general overview of the tool in Section 4.1 and discuss which input the user can provide and how this input is then successively processed by different, independent modules. A practical example is provided right after in Section 4.2 in which a sufficiently complex benchmark scenario is analysed with `CheckMATE` and the accessible intermediate and final results are examined in all detail. With the general structure of the program being understood, we continue with the discussion of some more advanced details in the subsequent sections. In Section 4.3 we provide some more information on the implemented detector tunings to improve the description of the ATLAS and CMS detector. Then, in Section 4.4, we discuss how analyses are embedded into the code framework, which particular LHC analyses can be found in the current version of the tool and how users can add new analyses to the `CheckMATE` framework on their own. We also illustrate how we check the consistency of the tool's prediction with the experimental results. For the exercise of adding a new analysis to `CheckMATE`, we provide another practical example in Section 4.5. We conclude in Section 4.6 and give an outlook to the current development status and the expected future of the tool.

The CheckMATE version 2.0 described in this chapter is in its final stages of completion but unfortunately is not public yet. It contains significant changes and improvements compared to version 1.0 which has been published in Ref. [178] and which has been used for the studies described in Chapter 5 and Chapter 6. Still, the fundamental concepts are very similar and thus we draw from this reference in our description of the detector tunings in Section 4.3 and the performance studies of those analyses in Section 4.4.2 which were already present in this original version.

A separate manual which focusses on the possibility to conveniently add analyses to the framework was published separately in Ref. [179]. The example which we discuss in Section 4.5 is already present in that reference but is updated to the 2.0 version of the code.

The current public CheckMATE version can be downloaded from the CheckMATE webpage http://checkmate.hepforge.org/. The yet unpublished private version of the 2.0 code which is described in this chapter and which has been used for the examples runs can be downloaded from http://checkmate.hepforge.org/private/CheckMATE-Thesis.tar.gz. A detailled installation tutorial can be found in Appendix B.1.

4.1 General Program Flow

CheckMATE incorporates many individual modules which cover a large amount of the steps necessary for model testing which we described in the previous chapter. A flowchart which illustrates which types of input data is internally passed between these modules in order to get the final result is given in Fig. 4.1. They are wrapped by a Python environment which takes care of the user prompts, the file handling and the setup of the core modules which we describe in more detail below.

4.1.1 FRITZ

FRITZ[1] (Flexible Rapid Interactive Tool Zipper) denotes the C++ core program of CheckMATE. Depending on the provided data and the given settings, it has the possibility to connect and run Pythia 8, Delphes, the AnalysisHandler — we explain below what these are — and all the analyses loaded by the user in any desired start/end combination. Intermediate data, i.e. the simulated Monte Carlo events generated by Pythia and/or the detector level objects produced by Delphes, is passed on-the-fly between the individual modules. This is a great improvement to the original CheckMATE version 1 in which the generated events as well as the detector level objects were necessarily stored on hard disk. The reason is that a typical BSM Monte Carlo event file including hadronised final states and a sufficiently high statistical sample of $\mathcal{O}$(few thousands) events easily reaches file sizes at the GiB scale and beyond. From hard drive perspectives it is very inpractical to store such a big file including detailled information on every individual event if in the end this information is read out event by event. Especially if a complex model like the MSSM requires lots of processes to be analysed simultaneously, this can lead to severe problems if disk space is limited. The virtual passing of eventwise information as performed by FRITZ hence saves a large amount of hard disk space. Also, the total runtime is halved for a single, independent run and the speed gain can be even better during a parallelised run since multiple read/write processes typically slow down the CPU even more.

[1] The name *Fritz* is derived from a German chess program of the same name, see Ref. [180], and the very first chess computer program the author got in contact with.

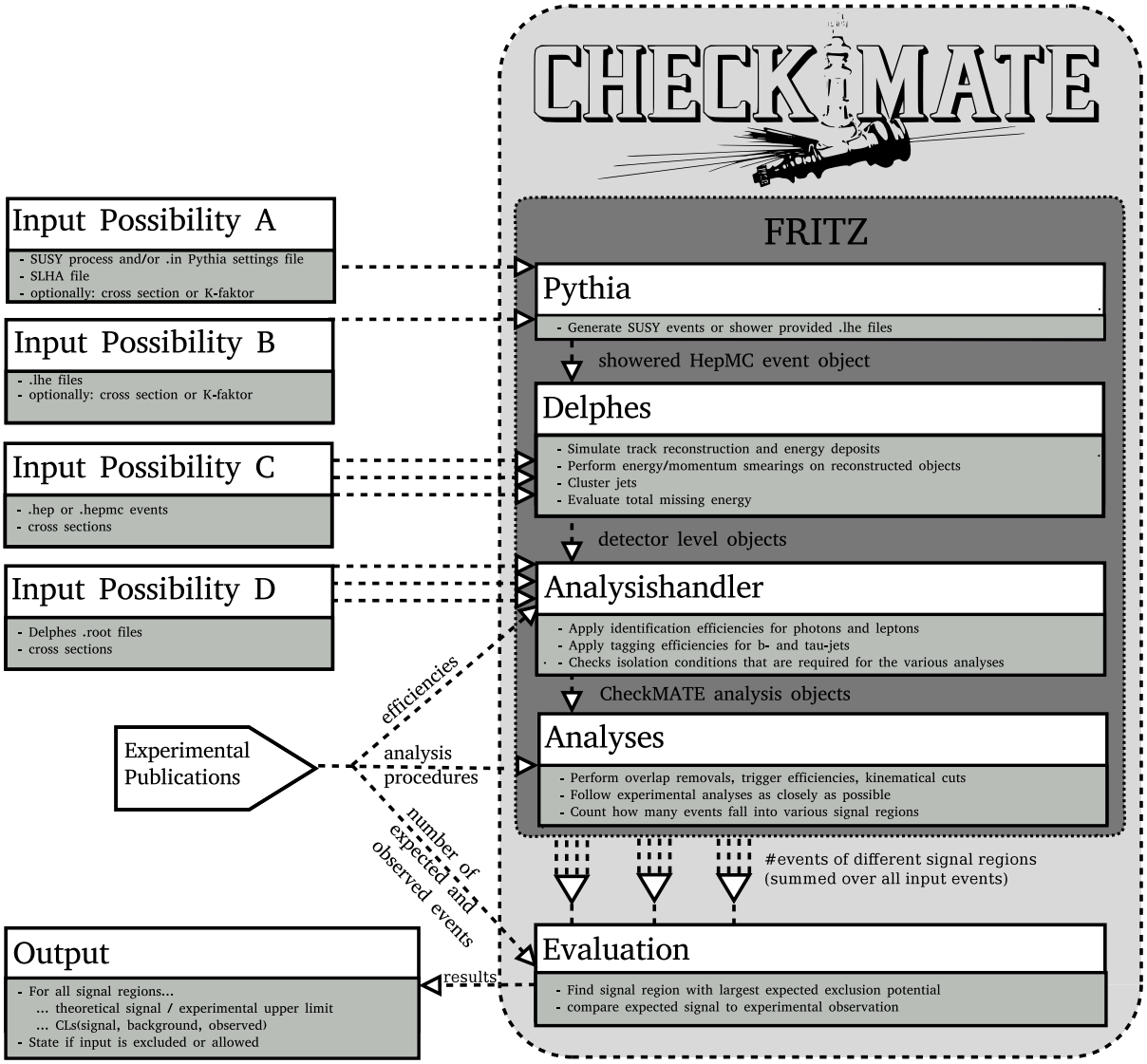

Figure 4.1: Flow chart to demonstrate the chain of data processing within `CheckMATE`.

4.1.2 Pythia

As we addressed in depth in Section 3.2, the core part of Monte-Carlo based collider phenomenology is the simulation of final state configurations that would be produced in a collider experiment if a particular particle model was true.

In the first version of the CheckMATE code described in Ref. [178], the event generation part had to be done externally by the user before running CheckMATE. Monte-Carlo event files and the corresponding cross sections, either from the same event generator or from an external cross section calculator, c.f. Section 3.2.8, were a mandatory input parameter which were then processed via Delphes within CheckMATE. Besides the practical inconvenience that every CheckMATE user had to somehow link an external event generator to the CheckMATE code, the forced split between event generation and detector simulation/analysis also yields a computational disadvantage as already explained in Section 4.1.1. This is why the new CheckMATE version provides an automatic link to the Pythia 8 event generation tool presuming that this tool is installed on the user's machine. If this is the case, CheckMATE provides different types of input modes to run Pythia 8:

Generate events entirely using Pythia 8: As mentioned in Sections 3.2.2 and 3.2.4, Pythia 8 is capable of generating hard matrix elements for various BSM models and also doing the complete parton showering and hadronisation of the final state. This functionality can be accessed by CheckMATE in two different ways.

One possibility is to provide the Pythia 8 setup via an .in file which uses a Pythia 8 internal syntax, see Refs. [147, 148], for setting the internal parameters properly. This mode allows for the full flexibility of the Pythia 8 program as all parameters can be changed via this input file method. Most importantly, the .in file is used to define the model and the list of processes which should be generated. Also, the SLHA file which specifies the to-be-simulated parameter point must be provided in this case, c.f. Section 3.1.

In the special case of SUSY pair production within the MSSM, the user can define the to-be-simulated processes directly within CheckMATE, e.g. by setting `Pythia8Process: p p > go go` to initiate gluino pair production. A full list available processes is given in Appendix B.2.

In both scenarios, CheckMATE will use Pythia 8 to simulate the given event types and directly processes these events with the subsequent detector simulation and analysis routines. As explained above the events are not manifestly stored on hard disk unless explicitly demanded by the user.

Furthermore, Pythia 8 also calculates the total cross section for the simulated process and automatically passes this number to CheckMATE's analysis routines, see below, to properly normalise the events. The user is also free in his choice to instead provide this cross section or a K-factor calculated via an external source, c.f. Section 3.2.8.

Shower externally provided .lhe files: In Chapter 3 we discussed how Monte Carlo events can be generated for in principle any model by means of the UFO format, which unfortuntely is not incorporated into the Pythia 8 framework. Hence, if the user wishes to analyse a model which is not hard-coded into Pythia 8, the use of a different tool is required. In this case, event generation has to be performed externally by e.g. any of the tools listed in Section 3.2.2. However, as explain in the previous chapter the hard matrix element simulation and the parton showering and hadronisation steps can be performed

rather independently and it is the latter which takes the most computational effort and most hard disk space if events need to be stored. Fortunately, CheckMATE can also take lightweight .lhe files produced by an external tool and use Pythia 8 in the same on-the-fly manner as above. A standard .in file is then used to define the hadronisation settings but if necessary users can also provide their own file instead.

4.1.3 Delphes

The previous step produced hadronised and showered events in HepMC data format. These event files can also be generated externally and provided by the user, as long as these files are either in the same or in the .hep format as it is for example produced by the MadGraph5_aMC@NLO tool. In all cases the events are further processed within CheckMATE by the fast detector simulation Delphes, c.f. Section 3.3.1. In CheckMATE 2.0, contrarily to the original CheckMATE version described in Ref. [178], Delphes mostly uses the respective standard detector settings for ATLAS and CMS. The only exception is the kinematic smearing of electrons and muons which for both experiments is replaced with new functions with a better large-energy behaviour, see Section 4.3. Besides, the output event object is slightly extended and in addition to the detector level objects includes those generator level particles which are required to perform an external phenomenological b- and τ-tagging algorithm, see Section 4.1.4 below.

Similarly to the previous step, the results of this simulation are stored in ROOT objects, c.f. Section 3.3.2, which are typically not stored on disk but instead immediately processed by the analysis framework described below. By setting the respective flag, see Appendix B.2, a .root ouput file can be created and this file can be used as an event file in a future CheckMATE run, see also Fig. 4.1.

If the user decided to test only ATLAS or only CMS analyses, Delphes only needs to run once per event. Otherwise, each input event is processed by two independent Delphes runs and independent detector level objects for ATLAS and CMS analyses are respectively created.

4.1.4 AnalysisHandler

The detector level objects created in the previous step contain reconstructed electrons, muons, photons, jets, tracks, clustered calorimeter cells and the missing momentum vector. These are now further processed by so-called AnalysisHandlers before being passed to the actual data analysis codes.

Depending on the list of analyses the user chose to be taken into account, final state objects are tested against a list of isolation, identification and tagging conditions which set individual tags on those candidates which pass the respective constraints. For that purpose, CheckMATE first determines which constraints have to be at all considered in order to provide all analyses with their respectively required information on the final state objects. As an example, let us assume the user chose three analyses out of which two require jets to contain information whether they pass b-tagging information with a particular working point efficiency x and the third requires a different b-tagging efficiency of y. Then the AnalysisHandler will apply two simplified b-tagging algorithms with the two chosen working point efficiencies on the given list of jets per event. Each of the two tests then sets an independent, object-specific tag and the AnalysisHandler bookkeeps which tag corresponds to which respective algorithm. In similar manner, the AnalysisHandler takes care of τ-tagging, lepton identification and object isolation

conditions[2].

CheckMATE uses a set of independent AnalysisHandlers with individual tagging efficiencies depending on the list of analyses chosen by the user. For now[3], there exist individual AnalysisHandlers for analyses performed on 7, 8 and 13 TeV data and for projective studies at 14 TeV centre-of-mass energy. For each of those there is an independent ATLAS and CMS version. We discuss the implemented tunings in more detail in Section 4.3.

4.1.5 Analyses

After all detector level objects have been properly prepared by the AnalysisHandler(s), these are event-wise processed by those of the supplied analyses the user selects when starting CheckMATE. They are internally coded in a well–structured framework that allows for an easy extension to new upcoming experimental results. It furthermore allows users to easily update given analyses or implement their own. We discuss this in more detail in Section 4.4.

The input data is processed event by event by checking isolation criteria, removing overlapping objects and implementing the cuts that define the signal regions, just as how we explained it in Section 3.3.2. The analysis program determines how many events in total satisfy certain signal region criteria and stores this information in human–readable output for each separate input event file or alternatively each separate Pythia run. In addition, the true number of Monte Carlo events, the efficiency times acceptance $\mathcal{A} \times \epsilon$ and the properly normalised number $N^{\text{th.}}$, c.f. Eq. (3.1), are stored as well. The proper normalisation is done by using the corresponding integrated luminosity L of the respective analysis, stored in CheckMATE, and the cross section σ provided either internally by Pythia 8 or externally by the user. In case of weighted events, the event weights are properly taken into account.

4.1.6 Evaluation

The final step of the program consists of a statistical evaluation of the results. For each individual signal region of all chosen analyses, the total number of expected signal events S is determined by summing up the results from each input event file as explained below in Section 4.2.3. The total 1σ uncertainty ΔS on this number is determined from both the statistical uncertainty, given by the number of Monte Carlo events, and the systematic uncertainty, which is estimated from the total uncertainty on the signal cross section given by the user as an optional parameter. These numbers are compared to the results from the respective experimental search which are implemented in CheckMATE. There are two possible ways of comparison:

1. Many experimental searches translate their results into model independent 95% upper confidence limits $S95$ on the number of signal events coming from new physics. A quick–and–easy way of comparison is given by computing the parameter,

$$r \equiv \frac{S - 1.96 \cdot \Delta S}{S^{95}_{\text{Exp.}}} \tag{4.1}$$

[2] In the original CheckMATE publication, all these steps have been performed within the Delphes framework by always generating a run-specific Delphes detector card. That made it impossible to re-use Delphes output files, either within CheckMATE to *a posteriori* test additional analyses or outside CheckMATE with a different Delphes-based analysis framework like e.g. MadAnalysis5 [174]. These tools therefore mutually agreed to switch to a final state postprocession ouside Delphes, see also Ref. [181].

[3] In the beta version 2.0 linked in the introduction of this chapter, all these handlers use the same efficiencies for all objects. It is however planned to soon update those for $\sqrt{s} = 13, 14$ TeV to new published results.

$$= \frac{95\%\text{ lower limit on the number of signal events, determined by CheckMATE}}{\text{Experimentally measured 95\% confidence limit on signal events}}. \quad (4.2)$$

In that case, a model can be considered as excluded to the 95% confidence level, if $r \geq 1$.

2. The user can ask for the explicit confidence level for the given signal. Following common use of experimental searches, CheckMATE uses a profile log–likelihood ratio test paired with the CL_Sprescription, c.f. Section 3.3.3 and Appendix A.2, to determine the confidence level that corresponds to the determined number of signal events and the expected and observed number of events at the experiment. Both the uncertainty on the signal and on the background are taken into account as log-normal probability density functions around the nominal values.

Besides those two means of model testing, CheckMATE optionally allows for the calculation of the likelihood of the final result. This allows for model parameter fits and corresponding confidence limit evaluations.

4.1.7 Output

The aforementioned parameters are determined for all signal regions of all selected analyses. If available from the experimental papers, not only the observed but also the expected limits are used. The signal region with the strongest expected limit is determined and the corresponding observed limit is used to state whether the input can be considered excluded or allowed, see also Section 4.2.3. This result is printed on screen together with the information which analysis and which signal region were determined to be most sensitive.

4.2 Example: Running CheckMATE and Understanding the Results

To illustrate how the individual steps explained in Section 4.1 work in practice, we discuss an example CheckMATE run. It is designed in such a way that it covers the most common scenarios to provide input data within the current CheckMATE version. It also attempts to apply some optional settings to illustrate their meaning. After the example run is completed, we take a closer look at the auxiliary files which are created along the way and which additional information the user can find in these.

4.2.1 Benchmark Model

Within this section we test a simplified supersymmetric model where the only kinematically accessible particles are the gluino with mass 1.5 TeV, the eight mass degenerate squarks of the first two generations, also with mass 1.5 TeV and a 100 GeV stable neutralino LSP. Here the gluino is expected to always decay democratically into a quark and the associated squark, i.e. $\tilde{g} \to \tilde{q}\bar{q}$, and the charge conjugate final state with equal probability. Quarks and squarks are from the first two fermion generations only. Each squark then decays to 100 % into the associated quark and also the neutralino. Such a simplified *squark-gluino-neutralino* model is an often used benchmark scenario in LHC searches for events with many jets and missing transverse energy, see e.g. Ref. [182]. The important parts of the SLHA file for this model, c.f. Section 3.1, looks as follows:

point.slha

```
[...]
Block MASS   # Scalar and gaugino mass spectrum
#  PDG code    mass    particle
   1000001     1500    # downL squark
   2000001     1500    # downL squark
   1000002     1500    # upL squark
   2000002     1500    # upL squark
   1000003     1500    # strangeL squark
   2000003     1500    # strangeL squark
   1000004     1500    # charmL squark
   2000004     1500    # charmL squark
   1000021     1500    # gluino
   1000022     100     # neutralino
   1000023     5000    # neutralino 2 (and similarly for all other particles)
 [...]
#         PDG         Width
DECAY   1000021  7.93203581E-05              # gluino decays
      0.25    3       1000022       -1   1   # gluino -> neutralino antidown down
      0.25    3       1000022       -2   2   # gluino -> neutralino antiup up
      0.25    3       1000022       -3   3   # gluino -> neutralino antistrange strange
      0.25    3       1000022       -4   4   # gluino -> neutralino anticharm charm
DECAY   1000001  6.47400131E+01         # downL decays
      1    2      1000022         1    # downL -> down neutralino
DECAY   1000002  6.47400131E+01         # upL   decays
      1    2      1000022         2    # upL -> up neutralino
DECAY   1000003  6.47400131E+01         # strangeL   decays
      1    2      1000022         3    # strangeL -> strange neutralino
DECAY   1000004  6.47400131E+01         # charmL   decays
      1    2      1000022         4    # charmL -> charm neutralino
DECAY   2000001  6.47400131E+01         # downR   decays
      1    2      1000022         1    # downR -> down neutralino
DECAY   2000002  6.47400131E+01         # upR   decays
      1    2      1000022         2    # upR -> up neutralino
DECAY   2000003  6.47400131E+01         # strangeR   decays
      1    2      1000022         3    # strangeR -> strange neutralino
DECAY   2000004  6.47400131E+01         # charmR   decays
      1    2      1000022         4    # charmR -> charm neutralino
```

Note that we decoupled all the irrelevant SUSY particles from the accessible spectrum by setting their masses to 5 TeV.

In proton-proton collisions, the most relevant production modes for such a model are the 2-body final states $pp \to \tilde{g}\tilde{g}, \tilde{g}\tilde{q}, \tilde{q}\tilde{q}$ and $\tilde{q}\tilde{q}^*$. In our example run, we use different approaches[4] to generate the events for these processes:

- For both processes $\tilde{q}\tilde{q}^*$ and $\tilde{q}\tilde{q}$, we use `Pythia 8` embedded in `CheckMATE` to generate events "on the fly". For the first, we state the to-be-generated process directly in `CheckMATE` while for the second, we provide our own `.in` `Pythia 8` setup file.
- For events of type $\tilde{g}\tilde{g}$, we provide partonic `.lhe` files generated with `MadGraph5_aMC@NLO` beforehand and perform the parton showering and hadronisation with `Pythia 8` directly within `CheckMATE`.
- Associated gluino-squark production has been performed completely externally and we provide two fully showered `.hepmc` files. The two files contain the same physics generated with different random seeds such that they contain statistically independent samples. Such a setup with multiple files per process can for example happen when event generation is parallelised on a computing cluster.

[4] The different input modes are only combined for illustrative purposes here. In practice, one would typically use the same tool setup for all the different hadronic SUSY final states.

4.2.2 Initialising and Starting CheckMATE

We assume that CheckMATE has already been properly installed in folder $CMDIR including Pythia functionality, see also Appendix B.1. Also, the pre-generated .lhe file for the $\tilde{g}\tilde{g}$ and the .hepmc file for the $\tilde{g}\tilde{q}$ process are located in /scratch/files. To run CheckMATE, some mandatory information has to be provided, either via a command line input or via a text-based parameter card. As the former only works for runs with single processes, we have to choose the second approach. A minimal working example for the above setup reads as follows:

checkmate_parameters.in

```
[Parameters]
Name: ThesisExample
SLHAFile: /scratch/files/point.slha

[squ_asq]
Pythia8Process: p p > sq sq~
MaxEvents: 1000

[squ_squ]
Pythia8Card: /scratch/files/pythiasqusqu.in
KFactor: 1.2

[glu_glu]
Events:    /scratch/events/glu_glu.lhe
XSectErr: 20 %

[glu_sq]
Events: /scratch/events/glu_squ_1.hepmc, /scratch/events/glu_squ_2.hepmc
XSect: 0.75 fb
```

The general structure of such a file consists of blocks separated by [] expressions which contain one or more Key: Value pairs.

The first such block, [Parameters], is a special block type which lists general settings for the CheckMATE run common to all processes. In our example, we first give our run a specific name ThesisExample which specifies the name of the output directory. Then we provide the above explained .slha spectrum file which informs Pythia 8 about the masses, mixing matrices and decay tables of all SUSY particles. This file is common to all processes as obviously the same physics scenario should be considered within one CheckMATE run. In our case, the SLHAFile is a mandatory parameter as we ask CheckMATE to use Pythia to simulate the events. Not providing this parameter would result in an immediate abort. If we however only provided .hepmc files, this parameter would not be mandatory as no model-dependent information would be required any more. Note that providing .lhe also requires an SLHA file if the BSM final state particles are not yet decayed. In this case, the SLHA must include the full decay table. Additional possible settings which can be changed via the [Parameters] block are summarised in Appendix B.2.

Besides the special [Parameters] block, any other [X] block combines the information for a particular production process X, where X is a freely chosen identifier. In our particular case, we need four such blocks for all the different production modes we wish to take into account. Within each such process block we have to provide the information in which form the Monte Carlo events for that particular process are given.

- We start with the block [squ_asq] responsible for $\tilde{q}\tilde{q}^*$ production. Here we explicitly state the 2-body final state, see also Appendix B.2, by making use of the Pythia8Process keyword and set CheckMATE to use Pythia 8 for the event generation. As we do not specified otherwise, CheckMATE generates 5,000 events. Since no cross section is provided,

CheckMATE uses the result from Pythia 8 determined during the generation of the events. We use the optional KFactor parameter to specify a K-factor, c.f. Section 3.2.8, which we determined with NLLfast [163]. It multiplies the Pythia leading order cross section with a fixed quantitiy to estimate the cross section at next-to-leading order plus next-to-leading log accuracy in QCD.

- For the simulation of $\tilde{q}\tilde{q}$ pair production, we set up a second block called [squ_squ]. Here, we also want the event generation to be done entirely internally via Pythia 8, however this time we explicitly provide the .in setting file for Pythia.

pythiasqusqu.in

```
PDF:pSet = 8 !(CTEQ6L1)

Beams:idA = 2212   ! first beam, p = 2212, pbar = -2212
Beams:idB = 2212   ! second beam, p = 2212, pbar = -2212
Beams:eCM = 8000.

SLHA:file = /scratch/files/point.slha
SUSY:qq2squarksquark = on
SUSY:idVecA =  1000001,1000002,1000003,1000004,2000001,2000002,2000003,2000004
```

  The meaning of the individual lines should be self explanatory. The last row specifies the set of squarks which should be taken into account and which we set to all left- and right-chiral squarks of the first two generations. In principle, any of Pythia 8's parameters listed in Ref. [148] can be changed via this file. Most importantly, if we wanted to generate events for a non-supersymmetric model, we necessarily would have to use this file as CheckMATE can for now only parse few standard setups via the Pythia8Process command used above.

  Note that for this block, we explicitly specify the number of generated events to be 1,000 via the optional parameter MaxEvents.

- The third process block [glu_glu] sets up the gluino pair production process for which we have pregenerated 1,000 events via MadGraph5_aMC@NLO. Here, we simply have to provide a reference to this file via the Events keyword. There is no other mandatory parameter in this case. Most importantly, CheckMATE uses standard Pythia settings for showering and hadronisation, see below, and takes the cross section from the .lhe file itself. In this example, we provide the optional parameter XSectErr to inform CheckMATE about the systematic error it should consider for this process, which we assume to be 20 % of the signal cross section. If no such parameter is provided, as we do for the other three processes, the systematic error is set to zero.

- Lastly, we provide two fully hadronic .hepmc files for associated gluino squark production in the [glu_squ] block. We can simply list all available files for a given process in one Events command and in the end the results of all files are properly averaged as explained below. Since the .hepmc file format can not store the cross section information determined by the respective event generator we *must* provide it explicitly. Otherwise CheckMATE aborts due to being incapable of properly normalising the final results. In our case, the provided cross section is taken from Pythia 8 which we used to simulate the events but we could have instead used NLLfast or Prospino.

With the above files ready, we can intuitively start CheckMATE via the following command[5]:

[5] Within this chapter, grayed text denotes input to be typed by the user.

Terminal

```
$CMDIR/bin:  ./CheckMATE checkmate_parameters.in
```

CheckMATE then responds with a summary of the used settings for the given run and asks the user for confirmation

Terminal

```
  ____ _               _    __  __    _  _____ _____ ____
 / ___| |__   ___  ___| | _|  \/  |  / \|_   _| ____|___ \
| |   | '_ \ / _ \/ __| |/ / |\/| | / _ \ | | |  _|   __) |
| |___| | | |  __/ (__|   <| |  | |/ ___ \| | | |___ / __/
 \____|_| |_|\___|\___|_|\_\_|  |_/_/   \_\_| |_____|_____|

The following settings are used:
Analyses:
        atlas_1308_1841 (0 lepton + large jets multi + missingET)
        atlas_1308_2631 (0 leptons + 2 b-jets + Etmiss [Sbottom/stop])
        [...]
        cms_sus_12_019 (2-leptons, jets and met (SF-OF))
E_CM: 8.0
Processes:
        Name: squ_asq
        Process: p p > sq sq~
        Input KFactor: 1.96
        Will run Pythia8

        Name: squ_squ
        Maximal number of generated/analysed events: 1000
        Will run Pythia8
                 Using settings in /scratch/files/pythiasqusqu.in

        Name: glu_glu
        Input cross section error: 20.0 %
        Input event file(s):
                /scratch/events/glu_glu.lhe
        Will run Pythia8

        Name: glu_sq
        Input Cross section: 0.75 fb
        Input event file(s):
                /scratch/events/glu_squ_1.hepmc
                /scratch/events/glu_squ_2.hepmc

Output Directory:
        $CMDIR/results/ThesisExample
Additional Settings:
         - SLHA file /scratch/files/point.slha will be used for event generation
Is this correct? (y/n)
```

If not specified otherwise, CheckMATE generates events at $\sqrt{s} = 8\,\text{TeV}$ centre of mass energy and tests against all implemented ATLAS and CMS analyses for that particular energy as currently only few 13 TeV analyses are implemented and therefore typically the 8 TeV analyses are most constraining[6].

As soon as we start CheckMATE with the anser y, it informs us that — since we did not specify otherwise — Pythia is set up to generate 5,000 events for the squ_asq process.

[6] As event files do not contain the information at which centre-of-mass energy the simulation has been performed, CheckMATE has to rely on the user to provide events generated at the correct value of $\sqrt{s}$ assumed in the tested analyses.

```
Terminal

        squ_asq:genPy8card(): Setting number of to-be-generated MC events to 5000.
                                    Use the 'maxEvents' Parameter to change this default behaviour.
```

After about fifteen minutes during which CheckMATE informs us about the current status of the analysis, it returns the following result[7]

```
Terminal

Evaluating Results
Test: Calculation of r = signal/(95%CL limit on signal)
Result:  Excluded
Result for r: 1.66561125658
Analysis: atlas_1405_7875
SR: SR02_3j
```

We find that after simulating all events, passing them through a detector simulation and performing about 40 different analyses, CheckMATE concludes that the input parameter point is excluded because in signal region SR02_3j of analysis atlas_1405_7875, see Ref. [183], the number of predicted signal events S exceeds the 95 % upper limit S95 in the r-test of Eq. (4.2). Fortunately, this agrees with the result of the experimental collaboration, see Ref. [184].

For the basic user, this information would be sufficient for checking the collider signature for a given model. Typically, one could perform the same test with the exact same setup for different values of $m_{\tilde{q}}$ and $m_{\tilde{g}}$ set in the SLHA file and by that scan for the interesting, still allowed regions in parameter space.

4.2.3 Structure of the Results Folder

We now take a closer look at the additional information that is stored within many files in the results folder. These file are of no interest for the ordinaty user who simply performs a test for a given parameter point. However, knowing which information can be found in these files can be very helpful if for instance a more detailled breakdown of intermediate results is required or if CheckMATE behaves unexpectedly. Furthermore, analysing these files aids us in understanding how CheckMATE internally works.

For our example case, the results folder would be located under $CMDIR/results/ThesisExample. It contains the following files and directories:

```
Terminal

$CMDIR/results/ThesisExample:  ls
   analysis  delphes  evaluation  fritz  internal  pythia  result.txt
```

The file result.txt stores the exact same information printed on screen at the end of the CheckMATE run. The other folders store the respective individual information of the modules explained in the introductory section and we discuss them in the same order.

Folder internal/

The internal folder stores all internally set CheckMATE parameters in a Python readable format such that *a posteriori* one is capable of reproducing the exact Python instance of CheckMATE and is most importantly needed if CheckMATE is run in add mode explained in Appendix B.2. They are hardly of relevance for the user and therefore we do not further discuss them here.

[7] Since we use random Monte Carlo samples without specifying a random seed, the shown result is not completely deterministic.

Folder `fritz/`

The `fritz` folder of our above example should contain the following files

Terminal

```
$CMDIR/results/ThesisExample/fritz:  ls
fritz_glu_glu.log        glu_glu.ini
fritz_glu_sq_event1.log  glu_sq_event1.ini
fritz_glu_sq_event2.log  glu_sq_event2.ini
fritz_squ_asq.log        squ_asq.ini
fritz_squ_squ.log        squ_squ.ini
```

Here, `.log` files contain the runtime output of `FRITZ` which was also printed on-screen while `CheckMATE` was running. There exists one `.log` file for each of the individually tested event files, i.e. five in our case as we have four processes with one which uses two separate `.hepmc` event files. The `.log` files informs the user about the order in which individual modules were initialised, combined and finalised in the end, for example:

fritz_squ_squ.log

```
Fritz: Initialising handlers from file $CMDIR/results/ThesisExample/fritz/squ_squ.ini
PythiaHandler 'pythia': Initializing Pythia8 with $CMDIR/bin/thesisexample/pythiasqusqu.in
PythiaHandler 'pythia': Output redirected to $CMDIR/results/ThesisExample/pythia/pythia_squ_squ.log
PythiaHandler 'pythia': Pythia8 initialized successfully!
PythiaHandler 'pythia': Pythia8 will generate 100000000 events
DelphesHandler 'atlas8tev': Initialising Delphes via linking to PythiaHandler 'pythia'
DelphesHandler 'atlas8tev': Initialising settings from $CMDIR/data/cards/delphes_skimmed_ATLAS.tcl
DelphesHandler 'atlas8tev': Delphes successfully initialised!
DelphesHandler 'cms8tev': Initialising Delphes via linking to PythiaHandler 'pythia'
DelphesHandler 'cms8tev': Initialising settings from $CMDIR/data/cards/delphes_skimmed_CMS.tcl
DelphesHandler 'cms8tev': Delphes successfully initialised!
AnalysisHandler 'atlas8tev': Initialising AnalysisHandler
AnalysisHandler 'atlas8tev': Loading Analysis atlas_1308_1841
AnalysisHandler 'atlas8tev': Successfully loaded analysis atlas_1308_1841
[...]
AnalysisHandler 'atlas8tev': Successfully loaded analysis atlas_conf_2015_004
AnalysisHandler 'atlas8tev': Linking to DelphesHandler 'atlas8tev' tree
AnalysisHandler 'atlas8tev': AnalysisHandler successfully linked to DelphesHandler 'atlas8tev'
AnalysisHandler 'cms8tev': Initialising AnalysisHandler
AnalysisHandler 'cms8tev': Loading Analysis cms_1301_4698_WW
AnalysisHandler 'cms8tev': Successfully loaded analysis cms_1301_4698_WW
[...]
AnalysisHandler 'cms8tev': Successfully loaded analysis cms_sus_13_016
AnalysisHandler 'cms8tev': Linking to DelphesHandler 'cms8tev' tree
AnalysisHandler 'cms8tev': AnalysisHandler successfully linked to DelphesHandler 'cms8tev'
Fritz: Fritz successfully loaded command line parameters!
Fritz:  >> Successfully initialized and linked all handlers! <<
Fritz: Starting event loop!
Fritz: Progress: 10 %
[...]
Fritz: Progress: 100 %
Fritz:  >> Finalising after 1000 events. <<
AnalysisHandler 'atlas8tev': Asking DelphesHandler 'atlas8tev' for cross section information
DelphesHandler 'atlas8tev': Asking PythiaHandler 'pythia' for cross section information
PythiaHandler 'pythia': Pythia8 returned cross section of 2.43366 fb
PythiaHandler 'pythia': Pythia8 returned cross section error of 0 fb
AnalysisHandler 'atlas8tev': Analyses successfully finished!
AnalysisHandler 'cms8tev': Asking DelphesHandler 'cms8tev' for cross section information
DelphesHandler 'cms8tev': Asking PythiaHandler 'pythia' for cross section information
PythiaHandler 'pythia': Pythia8 returned cross section of 2.43366 fb
PythiaHandler 'pythia': Pythia8 returned cross section error of 0 fb
AnalysisHandler 'cms8tev': Analyses successfully finished!
DelphesHandler 'atlas8tev': Delphes successfully finished!
DelphesHandler 'cms8tev': Delphes successfully finished!
```

```
PythiaHandler 'pythia': Pythia8 successfully finished!
Fritz:  >> Done <<
```

This file enables us to trace exactly which modules have been loaded using which settings and how they were respectively linked. In our particular example, for the squark pair production process we need a `PythiaHandler` which takes care of the event generation within `Pythia 8`[8]. Then, since we test against all 8 TeV analyses, we require two separate `Delphes` instances, one respectively for the ATLAS and the CMS detector description. Each of these `DelphesHandler`s takes its event information from the same single `PythiaHandler`, i.e. the same generated events are used for both ATLAS and CMS. The detector level objects are then respectively passed to two individual `AnalysisHandler`s which each perform flavour tagging and final state isolation checks according to the requirements of the respective analyses. These then pass their information to all the loaded analyses which perform the signal region categorisation independently of one another. In the end, the cross section information — which is needed by the individual analyses to properly normalise their final results — in this particular case is taken from `Pythia 8` itself.

The required set of handlers, their properties and how they are linked is determined by the `Python` part of `CheckMATE` and passed via a `.ini` file[9] .

glu_glu.ini

```
[...]
[Global]
nevents = 1000

[PythiaHandler: pythia]
settings = $CMDIR/results/ThesisExample/pythia/gluinoscard.in
logfile = $CMDIR/results/ThesisExample/pythia/pythia_gluinos.log

[DelphesHandler: atlas8tev]
settings = $CMDIR/data/cards/delphes_skimmed_ATLAS.tcl
logfile = $CMDIR/results/ThesisExample/delphes/delphes_gluinos.log
pythiahandler = pythia

[DelphesHandler: cms8tev]
settings = $CMDIR/data/cards/delphes_skimmed_CMS.tcl
logfile = $CMDIR/results/ThesisExample/delphes/delphes_gluinos.log
pythiahandler = pythia

[AnalysisHandler: atlas8tev]
analysistype = atlas8tev
outputprefix = gluinos
outputdirectory = $CMDIR/results/ThesisExample/analysis
logfile = $CMDIR/results/ThesisExample/analysis/analysis_output.log
delpheshandler = atlas8tev

[AnalysisHandler: cms8tev]
analysistype = cms8tev
outputprefix = gluinos
outputdirectory = $CMDIR/results/ThesisExample/analysis
```

[8] Note that for practical purposes, each process runs a separate `FRITZ` run. This is why only one `Pythia 8` instance appears in the above example logfile for the gluino run. Also note that the `PythiaHandler` quotes that it simulates a billion events. This is because in our setup the number of events is set globally by `FRITZ`, not locally by `Pythia`. This could be done by setting the number of generated events explicitly within the `Pythia .in` file.). As can be seen at the bottom of the logfile, the event generation loop indeed stops at 1,000 events as epected.

[9] The generalisation of the analysis `.ini` file including the automatised and generalised handler setup has been implemented by Torsten Weber.

```
logfile = $CMDIR/results/ThesisExample/analysis/analysis_output.log
delpheshandler = cms8tev
```

The two AnalysisHandlers responsible for respectively ATLAS and CMS analyses need to apply flavour tagging and isolation conditions after the detector simulation step. As explained in the introduction, CheckMATE first analyses the respective analysis implementation in order to create a list of all required settings and which analysis uses which one(s). All this is stored in the same .ini file:

glu_glu.ini

```
[ANALYSIS: atlas_1308_1841]
analysishandler = atlas8tev
jet_btags = atlas8tev7 atlas8tev8 atlas8tev9
electron_isolation = atlas8tev0 atlas8tev3 atlas8tev4
muon_isolation = atlas8tev0 atlas8tev11 atlas8tev12
photon_isolation = atlas8tev0

[ANALYSIS: atlas_1308_2631]
analysishandler = atlas8tev
jet_btags = atlas8tev5
electron_isolation = atlas8tev0 atlas8tev7
muon_isolation = atlas8tev0 atlas8tev9
photon_isolation = atlas8tev0 atlas8tev0

[...]

[ANALYSIS: atlas_1506_08616]
analysishandler = atlas8tev
jet_btags = atlas8tev2
electron_isolation = atlas8tev0 atlas8tev5
muon_isolation = atlas8tev0 atlas8tev5
photon_isolation = atlas8tev0

[BTAG: atlas8tev0]
eff = 70.
analysishandler = atlas8tev

[BTAG: atlas8tev1]
eff = 80.
analysishandler = atlas8tev

[...]

[BTAG: atlas8tev13]
eff = 75.
analysishandler = atlas8tev

[TAUTAG: atlas8tev0]
analysishandler = atlas8tev

[ELECTRONISO: atlas8tev0]
source = c
analysishandler = atlas8tev
dr = 0.2
ptmin = 0.1
absorrel = r
maxval = 0.2

[ELECTRONISO: atlas8tev1]
source = t
analysishandler = atlas8tev
dr = 0.2
ptmin = 1.
absorrel = r
```

```
maxval = 0.1

[..]

[ELECTRONISO: atlas8tev27]
source = c
analysishandler = atlas8tev
dr = 0.3
ptmin = 0.1
absorrel = r
maxval = 0.14

[MUONISO: atlas8tev0]
source = t
analysishandler = atlas8tev
dr = 0.05
ptmin = 0.5
absorrel = r
maxval = 0.2

[MUONISO: atlas8tev1]
source = t
analysishandler = atlas8tev
dr = 0.2
ptmin = 0.5
absorrel = a
maxval = 1.8

[...]

[MUONISO: atlas8tev24]
source = t
analysishandler = atlas8tev
dr = 0.2
ptmin = 0.4
absorrel = r
maxval = 0.10

[PHOTONISO: atlas8tev0]
source = c
analysishandler = atlas8tev
dr = 0.2
ptmin = 0.1
absorrel = r
maxval = 0.2

[PHOTONISO: atlas8tev1]
source = c
analysishandler = atlas8tev
dr = 0.4
ptmin = 0.1
absorrel = a
maxval = 4.0

[ANALYSIS: cms_1303_2985]
analysishandler = cms8tev
jet_btags = cms8tev3
electron_isolation = cms8tev0 cms8tev8
muon_isolation = cms8tev0 cms8tev9
photon_isolation = cms8tev0 cms8tev1

[...]

[PHOTONISO: cms8tev1]
source = c
```

```
analysishandler = cms8tev
dr = 0.3
ptmin = 0.1
absorrel = r
maxval = 0.2
[...]
```

We find that e.g. the 30 ATLAS analyses of our general 8 TeV run require in total 27 distinct isolation tests for electrons, 24 different muon isolation tests and 13 different b-tagging benchmark points[10].

The flexibility of FRITZ becomes apparent when checking the corresponding .log file for the $\tilde{g}\tilde{q}$ process for which we provided fully hadronised .hepmc files:

fritz_glu_sq_event1.log

```
Fritz: Initialising handlers from file $CMDIR/results/ThesisExample/fritz/glu_sq_event1.ini
DelphesHandler 'atlas8tev': Initialising Delphes via input event /scratch/events/glu_squ_1.hepmc
DelphesHandler 'atlas8tev': Input File determined to be HepMC.
DelphesHandler 'atlas8tev': Initialising settings from $CMDIR/data/cards/delphes_skimmed_ATLAS.tcl
DelphesHandler 'atlas8tev': Delphes successfully initialised!
DelphesHandler 'atlas8tev': Input file successfully opened!
[...]
Fritz:  >> Finalising after 1000 events. <<
AnalysisHandler 'atlas8tev': Asking DelphesHandler 'atlas8tev' for cross section information
DelphesHandler 'atlas8tev': Asking Eventfile 'glu_sq_event1' for cross section information
Eventfile 'glu_sq_event1':  Returning cross section of 0.75 fb
Eventfile 'glu_sq_event1':  Returning cross section error of 0 fb
AnalysisHandler 'atlas8tev': Analyses successfully Finished!
[...]
Fritz:  >> Done <<
```

One finds that no PythiaHandler is loaded in this case. The .hepmc files are directly loaded into Delphes and the cross section is taken from the user which is passed to FRITZ and by that to the analyses via the corresponding .ini file:

glu_sq_event1.ini

```
[...]

[EventFile: glu_sq_event1]
file = /scratch/events/glu_squ_1.hepmc
xsect = 0.75
xsecterr = 0.0

[...]
```

The analysis part, however, is the same for all processes.

Folder pythia/

The pythia folder contains all files that have been used to simulate the events with Pythia 8. In our particular case, these are

Terminal

```
$CMDIR/results/ThesisExample/pythia:  ls
glu_glucard.in      pythia_squ_squ.log
pythia_glu_glu.log  squ_asqcard.in
pythia_squ_asq.log
```

[10] As explained below in Section 4.3.2, τ tagging always involves three universally defined standard benchmark points, which is why only one TAUTAG item appears in the above list for each experiment.

The `.in` files correspond to setup files for `Pythia 8` which have been written by `CheckMATE` and which contain the commands to simulate the respective final state with the correct centre of mass energy using the SUSY parameter point given in the provided `.slha` file. We have one such card for the `[squ_asq]` process, for which we used the `Pythia8Process` command to let `CheckMATE` generate the `.in` file automatically.

squ_asqcard.in

```
! Settings used in the main program.
Init:showChangedSettings = on      ! list changed settings
Init:showChangedParticleData = on  ! list changed particle data
Next:numberShowInfo = 1            ! print event information n times
Next:numberShowProcess = 1         ! print process record n times
Next:numberShowEvent = 2           ! print event record n times

! For comparison with Pythia 6
PDF:pSet = 8 !(CTEQ6L1)

! Beam parameter settings. Values below agree with default ones.
Beams:idA = 2212                   ! first beam, p = 2212, pbar = -2212
Beams:idB = 2212                   ! second beam, p = 2212, pbar = -2212
Beams:eCM = 8000.

SLHA:file = /scratch/files/point.slha
SUSY:gg2squarkantisquark = on
SUSY:qqbar2squarkantisquark = on
SUSY:idVecA = 1000001,1000002,1000003,1000004,2000001,2000002,2000003,2000004
```

For $\tilde{g}\tilde{g}$ production, we also have a card which sets up `Pythia 8` for hadronisation of `.lhe` events:

glu_glucard.in

```
[...]
Next:numberShowEvent = 0           ! print event record n times

Beams:frameType = 4
Beams:LHEF = /scratch/events/glu_glu.lhe
```

The `.log` files contain the verbatim output produced by `Pythia 8` before, during and after the event generation. If the simulation finished successfully, this file ends with a summary of the numerically evaluated cross sections, for example:

pythia_gluinos.log

```
[...]
 *-------  PYTHIA Event and Cross Section Statistics  ------------------------------------------------*
 |                                                                                                    |
 | Subprocess                         Code |            Number of events       |      sigma +- delta    |
 |                                         |       Tried   Selected   Accepted |     (estimated) (mb)   |
 |                                         |                                   |                        |
 |-----------------------------------------|-----------------------------------|------------------------|
 |                                         |                                   |                        |
 | q q' -> ~d_L ~d_L + c.c.          1351 |         601         13         13 |   4.072e-14  4.625e-15 |
 | q q' -> ~d_L ~s_L + c.c.          1352 |          27          2          2 |   3.343e-15  1.606e-15 |
[...]
 | q q' -> ~t_2 ~d_L + c.c.          1423 |           0          0          0 |   0.000e+00  0.000e+00 |
 | q q' -> ~t_2 ~s_L + c.c.          1424 |           0          0          0 |   0.000e+00  0.000e+00 |
 |                                         |                                   |                        |
 | sum                                     |       27950       1000       1000 |   2.434e-12  3.819e-14 |
 |                                                                                                    |
 *-------  End PYTHIA Event and Cross Section Statistics -------------------------------------------*
[...]
```

Note that, as expected, the final numbers coincide with the cross section values quoted within the above `fritz_squ_squ.log` to have been used for the analysis normalisation.

If for some reason the event generation had to be aborted, this file can be checked for more information about the cause.

Folder `delphes/`

Analogously to the `pythia` folder, intermediate results of the detector simulation step are stored in the `delphes` folder.

terminal

```
$CMDIR/results/ThesisExample/delphes:  ls
delphes_glu_glu.log        delphes_squ_asq.log
delphes_glu_sq_event1.log  delphes_squ_squ.log
delphes_glu_sq_event2.log
```

For our example, this folder simply contains the log files produced by `Delphes` for each of the five independent event files. These do not contain any interesting information if a run succeeded but can be of assistance if the detector simulation encountered an unexpected problem.

Folder `analysis/`

A closer look into the `analysis` folder reveals a plethora of files.

terminal

```
$CMDIR/results/ThesisExample/analysis:  ls
analysis_output.log                              glu_sq_event2_atlas_conf_2013_024_signal.dat
glu_glu_atlas_1308_1841_cutflow.dat              glu_sq_event2_atlas_conf_2013_031_cutflow.dat
glu_glu_atlas_1308_1841_signal.dat               glu_sq_event2_atlas_conf_2013_031_signal.dat
[...]
glu_sq_event2_atlas_conf_2012_104_signal.dat     squ_squ_cms_smp_12_006_signal.dat
glu_sq_event2_atlas_conf_2012_147_cutflow.dat    squ_squ_cms_sus_12_019_cutflow.dat
glu_sq_event2_atlas_conf_2012_147_signal.dat     squ_squ_cms_sus_12_019_signal.dat
glu_sq_event2_atlas_conf_2013_021_signal.dat     squ_squ_cms_sus_13_016_cutflow.dat
glu_sq_event2_atlas_conf_2013_024_cutflow.dat    squ_squ_cms_sus_13_016_signal.dat
```

To be precise, each input event file results in two files per tested analysis, which in our case sums up to a total of 397 different files.

Each analysis in `CheckMATE` produces two types of output: `cutflow`-files show the absolute and relative amounts of events that pass the individual selection cuts of the corresponding analysis step-by-step, c.f. Section 3.3.2, whereas `signal`-files give the final number of events that respectively pass all signal region cuts defined within the analysis. As shown in the examples below, both files have a common structure. For the example we chose to the analysis `atlas_1405_7875` which `CheckMATE` determined to be responsible for the signal exclusion:

glu_glu_atlas_1405_7875_cutflow.dat

```
# ATLAS
# ATLAS-1405-7875
# 0 lepton, 2-6 jets, etmiss
# sqrt(s) = 8 TeV
# int(L) = 20.3 fb^-1

Inputfile:
XSect:           0.0591437 fb
 Error:          0.0118287 fb
MCEvents:        1000
 SumOfWeights:   1000
 SumOfWeights2:  1000
 NormEvents:     1.19582
```

```
Cut                        Sum_W  Sum_W2  Acc    N_Norm
a.2jl_CR01_all             1000   1000    1      1.19582
a.2jl_CR02_missETjetsPT    939    939     0.939  1.12287
a.2jl_CR07_dphiMin2J3J     765    765     0.765  0.914799
[...]
o.6jt+_CR12_Rmeff          156    156     0.156  0.186547
o.6jt+_CR13_meffIncl       149    149     0.149  0.178177
```

glu_glu_atlas_1405_7875_signal.dat

```
[...]
SR            Sum_W  Sum_W2  Acc    N_Norm
SR01_a.2jl    622    622     0.622  0.743797
SR01_b.2jm    326    326     0.326  0.389836
SR01_c.2jt    315    315     0.315  0.376682
SR01_d.2jW    21     21      0.021  0.0251121
SR02_3j       236    236     0.236  0.282212
SR03_a.4jl-   426    426     0.426  0.509417
SR03_b.4jl    426    426     0.426  0.509417
SR03_c.4jm    51     51      0.051  0.0609866
SR03_d.4jt    233    233     0.233  0.278625
SR03_e.4jW    6      6       0.006  0.00717489
SR04_5j       264    264     0.264  0.315695
SR05_a.6jl    119    119     0.119  0.142302
SR05_b.6jm    119    119     0.119  0.142302
SR05_c.6jt    80     80      0.08   0.0956653
SR05_d.6jt+   149    149     0.149  0.178177
```

These files start with some general information about the analysis and the analysed events in total. Note how the cross section error corresponds to 20 % of the total cross section as specified in the `CheckMATE` input file for the $\tilde{g}\tilde{g}$ process.

After this, a list of all individual cutflow milestones/signal regions follows. For each of these, `CheckMATE` lists the sum of weights and sum of squared weights of all events that passed the corresponding cut(s) (`Sum_W, Sum_W2`), the relative efficiency times acceptance factor (`Acc`) as well as the physically expected number of events after normalising to the given total cross section of the data and the luminosity of the respective analysis (`N_Norm`). In case of unweighted events, `Sum_W` and `Sum_W2` corresponds to the number of Monte Carlo events in the respective region. We see that in the above example files. If weighted events are used, they are properly taken into account and both `Sum_W` and `Sum_W2` are needed by `CheckMATE`'s evaluation routines to properly calculate the statistical error in the upcoming evaluation step.

The cutflow information, similarly to all the files discussed in the previous paragraph, can be used by the user for various purposes, e.g. validating analyses by comparing with the cutflows produced by the collaborations as discussed in Section 4.4.2. It is however currently not further processed by `CheckMATE`. The `signal` files, however, contain crucial information used for the subsequent evaluation step explained below.

Any output or warnings/error messages generated during the analysis runs is stored in a common `analysis_output.log`. However, after a successful `CheckMATE` run these files are typically empty.

Folder `evaluation/`

The `evaluation` folder of our example run contains the following files:

Terminal

```
$CMDIR/results/ThesisExample/evaluation:  ls
best_signal_regions.txt          squ_asq_eventResults.txt
glu_glu_eventResults.txt         squ_asq_processResults.txt
glu_glu_processResults.txt       squ_squ_eventResults.txt
glu_sq_event1_eventResults.txt   squ_squ_processResults.txt
glu_sq_event2_eventResults.txt   total_results.txt
glu_sq_processResults.txt
```

Files with name `X_eventResults.txt` simply collect the results returned by all signal regions in all analyses for a given event `X`. By standard, the stored results are the normalised number of predicted signal events (`signal_normevents`) and the total error on this number (`signal_err_tot`).

glu_glu_eventResults.txt

```
analysis            sr                      signal_normevents  signal_err_tot
atlas_1308_1841     SR01_8j50_a.0b          0.0251626          0.00744824763767
atlas_1308_1841     SR01_8j50_b.1b          0.0071893          0.00326829718337
[...]
atlas_1404_2500     SR3Llow                 0.0                0
atlas_1404_2500     SR3b                    0.0                0
atlas_1405_7875     SR01_a.2jl              0.743797           0.151718993922
atlas_1405_7875     SR01_b.2jm              0.389836           0.080901268657
[...]
cms_sus_13_016      SR1                     0.0                0
```

The error is determined by the quadratic sum of statistical error, calculated internally from the size of the Monte Carlo sample, and the systematic error provided by the user. These individual error sources and other possible additional columns can be requested by the user by setting the correct options in the `[Parameters]` block in the `CheckMATE` setup file, see Appendix B.2.

During the evaluation phase, results from all individual events of all independent processes are subsequently combined. First, results from events that correspond to the same process will be *averaged* by taking the corresponding weights properly into account. The statistical error is then calculated from the combined sum of weights and combined sum of squared weights. The statistical error for all signal regions with 0 Monte Carlo events at this stage is set to the corresponding statistical error of 1 Monte-Carlo event[11]. The results of this procedure is stored in `X_processResults.txt`.

glu_sq_event1_eventResults.txt

```
[...]
atlas_1405_7875     SR02_3j                 4.54955            0.26266969982
[...]
```

glu_sq_event2_eventResults.txt

```
[...]
atlas_1405_7875     SR02_3j                 4.51922            0.261792698017
[...]
```

glu_sq_processResults.txt

```
[...]
```

[11] This prescription for example ensures that insufficiently small provided Monte Carlo event samples always contribute with large statistical uncertanties to the final number, even if no signal event passed the cut.

```
atlas_1405_7875      SR02_3j                 4.53438612736      0.185425764341
[...]
```

For processes with only one event file, the corresponding `eventResults` and `processResults` files are trivially identical, except for the statistical error of signal regions with 0 events which is only set process-wise, not event-wise.

For the next step, results from different processes are *added* to determine the total expected number of signal events for each signal region. All errors are considered independent and hence added in quadrature. This is done for each signal region in each selected analysis separately. These results are then compared to the experimental limits via the chosen method, in our case via the conservative r–limit as defined in Eq. (4.2) since we did not specify anything else. The results for each analysis and each signal region are then stored in `total_results.txt`. Here, standard columns are the number of experimentally observed `o` and expected Standard Model events `b` $\pm$ `db` quoted by the experiments, the `CheckMATE` determined predicted number of signal events `s` and the corresponding error `ds`, the model independent 95 % observed and expected limits `s95obs` and `s95exp` and the conservative r values as in Eq. (4.2).

total_results.txt

```
analysis          sr              o      b      db     s       ds     s95obs s95exp robscons rexpcons
atlas_1308_1841 SR01_8j50_a.0b   40.0   35.0   4.0    0.0900  0.0544 20.0   16.0   0        0
atlas_1308_1841 SR01_8j50_b.1b   44.0   40.0   10.0   0.0224  0.0540 23.0   23.0   0        0
atlas_1308_1841 SR01_8j50_c.GE2b 44.0   50.0   10.0   0.00879 0.0534 22.0   26.0   0        0
[...]
atlas_1405_7875 SR01_d.2jW       0.0    2.3    1.4    2.15    0.279  4.8    4.0    0.334    0.401
atlas_1405_7875 SR02_3j          7.0    5.0    1.2    15.0    0.710  8.2    6.4    1.666    1.159
atlas_1405_7875 SR03_a.4jl-      2169.0 2120.0 110.0  13.2    0.601  270.0  240.0  0.0447   0.050
[...]
cms_sus_13_016  SR1              1.0    1.2    1.045  0.0     0.0514 4.0    3.9    0        0
```

(Note that we rounded the numbers of the above table compared to the actual file content to fit the page width.)

In the last step of the evaluation procedure, `CheckMATE` will search for the signal region with the largest expected sensitivity; for the r-limits this corresponds to the signal region with the largest `rexpcons`. The results of the most sensitive signal region of each analysis separately is written in the file `best_signal_regions.txt`.

best_signal_regions.txt

```
analysis            sr                o       b       db      s     ds     s95obs s95exp robscons rexpcons
atlas_1308_1841     SR06_GE8j50_420   37.0    45.0    14.0    0.15  0.058  20.0   23.0   0.002    0.002
atlas_1308_2631     SRA3              14.0    15.8    2.8     0.0   0.053  9.0    10.2   0        0
atlas_1402_7029     SR0taua20         0.0     0.29    0.18    0.0   0.053  2.9    2.9    0        0
atlas_1403_4853     L110              8.0     9.3     3.5     0.0   0.053  9.0    9.4    0        0
atlas_1403_5222     SR2B              1.0     2.4     0.9     0.0   0.053  3.4    4.5    0        0
atlas_1403_5294     WWa_DF            70.0    73.6    7.9     0.0   0.053  20.3   22.533 0        0
atlas_1404_2500     SR1b              10.0    4.7     2.1     0.0   0.053  13.3   8.0    0        0
atlas_1405_7875     SR02_3j           7.0     5.0     1.2     15.0  0.710  8.2    6.4    1.666    2.135
atlas_1407_0583     bCd_high1         16.0    11.0    1.5     0.0   0.053  13.2   8.5    0        0
atlas_1407_0600     SR0l7jA           21.0    21.2    4.6     0.01  0.053  13.9   13.8   0        0
atlas_1407_0608     M3                1776.0  1770.0  81.0    25.5  1.060  195.0  190.0  0.120    0.123
atlas_1411_1559     SRTotal           521.0   557.0   45.0    0.22  0.091  70.0   91.0   0.001    0.002
atlas_1502_01518    SR9               126.0   97.0    14.0    23.8  0.995  58.0   36.0   0.377    0.625
atlas_1503_03290    SR-Z              29.0    10.6    3.2     0.0   0.053  29.6   12.0   0        0
atlas_1506_08616    SRinB             20.0    14.1    2.8     0.0   0.053  16.1   11.2   0        0
atlas_conf_2012_104 el                10.0    9.0     2.8     0.00  0.015  9.9    9.3    0        0
atlas_conf_2012_147 4                 268.0   380.0   73.4    5.30  0.346  210.0  210.0  0.022    0.022
atlas_conf_2013_021 emumu             298.0   287.0   19.0    0.0   0.034  58.2   49.7   0        0
atlas_conf_2013_024 SR1               15.0    17.5    3.2     0.0   0.053  10.0   10.6   0        0
```

```
atlas_conf_2013_031 Higgs              3615.0  3450.0  180.0   0.0  0.055 484.0  363.0  0      0
atlas_conf_2013_036 SR1Z               3.0     1.3     1.0     0.0  0.055 6.5    4.5    0      0
atlas_conf_2013_049 SR_mT2_110_elmu    5.0     4.4     2.0     0.0  0.053 7.105  6.699  0      0
atlas_conf_2013_061 SR0L7JA            22.0    22.5    6.9     0.06 0.053 15.3   14.6   0      0
atlas_conf_2013_062 SoftLep1BHigh      6.0     4.0     1.1     0.01 0.053 7.9    6.3    0      0
atlas_conf_2013_089 SR1OF              87.0    103.0   15.0    0.0  0.053 24.0   31.0   0      0
atlas_conf_2014_014 SRa                59.0    53.0    10.0    0.0  0.053 30.2   27.0   0      0
atlas_conf_2014_033 emu                5067.0  4376.0  281     0.0  0.053 1176.0 566.0  0      0
atlas_conf_2014_056 sig                60424.0 60000.0 3600.0  0.0  0.053 6902.0 6717.0 0      0
atlas_conf_2015_004 M1                 539.0   578.0   48.4    0.0  0.053 73.0   96.0   0      0
cms_1301_4698_WW    combined           1111.0  1000.0  60.0    0.0  0.009 240.4  135.7  0      0
cms_1303_2985       23j_0b_875         25.0    16.1    1.7     7.98 0.447 18.5   10.1   0.383  0.701
cms_1405_7570       Zjj_030            20991.0 21364.0 859.0   0.0  0.051 1379   1595   0      0
cms_1408_3583       550                519.0   509.0   66.0    10.7 0.694 129.0  123.0  0.073  0.077
cms_1502_06031 SR01_GE2jets_c.highMET  7.0     12.8    4.3     0.0  0.051 7.6    7.6    0      0
cms_1504_03198      SR1                18.0    16.4    3.64    0.0  0.052 12.9   11.4   0      0
cms_smp_12_006      0e                 557.0   487.8   40.0    0.0  0.052 151.62 88.98  0      0
cms_sus_12_019      For_OF             155.0   155.0   16.4    0.0  0.051 31.8   31.8   0      0
cms_sus_13_016      SR1                1.0     1.2     1.05    0.0  0.051 4.0    3.9    0      0
```

This file is helpful in getting a good overview of which analyses yield a nonvanishing r value and hence generally show sensitivity to the input model. For our example, one would expect those analyses to be most sensitive which are designed to find events with large jet multiplicity and missing transverse energy in the final state. Indeed one examines three such analyses with sizable r-values: `atlas_1405_7875` [183], a zero lepton multijet search, the ATLAS monojet[12] search `atlas_1502_01518` [185] and the CMS search `cms_1303_2985` [186] which uses the α_T variable to identify BSM events with large hadronic activity.

`CheckMATE` then again chooses the most sensitive region among these. The corresponding observed result will be used to finally conclude whether the input can be considered excluded or not, i.e. in the case of the r-limit if `robscons` is larger than 1. In the above example, this best signal region would be `SR02_3jit` in analysis `atlas_1405_7875` which with an `robscons` value of about 1.7 yields excludes the input signal. This is exactly the result which was printed on-screen at the end of our original `CheckMATE` run.

With that, we have illustrated how `CheckMATE` can be used to test various input formats for BSM physics and which content can be found in all the produced output files. This knowledge should be sufficient for standard users to test their models of interest without much effort.

After finishing this detailed explanation of the main part of `CheckMATE` the user typically gets into contact with when running the program, we continue the discussion with some internal details which are required to make `CheckMATE` work and which are thus also worthwhile mentioning. This dicussion also illustrates for which other purposes the program can be used.

4.3 Detector Tunings

We already discussed the general concept of a detector simulation in Section 3.3.1. Within `CheckMATE`, each of the given event files will be processed with the fast multipurpose detector simulation `Delphes`. This tool attempts to reproduce the experimental resolutions and efficiencies of the two LHC multipurpose detectors, ATLAS and CMS by parametrising a large list of detector effects. Most importantly it

- simulates track reconstruction,

[12] Despite the name, this analysis allows for events with up to three hard jets in the final state and hence is also sensitive to our expected multijet signature.

- determines hadronic and electromagnetic energy deposits of all particles,
- applies identification efficiencies for photons and leptons,
- clusters jets,
- performs energy/momentum smearings of all reconstructed objects,
- evaluates total missing energy,
- checks isolation conditions for photons and leptons and
- applies b-/ τ-tagging on jets.

Due to the use of efficiency maps instead of proper simulation of individual particles in detector material, the time scale of a typical `Delphes` run is about an order of magnitude smaller compared to the overall computational time required for the generation, showering and hadronisation of the same events. For more details on Delphes in general, its implemented features and performance tests we refer to Ref. [165].

`CheckMATE` requires extra functionalities which lie beyond those in the public version of `Delphes`. Most importantly, as already explained in Section 4.1.4, the simultaneous testing of various analyses at once requires many different sets of final state objects passing different identification algorithms to be determined and stored in parallel. This forking of the same reconstructed to different identified final state objects is not possible within `Delphes`, which is why we have outsourced these parts of the detector simulation into the `AnalysisHandler`s objects discussed before. At the same time, we re-parametrised many of the efficiencies which are already present in `Delphes`' standard implementations of the ATLAS and the CMS detector. In the remainder of this section we describe these changes in detail. We show the implemented efficiency distributions and the data points these were fitted to. The functional forms of these distributions are listed in Appendix B.3.

4.3.1 Improved Description of Lepton Reconstruction

In order to properly estimate the measurement of leptons inside a detector, there are two main effects which have to be taken into account:

1. Inaccuracies in tracker, calorimeters and muon spectrometer lead to an uncertainty in the reconstruction of the kinematical properties of electron and muon candidates. These can be accounted for in the simulation by applying a Gaussian smearing on every candidate in dependence on its energy and position in the detector.

2. Algorithms to reconstruct electrons inside the calorimeter and to identify muons by associating tracks to hits in the muon chamber might fail. Hence a given generated lepton should only appear in the list of reconstructed lepton objects with a probability given by the reconstruction and identification efficiency $\epsilon_\ell \leq 1$.

There exist sophisticated experimental studies which provide quantitative statements for these effects, e.g. in the form of probability functions. In `CheckMATE`, the following parameterisations are included:

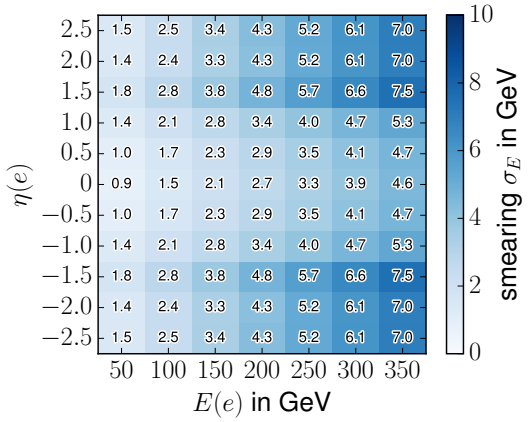

(a) Discretised version of continuous 2D function used for smearing electron energies.

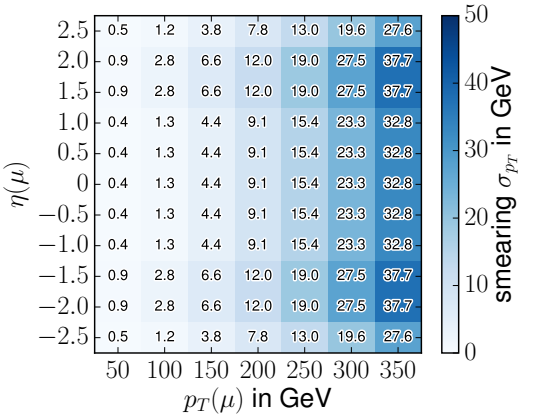

(b) Discretised version of continuous 2D function used for smearing muon momenta,

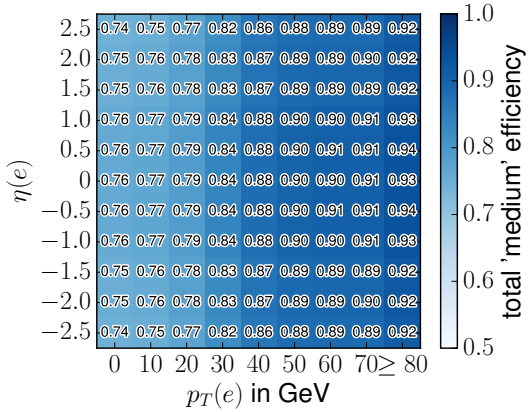

(c) Discretised version of continuous 2D efficiency map for 'medium' ATLAS electrons.

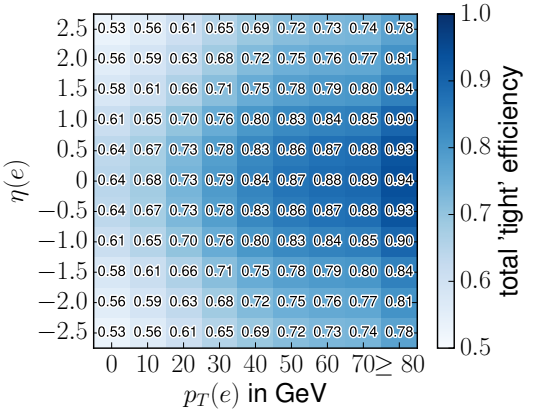

(d) Discretised version of continuous 2D efficiency map for 'tight' ATLAS electrons.

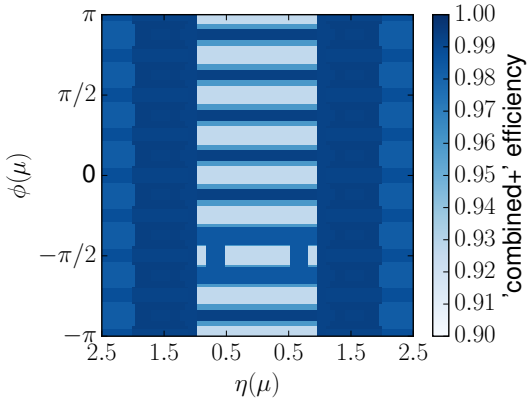

(e) Discrete 2D efficiency map for 'combined plus' ATLAS muons.

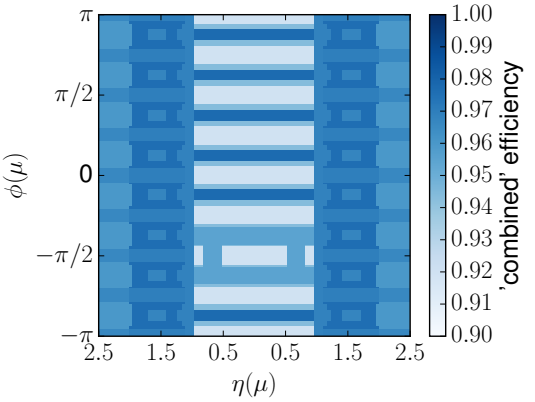

(f) Discrete 2D efficiency map for 'combined' ATLAS muons.

Figure 4.2: Lepton smearing and efficiency distributions used in `CheckMATE`.

- A Gaussian smearing of the muon momenta and electron energies is applied by using position- and energy/momentum-dependent widths taken from results in Refs. [187–191] and for high-energetic muons fitted[13] to match results in Ref. [192]. They are shown in Figs. 4.2a and 4.2b. Note that to improve readability we show the results in the form of a 2D histogram even though we use continuous functions internally.

- Detailed p_T- and η-dependent reconstruction and identification efficiency functions for 'medium' and 'tight' electrons[14] are determined from results in Refs. [189, 193]. They are shown in Figs. 4.2c and 4.2d. Again, we show histogrammed results to improve readability even though continuous functions are used.

- Muon reconstruction efficiencies for 'combined' and 'combined plus segment tagged' muons are implemented in dependence of the detector component that will measure the candidate. We use a ϕ–η map of the muon spectrometer from Ref. [188] and show the resulting dicrete two-dimensional efficiency maps in Figs. 4.2e and 4.2f.

4.3.2 Improved Description of Jet Tagging

Jets which originate from b-quarks or hadronically decaying τ-leptons can to a certain degree be distinguished from other, non-flavoured jets by e.g. measuring vertex displacements or by reconstructing distinctive track and calorimeter signatures. The experimental collaborations have determined sophisticated algorithms which are applied on every reconstructed jet object in order to identify whether they are likely to have originated from a b-quark or a τ-lepton. Since under different circumstances it is sometimes a high signal rate and sometimes a low background contamination which is targeted, these algorithms are defined with diferent discrete or even continuous working point efficiencies. The resulting working point dependent probabilities of correctly and incorrectly tagging jets which did or did not originate from a b/τ have been published and are used in fast detector simulation frameworks like ours. For the background, a typical quantity is the so called *rejection* which is simply the inverse of the background tagging efficiency.

- We consider p_T-dependent b-quark identification efficiencies and mis-tagging probabilities according to Refs. [194–197]. Results for ROC-curves, i.e. relations between signal- and background efficiencies, and the momentum dependence of these efficiencies are given in Fig. 4.3. The typically higher mistagging rate of jets which originate from c-quarks are considered separately. Various target working point efficiencies are used in different analyses and `CheckMATE` uses the Receiver Operating Characteristic (ROC) curve to determine the absolute background efficiency for a given working point and then uses the momentum-dependent functions to re-scale this probability, see also Appendix B.3.4.

  Note that the efficiencies in the above references have been determined to generally overestimate the number of Monte-Carlo b-jets which pass the tagging filter. Therefore the efficiencies have been scaled down in such a way that the cutflow validation procedure yielded globally better agreements between `CheckMATE` and the respective experimental result.

[13] This fit has been performed by Florian Jetter.
[14] 'loose' electrons are considered in a special manner, see Appendix B.3.

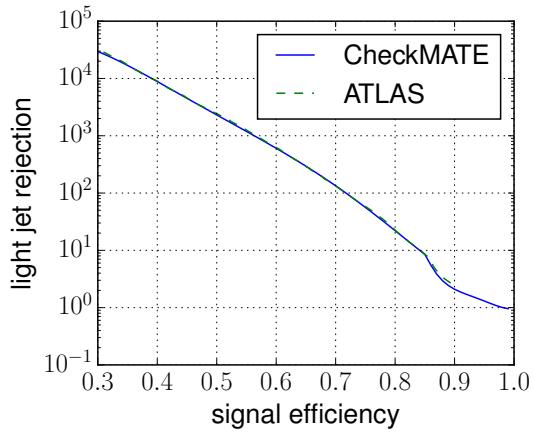

(a) b-tag ROC curve. Rejection considers jets from light quarks only.

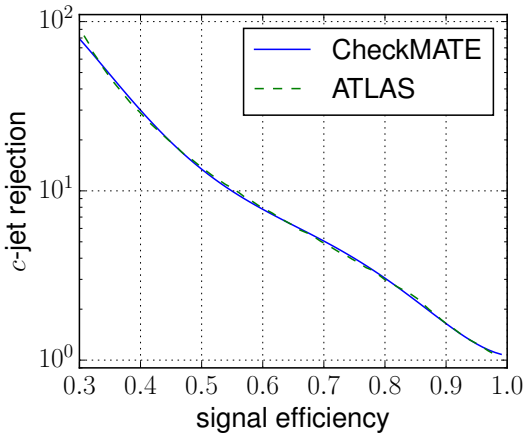

(b) b-tag ROC curve. Rejection considers jets from c quarks only.

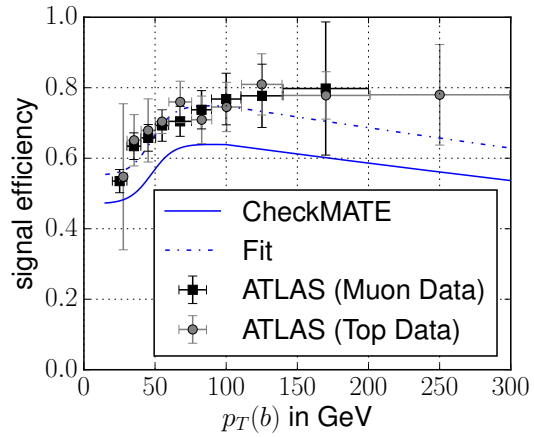

(c) p_T dependence of signal efficiencies for b-tagging for a working point efficiency of 70 %, determined by downscaling (see text) the combined information of two different search channels for [197, 198].

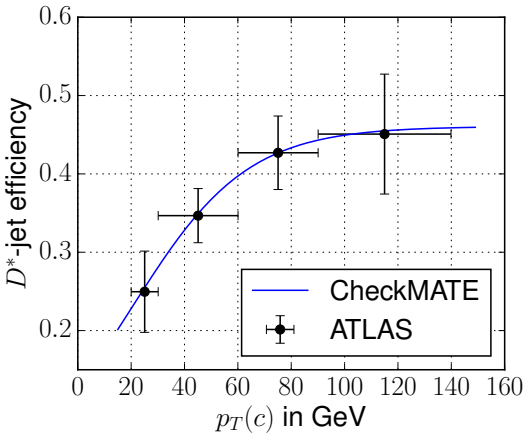

(d) p_T dependence of b-tagging background efficiency of jets containing D^* mesons for a working point efficiency of 70 %, determined from Ref. [197]. The inclusive efficiency on c–jets is assumed to be 40 % of this D^* efficiency.

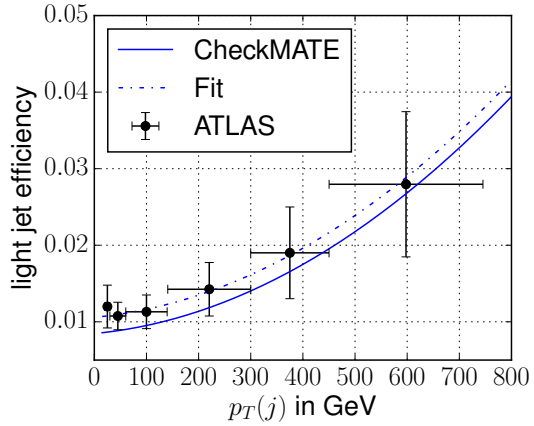

(e) b-tagging efficiency of jets containing light quarks for a working point efficiency of 70 % and $|\eta| < 1.3$, see Ref. [196].

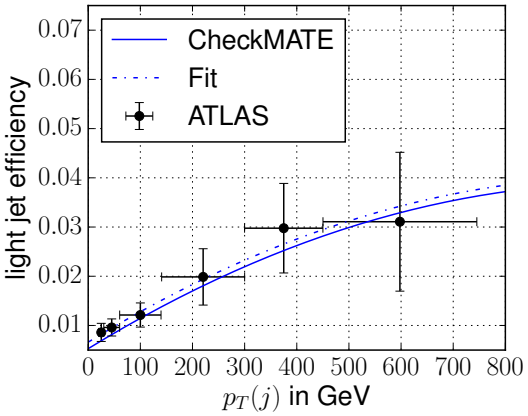

(f) same as Fig. 4.3e for $1.3 \leq |\eta| < 2.5$.

Figure 4.3: Distributions used to perform phenomenologic b-tagging in `CheckMATE`.

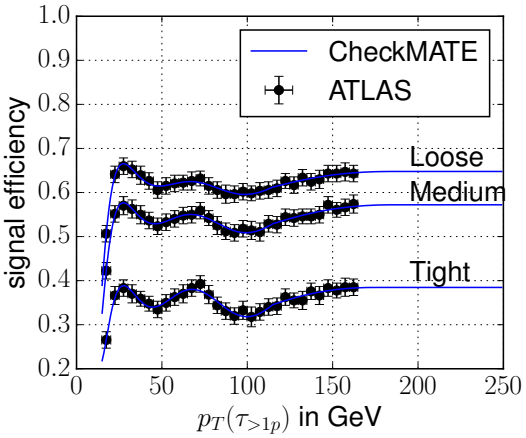

(a) τ-tagging efficiencies for multiprong τ candidates.

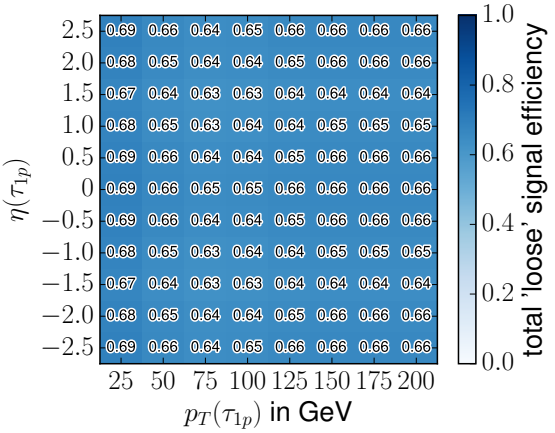

(b) 'loose' τ-tagging efficiency for 1-prong τ candidates,

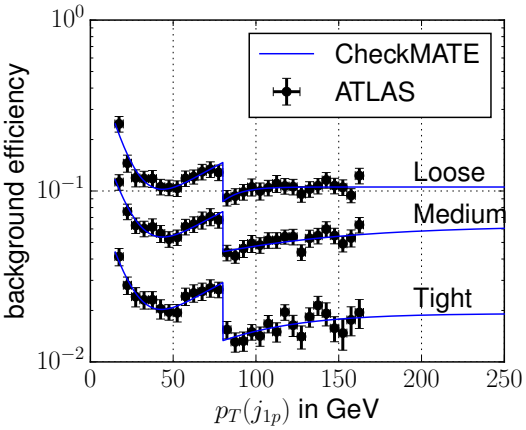

(c) τ-tagging background efficiencies for 1-prong jets.

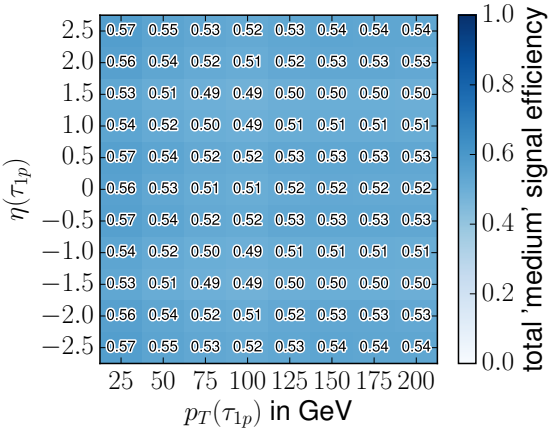

(d) 'medium' τ-tagging efficiency for 1-prong τ candidates.

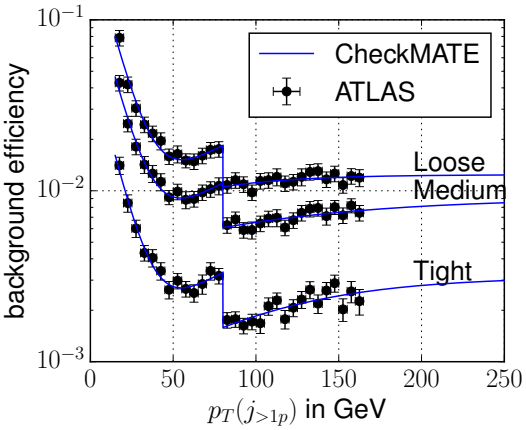

(e) τ-tagging background efficiencies for 3-prong jets.

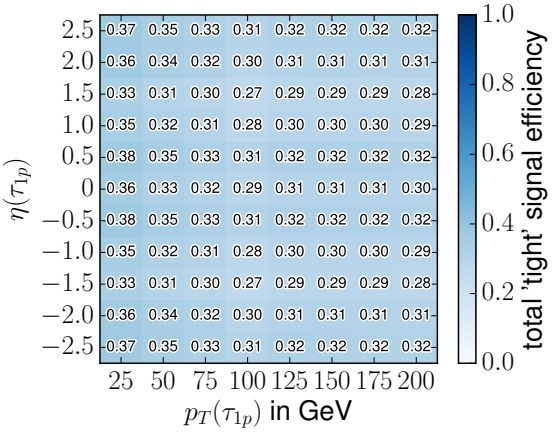

(f) 'tight' τ-tagging efficiency for 1-prong τ candidates.

Figure 4.4: Distributions used to perform phenomenologic τ-tagging in `CheckMATE`

- Similarly, we use p_T dependent τ-tagging efficiencies for signal and background which distinguish between candidates with 1 or more *prongs*, i.e. reconstructed and associated tracks, see Ref. [199]. The distributions used are shown in Fig. 4.4. ATLAS typically only uses three well-defined working points and thus we only need the distributions for these three cases. Note that hadronically decaying τ leptons with one charged final state hadron need to pass a special pseudorapidity-dependent tagging algorithm in order to filter electrons with similar detector signature. This is why the efficiencies for 1 prong candidates shows an additional position dependence and we again show discretised versions of internally continuous two-dimensional efficiency functions.

Note that all these tunings are only based on ATLAS results. For now, CheckMATE uses the exact same implementations also for the CMS detector as these two are expected to show similar performance in the reconstruction quality of final state objects. Currently, the same efficiencies are also used for 13 TeV and prospective 14 TeV analyses. However, an update especially for the current 13 TeV run is planned in the near future.

4.4 Details on the CheckMATE Analysis Framework

CheckMATE provides a large variety of different analyses against which the users can test their models. In this section we give an overview of what defines a particular analysis and which particular analyses are currently embedded into the code.

4.4.1 Properties of a CheckMATE Analysis

Analysis Code

CheckMATE analysis codes are written in the C++ programming language and consist of a .h header file and a .cc source file. The former is only needed to define additional functions or global variables and it is typically only the latter the user interacts with. In the source file, analyses are defined using a similar structure as the well-known Rivet [172] analysis framework. An initialisation function takes care of general analysis definitions as the setup of all to-be-used control-, cutflow- and signal regions. It is followed by a second function which runs on each provided event and which performs the actual analysis of the input data: The final state objects of interest are selected, conditions on the event in general and the final state objects in particular are subsequently tested and events which pass all constraints for a particular signal region are registered. Lastly, a finalisation function is available for routines which are supposed to run after the analysis is finished. Typically, this function is empty but can be useful for debugging purposes.

Technically, all analyses are defined as individual C++ classes which however are all derived from a common AnalysisBase class. This class automatically defines the relevant final state object containers and provides commonly used methods, e.g. kinematic filters, overlap removals of close-by-objects, advanced kinematic variables and simple tests if candidates contain isolation or flavour tags determined by the AnalysisHandler, c.f. Section 4.1.4. We encounter some in our example analysis implementation below in Section 4.5 and we refer to Ref. [179] for more code-related details.

Reference Data

In addition to the actual analysis code, `CheckMATE` needs to know various additional pieces of information, most importantly the following:

- The definitions of all isolation and tagging conditions which are required in the analysis cut procedure have to be defined such that the corresponding `AnalysisHandler` can account for them properly during runtime. Whilst tagging conditions are defined via their working point efficiencies, isolation is typically tested with respect to a well-defined, analysis-dependent set of final state objects, e.g. tracks or calorimeter cells in the vicinity of a given candidate.

- To do the statistical evaluation, a list of all signal regions and the corresponding numbers of observed and Standard Model expected events including the error are needed. To ensure proper normalisation, the integrated luminosity to which these numbers correspond to is required as well.

- The centre-of-mass energy to which the observed events numbers correspond is also required to such that `Pythia 8` generates proton-proton collisions properly. This information is also used as a security measure to prevent the user from accidentally applying analyses corresponding to different centre-of-mass energies to the same input event file.

This reference data typically comes from the corresponding experimental analysis publication and are stored in `Python` internal `var.j` files within the `data/analysis_info` subfolder of a given `CheckMATE` installation. To conveniently create these files, `CheckMATE` comes along with a helper-executable called `AnalysisManager`. It asks the user for the above information in an easy input/output interface and afterwards creates the necessary files at the appropriate places in the program environment. We show this in an explicit example in Section 4.5 below.

4.4.2 Validated and Unvalidated Analyses Implemented in `CheckMATE`

The analyses available in the public `CheckMATE` version already cover a wide range of possible final state configurations, most importantly those which predict a sizable amount of missing transverse momentum. In Table 4.1, we list and shortly describe all currently implemented and validated analyses in the most recent publicly available `CheckMATE` version.

Validation is mostly performed by testing detailed cutflow information predicted by `CheckMATE` against the corresponding published result for a given benchmark model. Such a test ensures that all experimental cuts perform as expected and puts the efficiency functions of the implemented detector tunes to the test. The majority of the cutflows we have evaluated with `CheckMATE` have an acceptance that is within 10% of the published value for the signal regions. If this accuracy is not achieved, the analysis has been checked thoroughly to ensure no bugs remain and possible or confirmed reasons for the discrepancy are clearly stated. We show examples for such cutflow tests in Tables 4.2 and 4.3 and we refer to the `CheckMATE` webpage in Ref. [210] for more detailed and updated information.

Due to the straightforward handling of the `AnalysisManager` to add a new analysis to the existing framework, see next section, physicists outside the `CheckMATE` collaborations can easily and independently add analyses to the framework. If the necessary validation steps have been performed, they can share their effort to the entire community by sending the necessary files

Name	Search designed for	$\sqrt{s}$	N_{SR}	Ref.
atlas_1308_2631	third-generation squark pair production in final states with $\not{E}_T$ and two b-jets	8	6	[200]
atlas_1402_7029	production of charginos and neutralinos in events with three leptons and $\not{E}_T$	8	24	[171]
atlas_1403_4853	top-squark pair production in final states with two leptons	8	12	[201]
atlas_1405_7875	squarks and gluinos in final states with jets and $\not{E}_T$	8	15	[183]
atlas_1407_0583	top squark pair production in final states with one isolated lepton, jets, and $\not{E}_T$	8	27	[202]
atlas_1502_01518	new phenomena in final states with an energetic jet and large $\not{E}_T$	8	9	[185]
atlas_conf_2012_104	Supersymmetry in final states with jets, $\not{E}_T$ and one isolated lepton	8	2	[203]
atlas_conf_2012_147	new phenomena in monojet plus $\not{E}_T$ final states	8	4	[204]
atlas_conf_2013_024	production of the top squark in the all-hadronic $t\bar{t}$ and $\not{E}_T$ final state	8	3	[205]
atlas_conf_2013_049	direct-slepton and direct-chargino production in final states with two opposite-sign leptons, $\not{E}_T$ and no jets	8	9	[206]
atlas_conf_2013_061	strong production of supersymmetric particles in final states with $\not{E}_T$ and at least three b-jets	8	9	[207]
atlas_conf_2013_089	strongly produced supersymmetric particles in decays with two leptons	8	12	[208]
cms_1303_2985	supersymmetry in hadronic final states with missing transverse energy using the variables α_T and b-quark multiplicity	8	59	[186]
cms_sus_13_016	new physics in events with same-sign dileptons and jets	8	1	[209]

Table 4.1: List of analyses which are available in the public alpha version of CheckMATE and which have been validated against published experimental results. Apart from atlas_1402_7029, all analyses have been implemented and validated by other members of the CheckMATE collaboration.

	Signal Region D		Signal Region ET	
Cut	ATLAS	Ch.M.	ATLAS	Ch.M.
Generated Monte Carlo events	20,000	50,000	20,000	50,000
In %	100 %	100 %	100 %	100 %
Jet cleaning *	99.8 %	-	99.8 %	-
0 lepton *	63.7 %	-	63.5 %	-
$\not{E}_T \geq 160\,\text{GeV}$	50.0 %	-	55.6 %	-
$p_T(j_1) > 130\,\text{GeV}$	49.3 %	47.7 %	55.6 %	54.4 %
$p_T(j_2) > 130\,\text{GeV}$	49.2 %	47.6 %	55.6 %	54.4 %
$p_T(j_3) > 60\,\text{GeV}$	48.6 %	47.1 %	55.4 %	54.2 %
$p_T(j_4) > 60\,\text{GeV}$	44.5 %	43.8 %	53.4 %	52.8 %
$p_T(j_5) > 60\,\text{GeV}$	34.4 %	34.8 %	46.3 %	46.6 %
$p_T(j_5) > 60\,\text{GeV}$ (only ET)	34.4 %	34.8 %	31.7 %	33.0 %
$\Delta\phi(j_{1,2,3}, \not{E}_T) > 0.4$	29.2 %	29.5 %	26.5 %	27.5 %
$\Delta\phi(j_k, \not{E}_T) > 0.2\ \forall k$ with $p_T(j_k) > 40\,\text{GeV}$	24.6 %	24.7 %	21.3 %	22.4 %
$\not{E}_T/m_{\text{eff}}(\text{all jets}) > 0.2(\text{D}), 0.25(\text{ET})$	21.6 %	21.2 %	12.0 %	11.2 %
$m_{\text{eff}}(\text{all jets}) > 1.6\,\text{TeV}(\text{D}), 1.5\,\text{TeV}(\text{ET})$	2.0 %	1.9 %	7.9 %	8.2 %
Monte Carlo Error	±0.1 %	±0.1 %	±0.2 %	±0.1 %

Table 4.2: Example cutflow for analysis atlas_1405_7875. The considered model assumes pair produced gluinos which decay into a chargino and a pair of quarks, with the chargino then subsequently decaying into a W and a neutralino LSP. In the left / right column, the mass of gluino, chargino and neutralino are respectively 1065 GeV, 785 GeV and 525 GeV / 1265 GeV, 865 GeV and 465 GeV. Cuts with a * symbol can not be individually performed by CheckMATE and an overall cleaning factor is applied instead. m_{eff} is defined in Section 4.5. This cutflow table has been created by Jamie Tattersall.

to the CheckMATE mailing list. We show an example cutflow validation performed by phenomenologists outside the CheckMATE collaboration in Table 4.4. This analysis validated from an outside source was subsequently added to CheckMATE.

Besides cutflow tables, many of the experimental analyses give exclusion curves for some popular, simplified models. Often these have been replicated by CheckMATE and in general the results lie within the 1σ theoretical uncertainty predicted by the model. Again, in the rare occasions that the required accuracy has not been met, possible reasons for the discrepancy are given. We show four example exclusion plots with different underlying benchmark models in Fig. 4.5 .

Besides the list of fully validated analyses, there exists an even longer list of implemented but unvalidated analyses. There are various reasons for the lack of validation material, ranging from missing necessary experimental information to an insufficient amount of labour force inside the CheckMATE collaboration. These analyses are listed in Table 4.5. Even though not validated, these analyses are still available to the physics community: since the beta version is publily available, users who need to consider these analyses can download this version of the code and use the extended analysis list at their own risk or only after they performed their own

Cut	ATLAS	CheckMATE
Generated Monte Carlo events	20,000	40,000
Normalised physial number of events ($\sigma \cdot \mathcal{L}$)	2,430	2,390
3 leptons with flavour $\tau^+\tau^-\ell$, $\ell \neq \tau$	34	33.6
b-jet veto	33	29.2
$\not{E}_T > 60\,\text{GeV}$	14	12.3
$\sum p_T^\tau > 110\,\text{GeV}$	10	7.56
$m_{\tau\tau} \in [70, 120]$ GeV	5	4.32
Monte Carlo Error	± 0.78	± 0.51

Table 4.3: Example cutflow for analysis atlas_1402_7029. Shown are number of events passing each cut normalised to a luminosity of 20.3 fb^{-1}. The model considers associated electroweak production of $\widetilde{\chi}_1^\pm \widetilde{\chi}_2^0$ with a degenerate mass of 130 GeV. These then decay into W, Z and two massless neutralino LSPs.

Cut	CMS		CheckMATE	
Generated Monte Carlo events	40,000		50,000	
Normalised physial events ($\sigma \cdot \mathcal{L}$)	37.7		37.7	
≥ 2 leptons($l^\pm l^\mp$), $p_T(\ell) > 20\,\text{GeV}$	11.9		11.8	
$m_{\ell\ell} \in [81, 101]$ GeV	10.7		10.4	
	CMS	Ch.M.	CMS	Ch.M.
$n_j > 2$ or 3	10.7	10.4	10.4	10.2
$\not{E}_T > 100\,\text{GeV}$	10.3	10.0	10.0	9.8
$\not{E}_T > 200\,\text{GeV}$	9.2	8.8	8.9	8.7
$\not{E}_T > 300\,\text{GeV}$	7.6	7.2	7.4	7.1
Monte Carlo Error	± 0.05	± 0.03	± 0.05	± 0.03

Table 4.4: Example cutflow for analysis cms_1502_06031. Shown are physical number of events after each cut, normalised to an integrated luminosity of 19.4 fb^{-1}. The model considers pair produced gluinos with a mass of 1100 GeV which promptly decay into a pair of quarks and a 800 GeV lightest neutralino. This then subsequently decays into a Z boson and a massless gravitino LSP. This cutflow table has been created by Junjie Cao, Liangliang Shang, Peiwen Wu, Jin Min Yang, Yang Zhang.

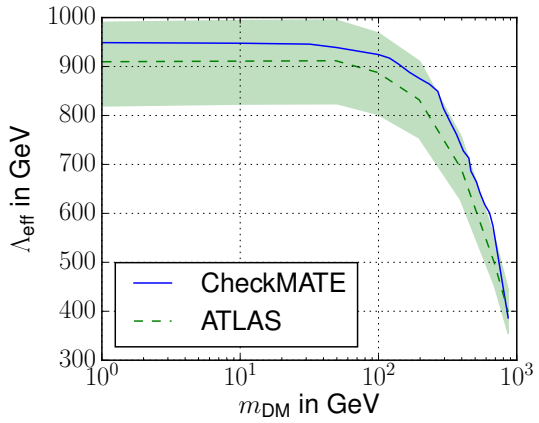

(a) Example model exclusion of a simplified dark matter model tested with `atlas_1502_01518`. The model assumes an effective interaction of a dark matter candidate χ with Standard Model quarks via the effective operator $\Lambda_{\text{eff}}^{-2}\bar{q}\gamma^\mu\gamma^5 q\bar{\chi}\gamma_\mu\gamma^5\chi$.

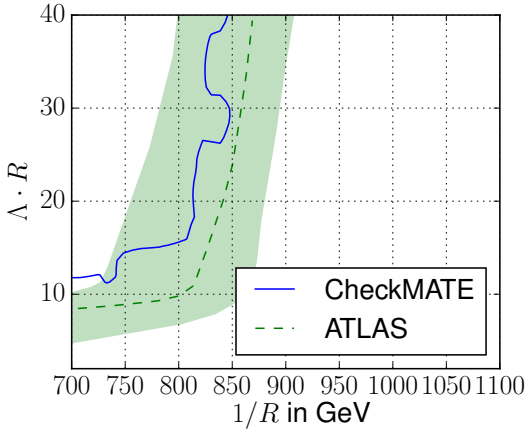

(b) Example exclusion of a model with minimal universal extra dimensions `atlas_conf_2013_089`. Here, R is the compactification radius of the extra dimension and Λ the cutoff scale.

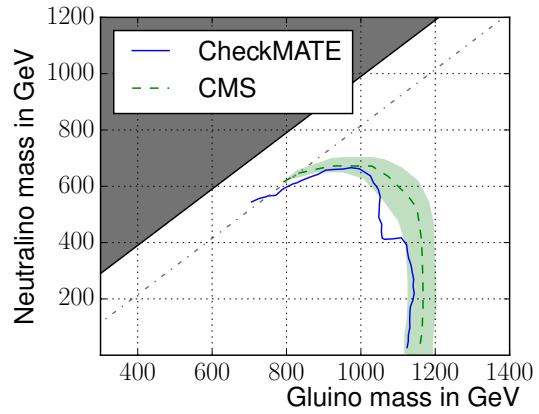

(c) Example model exclusion for a simplified SUSY scenario with direct gluino pair production decaying into $b\bar{b}$ and a neutralino LSP, tested with `cms_1303_2985`. Between shaded region and dot-dashed line, mass splittings are too small such that no limit can be set by this analysis.

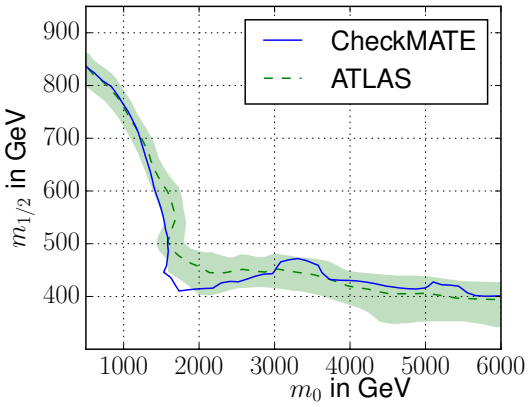

(d) Example model exclusion of the mSUGRA model via analysis `atlas_conf_2013_047`. m_0 and $m_{1/2}$ denote high scale unified soft SUSY breaking masses for the scalar chiral and fermionic vector partners, respectively. The unified trilinear parameter A_0 is fixed to $-2m_0$ and we have $\tan\beta = 30, \mu > 0$.

Figure 4.5: Example model exclusions performed with `CheckMATE` for different classes of models. We refer to the respective analysis references shown in Table 4.2 for more information on the respectively tested models. The `CheckMATE` results shown in these plots have been determined by other members of the `CheckMATE` collaboration.

performance tests. They are present in the 2.0 beta version linked in the introduction.

Name	Search designed for	$\sqrt{s}$	N_{SR}	Ref.
atl-phys-pub-2014 -010-sbottom	Supersymmetry at the high luminosity LHC in final states with zero leptons, two b-jets and $\not{E}_T$	14	6	[211]
atlas-phys-pub-2013 -011-stop	Supersymmetry at the high luminosity LHC in final states with zero or one lepton	14	4	[212]
atlas_1210_2979	WW production	7	1	[213]
atlas_1308_1841	new phenomena in final states with large jet multiplicities and $\not{E}_T$	8	19	[214]
atlas_1403_5222	top squark pair production in events with a Z boson, b-jets and $\not{E}_T$	8	5	[215]
atlas_1403_5294	production of charginos, neutralinos and sleptons in final states with two leptons and $\not{E}_T$	8	13	[216]
atlas_1404_2500	Supersymmetry in final states with jets and two same-sign leptons or three leptons	8	5	[217]
atlas_1407_0600	strong production of supersymmetric particles in final states with $\not{E}_T$ and at least three b-jets	8	9	[218]
atlas_1407_0608	pair-produced third-generation squarks decaying via charm quarks or in compressed supersymmetric scenarios	8	3	[219]
atlas_1411_1559	new phenomena in events with a photon and $\not{E}_T$	8	1	[220]
atlas_1503_03290	Supersymmetry in events containing a same-flavour opposite-sign dilepton pair, jets, and large $\not{E}_T$	8	1	[221]
atlas_1506_08616	pair production of third-generation squarks	8	11	[222]
atlas_1602_09058	Supersymmetry in final states with jets and two same-sign leptons or three leptons	13	4	[223]
atlas_2014_010_hl_3l	Supersymmetry at the high luminosity LHC with 3 $\ell + \not{E}_T$	14	9	[211]
atlas_conf_2013_021	WZ production	8	4	[224]
atlas_conf_2013_031	spin properties of the Higgs-like particle in the $h \to WW^{(*)} \to e\nu\mu\nu$ channel	8	2	[225]

Table 4.5: List of analyses which are available in the beta version of the CheckMATE in addition to those listed in Table 4.1. Analyses listed here are implemented and usable, however have no or only insufficient validation material. Users are appealed to only make use of these after performing their own crosschecks. All analyses in this table have been implemented by other members of the CheckMATE collaboration or the combined effort of Junjie Cao, Liangliang Shang, Peiwen Wu, Jin Min Yang and Yang Zhang.

Name	Search designed for	$\sqrt{s}$	N_{SR}	Ref.
atlas_conf_2013_036	Supersymmetry in events with four or more leptons	8	5	[226]
atlas_conf_2013_062	squarks and gluinos in events with isolated leptons, jets and $\not{E}_T$	8	19	[227]
atlas_conf_2014_014	pair production of top squarks decaying to a b quark, a τ lepton and weakly interacting particles	8	1	[228]
atlas_conf_2014_033	WW production	8	3	[229]
atlas_conf_2014_056	spin correlation in top–antitop quark events and search for top squark pair production	8	1	[230]
atlas_conf_2015_004	invisibly decaying Higgs boson produced via vector boson fusion	8	1	[231]
atlas_conf_2015_062	squarks and gluinos in final states with jets and $\not{E}_T$	13	7	[232]
atlas_conf_2015_067	pair-production of gluinos decaying via stop and sbottom in events with b-jets and large $\not{E}_T$	13	8	[233]
atlas_conf_2015_076	gluinos in events with an isolated lepton, jets and missing transverse momentum	13	6	[234]
atlas_phys_2014_010_300	Supersymmetry at the high luminosity LHC with jets + $\not{E}_T$	14	10	[211]
atlas_phys_2014 _010_sq_hl	Supersymmetry at the high luminosity LHC with jets and $\not{E}_T$	14	10	[211]
cms_1301_4698_WW	WW production	8	1	[235]
cms_1306_1126_WW	WW	7	1	[186]
cms_1405_7570	electroweak production of charginos, neutralinos and sleptons decaying to leptons and W, Z, and Higgs bosons	8	57	[236]
cms_1408_3583	dark matter, extra dimensions, and unparticles in monojet events	8	7	[237]
cms_1502_06031	physics beyond the Standard Model in events with two Leptons, jets, and $\not{E}_T$	8	6	[238]
cms_1504_03198	production of dark matter in association with top-quark pairs in the single-lepton final state	8	1	[239]
cms_smp_12_006	WZ production into 3ℓ	8	4	[235]
cms_sus_12_019	physics beyond the standard model in events with two opposite-sign same-flavor leptons, jets, and missing transverse energy	8	4	[240]

Table 4.6: Continuation of Table 4.5.

4.5 Example: Adding a New Analysis to CheckMATE

CheckMATE is not only meant to be simple to use and transparent. The philosophy of the program is that it is also supposed to be easy to extend with new ideas for analyses or users who need a particular analysis which has not been implemented yet. In this section we give a brief introduction to the most important steps that are necessary to implement a new analysis. Since it is not straightforward to see which files with which information have to be stored at which parts of the program, CheckMATE includes an AnalysisManager. This is an additional executable which can be used to add, edit and remove analyses and which in case of the first asks the user for all the necessary details. In order to not confuse the normal user, this binary is not created automatically with the ordinary compilation of the code. However, it can easily be added by typing

Terminal

```
$CMDIR:  make AnalysisManager
```

This should create a second binary AnalysisManager within the bin/ folder

In this part we add an analysis to the CheckMATE framework from the very first steps on. The example is a predecessor of the analysis atlas_1405_7875 which we encountered in our previous example run in Section 4.2. Again, we assume that CheckMATE is already installed in the directory $CMDIR.

Running the Analysis Manager

Starting the AnalysisManager via *./AnalysisManager* opens the introduction header and a first prompt:

Terminal

```
 ____ _               _    __  __    _  _____ _____ ____
 / ___| |__   ___  ___| | _|  \/  |  / \|_   _| ____|___ \
| |   | '_ \ / _ \/ __| |/ / |\/| | / _ \ | | |  _|   __) |
| |___| | | |  __/ (__|   <| |  | |/ ___ \| | | |___ / __/
 \____|_| |_|\___|\___|_|\_\_|  |_/_/   \_\_| |_____|_____|

                  /\  _  _ |   _. _  |\/| _  _  _  _  _ _
                 /--\| )(_||\/_)|_)  |  |(_|| )(_|(_)(-|
                           /                    _/

    What would you like to do?
        -(l)ist all analyses,
        -(a)dd a new analysis to CheckMATE,
        -(e)dit analysis information,
        -(r)emove an analysis from CheckMATE
```

Apparently we want to add something new, so we press a:

```
This will collect all necessary information to create a full analysis and
Takes care for the creation and implementation of the source files into the code.
Please answer the following questions.
Attention: Your input is NOT saved before you answered all questions!
```

The first block of questions gathers some general information on the analysis. At the beginning we are asked for the name of the analysis. This name should be short but clear[15] and must

[15] Note that we only added the letter X at the end of the analysis name to prevent the AnalysisManager from overwriting the already implemented atlas_conf_2013_047 analysis data.

not contain any spaces, since this string defines the names for all analysis-specific files. Then, the user's name and email address are requested. These are printed on the very first lines of the analysis code to make sure that the right author can be contacted in case of unexpected behaviour.

```
1. General Information to build analysis
  Analysis Name:
    atlas_conf_2013_047
  Your Name (to declare the analysis author):
    Guybrush Threepwood
  Your Email:
    threepwood@pirates.arr
```

The one-line description is the one used when someone types `l` in the `AnalysisManager`. It can also be found in the file `data/list_of_analyses.dat`. The multiline description is printed on the top of every output file the respective analysis code creates:

```
  Description (short, one line):
    ATLAS, 0 leptons + 2-6 jets + etmiss
  Description (long, multiple lines, finish with empty line:
    ATLAS
    ATLAS-CONF-2013-047
    0 leptons, 2-6 jets, etmiss
    sqrt(s) = 8 TeV
    int(L) = 20.3 fb^-1
```

The luminosity is important for the correct normalisation of the analysis results:

```
  Luminosity (in fb^-1):
    20.3
```

`CheckMATE` needs to know the centre-of-mass energy at which the original analysis has been performed in case that users use `Pythia 8` for the event generation and also to ensure that no input event file is tested against a set of analyses corresponding to different values of $\sqrt{s}$:

```
  center of Mass Energy (in TeV):
     8
```

Starting with the new `CheckMATE` version, to help users identifying the relevant analyses for their models the `AnalysisManager` allows for a list of tags which help categorising the analysis. This is a very new feature and for now we simply state that we have an analysis with a large amount of missing energy and many jets:

```
  If wanted, you can add tags which classify the analysis (e.g. stops, etmiss, ...)
  This makes it easier to later to find out if the analysis is useful for whatever
  the users think is most sensitive to their input model
  Tag (one per line, finish with empty line)
     etmiss
     multijet
```

At the end of this question block, the `AnalysisManager` asks whether control regions will be provided for the given analysis. If we choose "yes", it will produce a second analysis source file which can be run separately from within `CheckMATE`. In our case, we are only interested in implementing signal regions and cutflows for which we do not need a second analysis file.

```
  Do you plan to implement control regions to that analysis? [(y)es, (n)o)
    n
```

Now we go more into the details of the analysis. As the next step, we have to list all signal regions the analysis provides. If we check out the actual analysis publication, see Ref. [241], we find five main signal regions A–E which sometimes are split into subregions L(oose), M(edium) or T(ight). We enter them one by one

```
2. Information on Signal Regions
  List all signal regions (one per line, finish with an empty line):
    AL
    AM
    BM
    BT
    CM
    CT
    D
    EL
    EM
    ET
```

In our case, we implement an experimental study for which the experimental observation and Standard Model expectation are known.

```
Is the SM expectation B known? [(y)es, (n)o]?
    y
```

Now things become a little more involved: for each of the above signal regions, we have to provide a set of numbers to which `CheckMATE` can compare the model prediction. In its most simple form, this includes the observed number of events `obs` and the Standard Model expectation `bkg` including error `bkg_err`. Sometimes, the background error is split up into a statistical and systematical error and sometimes the systematical error is given in asymmetrical $\pm$ form. The different input options also allow for the data to be given in all these different formats. In our example, Table 4 in Ref. [241] gives us the minimal set: `obs`, `bkg` and `bkg_err`.

```
Information: We are now going to ask you which numbers you want to provide for each signal region.
The following items are possible:
    obs:                    Observed number of events
    bkg:                    Expected number of background events
    bkg_err:            Expected total error on bkg
    bkg_errp:         Expected total upper error (in case of asymmetric errors)
    bkg_errm:         Expected total lower error (in case of asymmetric errors)
    bkg_err_stat: Expected statistical error on bkg
    bkg_err_sys:    Expected systematical error on bkg (in case of symmetric errors)
    bkg_errp_sys: Expected systematical upper error (in case of asymmetric errors)
    bkg_errm_sys: Expected systematical lower error (in case of asymmetric errors)
Note that not all of these numbers have to be given (e.g. you don't have to give the total error
if you give the individual stat and sys contributions)  However, there are some requirements,
about which you will be warned if you don't meet them (e.g. giving xyz_errp without xyz_errm)
The standard, minimum set of information consists of obs, bkg and bkg_err
    List all categories you want to supply (one per line)

        obs
        bkg
        bkg_err

The set of information you entered is valid.
```

The `AnalysisManager` would reject the input list if it was not complete: for example, if we entered only the statistical error `bkg_stat` but no systematical error.

Next, we have to enter the actual numbers for all the above categories for each and every one of the listed signal regions:

```
        You now have to add the numbers for each of the given signal regions.
        Note that while you enter more numbers, the corresponding model independent
         95% confidence limits for the items you have already entered are calculated
         in the background.
        AL
            obs:
                5333
```

```
        bkg:
            4700
        bkg_err:
            500
        S95obs and S95exp values are calculated internally (progress: 0 / 2)
    AM
        obs:
            135
        bkg:
            122
        bkg_err:
            18
        S95obs and S95exp values are calculated internally (progress: 0 / 4)
    [...]
    ET
        obs:
            5
        bkg:
            2.9
        bkg_err:
            1.8
        S95obs and S95exp values are calculated internally (progress: 3 / 20)
```

To allow for a fast statistical evaluation of the result in CheckMATE, it is convenient to first translate observation and expectation into a model independent upper limit on any new signal prediction S^{95}, c.f. Eq. (4.2). These numbers are calculated internally by the AnalysisManager. As this calculation takes some time, it is queued and calculated in the background while the user enters the detector related information.

The next set of questions are all about detector level objects:

```
3. Settings for Detector Simulation
    3.1: Miscellaneous
        To which experiment does the analysis correspond? [(A)TLAS, (C)MS]
            A
```

As a next step we have to enter information regarding lepton isolation criteria. Normally, these are defined within the experimental publications and are needed to distinguish signal leptons from leptons within jets. In our example, however, there are no signal leptons and therefore we do not require any particular isolation criteria for neither electrons, muons nor photons.

```
    3.2: Electron Isolation
        Do you need any particular isolation criterion? [(y)es, (n)o]
            n
    3.3: Muon Isolation
        Do you need any particular isolation criterion? [(y)es, (n)o]
            n
    3.4: Photon Isolation
        Do you need any particular isolation criterion? [(y)es, (n)o]
            n
```

Note that even though we entered no, internally there will always be a soft isolation condition that cannot be overwritten by the user and which is automatically applied on electrons, muons and photons. This ensures that objects that would not have been reconstructed due to overlapping detector activity are automatically removed internally.

The final questions relate to potential flavour tags we have to apply on jets. The given analysis considers b-tags with a reconstruction efficiency of 70%. We therefore simply enter

```
Do you want to use b-tagging? [(y)es, (n)o]
    y
b-Tagging 1:
    What is the signal efficiency to tag a b-jet? [in %]
        70
Do you need more b tags? [(y)es, (n)o]
    n
Do you want to use tau-tagging? [(y)es, (n)o]
    n
```

Depending on how quickly we entered the above information, the `AnalysisManger` either finished the internally started S^{95} calculations or will wait until these are complete. When the evaluation ends, the results are shown and should be briefly checked to make sure that all numbers are sensible.

```
All necessary information has been entered. Before the AnalysisManager
 can create all required files, the internal S95obs and S95exp
 calculations have to finish. The calculation should take 10s up to a minute
 per point.
        ... done!
Please check the below results for sanity. If anything looks
 suspicious, please contact the CheckMATE authors.
   obs    bkg    bkgerr    S95obs    S95exp
   5333    4700    500    1400    985
   135    122    18    50    40
   29    33    7    14    17
   4    2.4    1.4    6.9    5.8
   228    210    40    87    79
   0    1.6    1.4    3.0    3.4
   18    15    5    15    13
   166    113    21    90    54
   41    30    8    28    21
   5    2.9    1.8    8.2    6.6
   (Press any key to continue)
```

Note that due to numerical effects, the above numbers are not fully deterministic. Comparing the calculated numbers to the ones in Ref. [241] tells us that the numbers are acceptable. Usually, the experimental numbers slightly differ from the ones calculated by the `AnalysisManager`. This is mainly caused by different parametrisations of the background uncertainties, taking information on individual error sources into account to which `CheckMATE` does not have access. `CheckMATE` still prefers to calculate and use its own numbers as the exact same statistical routines for S95 are used for the proper CL_S calculation in the `CheckMATE` evaluation routines such that the results of the two approaches are more consistent with each other.

We therefore accept the numbers and finish the `AnalysisManager` section:

```
    - Reference file created
    - Variable values saved in $CMDIR/data/analysis_info/atlas_conf_2013_047x_var.j
Analysis atlas_conf_2013_047x has been added successfully!
Run 'make' from the main CheckMATE folder to compile it!
```

Looking at the Skeleton Analysis Code

The `AnalysisManager` is mainly responsible to gather all the information for the detector simulation and the statistical evaluation sections of `CheckMATE`. What is still left to do is to define the analysis code that is used to analyse the events the user provides. In this section we describe how to do this by continuing our example of `atlas_conf_2013_047X`. Note that the code we develop here differs slightly from the actual code implemented in `CheckMATE` since we, for the sake of understanding, change the order of some steps here and shorten the code where possible. It still gives the exact same results for the signal region tests though.

As the AnalysisManager has told us, source files for our analysis have already been created. They can be found in $CMDIR/tools/analysis/include/atlas_conf_2013_047x.h and $CMDIR/tools/analysis/src/atlas_conf_2013_047x.cc and are already filled with skeleton code that properly compiles and embeds the analysis into the existing framework. What should concern us most is the source file which contains the actual analysis code. Every CheckMATE analysis contains three main functions.[16]

initialize(): This function is called once at the beginning of an analysis. It is therefore used to setup overall information, initialise variables and open files that are used throughout the analysis. By default, AnalysisManager data that is important for the analysis is already embedded[17]:

atlas_conf_2013_047x.cc

```
#include "atlas_conf_2013_047X.h"
// AUTHOR: Guybrush Threepwood
//  EMAIL: threepwood@pirates.arr
void Atlas_conf_2013_047x::initialize() {
  setAnalysisName("atlas_conf_2013_047X");
  setInformation(""
    "# ATLAS\n"
         "# ATLAS-CONF-2013-047\n"
         "# 0 leptons, 2-6 jets, etmiss\n"
         "# sqrt(s) = 8 TeV\n"
         "# int(L) = 20.3 fb^-1\n"
  "");
  setLuminosity(20.3*units::INVFB);
  bookSignalRegions("AL;AM;BM;BT;CM;CT;D;EL;EM;ET;");
}
```

The setAnalysisName and setInformation functions define human readable headers and the prefix of all analysis-related output files. They must not be changed to not spoil the CheckMATE internal data flow. setLuminosity is used to properly normalise the input to a physical number of events given the cross section the user provides in the CheckMATE input card. This number can be used to rescale the overall output, e.g. to take a global event-cleaning efficiency into account. Finally book functions are defined for SignalRegions and CutflowRegions. These functions make sure that the respective _signal.dat and _cutflow.dat analysis output files contains numbers for each of the booked signal/cutflow regions. No matter in which order the signal regions are booked they will always be sorted alphabetically in the output.

analyze(): This function is the heart of any analysis: It is called once per event and contains the physics that is used to quantify the given data. Except for some comments and tips, this function does not contain any code yet and we will fill it in the next part of this tutorial.

finalize(): As the name suggests, this function is called once at the end of a given analysis. Usually this function is empty, however it can be used to e.g. free pointers that have been defined during initialize or to close some extra files that have been opened and filled before.

Now that we have understood the structure let us start to implement the analysis code.

Selection of Final State Objects

As the first step, we should define all the final state objects that we need and apply the appropriate kinematical cuts. The given analysis requires the following objects:

[16] The three-function structure is similar to the one used in the Rivet [172] framework.

[17] Note that the actual source file includes many extra lines of explanatory comments which we have removed for this tutorial.

- missing transverse energy,
- electrons with $p_T > 10$ GeV and $|\eta| < 2.47$ that pass minimal selection criteria,
- muons with $p_T > 10$ GeV and $|\eta| < 2.4$ reconstructed with combined data from tracker and muon spectrometer,
- photons with $p_T > 130$ GeV and $|\eta| < 2.47$ excluding $1.37 < |\eta| < 1.52$ and
- jets with $p_T > 20$ GeV and $|\eta| < 2.8$.

In the code, all the above objects are already predefined and we just have to select the right kinematic range using the `filterPhaseSpace` function of the analysis base class:

```
void Atlas_conf_2013_047::analyze() {
  missingET->addMuons(muonsCombined);
  electronsLoose = filterPhaseSpace(electronsLoose, 10., -2.47, 2.47);
  muonsCombined = filterPhaseSpace(muonsCombined, 10., -2.4, 2.4);
  jets = filterPhaseSpace(jets, 20., -2.8, 2.8);
  photons = filterPhaseSpace(photons, 130., -2.47, 2.47, true);
```

The missing energy vector *a priori* does not contain muon contributions as different analyses can have different definitions of the construction of the missing momentum vector. We therefore add the contribution of all reconstructed muons by using the `addMuons` function. Furthermore, the area $1.37 \leq |\eta| \leq 1.52$ is often excluded for objects reconstructed in the electromagnetic calorimeter. The `filterPhaseSpace` function therefore has an optional last parameter which — if set to `true` — ignores objects in exactly that region.

These objects are then tested against different overlap conditions. In our case, these are defined as follows:

1. First, any jet with $\Delta R(j, e) < 0.2$ to a nearby electron is removed.
2. Then, any electron and any muon with $\Delta R(\ell, j) < 0.4$ is removed.

Functions that take care of these removals are fortunately already available in the `AnalysisBase` class:

```
  jets = overlapRemoval(jets, electronsLoose, 0.2);
  electronsLoose = overlapRemoval(electronsLoose, jets, 0.4);
  muonsCombined = overlapRemoval(muonsCombined, jets, 0.4);
```

Note that the order of these steps is crucial. Due to the setup of the detector simulation most electrons will also be reconstructed as jets. An overlap removal with respect to these two objects is therefore always necessary to avoid severe double counting issues.

Event Selection

Now that we have finished the object reconstruction step, we can start checking whether a given event fulfils the criteria of the given analysis. In our example, we should ignore events with leptons and hard photons. This is done very easily by using the `return` statement which ends the current run of the `analyze()` function and hence effectively vetoes the currently processed event:

```
if(!photons.empty() || !electronsLoose.empty() || !muonsCombined.empty())
  return;
```

We now start to look at the signal region criteria which are summarised in Table 1 in Ref. [241]. Firstly all signal regions require $\not{E}_T \geq$ 160 GeV and at least two reconstructed jets. From these the leading jet must have a p_T of least 130 GeV and the sub-leading jet $p_T > 60$ GeV. All objects in CheckMATE analyses have a PT member that can be directly accessed for this purpose:

```
if(missingET->PT < 160.0)
  return;
if(jets.size() < 2 || jets[0]->PT < 130 || jets[1]->PT < 60)
  return;
```

Note that all object vectors are automatically sorted with respect to p_T such that leading and sub-leading jet are simply the first and the second object in the jet vector.[18] Furthermore the angular separation of the missing momentum vector and the leading two jets must be at least 0.4. We make use of the P4() function of each object which returns the corresponding TLorentzVector object defined in ROOT. This class comes with a large list of procedures to calculate 4-momentum parameters like the $\Delta\phi$ separation we need:

```
if (fabs(jets[0]->P4().DeltaPhi(missingET->P4())) < 0.4)
   return;
if( fabs(jets[1]->P4().DeltaPhi(missingET->P4())) < 0.4)
   return;
```

There are more constraints on further 'hard jets' with $p_T > 40$ GeV: If a third 'hard jet' exists, it has to pass the above criterion too. For some signal regions, an additional constraint is applied if extra jets appear in the event. Here the looser constraint that $\Delta\phi > 0.2$ is applied to the fourth jet onwards:

```
std::vector<Jet*> hardjets = filterPhaseSpace(jets, 40., -2.8, 2.8);
bool validJet3 = (hardjets.size() < 3 || fabs(hardjets[2]->P4().DeltaPhi(missingET->P4())) > 0.4);
bool validMultiJet = validJet3;
for (int j = 3; j < hardjets.size(); j++) {
    if (fabs(jets[j]->P4().DeltaPhi(missingET->P4())) < 0.2)
        validMultiJet = false;
}
```

For our selection we need the ratio of $\not{E}_T$ to the total effective mass $m_{\text{eff}}(Nj)$ as well as to $\sqrt{H_T}$. H_T is defined to be the scalar p_T sum of of all jets with $p_T > 40$ GeV whereas $m_{\text{eff}}(Nj)$ is the scalar p_T sum of the leading N jets plus $\not{E}_T$. There is also a requirement on $m_{\text{eff}}(\text{incl}) \equiv H_T + \not{E}_T$. We have to calculate these explicitly for all allowed number of jets[19].

```
double HT = 0.;
for(int j = 0; j < hardjets.size(); j++)
   HT += hardjets[j]->PT;
double mEffincl = HT + missingET->PT;

double mEff2 = missingET->PT + jets[0]->PT + jets[1]->PT;
double rEff2 = missingET->PT/mEff2;

double mEff3 = 0;
```

[18] Standard C++ vectors do not catch out-of-bound indices. Users therefore have to ensure semantically that jets[i] is only accessed if jets contains at least $i+1$ members.

[19] We are aware that the conditions could be formulated more concisely by using the ternary ? operator, e.g. double mEff4 = jets.size() >= 4 ? mEff3 + jets[3]->PT : 0; For this manual we however preferred to use the easier to read version using if that most readers should be familiar with.

```
    if (jets.size() >= 3)
        mEff3 =  mEff2 + jets[2]->PT;
    double rEff3 = 0;
    if (jets.size() >= 3)
        rEff3 = missingET->PT/mEff3;

    double mEff4 = 0;
    if (jets.size() >= 4)
        mEff4 =  mEff3 + jets[3]->PT;
    double rEff4 = 0;
    if (jets.size() >= 4)
        rEff4 = missingET->PT/mEff4;
    [...]

    double rEffHT = missingET->PT/sqrt(HT);
```

The last requirement we have to check is that the momentum of the leading N jets in a given signal region is larger than 60 GeV. For that we simply count the number of jets after cutting to the signal phase space:

```
    int nSignalJets = filterPhaseSpace(jets, 60., -2.8, 2.8).size();
```

With all these numbers at hand we can go ahead and check the various signal regions. Whenever an event passes the respective criteria, we just have to call the `countSignalEvent` function:

```
    if (validJet3) {
        if(nSignalJets >= 2 && rEff2 > 0.2 && mEffincl > 1000.)
            countSignalEvent("AL");
        if(nSignalJets >= 2 && rEffHT > 15. && mEffincl > 1600.)
            countSignalEvent("AM");
        if(nSignalJets >= 3 && rEff3 > 0.3 && mEffincl > 1800.)
            countSignalEvent("BM");
        if(nSignalJets >= 3 && rEff3 > 0.4 && mEffincl > 2200.)
            countSignalEvent("BT");
    }
    if (validMultiJet) {
        if(nSignalJets >= 4 && rEff4 > 0.25 && mEffincl > 1200.)
            countSignalEvent("CM");
        if(nSignalJets >= 4 && rEff4 > 0.25 && mEffincl > 2200.)
            countSignalEvent("CT");
        if(nSignalJets >= 5 && rEff5 > 0.2 && mEffincl > 1600.)
            countSignalEvent("D");
        if(nSignalJets >= 6 && rEff6 > 0.15 && mEffincl > 1000.)
            countSignalEvent("EL");
        if(nSignalJets >= 6 && rEff6 > 0.2 && mEffincl > 1200.)
            countSignalEvent("EM");
        if(nSignalJets >= 6 && rEff6 > 0.25 && mEffincl > 1500.)
            countSignalEvent("ET");
    }
```

These lines finish the analysis code. The full code is listed in Fig. 4.6.

The `CheckMATE` installation files then need to be created with the following commands, see also Appendix B.1: `autoreconf; ./configure {parameters};`. Then, `make; make install;` within the `CheckMATE` main folder should compile the analysis and make it available in the same manner as any other `CheckMATE` analysis.

More examples covering more complicated cut prescriptions and the adding of prospective future analyses can be found in Ref. [179]. The latter feature is used in our Higgs Portal analysis in Chapter 5 to estimate the sensitivity of the high luminosity LHC. This works similarly to the above prescription, with the only difference that we have to anser `n` when asked `Is the SM expectation B known?`. Then, `CheckMATE` skips asking for the respective numbers but

atlas_conf_2013_047x.cc

```
void Atlas_conf_2013_047x::analyze() {
    missingET->addMuons(muonsCombined);
    electronsLoose = filterPhaseSpace(electronsLoose, 10., -2.47, 2.47);
    muonsCombined = filterPhaseSpace(muonsCombined, 10., -2.4, 2.4);
    jets = filterPhaseSpace(jets, 20., -2.8, 2.8);
    photons = filterPhaseSpace(photons, 130., -2.47, 2.47, true);

    jets = overlapRemoval(jets, electronsLoose, 0.2);
    electronsLoose = overlapRemoval(electronsLoose, jets, 0.4);
    muonsCombined = overlapRemoval(muonsCombined, jets, 0.4);

    if(!photons.empty() || !electronsLoose.empty() || !muonsCombined.empty())
        return;
    if(missingET->PT < 160.0)
        return;
    if(jets.size() < 2 || jets[0]->PT < 130 || jets[1]->PT < 60)
        return;
    if (fabs(jets[0]->P4().DeltaPhi(missingET->P4())) < 0.4)
        return;
    if( fabs(jets[1]->P4().DeltaPhi(missingET->P4())) < 0.4)
        return;

    std::vector<Jet*> hardjets = filterPhaseSpace(jets, 40., -2.8, 2.8);
    bool validJet3 = (hardjets.size() < 3 || fabs(hardjets[2]->P4().DeltaPhi(missingET->P4())) > 0.4);
    bool validMultiJet = validJet3;
    for (int j = 3; j < hardjets.size(); j++) {
        if (fabs(hardjets[j]->P4().DeltaPhi(missingET->P4())) < 0.2)
           validMultiJet = false;
    }

    double HT = 0.;
    for(int j = 0; j < hardjets.size(); j++)
        HT += hardjets[j]->PT;
    double mEffincl = HT + missingET->PT;
    double mEff2 = missingET->PT + jets[0]->PT + jets[1]->PT;
    double rEff2 = missingET->PT/mEff2;

    double mEff3 = 0;
    if (jets.size() >= 3)
        mEff3 =  mEff2 + jets[2]->PT;
    double rEff3 = 0;
    if (jets.size() >= 3)
        rEff3 = missingET->PT/mEff3;
    double mEff4 = 0;
    if (jets.size() >= 4)
        mEff4 =  mEff3 + jets[3]->PT;
    double rEff4 = 0;
    if (jets.size() >= 4)
        rEff4 = missingET->PT/mEff4;
    double mEff5 = 0;
    if (jets.size() >= 5)
        mEff5 =  mEff4 + jets[4]->PT;
    double rEff5 = 0;
    if (jets.size() >= 5)
        rEff5 = missingET->PT/mEff5;
    double mEff6 = 0;
    if (jets.size() >= 6)
        mEff6 =  mEff5 + jets[5]->PT;
    double rEff6 = 0;
    if (jets.size() >= 6)
        rEff6 = missingET->PT/mEff6;
    double rEffHT = missingET->PT/sqrt(HT);

    int nSignalJets = filterPhaseSpace(jets, 60., -2.8, 2.8).size();
    if (validJet3) {
        if(nSignalJets >= 2 && rEff2 > 0.2 && mEffincl > 1000.)
            countSignalEvent("AL");
        if(nSignalJets >= 2 && rEffHT > 15. && mEffincl > 1600.)
            countSignalEvent("AM");
        if(nSignalJets >= 3 && rEff3 > 0.3 && mEffincl > 1800.)
            countSignalEvent("BM");
        if(nSignalJets >= 3 && rEff3 > 0.4 && mEffincl > 2200.)
            countSignalEvent("BT");
    }
    if (validMultiJet) {
        if(nSignalJets >= 4 && rEff4 > 0.25 && mEffincl > 1200.)
            countSignalEvent("CM");
        if(nSignalJets >= 4 && rEff4 > 0.25 && mEffincl > 2200.)
            countSignalEvent("CT");
        if(nSignalJets >= 5 && rEff5 > 0.2 && mEffincl > 1600.)
            countSignalEvent("D");
        if(nSignalJets >= 6 && rEff6 > 0.15 && mEffincl > 1000.)
            countSignalEvent("EL");
        if(nSignalJets >= 6 && rEff6 > 0.2 && mEffincl > 1200.)
            countSignalEvent("EM");
        if(nSignalJets >= 6 && rEff6 > 0.25 && mEffincl > 1500.)
            countSignalEvent("ET");
    }
}
```

Figure 4.6: Full source code of the simplified reimplementation of atlas_conf_2013_047 into CheckMATE.

adds the analysis such that it can be used like any other analysis. However, as long as the Standard Model expectation is not provided, CheckMATE will skip the statistical evaluation if such an incomplete analyis is run on input data. The standard way to proceed is to generate Standard Model background samples, use CheckMATE to determine the number of background events which pass all the cuts, and from that determine the numbers bkg and bkg_err. For a prospective study, obs is typically set to bkg. These numbers can be added by choosing to (e)dit analysis information during the start prompt of the AnalysisManager. When all numbers are provided, the statistical evaluation is re-enabled for the new analysis.

4.6 Summary and Outlook

CheckMATE is an easy-to-use tool for phenomenologists to quickly test their BSM models of interest against a large set of results from ATLAS and CMS. This is done by either providing simulated events from an external event generator or by making use of Pythia 8 within CheckMATE. In both cases, events are automatically passed through the detector simulation Delphes with standard settings for the ATLAS and CMS detector. Resulting detector level objects are then post-processed via AnalysisHandlers which take care of the proper tagging of final state objects depending on all the requirements of all analyses chosen by the user. The respectively used tagging efficiencies have been determined from sophisticated fits to experimental performance studies. The analyses then determine how many of the provided events pass the given signal region cuts and determine the physical number of predicted signal events for each such region. A statistically well-founded comparision to observed and expected results then yields a statement whether the input can be excluded or not at the 95 % confidence level. This statement is returned by CheckMATE and thus easily allows the users to quickly separate the Allowed from the Excluded parameter region of their model of interest. If published analyses other than those implemented in CheckMATE exist, an implemented AnalysisManager allows users to easily add these to the existing framework.

In the time since the original CheckMATE version 1.0 was published in Ref. [178] it has become an invaluable tool for the particle physics community. The approximately one hundred publications by phenomenologists all around the globe which use CheckMATE to test their models of interest cover a wide range of possible applications to various theories beyond the Standard Model. They are solid proof that the program indeed works out-of-the-box and model independently. We make use of CheckMATE ourselves in the upcoming two chapters of this thesis: in Chapter 5 we use the AnalysisManager to easily project an 8 TeV analysis to a high luminosity LHC with $\sqrt{s} = 14\,\text{TeV}$ and in Chapter 6 we make use of the wide coverage of analyses with b-jets and large amount of $\not{E}_T$ in order to test the LHC sensitivity to a natural NMSSM model.

The unvalidated analyses implemented in CheckMATE already include some of the first LHC results from 13 TeV data and more are expected to be added in the near future. The tool is ready to incorporate these results and to allow for a potential retuning of the detector efficiencies for the upgraded LHC without affecting the implemented and validated 8 TeV results which still put the most important constraints on various final state topologies.

With the soon-to-be-published version 2.0 described in this chapter, CheckMATE will start removing the strict separation of event generation and collider testing. Though for now Pythia 8 is restricted to only being able to simulate those models which are explicitly implemented into the code, it was recently extended with the functionality to link to the MadGraph5_aMC@NLO event generator which then can perform the partonic event generation. As explained in Section 3.2.2,

this tool can make use of the UFO file format to in principal simulate events for any possible BSM model. A proper inclusion of this feature into the CheckMATE code would make it a completely model-independent collider phenomenology tool without any necessity of the user to actively simulate events.

At the same time, the automatised setup of Pythia 8 itself by CheckMATE also has to be improved. For now, standard settings are used if the user provides a single .lhe file. As we discussed in Section 3.2.5, matching and merging algorithms require more than one partonic event sample which then have to be properly combined to avoid double counting. Both steps are foreseen to be realised in the not so far future.

CHAPTER 5

Probing the Higgs Portal at the LHC via Monojets

As explained in Section 2.2 the Standard Model cannot account for the right matter density of our Universe and thus it seems necessary to extend the field content by further particles which interact weakly with the Standard Model. We introduced a setup called the *Higgs Portal* with a scalar singlet S which is charged under a dark gauge group $U(1)_X$ and a dark gauge boson Z' which gained mass by spontaneously breaking the dark gauge group through a vacuum expectation value z of the singlet field. The only renormalisable term which couples the dark sector to the Standard Model is the scalar mixing term $\lambda_{HS} H^\dagger H S^\dagger S$ which yields two mixed mass eigenstates if both fields acquire a vev. This results in two scalar fields h, H which both couple to Standard Model particles, the hidden gauge bosons and each other. The relevant terms in the Lagrangian read

$$\mathcal{L}_{h/H(\mathrm{SM})(\mathrm{SM})} = \Big(h\cos\alpha + H\sin\alpha\Big)\left(\frac{\sqrt{2}m_W^2}{v} W_\mu^+ W^{\mu,-} + \frac{m_Z^2}{\sqrt{2}v} Z_\mu Z^\mu - \sum_f \frac{m_f}{\sqrt{2}v}\bar{f}f\right), \tag{5.1}$$

$$\mathcal{L}_{h/HZ'Z'} = \Big(h\sin\alpha - H\cos\alpha\Big)\tilde{g} m_{Z'} Z'_\mu Z'^{,\mu}, \tag{5.2}$$

$$\mathcal{L}_{Hhh} = \frac{2m_h^2 + m_H^2}{2\sqrt{2}v}\sin(2\alpha)\left(\cos\alpha + \sqrt{2}\tilde{g}\frac{v\sin\alpha}{m_{Z'}}\right) H h^2. \tag{5.3}$$

In this section, we discuss the sensitivity of the future high luminosity LHC running at its full center-of-mass energy to this model by looking at monojet final states. After briefly summarising the current most important existing limits from theory and experiment in Sections 5.1 and 5.2 we show the still unconstrained parameter space in Section 5.3 before discussing the proposed analysis and our results in detail in Sections 5.4 and 5.5.

The main results of this chapter have already been published in Ref. [242]. However, a more careful consideration of existing limits on our target parameter space is performed within this thesis. Note also that for consistency reasons the nomenclature of particles and normalisation of parameters is slightly different.

5.1 Theoretical Constraints

In Eqs. (2.49) to (2.51), we re-expressed the theory parameters $\lambda_H, \lambda_S, \lambda_{HS}$ via the phenomenological parameters m_h, m_H and $m_{Z'}$, which together with the dark gauge coupling $\tilde{g}$ fully specify our model. If we choose particular mass values for our collider study, we have to ensure that

these are theoretically possible; most importantly if we translate them back into theory parameters those should be small enough to allow a perturbative phenomenological discussion and the resulting scalar potential in Eq. (2.40) should allow for spontaneous symmetry breaking. We illustrate the main ideas and constraints within this section, however Refs. [243–247] give a more thorough analysis including considerations of higher order effects.

5.1.1 Stability of the Potential and Existence of a Nontrivial Minimum

e Lastly, for positive λ_{HS} the necessary conditions to ensure $v, z \neq 0$ mentioned below Eq. (2.42) are automatically fulfilled if $\lambda_{HS}^2 < \lambda_H \lambda_S$. As this is the determinant of the mass matrix, Eq. (2.45), choosing posive values for m_h^2, m_H^2 automatically ensures that valid solutions for μ_H^2 and μ_S^2 can be found such that solutions $v, z \neq 0$ exist.

As we see, we can trivially fulfill the required theoretical constraints on the vacuum structure at the weak scale by simply choosing physical values for m_h, m_H and by keeping the mixing angle positive. However, within a fully specified, ultraviolet complete model, the renormalisation group equations (RGEs) should be used to check that the stability conditions hold even when evolving the parameters up to higher scales, e.g. the Planck scale. As can be seen in the above cited references in which such a more sophisticated study is performed, this restricts the possible choices of the low scale parameters. In our scenario, however, we have many additional degrees of freedom to change the result of such an analysis without affecting the collider phenomenology discussed below. For example, additional particles in the hidden sector will affect the RGE evolution if they are charged under the dark gauge group. However, they can be ignored for a collider study as long as they do not interact with S or as long as their mass is sufficiently high to not be produced at LHC energies. Also, specifying the high scale model which avoids low scale kinetic mixing of $U(1)_X$ and $U(1)_Y$ can affect the RGE evolution, see e.g. Ref. [248].

For a phenomenological study as we perform within this thesis, it is therefore reasonable to ignore these additional constraints here. They become especially important as soon as the dark sector is designed to match cosmological observations, see e.g. Refs. [243, 246].

5.1.2 Perturbativity

If coupling constants become too large, non-perturbative effects like the formation of bound states have to be considered. To avoid this, we require all three λ_H parameters and $\tilde{g}$ to be smaller than $\sqrt{4\pi}$. From Eqs. (2.49) to (2.51) we can translate this condition into constraints on the physical parameters

$$\cos(2\alpha) < \frac{4\sqrt{\pi}v^2 - (m_h^2 + m_H^2)}{m_H^2 - m_h^2}, \tag{5.4}$$

$$\cos(2\alpha) > \frac{m_h^2 + m_H^2 - \frac{2\sqrt{\pi}}{\tilde{g}^2} m_{Z'}^2}{m_H^2 - m_h^2}, \tag{5.5}$$

$$\sin(2\alpha) < \frac{4\sqrt{2\pi}}{\tilde{g}} \frac{v m_{Z'}}{(m_H^2 - m_h^2)} \tag{5.6}$$

These conditions put constraints on the valid physical parameter regions of our model and, most importantly, limit the possible branching ratios into the final states of interest. We show these bounds and discuss their impact later in Section 5.2.2.

Again, it should be emphasised that a higher order calculation would change the tree level relations of theoretical and observable parameters in Eqs. (2.49) to (2.51) and can change the above constraints drastically. Similarly, the na¨ively chosen upper limit of $\sqrt{4\pi}$ can only be verified if the actual numerical contribution from loop diagrams is compared to the tree level result. We therefore should not interpret the perturbativity limits shown in the following results as entirely forbidden parameter combinations but as regions with a low probability to not violate theoretical conditions on the model. Again, they should be analysed in more detail within a well defined model as e.g. done in the references listed in the introductory paragraph of this section.

5.2 Experimental Constraints

The signature we analyse within this work focusses on invisible decays of the heavy singlet-like scalar particle and the sensitivity of a high luminosity LHC at its full energy. However, during the first run at $\sqrt{s} = 7$ and 8 TeV, both ATLAS and CMS have already searched for such particles and due to the absence of any deviations from the Standard Model expectation, bounds have been put on possible production cross sections times branching ratios. Furthermore, due to the mixing in the scalar sector the Standard Model like Higgs boson h has a $\cos\alpha$ reduced coupling to all other Standard Model particles. This should not be in conflict with the observation that so far all channels are in good agreement with the assumption of Standard Model like coupling strengths. Therefore mixing should be small and $\cos\alpha$ should not deviate largely from 1. Many of the LHC constraints have been analysed in previous studies of various manifestations of the Higgs Portal model, e.g. Refs. [249–253] and we refer to these and references therein for more detailled information.

Apart from direct collider searches, precise measurements of electroweak observables could be sensitive to the presence of a second heavy scalar which interacts with both the W and Z and thus put further constraints on our model. Also, we originally motivate the dark sector to solve the dark matter problem and hence a properly specified model should check constraints from these experiments. In this section, we summarise the most important of all these constraints and how they effect our accessible parameter space.

5.2.1 Limits from Standard Model Higgs Boson Searches

With the respective interaction terms known from Eqs. (5.1) to (5.3), we can easily relate the relevant production cross sections and decay widths of our model to quantities well studied for the Standard Model Higgs boson h,

$$\sigma_{pp\to h} = \cos^2(\alpha) \times \sigma^{\mathrm{SM}}_{pp\to h}, \tag{5.7}$$

$$\Gamma_{h\to(\mathrm{SM})} = \cos^2(\alpha) \times \Gamma^{\mathrm{SM}}_{h\to(\mathrm{SM})}. \tag{5.8}$$

Due to the mixing, the Standard Model production cross section and decay widths for the observed 125 GeV boson are each reduced by $\cos^2(\alpha)$. Because of this constant factor, the branching ratios of all final states are unaffected[1]. The Higgs portal scenario therefore predicts

[1] This statement is true as long as no new final states are present. As we explicitly avoid the possibility of $h \to Z'Z'$ decays, this is indeed the case.

a reduced *signal strength modifier* μ

$$\mu \equiv \frac{(\sigma \times \mathrm{BR})_{\mathrm{obs}}}{(\sigma \times \mathrm{BR})_{\mathrm{SM}}} = \cos^2(\alpha). \tag{5.9}$$

The most recent combination of all $\sqrt{s} = 8\,\mathrm{TeV}$ searches for the Standard Model Higgs boson at ATLAS and CMS results in a best fit value of $\mu = 1.09^{+0.11}_{-0.10}$ [254] , from which a lower 95 % confidence limit on $\mu \geq 0.89$ and thus $\sin\alpha \leq 0.33$ can be derived. By the time this work was completed, the combination of both experiments had not yet been published and only the signal strength limits of the individual channels were available (most importantly Refs. [255–257]). The strongest lower limit was set by the ATLAS $h \to 4\ell$ search with $\mu = 1.44^{+0.40}_{-0.33}$ and thus $\sin\alpha \leq 0.45$. This is why the results we show in the following include benchmark scenarios with $\sin\alpha = 0.4$ even though they are in strong tension with the updated experimental results. In the discussion we focus on the still viable $\sin\alpha = 0.3$ case.

If the dark matter candidate Z' was lighter than $\approx 62\,\mathrm{GeV}$, a new decay mode $h \to Z'Z'$ would open. The corresponding decay width can be calculated to be

$$\Gamma_{h\to Z'Z'} = \frac{\tilde{g}^2 \sin^2(\alpha) m_h^3}{32\pi m_{Z'}^2} \sqrt{1 - \frac{4m_{Z'}^2}{m_h^2}} \left(1 - \frac{4m_{Z'}^2}{m_h^2} + \frac{12 m_{Z'}^4}{m_h^4}\right). \tag{5.10}$$

Such an additional final state would result in a reduced branching ratios into all visible final states and thus an even smaller predicted value for μ. The corresponding limit on $\sin\alpha$ from the above analysis would therefore become even tighter for increasing $\tilde{g}$ and/or smaller $m_{Z'}$.

However, direct searches for invisible decay modes of the Standard Model like Higgs boson yield even more important constraints. There exist various fits from ATLAS [258] and CMS [255] using their combined set of Standard Model Higgs boson measurements. These fits allow various subsets of Higgs couplings to deviate from their Standard Model values while keeping the others fixed. Some of these consider $\mathrm{BR}(h \to \mathrm{inv.})$ as an additional degree of freedom and the resulting confidence limits on this parameter depend on the chosen subset of fitted couplings. The most general and hence most conservative fit allows for all couplings to fermions and gauge bosons to vary freely while only requring the coupling to vector bosons to not exceed the Standard Model value. Here, ATLAS quotes the strongest limit with $\mathrm{BR}(h \to \mathrm{inv.}) \lesssim 25\,\%$ which can be used to constrain the angle α and the mass $m_{Z'}$ by using

$$\mathrm{BR}(h \to \mathrm{inv.}) = \frac{\Gamma_{h\to Z'Z'}}{\Gamma_{h\to Z'Z'} + \cos^2(\alpha) \cdot \Gamma_h^{\mathrm{SM}}}. \tag{5.11}$$

This can be reformulated as

$$\frac{\Gamma_{h\to Z'Z'}}{\cos^2(\alpha)} \leq \Gamma_h^{\mathrm{SM}} \frac{\mathrm{BR}(h \to \mathrm{inv.})^{\max}}{1 - \mathrm{BR}(h \to \mathrm{inv.})^{\max}}. \tag{5.12}$$

To illustrate the severity of this constraint, we can check the implications for $m_{Z'} \ll m_h$. Here the parameter dependence of Eq. (5.10) factorises conveniently and the invisible branching ratio limit can be translated into a limit on the parameter product $\tilde{g}\tan\alpha/m_{Z'}$:

$$\frac{\tilde{g}\tan\alpha}{m_{Z'}} \leq \sqrt{\frac{32\pi\Gamma_h^{\mathrm{SM}}}{m_h^3} \frac{\mathrm{BR}(h \to \mathrm{inv.})^{\max}}{1 - \mathrm{BR}(h \to \mathrm{inv.})^{\max}}} \approx 2.6 \times 10^{-4} \frac{1}{\mathrm{GeV}}, \tag{5.13}$$

where we have used the Standard Model Higgs width $\Gamma_h^{\mathrm{SM}} = 4\,\mathrm{MeV}$ and $m_h = 125\,\mathrm{GeV}$. Since $m_{Z'}$ can be at most 65 GeV, this requires $\tilde{g}$ and/or α to be extremely small. Such a strong limit would constrain parameter space far more than could be achieved by the signature we propose in the following. We therefore restrict our discussion to dark gauge boson masses $m_{Z'} \geq 65\,\mathrm{GeV}$ which is clearly above the threshold for invisible h decays.

5.2.2 Limits from Heavy Higgs Boson Searches

The analogous expressions of Eqs. (5.8) and (5.10) for the singlet like heavy scalar are given by

$$\sigma_{pp\to H} = \sin^2(\alpha) \times \sigma^{\mathrm{SM}}_{pp\to h(m_h=m_H)}, \tag{5.14}$$

$$\Gamma_{H\to(\mathrm{SM})} = \sin^2(\alpha) \times \Gamma^{\mathrm{SM}}_{h(m_h=m_H)\to(\mathrm{SM})}, \tag{5.15}$$

$$\Gamma_{H\to Z'Z'} = \cos^2(\alpha) \times \frac{\tilde{g}^2 m_H^3}{32\pi m_{Z'}^2}\sqrt{1-\frac{4m_{Z'}^2}{m_H^2}}\left(1-\frac{4m_{Z'}^2}{m_H^2}+\frac{12m_{Z'}^4}{m_H^4}\right). \tag{5.16}$$

In addition, if $m_H > 2m_h$ an additional Higgs-to-Higgs decay channel opens. The corresponding partial width is given as

$$\Gamma_{H\to hh} = \frac{1}{8\pi m_H}\frac{(2m_h^2+m_H^2)^2}{8v^2}\sin^2(2\alpha)\left(\cos\alpha+\sqrt{2}\tilde{g}\frac{v\sin\alpha}{m_{Z'}}\right)^2\sqrt{1-\frac{4m_h^2}{m_H^2}}. \tag{5.17}$$

The Run 1 CMS search for heavy Higgs bosons via $H \to WW, ZZ$ decays [259] accounts for a possible reduced production cross section and a potential invisible decay mode. Limits are then put on the ratio $\sigma^{\mathrm{vis}}/\sigma_{\mathrm{SM}}$, in our case predicted to be $\sin^2(\alpha)(1-\mathrm{BR}(H\to\mathrm{inv.}))$. These limits depend on the heavy Higgs mass m_H and vary according to statistical fluctuations in the experimental channels. They range between $\sigma^{\mathrm{vis}}/\sigma_{\mathrm{SM}} \lesssim 0.15$ for $m_H \approx 145\,\mathrm{GeV}$ and $\lesssim 0.075$ for $m_H \approx 330\,\mathrm{GeV}$ and can exclude parameter regions with a too small invisible branching fraction even in case of a mild mixing of $\sin\alpha = 0.3$. Analogous limits from ATLAS [258, 260] are only given for individual WW and ZZ channels but still yield comparable limits. We show and discuss the parameter regions excluded by these constraints in the upcoming section.

5.2.3 Limits from Higgs–to–Higgs Decays

Heavy scalars decaying via the rate given in Eq. (5.17) can be observed in channels with two reconstructed Standard Model like Higgs bosons which form an invariant mass peak. Both ATLAS [261] and CMS [262] have performed searches for such resonances and due to their absence have put limits on cross section times branching ratio. These could in principle constrain our allowed parameter space for $m_H > 2m_h = 250\,\mathrm{GeV}$.

Let us consider the limits in Ref. [261] which already combine the results of individual Higgs boson decay channels. These bounds constrain $\sigma_{gg\to H} \times \mathrm{Br}(H\to hh)$ of the order 0.5 – 1 pb and larger. Since the gluon fusion cross section for a Standard Model like Higgs of 250 GeV by itself is already only 5 pb (see Ref. [263]), one easily finds that for our benchmark values of interest ($\sin\alpha \approx 0.3$, $\mathrm{BR}(H\to\mathrm{inv.}) \gtrsim 50\,\%$) current limits from Higgs–to–Higgs decays do not restrict the accessible parameter space.

5.2.4 Limits from Electroweak Precision Data

The appearance of an additional scalar boson which interacts weakly with Standard Model gauge bosons and fermions via the interaction terms in Eq. (5.1) can affect various observables of the electroweak sector. Most importantly, higher order corrections to gauge boson masses as well as absolute and relative decay widths could violate precision measurements from LEP and the Tevatron. Such an analysis has been performed in e.g. Refs. [245, 264]. As an example, Ref. [245] uses various observables from Ref. [265] and finds that it is only for $m_H \gtrsim 500\,\text{GeV}$ where these constraints dominate those drawn from heavy Higgs boson searches as explained above. As becomes apparent from our results below, our analysis is not sensitive to such heavy scalar particles and therefore we do not have to consider electroweak precision bounds on our parameter space.

5.2.5 Limits from Dark Matter Experiments

We motivated the Higgs Portal scenario to explain dark matter. Constraints from direct detection and relic density measurements can put important constraints on the hidden sector. Limits on the setup as we describe it here, i.e. a stable massive Z' of a gauge group with coupling $\tilde{g}$ which couples respectively to two scalars h and H with $\tilde{g}\cos\alpha$ and $\tilde{g}\sin\alpha$, are analysed in e.g. Refs. [243, 246, 249, 252, 264, 266, 267]. Non-trivial limits on the combined $\tilde{g} - m_H - m_{Z'} - \alpha$ parameter space can be set by requiring consistency with dark matter direct detection experiments and the correct energy density $\rho_{Z'}$ expected for dark matter. These can put limitations to those parameter regions we analyse within this work. As an example, for $m_H = 200\,\text{GeV}$, $m_{Z'} = 70\,\text{GeV}$ and $\sin\alpha = 0.3$, values for $\tilde{g}$ larger than 0.2 violate direct detection limits from XENON100 [246]. However, similarly to the discussion of the high scale behaviour of our theory, these constraints will change significantly by extending the particle content of the dark sector which would have no impact on the results of this study. For example, if not Z' but a lighter $U(1)_X$-charged fermion would be the dark matter candidate, relic density limits would depend on the mass and the quantum numbers of this hidden fermion. Also, direct detection limits would be damped as only higher order loop interactions between these fermions and nucleons would take place. We can therefore again ignore these constraints for our phenomenological study.

5.3 Available Parameter Space and Invisible Branching Ratios

Our signature of interest requires the heavy singlet like scalar H to decay invisibly into a pair of Z's. The corresponding invisible branching ratio can be calculated from the respective decay widths in Eqs. (5.15) to (5.17) as

$$\text{BR}(H \to \text{inv.}) = \frac{\Gamma_{H\to Z'Z'}}{\Gamma_{H\to Z'Z'} + \Gamma_{H\to hh} + \sum_{(\text{SM})} \Gamma_{H\to(\text{SM})}} \tag{5.18}$$

In Fig. 5.1, we show the countour plots of branching ratios in the m_H—$m_{Z'}$–plane for $\sin\alpha = 0.3, 0.4$ and four representative choices of $\tilde{g}$. The values for the total Standard Model width at various Higgs masses, needed to evaluate $\sum_{(\text{SM})} \Gamma_{H\to(\text{SM})}$, have been taken from Ref. [263]. In each plot, we also show the parameter region which either violates the kinematic condition $m_{Z'} < m_H/2$, the perturbativity constraints in Eqs. (5.4) to (5.6) or the experimental limits in

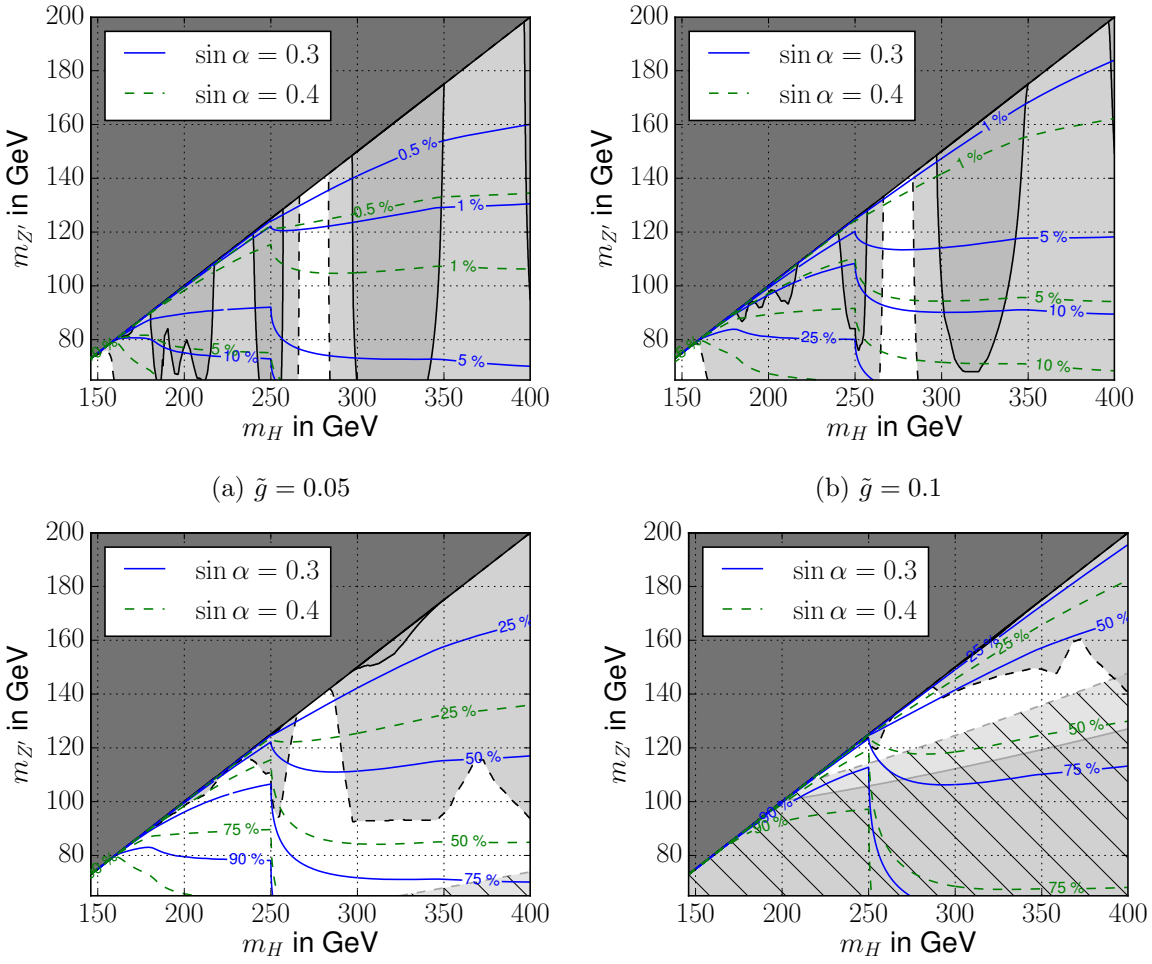

(a) $\tilde{g} = 0.05$

(b) $\tilde{g} = 0.1$

(c) $\tilde{g} = 0.5$

(d) $\tilde{g} = 1$

Figure 5.1: Allowed parameter regions in the m_H–$m_{Z'}$ plane and contour plots of the invisible branching ratio BR($H \to$ inv.) for different exemplary values of $\tilde{g}$. Each plot shows branching ratio contours for $\sin\alpha = 0.3$ (blue solid) and $\sin\alpha = 0.4$ (green dashed). The darkened triangular region in the top left corner corresponds to the kinematic region where $m_H < m_{Z'}/2$ and thus no decay $H \to Z'Z'$ is possible. The dark grayed regions below violate LHC constraints from heavy Higgs searches as explained in Section 5.2.2. The bottom hatched parameter region visible in (c) and (d) violates either of the perturbativity constraints in Eqs. (5.4) to (5.6). In both cases, the interior solid line denotes the weaker limit for $\sin\alpha = 0.3$ and the outer dashed line the stronger for $\sin\alpha = 0.4$.

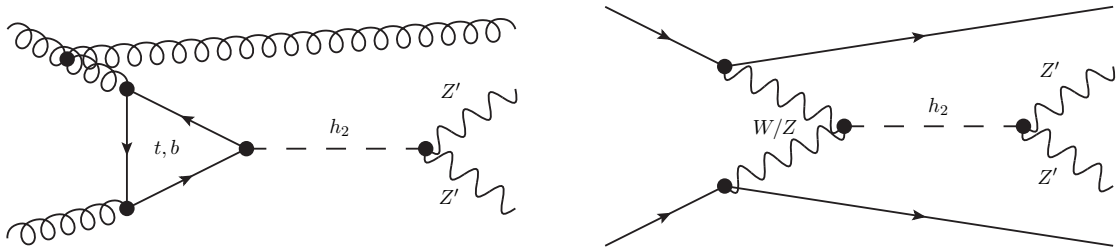

(a) gluon fusion plus ISR jet

(b) vector boson fusion

Figure 5.2: Example diagrams for different heavy Higgs production modes with monojet signatures.

Ref. [259] from visible heavy Higgs decays. As explained in the previous section, we concentrate on regions with $m_{Z'} > 65\,\text{GeV}$ to avoid the tight constraints from invisible h decays.

As the decay width $\Gamma_{H\to Z'Z'}$ grows proportionally to $\tilde{g}^2$, the size of this coupling crucially defines the order of magnitude of the resulting invisible branching ratio. It ranges from less than one percent in case of $\tilde{g} \leq 0.05$ to beyond 90 % for $\tilde{g} \geq 0.5$. For m_H larger than 250 GeV, $H \to hh$ decays are kinematically allowed which leads to a sizable reduction of the decay rate into Z' pairs beyond this threshold.

For certain ranges of m_H, most importantly $m_H \approx 200, 250, 320\,\text{GeV}$, results from visible heavy scalar searches require an invisible branching ratio of at least 15 % for $\sin\alpha = 0.3$ and 40 % for $\sin\alpha = 0.4$. This excludes large regions of parameter space for $\tilde{g}$ below 0.5.

However, for larger couplings limits from perturbativity — most importantly Eq. (5.6) — become relevant and restrict the theoretical parameter space with too light $m_{Z'}$. While this largely reduces the viable mass regions for $\sin\alpha = 0.4$ it only plays a minor role for the $\sin\alpha = 0.3$ scenario. Here, for e.g. $\tilde{g} = 0.5$ practically no restrictions on the kinematically allowed mass combinations of m_H and $m_{Z'}$ are set. For larger $\tilde{g}$, however, only heavy $m_{Z'}$ are allowed, as the required hidden vev $z = \sqrt{2}m_{Z'}$ would otherwise be too small to reach $m_H = \mathcal{O}(200\,\text{GeV})$ with perturbative couplings in Eq. (2.47).

We therefore find that for our considered Higgs Portal model with a heavy Z' and a sizable mixing of $\sin\alpha = 0.3$ a wide range of invisible branching ratios between 20–95 % is still allowed and uncovered by existing experimental searches for visibly decaying heavy scalars. It therefore seems plausible to analyse the LHC sensitivity to invisible decays of H to hopefully fill the remaining gaps observed in Fig. 5.1.

5.4 Future Limits from LHC Monojet Searches

As outlined before, we are mostly interested in the parameter region with a large probability of eventually produced heavy scalar particles to decay invisibly — a collider signature which commonly appears in models with WIMP dark matter particles (see e.g. Ref.[268] and references therein). Since a fully invisible final state would not be triggered by the detector, collider searches typically require the existence of one high energetic jet, photon or gauge boson from the initial state. This often results in a boost of the mediator particle, in our case the heavy scalar, and hence yields a larger amount of missing energy in the event which improves the distinguishability from Standard Model background. In the following, we focus on the case with a single jet, often called *monojet search*. Another interesting channel would be the specific signature of two jets with a large rapidity gap as it appears in the vector boson fusion process.

Cut	M1	M2	M3	M4	M5
lepton veto			yes		
$N_j(p_T > 30\ \text{GeV}, \lvert\eta\rvert < 2.8)$			≤ 3		
$\Delta\phi(\vec{p}_{\text{jet}}, \vec{p}_T^{\text{miss}})$			> 0.4		
p_T(leading jet) in GeV	≥ 280	≥ 320	≥ 450	≥ 500	≥ 550
E_T^{miss} in GeV	≥ 220	≥ 320	≥ 450	≥ 500	≥ 550

Table 5.1: Selection cuts used for the $\sqrt{s} = 14$ TeV monojet analysis.

This signature has been analysed in more detail within Ref. [269] and comparable sensitivities can be achieved.

5.4.1 8 TeV Results and 14 TeV Analysis Implementation

Existing limits on $\sigma_{pp\to H} \times \text{BR}(H \to \text{inv.})$ which can be derived from ATLAS [185, 270] and CMS [237] monojet searches lie above the total production cross section $\sigma^{\text{SM}}_{pp\to h(m_h=m_H)}$ for heavy scalars of a given mass (see e.g. Ref. [271]). As our model predicts a $\sin^2(\alpha)$ reduced production rate and only a fractional invisible branching ratio, the existing searches are clearly not sensitive. In this study, we examine to what extent the Higgs Portal can be probed by the LHC if it runs at its full center of mass energy of 14 TeV which increases the probability to produce high energetic jets in the final state. For that purpose, we use `CheckMATE` and translate the existing 8 TeV study to 14 TeV to estimate the future sensitivity[2].

As a template of the 14 TeV analysis we used the existing ATLAS monojet study in Ref. [270][3]. We implemented the relevant kinematic selection cuts of all the signal regions into `CheckMATE` by making use of the `AnalysisManager` as explained in Section 4.5. These regions demand a lepton veto and at most three high energy jets with $p_T > 30$ GeV. It is important to note that the latter constraint means that in addition to the hard signal monojet two further soft jets are allowed in the event. This is why not only gluon fusion plus with initial state radiation (see Fig. 5.2a) but also vector boson fusion signatures (see Fig. 5.2b) provide an important contribution even though strictly speaking the second do not yield *mono*jet final states.

An additional requirement is imposed on the azimuthal angle between the missing transverse vector and the jets, $\Delta\phi(\vec{p}_{\text{jet}}, \vec{p}_T^{\text{miss}}) > 0.4$, in order to suppress QCD multijet background. The events which pass these constraints are categorised according to three signal regions M1 to M3 with increasing requirements on the transverse momentum of the leading jet and the total missing transverse energy of the event. Two more signal regions, M4 and M5, with even tighter constraints on these parameters were defined in addition to account for the possibility that monojet searches at higher center of mass energy could have an impoved sensitivity for higher energies than could be reached for 8 TeV. A combined list of all signal regions' definitions is given in Table 5.1.

[2] The analysis implementation into `CheckMATE` and the generation of Monte Carlo samples for signal and $t\bar{t}$ background has been performed by Jong Soo Kim

[3] The more recent monojet study Ref. [185] was published after the main work for this project had been completed.

5.4.2 Background Expectation

The dominant Standard Model contribution to the monojet signature are the associated production of gauge bosons bosons and an initial state jet. Most importantly, Z bosons decaying into neutrinos or W bosons decaying into a neutrino and a hadronically decaying tau or unidentified electrons and muons have to be considered as they lead to events with a large amount of missing energy. An additional small but non-negligible contribution is the production of $t\bar{t}$ pairs. Single top channels can also populate the given signal regions but can be neglected compared to the other background sources (see e.g. the corresponding numbers at 8 TeV in Ref. [270]). For the same reason, we have neglected decays of Z/γ^* into charged leptons, diboson production as well as QCD multijet backgrounds. All these backgrounds are sufficiently well reduced by applying the cuts in Table 5.1.

We numerically estimate the dominant SM backgrounds as follows: The Wj and Zj backgrounds are generated with `Sherpa2.1.1` [146] including up to 3 partons with `CTEQ10` PDF [272]. The $t\bar{t}$ background has been simulated with `POWHEG2` [273] and the parton level events were passed to `Pythia6.4.25` [147] with `CTEQ6L1` parton distribution function [132]. The $t\bar{t}$ cross section has been determined with `Top++2.0` [274]. The respective numbers of events after the event selection via `CheckMATE` are listed in Table 5.2. The same numbers for $\sqrt{s} = 8\,\text{TeV}$ were determined and sufficient agreement with the results in Ref. [270] was found.

5.4.3 Signal Generation

The only model parameter relevant for the Monte-Carlo based part of our collider phenomenological study is the mass of the heavy scalar as it directly affects the kinematics of the event, that is the jet momenta and the total amount of missing energy. Other parameters, like $\sin\alpha$ and $\tilde{g}$ only affect the overall production and decay rate and results can easily be rescaled by making use of Eqs. (5.14) and (5.17).

We have generated the parton level signal events for various H masses within the `POWHEG2` framework [275–277] which then have been passed to `Pythia6.4`. As shown in Fig. 5.2, we considered both production via the dominant gluon fusion channel $gg \to Hg$ [278] and the subdominant but still sizable vector boson fuction process $qq \to qqH$ [279]. We assume an on-shell production of the heavy singlet like scalar to avoid complications due to off-shell interference effects. An interesting study which proposes a different signature to make use of these effects can be found in Ref. [280].

We have omitted the associated vector boson production channel $q\bar{q} \to W/ZH$ as it has negligible cross section compared to the others. The cross sections for the various signal production modes have been taken from Ref. [263]. Final event numbers for $\sqrt{s} = 8\,\text{TeV}$ were validated against the results on invisible Higgs decays from Ref. [185]. The final numbers for our $\sqrt{s} = 14\,\text{TeV}$ study are listed in Table 5.2 for a specific benchmark scenario. We also calculate the significance measure $S/\sqrt{B}$ which provides a na¨ive indicator for a possible sensitivity of a given analysis if its numerical value exceeds 1.

5.5 Results

5.5.1 Expected Signal and Background Event Numbers

In Table 5.2 we list our numbers for all background sources and one example signal benchmark point. As expected, the background is dominated by Z+jets, followed by W+jets and only

SR	Zj	Wj	$t\bar{t}$	total	example signal	$S/\sqrt{B}$
M1	2,378,934	2,024,466	67,821	4,471,221	5597	2.6
M2	742,710	442,296	13,327	1,198,333	2065	1.9
M3	207,804	102,852	2,656	313,312	638	1.1
M4	80,730	30,036	1,118	111,884	398	1.2
M5	33,252	11,610	625	45,487	251	1.2

Table 5.2: Number of background and signal events for all signal regions M1 to M5 at the LHC with $\sqrt{s} = 14$ TeV and an integrated luminosity of 600 fb^{-1}. The signal was calculated for the benchmark case $m_H = 200$ GeV, $\sin\alpha = 0.3$ and BR($H \to$ inv.) $= 0.75$. In the last column, we have estimated the statistical significance with $S/\sqrt{B}$.

minor contributions from $t\bar{t}$ due to the restriction on the number of high energetic jets. For the given signal benchmark, signal region M1 appears to be the most dominant with $S/\sqrt{B}$ of roughly 2.6. The discussed monojet search would therefore be very sensitive to that particular benchmark scenario.

It must be noted that no systematic error on the background has been considered here and in the upcoming results. This renders the sensitivity lines shown in the following as overly optimistic approximations. Due to the large event rates, especially in region M1 with a rather mild monojet cut, the statistical error is considerably small and as such even tiny systematic uncertainties are expected to have an impact on the signal sensitivity. However, at the current stage it is difficult to quantify the accuracy of ATLAS in the far future. We therefore show limits without assuming systematic uncertainties for now and come back to the discussion of their possible impact at the end of this chapter.

5.5.2 Dark Sector Independent Limits on $\sin\alpha$ and BR($H \to$ inv.)

We start the discussion of the expected sensitivity to the Higgs Portal independently of the details of the dark sector. That means we only consider the limits on the invisible decay of a heavy Higgs-like scalar, regardless of the actual decay mode and its parameter dependence. In Fig. 5.3a, we present our determined 95% C.L exclusion limits for BR($H \to$ inv.) as a function of the mass m_H of the heavy scalar for an integrated luminosity of 600 fb^{-1}. The limits have been determined by using the CL$_S$ test implemented in `CheckMATE` and we choose the strongest limit from the given five signal regions.

We choose the same two benchmark values for $\sin\alpha$ as in the previous discussion, which will affect the expected number of produced heavy scalars in our model. Conversely, in Fig. 5.3b, we fix the invisible branching ratio to three benchmark values and show the respective limits on $\sin\alpha$. In both plots, we again draw the existing limits from the search for heavy Higgses at CMS discussed in Section 5.2.2. However, as we do not specify the details of the invisible decay yet (i.e. $\tilde{g}$ and $m_{Z'}$), no general perturbativity limit can be infered and therefore no equivalent lines are drawn at this stage.

We observe that for a general heavy Higgs scenario with a $\sin^2(\alpha)$ reduced production cross section the discussed monojet search would be sensitive to invisible branching ratios down to 70% for $\sin\alpha = 0.3$ and 40% for $\sin\alpha = 0.4$ for rather light $m_H \approx 180\,\text{GeV}$. Heavier H are less often produced and therefore are less constrained. This leads to a maximum sensitivity limit

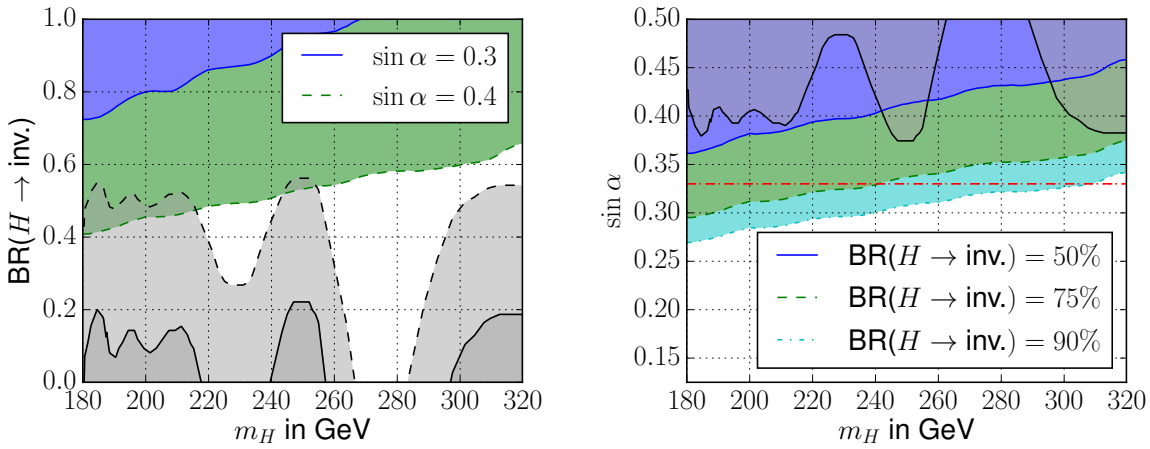

(a) Limit on $\mathrm{BR}_{\mathrm{inv}}$ for fixed $\sin\alpha$.

(b) Limit on $\sin\alpha$ for fixed $\mathrm{BR}_{\mathrm{inv}}$.

Figure 5.3: Expected future 95% CL limits on invisible heavy Higgs decays via monojet events at $\sqrt{s} = 14$ TeV with an integrated luminosity of 600 fb^{-1}. Coloured regions correspond to the excludable region for a particular value of $\sin\alpha$ (a) or BR($H \to$ invisible) (b). Grayed regions correspond to existing CMS limits from heavy Higgs searches. In (a), the dashed (solid) contoured grey region corresponds to the CMS limit if $\sin\alpha = 0.3$ (0.4) is assumed. In (b), the area bounded by a solid line corresponds to the visible heavy Higgs limit for an invisible branching ratio of 50 %. The corresponding lines for 75 % and 90 % lie outside the visible range. Here, the red dot-dashed line denotes the $\sin\alpha \leq 0.33$ limit from Standard Model Higgs measurements.

for m_H determined by the point at which $\mathrm{BR}(H \to \mathrm{inv.})^{\mathrm{min}} \geq 1$. As can be seen in Fig. 5.3a, a value of 0.3 for $\sin\alpha$ can be sensitive to heavy Higgs masses up to 270 GeV, whereas the entire considered m_H range $180 - 320\,\mathrm{GeV}$ would be covered for $\sin\alpha = 0.4$

For fixed invisible branching ratio of the heavy scalar, mixing angles down to $\sin\alpha \approx 0.27$ can be tested for an almost entirely invisibly decaying heavy scalar. If we take into account the above mentioned limit on $\sin\alpha \lesssim 0.33$ from combined Standard Model Higgs measurements, one finds that the invisible branching ratio must be of order 75 % or beyond and the heavy scalar lighter than 310 GeV in order to improve on the existing limit. This is why we chose not to analyse heavier mass values.

5.5.3 Dark Sector Dependent Limits on $\tilde{g}$ and $m_{Z'}$

As illustrated in Section 5.3, a fixed invisible branching ratio can ambiguously be constructed from different combinations of the dark gauge coupling $\tilde{g}$ and the dark gauge boson mass $m_{Z'}$. We therefore show limits on one parameter by fixing the other to well chosen benchmark values. For translating limits on the branching ratio into bounds on the coupling constant $\tilde{g}$, we choose the dark gauge boson mass according to the following three benchmark cases:

- $m_{Z'} = 65\,\mathrm{GeV}$, which is the lightest possible value to evade $h \to Z'Z'$ constraints,
- $m_{Z'} = \frac{1}{4} m_H$ corresponding to an intermediate mass[4] and

[4] Strictly speaking, limits for this scenario are only meaningful for $m_H > 260\,\mathrm{GeV}$ as for lighter m_H the corresponding $m_{Z'}$ is below the 65 GeV threshold.

- $m_{Z'} = \frac{1}{2} m_H - 5\,\text{GeV}$, chosen to be very close to the kinematic threshold for $H \to Z'Z'$.

Alternatively, when showing limits on the mass $m_{Z'}$ we fix $\tilde{g}$ to the three benchmark values $0.25, 0.5$ and 0.75. Note that these are chosen differently to those in the earlier analogous plot in Fig. 5.1. The explanation is given by the results of the previous paragraph which showed that we require an invisible branching ratio of at least 40 % in order to be sensitive to our given model. It is clear from the results shown in Fig. 5.1 that this cannot be achieved for too small dark gauge couplings below 0.1.

Analogously to Fig. 5.1 we translate the existing limits from visibly decaying scalars into the same parameter planes. Furthermore, with all parameters being known, we can show the perturbativity limits in addition.

The resulting limits are shown in Fig. 5.4, again for the two benchmark cases for $\sin\alpha$. For the still viable and therefore more interesting case of $\sin\alpha = 0.3$ one finds that within the perturbatively allowed areas the high luminosity monojet search can cover important regions of parameter space down to $\tilde{g} = 10^{-1}$ and up to $m_{Z'} = 120\,\text{GeV}$. This would put important complementary bounds combined with those from searches for visibly decaying Higgs boson. Regarding the general sensitivity to the heavy scalar mass, an upper cutoff at 250 GeV can be observed. For m_H beyond this threshold, $H \to hh$ decays reduce the invisible branching ratio, see Fig. 5.1. The required change of parameters to make up for this loss of branching ratio would push the theory into a dangerously unperturbative region and/or require a gauge boson mass below the $h \to Z'Z'$ threshold.

If we compare the overlap of these expected invisible monojet bounds to the existing visible Higgs decay limits, we find that at first sight a large region of parameter space would still be covered by neither of the two. However, a high luminosity LHC will most likely significantly push the lower limits on $\tilde{g}$ from visible decays, if we assume that still no deviation from the Standard Model will be found in the far future. Also, as 8 TeV results are not far away from being sensitive to $H \to hh$ decays, with enough data being taken the high luminosity LHC could cover regions beyond the $m_H = 250\,\text{GeV}$ threshold by looking for these final states. All in all, we can expect a good coverage of the high luminosity LHC on the Higgs Portal model by combining results from various channels.

5.5.4 Impact of Systematic Uncertainties

As mentioned before the shown limits only consider statistical uncertainties due to Poisson statistics of the data and no contribution from systematic uncertainties. Therefore, the expected sensitivities are overoptimistic and a proper consideration of the background uncertainties will most likely lead to a reduced coverage to the Higgs Portal parameter space. To estimate the required systematic accuracy for our given results to hold, let us use as an example the event rates of background and benchmark signal model in Table 5.2. Here we saw that signal regions M4 and M5 have a significance of roughly 1, with a value of 2 being a target value close to the 95 % confidence limit. The respective signal rates are of the order 0.5 % of the expected background. It follows that the systematic uncertainty of the background expectation should be at the sub-percent level in order to not weaken the given confidence limits significantly.

From the updated monojet search performed on 8 TeV data in Ref. [185], the total systematic uncertainty on the background estimate ranges from 2.7 % to 6.2 % for those signal regions with similar selection cuts than in Table 5.1. Potential for improvement could be anticipated for measurements of lepton reconstruction and tracking isolation efficiencies due to the larger

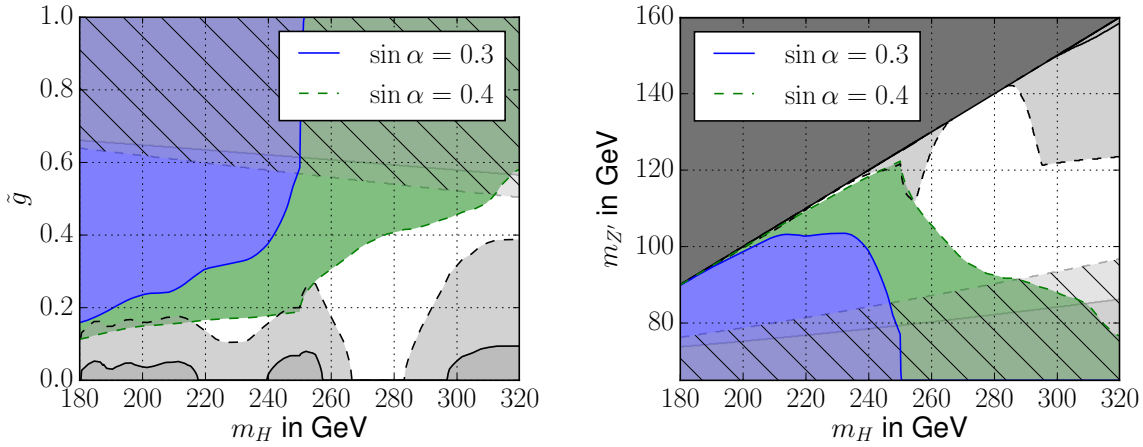

(a) $m_{Z'} = 65\,\text{GeV}$ (b) $\tilde{g} = 0.75$

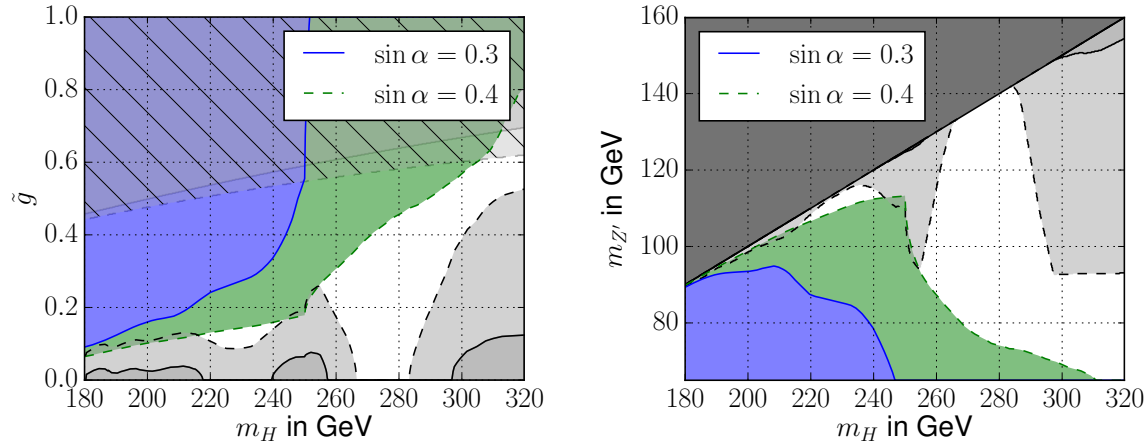

(c) $m_{Z'} = \frac{1}{4}m_H$ (d) $\tilde{g} = 0.5$

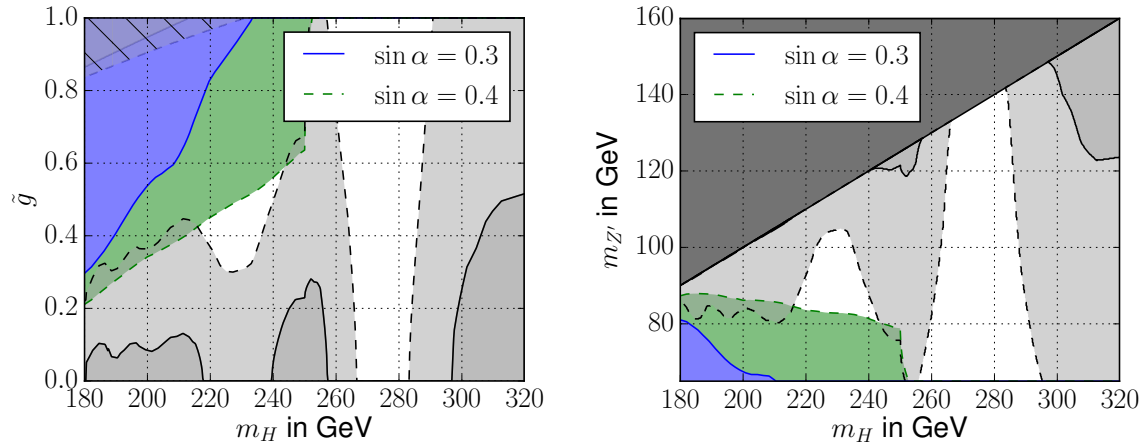

(e) $m_{Z'} = \frac{1}{2}m_H - 5\,\text{GeV}$ (f) $\tilde{g} = 0.25$

Figure 5.4: Expected future 95% CL limits on $\tilde{g}$ and $m_{Z'}$ from monojet events at $\sqrt{s} = 14$ TeV with an integrated luminosity of 600 fb^{-1}. The left column shows limits on $\tilde{g}$ for three different choices of $m_{Z'}$ and vice versa in the right column. The colouring scheme is the same as in Fig. 5.1, with the blue (green) shaded area bound by a solid (dashed) line showing the sensitivity region of the monojet search for $\sin\alpha = 0.3(0.4)$.

amount of available data at a high-luminosity LHC and thus an improved accuracy of data-driven background estimate techniques. By a similar argument, measurements of lepton energy uncertainties and calibration of the $\not{E}_T$ vector could also improve on long term. Lastly, QCD uncertainties which strongly affect the estimate of the $t\bar{t}$ background might be reduced from the theory side by improved higher order calculations included in the respectively used event generators. Clearly, the required level of precision for our study would require a challenging level of improvement with respect to these sources, still they do not seem impossible to achieve for the long term LHC.

5.6 Conclusion

Within this chapter, we continued the phenomenological discussion of the Higgs Portal model described in Section 2.2. Such a model would predict an additional scalar particle in the context of a dark sector which does not interact with the Standard Model particle content and designed to solve the dark matter problem by predicting a massive dark gauge boson. It is the scalar field of that sector which can mix with the Standard Model Higgs field and thus yield two scalar particles which can both interact with the Standard Model and the hidden gauge boson. We focussed on the case where the lighter of the two is the Standard Model like Higgs particle and summarised the most relevant constraints from theory and experiment, most importantly from measurements of Standard Model Higgs decays and searches for visibly decaying heavy Higgs-like particles. We then discussed the future sensitivity of a high luminosity LHC to this model by searching for invisibly decaying heavy scalars produced in association with a hard jet from the initial state.

We showed that for a sizable mixing of $\sin\alpha = 0.3$, which is in agreement with current combined limits on Standard Model Higgs observables from ATLAS and CMS during the first LHC run, the described analysis could be sensitive to heavy scalars up to a mass of 250 GeV with an invisible branching ratio as low as 70 %. For an almost entirely invisibly decaying heavy scalar, mixing angles down to $\sin\alpha = 0.27$ can be probed. If the invisible decay is caused by the coupling to a heavy gauge boson of the dark sector which gained its mass via spontaneously breaking a hidden $U(1)_X$ gauge group, these limits could would be sensitive to gauge couplings of that dark gauge group of 0.1 or higher or alternatively dark gauge boson masses below 105 GeV. These bounds would be complementary to those from visible decay searches which typically limit small invisible branching ratios, however would require a significant reduction of the systematic error of the background estimate.

CHAPTER 6

Natural NMSSM Decay Chains at the LHC

In Section 2.5 we introduced the concept of a natural next-to-minimal supersymmetric Standard Model, or NMSSM. This extension of the MSSM with an extra gauge singlet superfield $\widehat{S}$ creates an effective dimensionful parameter μ_{eff} by giving a vev z to the scalar component S. This naturally causes μ_{eff} to be of the electroweak scale as it should be according to the conditions on the Higgs potential, see Eq. (2.108), and therefore solves the μ-problem of the MSSM. This results in higgsino and singlino masses of a few hundred GeV, as shown in Section 2.5.3.

Furthermore, due to mixing with the extra singlet scalar the Standard Model like Higgs boson mass can reach its experimentally observed value of 125 GeV, see Eq. (2.116), without requiring large radiative corrections from heavy scalar top partners. This is appreciated since stop masses beyond approximately 1 TeV create unnaturally large corrections to the parameters of the Higgs potential, see Eq. (2.93), and are hence expected to be light in a natural theory. Similar arguments could be formulated for the gluino and, since it is located in the same $SU(2)_L$ doublet as the stop, also for the sbottoms. Since none of the other SUSY partners are required by naturalness principles to be light enough to be seen at the LHC, we simply decouple these from our spectrum in this study.

Such a natural spectrum results in a very characteristic signature for a collider experiment. In this chapter, we analyse how a combined analysis of various search channels from the 8 TeV LHC run can put constraints on the natural NMSSM as we defined it above. We are particularly interested if the differences we expect with respect to the MSSM, namely an additional particle in the decay chain, improves the limit due to a higher final state multiplicity or worsens the limit due to the associated objects having smaller momentum. In Section 6.1 we start with a short summary of previous studies in the context of natural Supersymmetry. We explain the benchmark scenarios of our study in Section 6.2 and our analysis procedure in Section 6.3 before discussing the results in Section 6.4.

The analysis and the corresponding results of this chapter have been published in Ref. [281] and consequently we draw heavily from this source. This project had been published before the LHC started taking new data at a higher centre-of-mass energy of 13 TeV and therefore only focusses on 8 TeV results. We will briefly mention the impact of updated results in the following summary of existing limits in Section 6.1.

6.1 Motivation

In the context of the MSSM, naturalness is now used as a guiding principle for many LHC searches to find gluinos, stops and/or sbottoms. At 8 TeV, these studies already set various combined bounds on the masses of these particles but with a strong dependence on the considered decay chains. A general summary of the Run 1 mass limits for a representative sample of

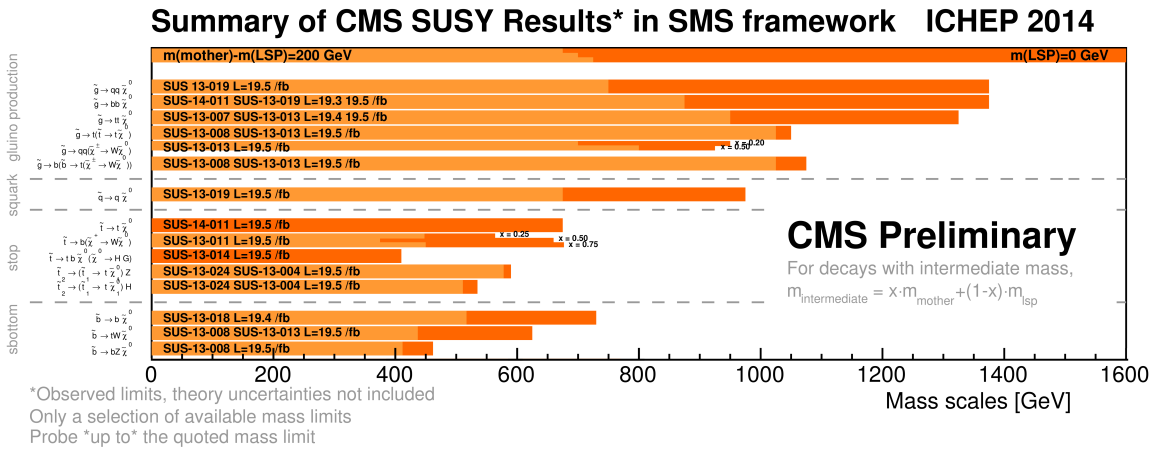

(a) CMS [282]

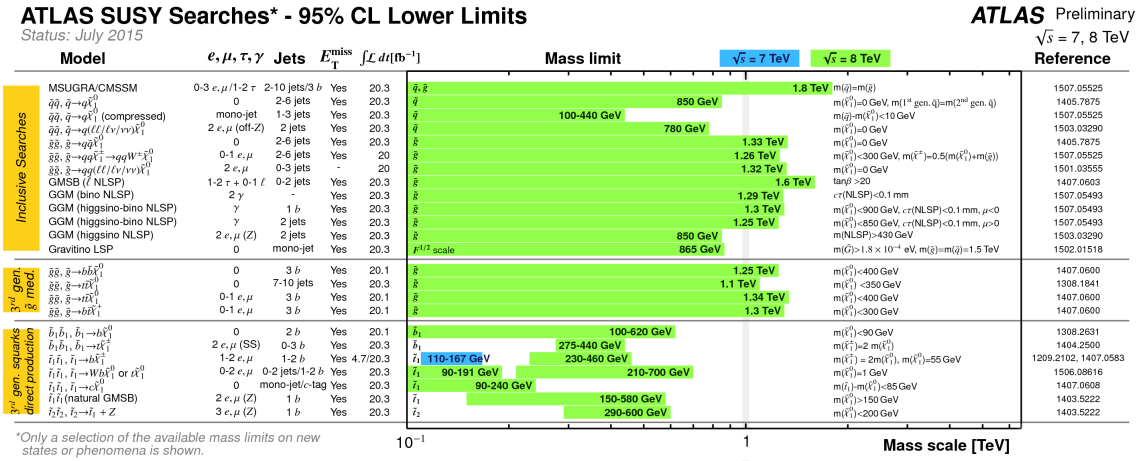

(b) ATLAS [283]

Figure 6.1: Overview of limits on SUSY masses for (a) CMS and (b) ATLAS from LHC Run 1. Note that CMS limits are given without consideration of the theoretical uncertainty while ATLAS quotes the observed limits minus 1σ theory cross section error. To reduce size, the tables have been cropped to mainly show limits on gluino, stop and sbottom masses. Full versions and further links to the corresponding publications can be found under the respective quoted references.

benchmark decay scenarios can be found in Fig. 6.1. For the gluino, lower limits range between 700 GeV for a rather degenerate gluino-NLSP-LSP scenario up to almost 1.4 TeV in case of a direct gluino decay into two quarks and a massless LSP neutralino. An exhaustive summary of all ATLAS searches for strongly coloured SUSY particles can be found in Ref. [182] and a summary of CMS limits on various simplified topologies in Ref. [282]. One finds that the best-case limit also holds for decays with intermediate stop squarks which typically happens in natural setups where these particles are light. The lower gluino mass limit can be as low as 500 GeV for a sufficiently degenerate mass spectrum which can be identified with monojet signatures [284].

The first results from the 13 TeV run with an integrated luminosity of only about $3\,\text{fb}^{-1}$ already improve the best-case lower limits to above 1.5 TeV for decays into light quarks and 1.6 TeV for decays into top quark pairs plus a light neutralino LSP [232–234, 285, 286]. The LHC is expected to be sensitive to gluinos as heavy as 3 TeV in the long term [287, 288] which would already be in very strong tension with naturalness arguments as we discussed in Section 2.4.2.

The situation is similar for the squarks of the third generation, for which again a representative overview can be found in Fig. 6.1 and a more detailed Run 1 summary in Refs. [222, 282]. Best-case lower limits from the LHC 8 TeV run reach almost $m_{\widetilde{t}_1} \geq 700$ GeV for a dominant decay mode $\widetilde{t}_1 \to t\widetilde{\chi}_1^0$ and $m_{\widetilde{t}} \gtrsim 500$ GeV if an intermediate chargino is present, i.e. $\widetilde{t}_1 \to b\widetilde{\chi}_1^+, \widetilde{\chi}_1^+ \to W^+\widetilde{\chi}_1^0$. Again, if the spectrum is compressed, the bounds weaken significantly and the limit drops to stop masses only slightly above the Standard Model top quark mass. Furthermore there are sensitivity gaps in regions of parameter space where the stop is only slightly heavier than the neutralino and the top it decays into. Then, due to the small available energy in the event no limit can be set at all since the kinematics very closely resemble the SM $t\bar{t}$ background but with a substaintially smaller production cross-section [222, 289–292]. Sbottom limits are similar to those of stops, i.e. up to $m_{\widetilde{b}} \geq 650$ GeV for light $\widetilde{\chi}_1^0$ and $m_{\widetilde{b}} \geq 250$ GeV in compressed regions, but are typically more robust and do not contain holes as we move across the mass plane [222, 293–295].

At 13 TeV, limits have again slightly improved to up to 800 GeV for stops and sbottoms in the optimal channels and sensitivities beyond 1 TeV are expected for the high luminosity LHC [287, 288].

Whilst the Higgs mass plays an important role in determining the feasible masses of the third generation squarks in the MSSM, these two sectors become more decoupled in the NMSSM where the mixing with the extra singlet loosens the constraints on the stop mass. In addition, the above limits can be expected to be different in the NMSSM due to the presence of the light singlino in the spectrum. As the singlino does not couple directly to the squarks the singlino is not expected to appear as an intermediate step in any SUSY decay chain as the branching ratios of squarks and gluinos into MSSM-like neutralinos and charginos will by far dominate. It is only when the singlino is the LSP when the MSSM-like NLSP will decay into it as it this would be the only allowed decay mode, hence adding another step to the decay chain which could change the final state efficiency.

An exhaustive overview of LHC signatures of the NMSSM can be found in Ref. [296]. Studies of the NMSSM with light stops [297, 298], sbottoms [299], gluinos [300], electroweakinos [301, 302] or light extra scalar particles [303–308] have been performed within various benchmark setups of the NMSSM. Efforts to establish methods to differenciate MSSM and NMSSM can be found in Ref. [309].

Since natural Supersymmetry has been exhaustively tested by both ATLAS and CMS in the context of the MSSM, the question arises how these limits behave if the model is promoted to the NMSSM. This question has been first studied in Refs. [310, 311] and there it has been shown that limits on MSSM models with high scale unification are always weakened if an extra singlino LSP is added to the decay chain. The extra decay step reduces the momentum of the visible particles as well as the missing energy of the event which reduces the distinguishability from Standard Model background and thus decreases the sensitivity.

However, their constrained scenarios typically result in spectra with light squarks and bino/wino-like neutralinos and thus the typical LHC signatures involve multijets, leptons and missing energy. As we discuss in Section 6.2, a natural spectrum is typically associated with light third generation squarks which produce a significant amount of b-jets in the final state. The presence of b-jets might already be distinctive enough such that the additional leptons or jets produced through the additional decay step might improve the limit even though the final state is softer as in Refs. [310, 311]. Also, since our natural setup involves higgsino-neutralinos, NLSP-to-LSP decays are expected to produce Higgs bosons if the mass splitting is high enough and as such extra b-jets from $h \to \bar{b}b$ could also lead to an improved sensitivity.

The guiding question of this study is therefore whether the statement of Refs. [310, 311], i.e. that the presence of a singlino LSP weakens the limit due to a softer final state, also holds for natural NMSSM setups or if here the additional final state particles in fact improve the MSSM bounds.

6.2 Spectrum and Decays in the Natural NMSSM

We distinguish two main limits of the NMSSN, steered by the size of the dimensionless coupling parameter λ:

large $\boldsymbol{\lambda \equiv \lambda_L}$ When the coupling λ is large, Eq. (2.116) suggests that we can reach a large enough Higgs mass if $\sin 2\beta$ is large. In our analysis we choose $\lambda = 0.7, \tan\beta = 2$, with the value for λ chosen at the typical maximum possible value which does not run into Landau poles at higher scales (see e.g. Ref. [312]). In this setup, no large radiative corrections are required and as such it is expected that one can keep both stops and sbottoms rather light while still being able to reach the correct Higgs mass. As a consequence all third generation scalars may be kinematically accessible at the LHC. The neutralinos largely mix in this scenario and thus direct decays of coloured scalars into singlets and singlino LSPs are possible [313].

small $\boldsymbol{\lambda \equiv \lambda_S}$ In the case of a very small λ, the Higgs mass which can be derived from Eq. (2.114) is very MSSM like as the singlet-components largely decouple[1]. To maximise the tree level value one needs large $\tan\beta$ just as in the MSSM which is why we define this point via $\lambda = 0.01, \tan\beta = 15$. Large radiative corrections as in Eq. (2.87) are needed which asks for at least one heavy stop. The sparticles of the MSSM sector decouple from the singlet states and experimentally, the only difference between the MSSM and the NMSSM would be sparticle decays into the singlino LSP. Contrarily to the previous case,

[1] For very small λ but fixed μ_{eff}, the scalar vev z must be large which translates into a somewhat unnatural hierarchy $z \gg v_u, v_d$. However, as shown in Section 6.4 it is easier to compare the MSSM and NMSSM in this scenario as they only differ by the presence of a new LSP. This is why we keep this benchmark scenario for our analysis even though it does not quite fulfill the conditions of a natural setup.

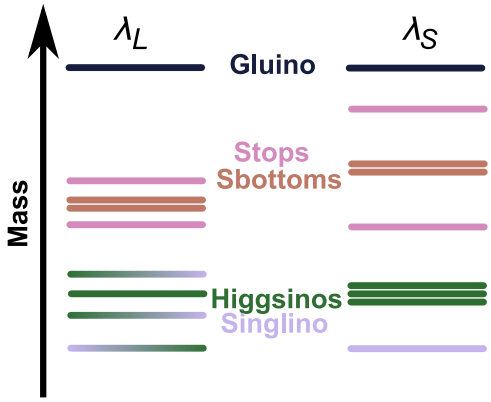

Figure 6.2: Schematical setups of the considered benchmark models λ_S and λ_L, their hierarchies and the respective expected mass splittings and neutralino mixing patterns.

this scenario will come along with a rather split sector of third generation squarks, mostly degenerate higgsinos and a mostly decoupled singlino and a singlet scalar sector.

The resulting hierarchies of both scenarios are schematically pictured in Fig. 6.2: to avoid having an LSP–like chargino, we always require the singlino to be lighter than the higgsinos. Furthermore, we always require the gluino to be heavier than the stops to avoid the consideration of loop-induced 2–body or off-shell 3–body decays. Whilst the relative hierarchy between stops/sbottoms and the higgsinos is not fixed by our setup, we will nevertheless find that it is often as depicted.

6.2.1 Signatures of Interest

The spectrum described in the previous section leads to interesting signatures for the LHC: due to the light $\tilde{t}$ and $\tilde{b}$ scalars we expect final states with many t and b quarks. The hadronised jets originating from b–quarks have a high probability of being correctly tagged as b-jets as explained in Section 3.3.2 and many analyses from both ATLAS and CMS have been designed to specifically tag final states with these objects as discussed below in Section 6.3.2. In the following we only focus on final states with these objects and neglect other signatures:

In this work, we consider third generation squark and gluino hadro-production via the strong interaction. In general, the gluon fusion diagrams will be the dominant production channel for not too heavy gluino and third generation scalar masses and the cross section is only determined by the respective mass of the respective final state sparticle,

$$pp \to \tilde{g}\tilde{g}, \quad \tilde{t}_i\tilde{t}_i^*, \quad \tilde{b}_i\tilde{b}_i^* \qquad i \in \{1,2\}. \tag{6.1}$$

Here, we have omitted the production of electroweakino pairs since the cross section is negligible compared to the production of coloured sparticles unless the higgsino and the singlino are the only kinematically accessible sparticles at the LHC [301, 302] — a scenario we are not going to assume. In addition, we have not considered compressed spectra where a hard initial state radiation jet has to be taken into account. As here the sensitivity is given by the ISR jet, we expect the bounds to be very similar for MSSM and NMSSM.

Let us now turn to the discussion of the decay modes. The decay chains can be very complicated in natural SUSY and typically depends on the details of the mass spectrum and the

mixing angles. Since we define that the gluino is always the heaviest sparticle in our setup, the following strong two body decay modes are the dominant gluino decay channels

$$\tilde{g} \to \tilde{t}_i t_i, \quad \tilde{b}_i b_i \qquad i \in \{1, 2\}. \tag{6.2}$$

There is no tree level coupling between the squarks and the singlino in the NMSSM and thus the decays to neutralino states with a significant singlino component are suppressed. As the λ_S scenario contains an almost pure singlino LSP, direct decays of the squarks to the LSP very rarely occur. Even in the λ_L scenario, which can contain an LSP that is a higgsino-singlino mix, the large singlino component significantly suppresses the direct decay to this state. This situation is different to the natural MSSM where stop decays into the LSP are common and consequently we expect longer and more complicated decay chains in the natural NMSSM. A by-product of such longer decay chains is that the individual particles produced are necessarily softer and E_T^{miss} can be expected to be reduced.

However in common with the natural MSSM, the sparticles decay into final states with third generation SM quarks which gives rise to a high b-jet multiplicity,

$$\tilde{t}_i \to \widetilde{\chi}^0_{2/3} t, \quad \widetilde{\chi}^+_1 b, \tag{6.3}$$

$$\tilde{b}_i \to \widetilde{\chi}^0_{2/3} b, \quad \widetilde{\chi}^-_1 t. \tag{6.4}$$

In addition, the large expected squark mass splittings in the λ_S scenario can lead to the following squark-to-squark decays with additional gauge bosons and Higgs scalars

$$\tilde{t}_2 \to \tilde{t}_1 X^0, \quad \tilde{b}_i X^+, \tag{6.5}$$

$$\tilde{b}_2 \to \tilde{b}_1 X^0, \quad \tilde{t}_1 X^-, \tag{6.6}$$

with $X^0 \in \{Z^0, h, H, H_3, A_1, A_2\}$ and $X^\pm \in \{H^\pm, W^\pm\}$. As the production rate of the heavy squarks in such a case is largely suppressed compared to $\tilde{t}_1/\tilde{b}_1$, this decay is however not expected to contribute significantly to the observed event rates.

The biggest difference between the natural MSSM and the natural NMSSM is that we can now have a singlino LSP. This leads to additional decays of the now NLSP higgsinos $\chi^0_{2/3}$ such as,

$$\widetilde{\chi}^0_{2/3} \to \widetilde{\chi}^0_1 X^0 \tag{6.7}$$

$$\widetilde{\chi}^\pm_1 \to \widetilde{\chi}^0_1 X^\pm. \tag{6.8}$$

Generally, a light singlino is accompanied by relatively light singlet scalars. Depending on the mass difference between the NLSP and the LSP and the mass of the decay products X, differences between the MSSM and the NMSSM will arise, which may modify the decay patterns of the higgsino in a MSSM scenario.

Of course, for each of the above listed decays there exists a mode with all involved particles charge conjugated. Obviously the listed decay modes are only possible subject to kinematic constraints and all decay modes mentioned above can have a related three (or four) body decay mode if one (or more) of the final state particles are virtual.

We have not listed the tediously large list of possible decays for the neutral scalars {h, H, H_3, A_1, A_2}. These generally involve Standard Model like Higgs decays, decays of heavy into light scalars and decays of heavy scalars into pairs of lighter squarks or electroweakinos. However, in

most cases the Higgs mass constraint puts us into the decoupling limit (see Section 2.4.1) and thus the heavy scalars H_3 and A_2 do not appear in the observed decay chains and thus their decay modes are of little relevance in the following discussion. It is mostly the Standard Model like Higgs and the singlet like scalars which are of importance and their decays are practically Standard Model like after having applied the experimental constraints as explained in upcoming Section 6.3.1.

6.3 Model Test Methodology

As described at the end of Section 2.5.5, our natural NMSSM setup can be described by 12 free parameters:

$$\lambda, \kappa, A_\lambda, A_\kappa, \mu_{\text{eff}}, \tan\beta, m^2_{\widetilde{Q}_3}, m^2_{\widetilde{U}^c_3}, m^2_{\widetilde{D}^c_3}, A_t, A_b, M_3. \tag{6.9}$$

To simplify the discussion, we assume a degeneracy[2] of the soft parameters in the third generation, i.e.

$$A_{\tilde{q}3} \equiv A_t = A_b, \tag{6.10}$$

$$M^2_{\tilde{q}3} \equiv m^2_{\widetilde{Q}_3} = m^2_{\widetilde{U}^c_3} = m^2_{\widetilde{D}^c_3}. \tag{6.11}$$

This assumption always fixes the mass of the bottom squarks for given stop masses in a way as depicted in Fig. 6.2. In the following we explain how we fix the free parameters of our model

$$\lambda, \kappa, A_\lambda, A_\kappa, \mu_{\text{eff}}, \tan\beta, A_{\tilde{q}3}, M_{\tilde{q}3}, M_3 \tag{6.12}$$

with respect to the hierarchies of the models we want to consider. We follow with a discussion on how we test the respective parameter combination.

6.3.1 Scan Setup and Definitions

Each of the scan points that we are going to analyse in Section 6.4 is defined by the following phenomenological parameters:

1. The NMSSM scenario λ_S or λ_L,
2. the mass $m_{\tilde{g}}$ of the gluino,
3. the mass $m_{\tilde{t}_1}$ of the lightest stop,
4. the higgsino mass parameter μ_{eff} and
5. the singlino mass parameter $m_{\tilde{S}} \equiv 2\frac{\kappa}{\lambda}\mu_{\text{eff}}$

This fixes the following parameters in Eq. (6.12):

$$\lambda = 0.7 \text{ for } \lambda_L, \qquad 0.01 \text{ for } \lambda_S, \tag{6.13}$$

[2] To be more precise, the degeneracy is assumed to hold at the scale $\Lambda_{\text{SUSY}} = 5$ TeV with the exact choice being of minor relevance for the numerical results. Note that this is also the scale to which we put the decoupled SUSY particles.

$$\tan\beta = 2 \quad \text{for } \lambda_L, \qquad 5 \quad \text{for } \lambda_S, \tag{6.14}$$

$$\kappa = \lambda/2 \cdot m_{\tilde{s}}/\mu_{\text{eff}} \tag{6.15}$$

The remaining five parameters are found as follows: We require a natural, realistic particle content, that is we aim for a spectrum with as light as possible stops while having a Higgs boson at the correct mass. In addition we demand that the Higgs boson passes the most relevant theoretical and phenomenological constraints. Such a spectrum is found by using the public tool `NMSSMTools4.3.0` [111]. This allows us to specify the above mentioned parameters to get the corresponding physical particle masses, mixing matrices, branching ratios and test against a variety of observational tests, see below.

In order to find a parameter combination with a viable, natural spectrum, we perform the following chain of actions:

Loop over the heavy stop mass $m_{\tilde{t}_2}$: We are interested in stops that are as light as possible, i.e. we aim to find the lightest spectrum that passes the most important phenomenological constraints. For that purpose, with $m_{\tilde{t}_1}$ set above, we perform a loop over $m_{\tilde{t}_2}$: Starting from $m_{\tilde{t}_1}+25$ GeV and using a stepsize of 5 GeV, we steadily increase the heavy stop mass and try to find a valid parameter point according to the steps described next. As soon as a valid point is found, that one is taken for the further collider study.

Fix the strong sector M_3, $A_{\tilde{q}3}$, $M_{\tilde{q}3}$: The masses of the stops and the gluino are mostly determined by these three parameters, see Section 2.5.4. Given the target values $m_{\tilde{t}_1}$, $m_{\tilde{g}}$ and the looped value for $m_{\tilde{t}_2}$, we use `NMSSMTools`[3] to scan over M_3, $A_{\tilde{q}3}$ and $M_{\tilde{q}3}$ and find the combination that reproduces the desired masses[4] best. For this scan, the values of A_λ and A_κ are barely of relevance as they have only a minor impact on the third generation stop masses. Consequently they are therefore fixed to the central values of the "scalar sector scan" described below. Note that at this stage we use `NMSSMTools` solely to find the correct mapping of physical masses to parameters. No phenomenological constraints are applied at this stage.

Explore the scalar sector A_λ, A_κ: Having the strong sector fixed we start a new grid scan over the scalar trilinear parameters A_λ, A_κ in order to find a phenomenologically allowed scalar sector. We test A_λ in the range 0 to $2(\mu_{\text{eff}}/\sin 2\beta - m_{\tilde{S}})$, which is chosen such that the central value minimises the negative contribution from higgsino-singlino mixing in Eq. (2.114) and hence maximises the SM-like Higgs boson mass [314]. A_κ is scanned without any prefered scale in the range $[-550\text{ GeV}, 450\text{ GeV}]$.

For each point, `NMSSMTools` tests[5]

- the absence of tachyonic masses,
- whether minima in the scalar potential with any v_u, v_d or $z = 0$ are deeper than the desired one with $v_u, v_d, z \neq 0$,

[3] `NMSSMTools` has been modified to allow scanning over $A_{\tilde{q}3}$ and $M_{\tilde{q}3}$ which the public version does not allow.
[4] The mass calculation performed by `NMSSMTools` first uses 2-loop RGEs to run the parameters from Λ_{SUSY} down to $\Lambda_{\tilde{t}} = M_{\tilde{q}3}$ and then evaluates the pole mass at $\Lambda_{\tilde{t}}$ using next-to-leading order corrections in $\mathcal{O}(\alpha_s)$.
[5] Unfortunately most of the phenomenological constraints are hard-coded by hand without giving proper reference to an original source. Therefore we cannot provide a concise list of all considered experimental bounds and can only refer to the general documentation in Ref. [111] and the website of the code itself in Ref. [315]

- the existence of a $\mathcal{CP}$-even boson in the mass window 121 to 129 GeV[6],
- consistency with all other implemented collider constraints, i.e. LEP, Tevatron and LHC limits on the Higgs, neutralino and chargino sector and
- consistency with all other implemented low energy observables. (e.g. $b \to s\gamma$ and $B_s \to \mu^+\mu^-$)[7].

To consider more recent collider results from LEP, Tevatron and the LHC that constrain the scalar sector, we further use `HiggsBounds 4.1.2` [316] and `HiggsSignals 1.2.0` [317] to perform final tests on the scalar sector of the considered parameter points. `HiggsBounds` is a tool which takes calculated signal strengths of all scalars in a given model and checks whether any of those violates limits from negative Higgs boson searches at LEP, Tevatron and the LHC. We use it with the `LandH` setup, which tests both constraints from lepton and hadron colliders. Any tested parameter combination is discarded if `HiggsBounds` returns "excluded". Complementarily, `HiggsSignals` tests if there is one scalar particle which fulfills the properties of the 125 GeV Higgs boson observed at the LHC. For that purpose we fix the mass uncertainty for all Higgs bosons to be 4 GeV in accordance to the mass window we set above for the `NMSSMTools` scan. We choose the `both` setting which performs both a mass centered and a peak centered method and test against `latestresults`. Here, our parameter point is discarded if it produces a p-value smaller than 0.05.

Exit $m_{\tilde{t}_2}$ scan: If at the end of this stage no allowed A_λ, A_κ combination is left, the $m_{\tilde{t}_2}$ loop starts with the next iteration. If however a parameter combination of M_3, $A_{\tilde{q}3}$, $M_{\tilde{q}3}$, A_λ and A_κ passes all the aforementioned constraints, this parameter point is used for the collider phenomenology part described next.

Note that we use naturalness as the original motivation for setting up the spectrum as explained before. The degree of naturalness can in principle be quantified by determining the dependence of the terms in Eq. (2.88) on the fundamental parameters of the theory [318]. Such a *fine-tuning measure* is however very dependent on the high-scale completion of a given theory and different definitions can yield very different answers, see e.g. Ref. [319, 320]. Since we do not specify how we e.g. re-introduce the decoupled sparticles at a higher scale, we cannot reliably determine the fine-tuning of our model.

6.3.2 Collider Phenomenology

As explained in Section 6.2.1, we assume that pair production of the light $\tilde{g}, \tilde{t}_i$ and $\tilde{b}_i$ dominates the expected signal. Production cross sections for these particles are calculated using `NLLFast 2.1` [163] using `CTEQ6.6NLO` PDF [321], see also Section 3.2.8. Uncertainties due to scale variations, parton density functions and α_s are provided by this tool and we take the quadratic sum of these to set the total theory error $\Delta\sigma$. For each of the five production modes, 50,000

[6] The window for m_h is motivated by theory uncertainties and the fact that the decoupled sector, most importantly the electroweakinos, can influence the Higgs mass by higher order corrections if they are of order $\mathcal{O}$(few TeV), see e.g. [110]. The exact details of the heavy electroweakino sector would not affect our collider analysis at all and thus are incorporated by a looser constraint on the light Higgs boson mass.

[7] Even though implemented, we explicitly skip testing the magnetic moment of the muon as our model is not designed to fix the already existing discrepancy of Standard Model calculation and observation, see also Section 2.1.5

Ref.	CheckMATE identifier	Sensitive to which decay scenario(s)
[322]	atlas_conf_2013_024	$\widetilde{t}_i/\widetilde{b}_i$ decay chains with a purely hadronic final states
[323]	atlas_conf_2013_061	$\widetilde{g}\widetilde{g} \to t\bar{t}\widetilde{t}\widetilde{t}^*, b\bar{b}\widetilde{b}\widetilde{b}^*$ and/or decays involving $h \to b\bar{b}$.
[324]	atlas_conf_2013_062	$\widetilde{t}_i/\widetilde{b}_i$ decay chains with 1 isol. lepton from W/Z
[200]	atlas_1308_2631	$\widetilde{t} \to b\widetilde{\chi}^{\pm}, t\widetilde{\chi}^0$ with a purely hadronic final state
[201]	atlas_1403_4853	$\widetilde{t} \to b\widetilde{\chi}^{\pm}, t\widetilde{\chi}^0$ with an OS isol. lepton pair
[217]	atlas_1404_2500	$\widetilde{g}\widetilde{g}$ with decays into $\widetilde{t}_i/\widetilde{b}_i$ and 2 isol. SS or 3 leptons
[202]	atlas_1407_0583	$\widetilde{t}_i/\widetilde{b}_i$ decay chains with 1 isol. lepton from W/Z

Table 6.1: Summary of the expected most sensitive analyses within CheckMATE to the considered natural model, listed in alphabetical order. All analyses require a significant amount of missing transverse momentum in the final state and have at least one signal region which requires b-tagged jets.

signal events are generated using Herwig++ 2.7.0 [145] with the NMSSM model setting. For practical reasons, decay tables of all relevant particles are calculated within Herwig++, which contains all tree level 2– and 3–body decays and effective implementations of the loop-induced decays $h_i \to \gamma\gamma, gg$.

To test the model against a variety of LHC results, we use CheckMATE. The compatibility of signal and observation is tested by comparing the predicted signal $S \pm \Delta S$ to the model independent 95% CL limit $S95$, determined by using the CL_S method [175], see Section 3.3.3 and Appendix A.2. Here, ΔS considers both the MC error on our statistics as well as the theory error on the total cross sections. CheckMATE considers a large list of ATLAS and CMS analyses, however due to the signatures described in Section 6.2.1 it is expected that only a subset of these will be sensitive to the characteristics of our model. We list these analyses in Table 6.1. They all require a significant amount of missing transverse momentum due to the expected undetected LSP in the final state and have signal regions that check for b–jets. They mainly differ by the final state jet multiplicities and the total amount and relative charge of final state isolated leptons (i.e. electrons and muons). The analyses also differ in the kinematics of the respective signal regions that are designed and tuned for particular final states. As we expect different final state signatures in our model, it is highly favourable to check all these possibilities in parallel and filter out the most sensitive one for each case. Fortunatetly, CheckMATE allows for an easy comparison of that kind.

Let us make some notes here regarding the difference between the list of most sensitive analyses quoted in Fig. 6.1 and the analyses we used in CheckMATE listed in Table 6.1:

- CMS analyses generally seem equally sensitive as the corresponding signatures tested by ATLAS. As CheckMATE uses an ATLAS-focussed detector tuning, we focus on ATLAS analyses in our study.

- Both ATLAS analyses listed to target gluino decays have unfortunately not been used within our CheckMATE model test: analysis 1308.1841 [214] is a general multijet plus missing energy search which is generally sensitive to hadronically decaying gluinos whereas 1407.0600 [218] is a naturalness motivated search which requires at least 3 b-tagged jets as they typically appear from light gluino decays via on- or off-shell third generation squarks. As can be seen from Fig. 6.1b, they can set lower limits on the gluino mass between 1.1 and 1.3 TeV, depending on the considered final state quark flavours. This is

close to the bounds we find in our study, see following Section 6.4.1, using the limited selection in Table 6.1 which mainly uses earlier conference notes with similar signatures. Thus we also expect that for an NMSSM study the sensitivities of these analyses do not differ by much. Note that both analyses shown in Fig. 6.1b have been implemented into the CheckMATE code since the main work of this project has been completed, see Table 4.1.

- Regarding third generation squarks, four of the quoted analyses, i.e. `atlas_1308_2631` [200], `atlas_1404_2500` [217], `atlas_1407_0608` [219] and `atlas_1407_0583` [202], have indeed been used in our study. Analysis `1506.08616` [222] has been published later and was only added to `CheckMATE` after this project was finalised. It combines various older signatures for third generation squark decays and adds some additional signal regions to fill remaining sensitivity gaps. These additional signatures seem indeed to improve bounds on the stop mass from other searches and might also slightly improve the bounds we quote here. Lastly, Fig. 6.1b quotes analysis `1403.5222` [215] to be specifically sensitive to stop - to - stop decay via on-shell Z-bosons and again was added to `CheckMATE` after this project was finalised. However, due to the higgsino nature of our neutralinos and charginos, we expect most of the heavier stops — if at all kinematically accessible — to decay into higgsinos instead of the light stop such that this analysis is not expected to change the results of our study.

6.4 Results

In the following we show exclusion lines in the parameter space of the model explained above. Since we still have $m_{\tilde{g}}, m_{\tilde{t}_1}, m_{\tilde{\chi}_1^\pm}$ and $m_{\tilde{\chi}_1^0}$ as continuous degrees of freedom, we choose to present results for specific chosen benchmark scenarios.

As one of our considered decay chains in Section 6.2.1 starts with the production of gluinos and ends with the decay into the singlino LSP, we first choose to show exclusion lines in the plane spanned by the masses of these two particles in Section 6.4.1. We do so for various choices of $m_{\tilde{t}_1}, m_{\tilde{\chi}_1^\pm}$ and always compare the results for λ_L and λ_S. As it will turn out, light gluinos mostly lead to severly constrained models. Thus we will follow with a scenario in which the gluino is decoupled from the spectrum as well in Section 6.4.2. We then show exclusion lines in the $m_{\tilde{t}_1}$–$m_{\tilde{\chi}_1^0}$–plane for different chargino masses, again putting the results for λ_L and λ_S side by side. For the specific case of a light LSP, we also present results in the $m_{\tilde{t}_1}$–$m_{\tilde{\chi}_1^\pm}$–plane to illustrate the dependence on the chargino mass for both λ scenarios.

To keep the discussion compact, we only show figures which show the 95% exclusion lines in different parameter planes within this section. An exhaustive list of auxiliary plots with distributions of masses, cross sections and branching ratios can be found in Appendix C.1 and we refer to a few of these in the following discussion.

6.4.1 Gluino–LSP–Plane

In Figs. 6.3 to 6.7 we show the 95% exclusion region in the gluino-LSP mass plane, using fixed stop masses in the range $m_{\tilde{t}_1} = 400$ to 800 GeV. For each case, the λ_L and λ_S scenarios are compared in the left and right panel, respectively. Within each panel we compare the exclusion regions for different chargino mass values that obey $m_{\tilde{\chi}_1^\pm} < m_{\tilde{t}_1}$. Since the chargino must not be lighter than the LSP, each exclusion line has an individual upper limit on the $m_{\tilde{\chi}_1^0}$ axis,

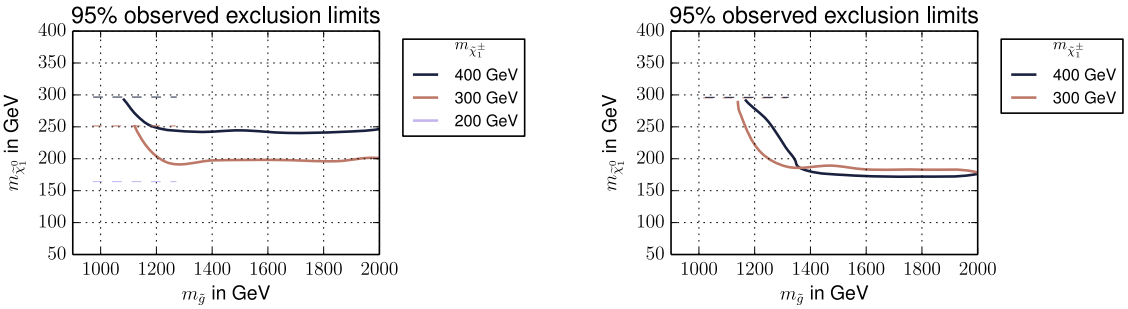

Figure 6.3: Observed 95% C.L. exclusion limits for $m_{\tilde{t}_1} = 400$ GeV. Left: λ_L. Right: λ_S

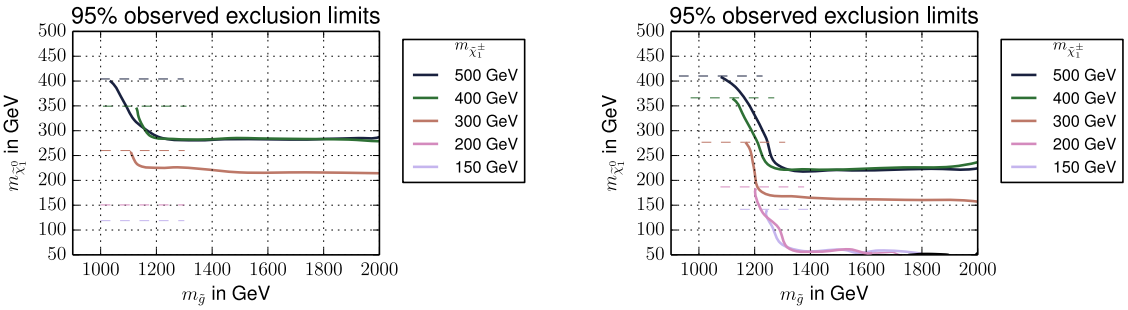

Figure 6.4: Observed 95% C.L. exclusion limits for $m_{\tilde{t}_1} = 500$ GeV. Left: λ_L. Right: λ_S

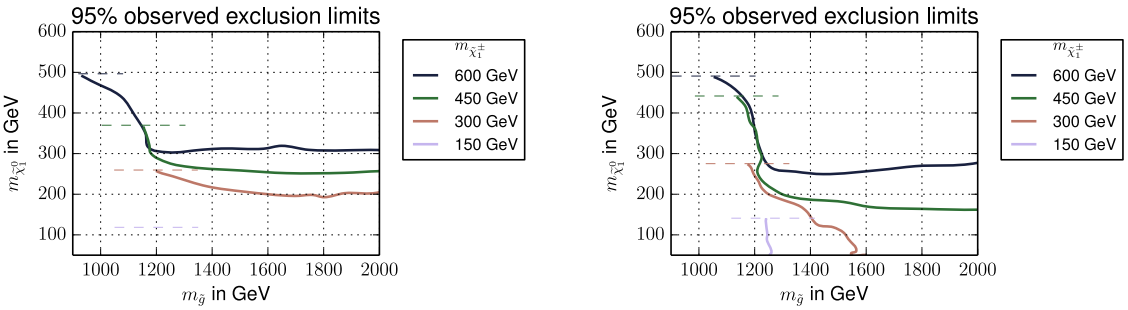

Figure 6.5: Observed 95% C.L. exclusion limits for $m_{\tilde{t}_1} = 600$ GeV. Left: λ_L. Right: λ_S

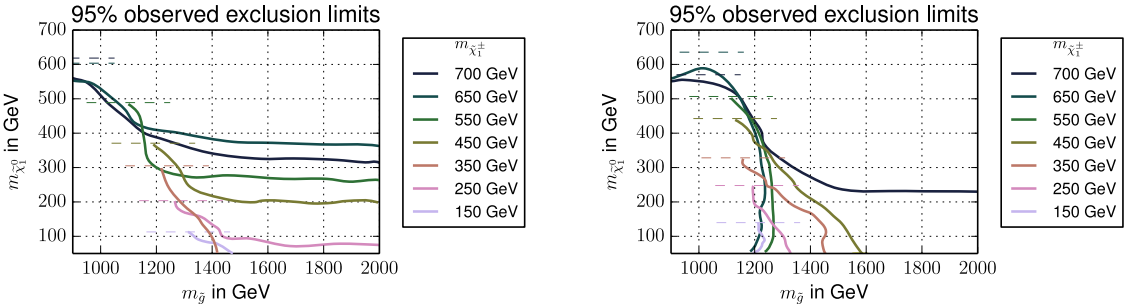

Figure 6.6: Observed 95% C.L. exclusion limits for $m_{\tilde{t}_1} = 700$ GeV. Left: λ_L. Right: λ_S

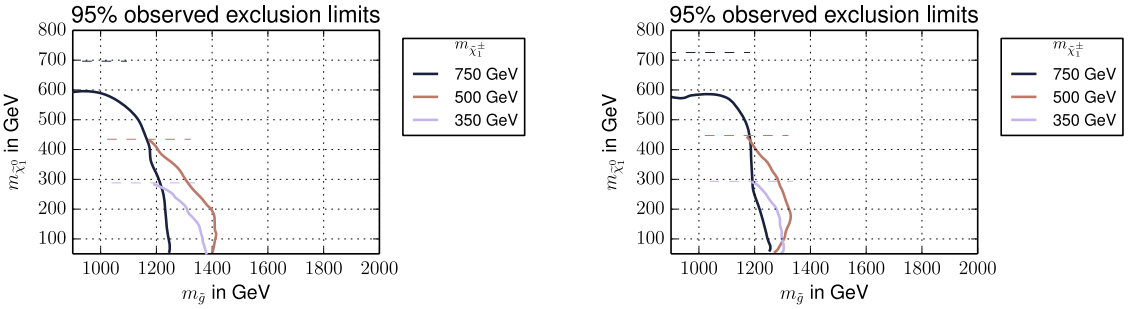

Figure 6.7: Observed 95% C.L. exclusion limits for $m_{\tilde{t}_1} = 800$ GeV. Left: λ_L. Right: λ_S

drawn by dashed horizontal lines[8]. Chargino mass values that are listed in the legend but do not appear in the plot should be interpreted as being entirely excluded across the whole mass plane.

Generally, the exclusion lines split the parameter space into two regions of interest and we discuss these regions separately:

Light Gluinos

For $m_{\tilde{g}} \lesssim 1100$ GeV, Figs. 6.3 to 6.7 show that the limits are mostly independent of the chargino mass and apparently primarily driven by the gluino decay products in the decays $\tilde{g} \to b\tilde{b}, t\tilde{t}$.

As the bounds in that region do not seem to vary significantly as we change the mass of the electroweakinos and only barely if we change the mass of the lightest stop, we conclude that the details of the decay chain of the third generation scalars into the LSP is almost irrelevant when setting limits on the model. The only exception is if very small mass splittings occur in the decay chain, for example between the gluino and the stop or the stop and the higgsinos. We can see the effect in the left parts of Fig. 6.7 and also can be observed for all scenarios with $m_{\widetilde{\chi}_1^\pm} \lesssim m_{\tilde{t}_1}$ in Figs. 6.5 to 6.7.

When we compare the λ_S and λ_L limits we also see that the limits are stable between the two scenarios once gluino production is dominant. Consequently, we again conclude that the precise decay modes of the $\tilde{t}/\tilde{b}$ and the various $\widetilde{\chi}_1^0, \widetilde{\chi}_1^\pm$ do not effect the LHC phenomenology in this region of parameter space. Although our gluino mass limit lies very close to the maximum sensitivity limit quoted in Fig. 6.1 it is slightly weaker as we do not have a pure decay scenario but several dominant decay modes which reduce the individual branching ratios and thus the event rate of each individual signal region.

This observed independence on the details of the NMSSM spectrum is interesting in the light of the initially discussed expectation that intermediate extra particles soften the respective decay products and the total missing energy and thus should weaken the limit. Fortunately, the many different signatures covered by `CheckMATE` in this region of parameter space are able to still exclude almost the entire light gluino region. To see which role the combination of individual analyses plays, we focus on four benchmark cases in Fig. 6.8 and for each individual parameter point we show the most sensitive analysis quoted by `CheckMATE`.

We see that the signal regions used to constrain the models are different between the two scenarios. In particular the λ_S scenario generically contains longer decays, as explained in more detail in the upcoming section, and in fact is better constrained by signal regions that have a larger final state particle multiplicity. More specifically, in the gluino dominated region it is the ATLAS search `atlas_conf_2013_061` [323] which require at least 3 b-jets which is very sensitive for both λ scearios. However, whilst the λ_L scenario is often best constrained with the 4-jet signal region `SR0L4JC`, the 6-jet region `SR1L7JB` dominates for λ_S almost everywhere. In addition, this multi b-jet ATLAS search demands moderate missing transverse momentum and hence the reduction of the total missing energy in the NMSSM as compared to the MSSM does not significantly change the efficiency in the signal regions.

The demands of the signal region for exclusion therefore translates only into the necessity of a sufficiently large gluino production cross section which is automatically given if the gluinos

[8] For given $m_{\widetilde{\chi}_1^\pm} \approx \mu_{\text{eff}}$, this theoretical upper limit should appear for $m_{\widetilde{\chi}_1^\pm} = m_{\widetilde{\chi}_1^0}$. However, since μ_{eff} also sets the scale of the neutral higgsinos in our setup, mixing in the neutralino sector never yields points which fulfill this equality. Therefore the dashed horizontal lines appear slightly below the $m_{\widetilde{\chi}_1^\pm} = m_{\widetilde{\chi}_1^0}$ line, namely at the heaviest singlino-like $\widetilde{\chi}_1^0$ that can be achieved for given μ_{eff} by diagonalising Eq. (2.117)

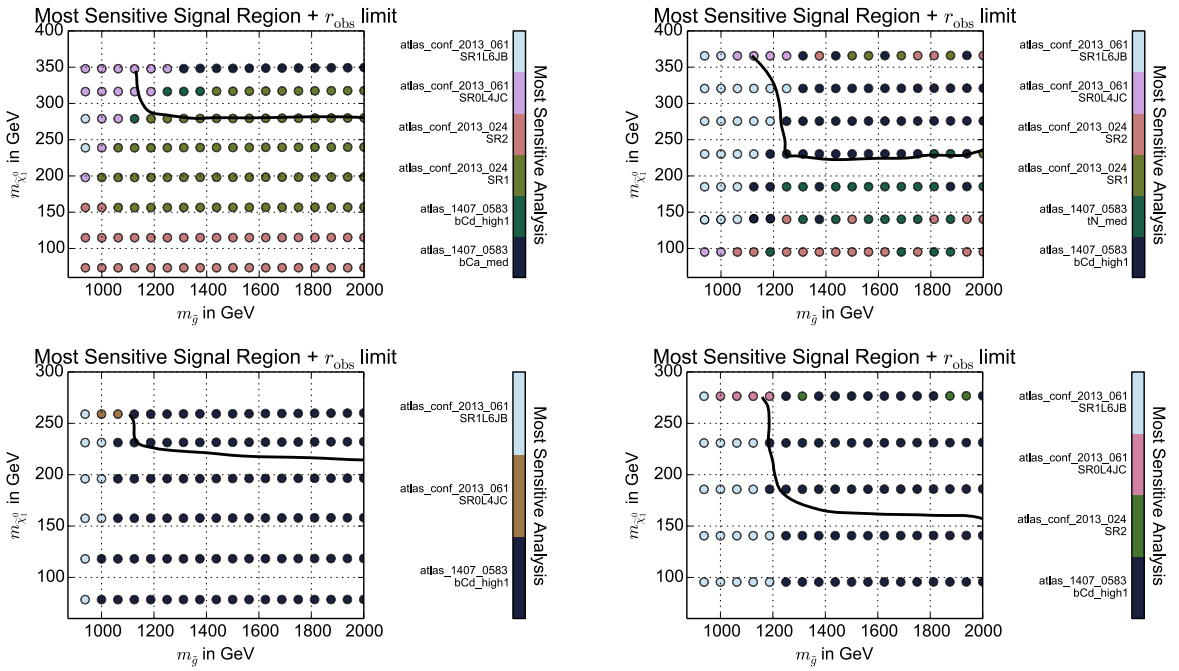

Figure 6.8: Most sensitive signal region for each individual point in the gluino-LSP scan, using $m_{\tilde{t}_1} = 500$ GeV, $m_{\tilde{\chi}_1^\pm} = 400$ GeV (top) and 300 GeV (bottom). Left: λ_L. Right: λ_S.

are sufficiently light — see Fig. C.2 in the appendix — and if a sizable mass splitting of gluinos and squarks/squarks and electroweakinos is present. It is thus expected that limits should not depend significantly on the λ scenario and only on mass differences close to threshold as can be seen in our results.

Heavy Gluinos

For gluinos with mass above the production threshold of about 1.2 TeV, the exclusion sensitivity will be dominantly driven by the production of the third generation sparticles $\widetilde{t}_{1/2}, \widetilde{b}_{1/2}$ if they are sufficiently light. To illustrate this, we show the total production cross section for gluinos in Fig. C.2 of the appendix and third generation squark production for fixed $m_{\tilde{t}_1}$ in Fig. C.3. For $m_{\tilde{g}} > 1.2$ TeV ($m_{\tilde{t}_1} < 800$ GeV), the production cross section drops below (reaches above) 1 fb respectively, see also Ref. [325]). Thus, in this parameter region one expects far more $\widetilde{t}_1$ than gluinos to be produced. Moreover, in the λ_L scenario large numbers of events with sbottoms and heavier stops are expected in addition as these particles can be light. Therefore, beyond the gluino threshold we observe a gluino-independent upper limit on the mass of the lightest neutralino. However, contrarily to the gluino-dominated region, one now finds significant dependencies of the limits on the chargino mass parameter and the λ scenario in Figs. 6.3 to 6.7. In general, we observe that for a fixed mass of the lightest stop, limits on the LSP mass become weaker the lighter we chose the intermediate chargino. Also, throughout all cases we find consistently better limits in the λ_L scenario than for λ_S.

To understand these differences, we first have to shed light on the analyses and signal regions which define our exclusion limits in this part of parameter space. In Fig. 6.8, we take the specific example of a light stop mass of 500 GeV and show the most sensitive signal regions for

chargino masses of 400 and 300 GeV, comparing λ_L on the left to λ_S on the right. One finds two main classes of final states to be of importance here:

1. Signal regions from `atlas_conf_2013_024` and '`tN`-type' regions in `atlas_1407_0583` focus on final states that originate from direct $\widetilde{t} \to t\widetilde{\chi}_1^0$ decays. That is, they require missing transverse momentum, b-jets and final state objects whose invariant mass lie close to the top-quark mass.

2. '`bC`-type' regions in `atlas_1407_0583` have been designed to tag events of type $\widetilde{t} \to b\widetilde{\chi}_1^\pm$ with subsequent $\widetilde{\chi}_1^\pm \to W^\pm\widetilde{\chi}_1^0$ by using kinematic variables that are sensitive to intermediate decay steps.

In the following, we will refer to these as `tN`-like and `bC`-like analyses and signal regions, respectively.

In our model setup, the choice of the Higgs mass parameter μ_{eff} which sets the masses $m_{\widetilde{\chi}_1^\pm}$ and $m_{\widetilde{\chi}_{2,3}^0}$ is crucial to determine how many events are expected to be counted for the above most sensitive signal regions. Its value sets the kinematically open channels from the full list in Section 6.2.1, fixes the branching ratios and determines the energy distribution among the final state particles:

Heavy Higgsinos For $m_{\widetilde{\chi}^\pm} \geq m_{\tilde{t}_1}$, the branching ratio for $\tilde{t}_1 \to t\widetilde{\chi}_1^0$ is practically 100% — regardless of λ — and thus the upper LSP mass limits in both scenarios are determined by results from `tN`-like signal regions. Note that as soon as the chargino is heavier than the lightest stop, it plays almost no role in the expected sensitivity any more as the lightest stop will always decay into the LSP. This is why we do not show results with $m_{\widetilde{\chi}^\pm} \geq m_{\tilde{t}_1}$ as they are almost[9] identical to the shown $m_{\widetilde{\chi}^\pm} = m_{\tilde{t}_1}$ case.

If the $\widetilde{t}_1$ was the only squark kinematically available, the limits of λ_L and λ_S would be expected to coincide. Comparison of the corresponding $m_{\tilde{t}_1} = m_{\widetilde{\chi}^\pm}$ lines in Figs. 6.3 to 6.7 however shows that λ_L yields stronger limits, with the difference being larger for lighter $m_{\tilde{t}_1}$. The reason here is that λ_L can allow for additional lighter 3rd generation squarks while still being able to get the right SM Higgs mass, as in Eq. (2.87). These lighter squarks have a larger production cross section and thus contribute more to the observable events, e.g. via decays $\tilde{b}_1 \to t\widetilde{\chi}^\pm$ which can also pass the signal region cuts. If a light $\tilde{t}_1$ is present in a λ_S scenario however, the additional 3rd generation squarks are required to be much heavier

Light Higgsinos For $m_{\widetilde{\chi}^\pm} \lesssim m_{\tilde{t}_1}$, the decay $\tilde{t}_1 \to b\widetilde{\chi}^\pm$ opens kinematically and the two considered cases for λ now start to show different behaviour: Within the λ_S scenario we have an almost pure singlino LSP which causes the branching ratio for $t\widetilde{\chi}_1^0$ final states to become almost immediately disfavoured below the chargino threshold. Thus in this scenario almost all stops have to decay via intermediate higgsinos. Interestingly, `tN`-like analyses are still most significant to set the limit if the charginos are not too light, see Fig. 6.8 top right. The reason is that events with intermediate charginos can lead to $bW^+\widetilde{\chi}_1^0$ final states misidentified as top quarks within `tN`-like signal region selections if the neutralino is light enough because of its

[9] Small differences can arise from $\widetilde{t}_2 \to b\widetilde{\chi}^\pm$ decays which however happen rarely as the heavy stop is either heavy and therefore out of kinematic reach or close in mass to the lighter stop such that this decay is phase-space suppressed. The differences were in any case barely visible in Figs. 6.3 to 6.7 which is why we decided to remove them to keep the already large number of shown benchmark results at a minimum.

wide reconstructed top mass window $130 < m_t^{\text{rec}} < 250$ GeV. In addition one expects a significant contribution of sbottoms decaying into $t\widetilde{\chi}^{\pm}$ final states which can also look tN-like. For even lighter charginos, the limit is however only set by bC-like analyses (see again Fig. 6.8). Decreasing the chargino mass further leads to softer decay products in the decay $\widetilde{\chi}^{\pm} \to W^{\pm}\, \widetilde{\chi}_1^0$ which weakens the resulting upper limits on the $\widetilde{\chi}_1^0$ mass. Finally, decays into $t\widetilde{\chi}_{2/3}^0$ can reduce the branching ratio into the above mentioned decays once the chargino — and due to $m_{\widetilde{\chi}_{2/3}^0} \approx m_{\widetilde{\chi}^{\pm}} \approx \mu_{\text{eff}}$ also the neutral higgsinos — becomes light enough, see also Fig. C.4. This results in a significant number of events displaying an asymmetric topology with two different decay chains which is less constrained by experiment, see Ref. [222]. These are not present in the analyses we considered and thus our sensitivity is poor.

Most of the explanations in the above discussion apply similarly to the λ_L scenario. However, a distinctive feature is the strong mixing in the neutralino sector which allows for the LSP to have a large higgsino component and thus $t\widetilde{\chi}_1^0$ decays still having a large branching fraction below the chargino threshold. For example one finds that for $m_{\tilde{t}_1} - m_{\widetilde{\chi}^{\pm}} \lesssim 150$ GeV direct stop-to-top decays still happen with more than 20% probability, see Fig. C.4. We therefore expect, and observe, that also within λ_L the tN signal regions set the limit for charginos within that mass region, see Fig. 6.8 top left. For lighter charginos, the limits become weaker due to the decreasing branching ratio of the 'golden channel' $\widetilde{t}_1 \to t\widetilde{\chi}_1^0$ and eventually the bC signal regions dominate and sets the limits thereafter, see Fig. 6.8 bottom left. The overall stronger exclusions within the λ_L scenario can therefore be attributed to two different reasons. Firstly, the other 3rd generation squarks will again be lighter in the λ_L scenario due to the additional singlet contributions to the Higgs mass. Secondly, the increased branching ratio of $\widetilde{t}_1 \to t\widetilde{\chi}_1^0$ which the LHC analyses are particularly sensitive to also helps.

Interestingly, in both λ scenarios, charginos lighter than $m_{\tilde{t}_1} - m_t$ open decay channels of the type $\tilde{t}_1 \to t\widetilde{\chi}_{2/3}^0$ due to $m_{\widetilde{\chi}_{2/3}^0} \approx m_{\widetilde{\chi}^{\pm}}$. These could lead to NMSSM specific final states as discussed in Section 6.2.1. However, we do not observe any improvement on the LSP limits in these cases. Quite the contrary, the reduction of the branching ratio into $b\widetilde{\chi}^{\pm}$ final states resulting from the new decay channel and asymmetric final states mentioned above weakens the limits even more as can be observed when comparing the limits in Figs. 6.3 to 6.7 above or below this threshold. We investigate the impact of this threshold more closely in the upcoming section.

6.4.2 Stop-Electroweakino-Plane

As we saw in the previous set of results, below the gluino production threshold, the LHC limits only have a small dependence on the details of the natural spectrum. However, as we decouple the gluino, the masses and couplings of the electroweakino sector become more important. For that reason we also show results in the $m_{\tilde{t}_1}$–$m_{\widetilde{\chi}_1^0}$–plane for a decoupled gluino of mass 2 TeV in Figs. 6.9 to 6.12. With one degree of freedom less, we are now able to show one exclusion limit per plot for specific values of $m_{\widetilde{\chi}_1^{\pm}}$, again comparing λ_L on the left to λ_S to the right. The parameter space that we investigate does not include the region where $m_{\tilde{t}_1}$ becomes close to $m_{\widetilde{\chi}_1^0}$. This is shown by the diagonal dashed line within each plot which shows the kinematic range for which $m_{\tilde{t}_1} < m_b + m_W + m_{\widetilde{\chi}_1^0}$ and only 4-body final states or flavour changing neutral current decays such as $\tilde{t}_1 \to c\widetilde{\chi}_1^0$ are possible. Given the small mass difference, initial state radiation searches provide the most constraining limits in this region, see e.g. Refs. [326, 327]. These searches are relatively insensitive to the details of the decay chain in question and thus

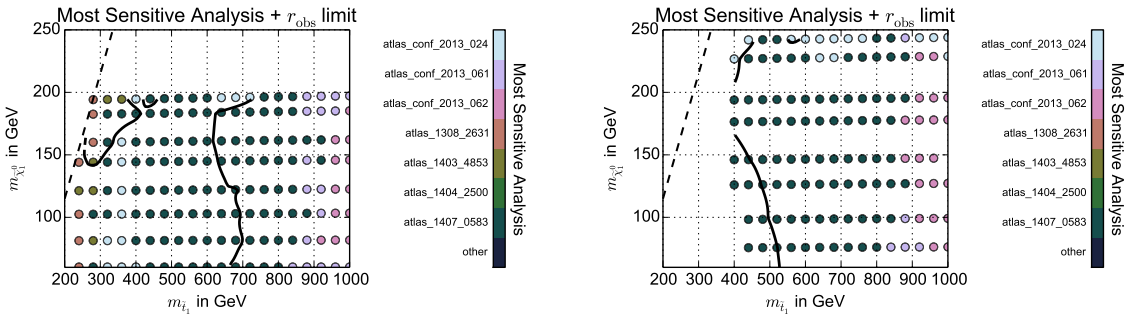

Figure 6.9: Observed 95% C.L. exclusion limit and most sensitive analysis per point for $m_{\tilde{\chi}_1^\pm} = 250$ GeV. Left: λ_L. Right: λ_S

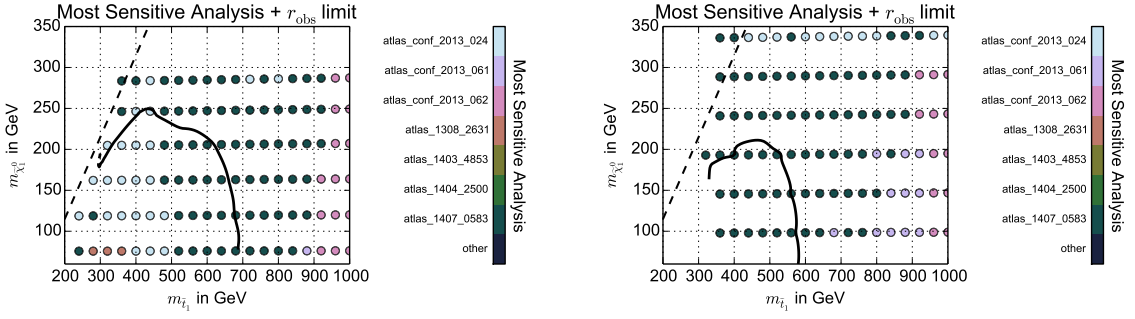

Figure 6.10: Observed 95% C.L. exclusion limit and most sensitive analysis per point for $m_{\tilde{\chi}_1^\pm} = 350$ GeV. Left: λ_L. Right: λ_S

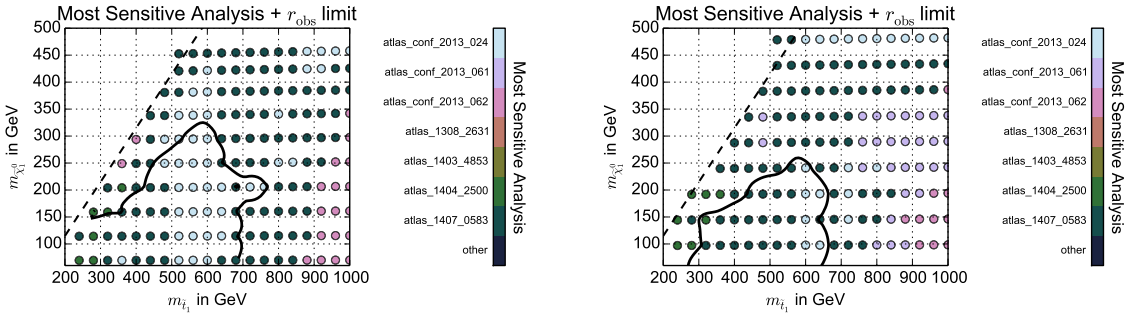

Figure 6.11: Observed 95% C.L. exclusion limit and most sensitive analysis per point for $m_{\tilde{\chi}_1^\pm} = 500$ GeV. Left: λ_L. Right: λ_S

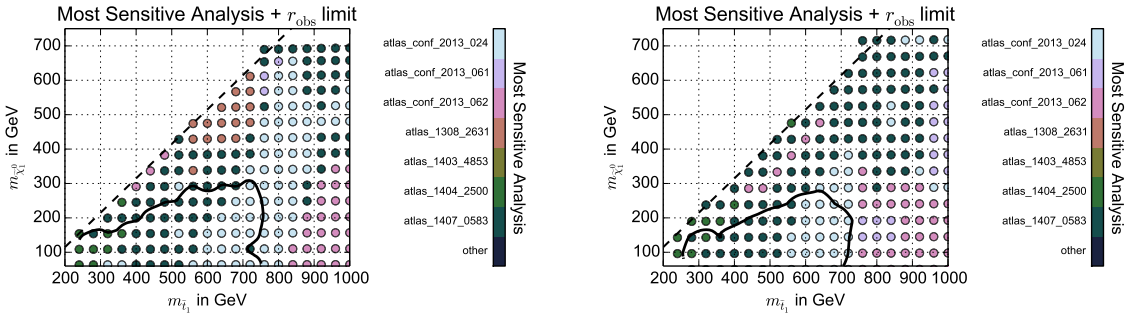

Figure 6.12: Observed 95% C.L. exclusion limit and most sensitive analysis per point for $m_{\tilde{\chi}_1^\pm} = 750$ GeV. Left: λ_L. Right: λ_S

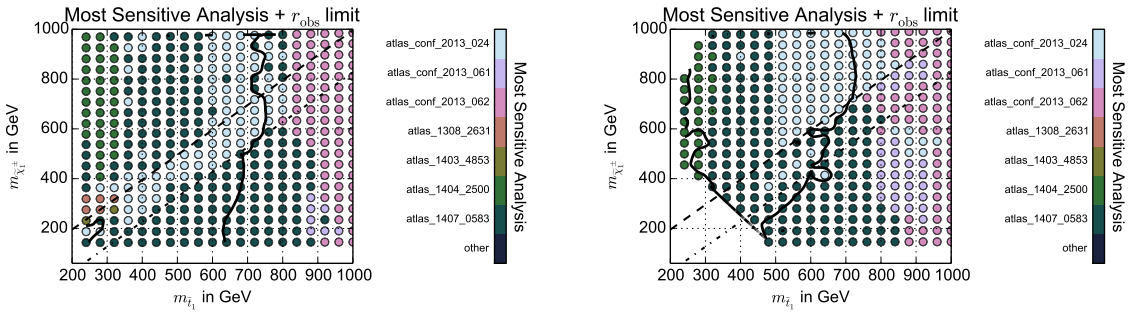

Figure 6.13: Observed 95% C.L. exclusion limit and most sensitive analysis per point for $m_{\chi_1^0} = 100$ GeV. Diagnoal dashed (dashed-dotted) lines show shows the threshold for $\tilde{t}_1 \to \tilde{\chi}_1^\pm b$ ($\tilde{t}_1 \to \tilde{\chi}_{2/3}^0 t$). Left: λ_L. Right: λ_S

we expect the results to be very similar to those of the MSSM.

Similarly to the gluino-LSP scan, the upper limit on the LSP mass is set by requiring $m_{\tilde{\chi}_1^0} < m_{\tilde{\chi}_1^\pm}$. For the λ_L case, mixing in the neutralino sector leads to a maximum achievable value of $m_{\tilde{\chi}_1^0}$ which lies somewhat below $m_{\tilde{\chi}_1^\pm}$. Note that within the λ_S scenario, realistic parameter points which pass all the constraints listed in Section 6.3.1 are not possible with $m_{\tilde{t}_1} \lesssim 400$ GeV if $m_{\tilde{\chi}_1^\pm} \approx \mu_{\text{eff}}$ is small.

In all plots we again show, for each individual considered data point, the most sensitive analysis that has been used to calculate the confidence level of that particular point. However, we do not show the numerous individual signal regions as we did for Fig. 6.8 to keep the amount of different values to a reasonable level.

We again observe that the choice of analysis responsible for the limit setting is strongly correlated with the branching ratio of the lightest stop and from Fig. C.4 we expect four main regions of interest. These are respectively, direct decays of the stop into the LSP and an a) on- or b) off-shell top, c) intermediate decays via charginos or d) via neutral higgsinos. The thresholds for these regions often coincide with a similar threshold for sbottom decays, as can be seen in Fig. C.6. As an example the $\tilde{b}_1 \to t\tilde{\chi}^\pm$ and the $\tilde{t}_1 \to t\tilde{\chi}_{2/3}^0$ lie very close in the λ_L scenario.

Using the branching ratio information, we can closely follow the explanations from the last section to understand the limits in Figs. 6.9 to 6.12. For stops lighter than the given chargino, only direct decays $\tilde{t}_1 \to t^{(*)}\tilde{\chi}_1^0$ are kinematically allowed. `tN`-like analyses are therefore the most sensitive and lead to similar limits for λ_L and λ_S, with the former being slightly stronger than the latter due to the lighter sbottoms in this model. In λ_S, a strip for $m_{\tilde{t}_1}$ - $m_{\tilde{\chi}_1^0} < m_t$ cannot be excluded as the final state with an off-shell top is not observed by `tN`-like analyses and hard to distinguish from the SM background. Within λ_L, this region can still be explored since it is possible that the spectrum also contains a light $\tilde{b}_1$. This can be excluded via $\tilde{b} \to t\tilde{\chi}_1^\pm$ specific selections in `atlas_1404_2500`, see e.g. Figs. 6.11 and 6.12.

For kinematically allowed chargino decays, a transition from `tN` into `bC` signal regions can be observed for increasing $m_{\tilde{t}_1}$, that is for larger stop-chargino splitting. As in the previous setup, λ_L profits from the higgsino fraction of the LSP and the generally lighter 3rd generation squarks. The highest sensitivities up to $(m_{\tilde{\chi}_1^0})^{\text{max}} \approx 325$GeV are reached via `tN` final states in `atlas_conf_2013_024`. In λ_S, `bC` signal regions dominate the limit earlier, which require lighter neutralinos to observe the intermediate chargino decay step. The experimental reach to the

LSP mass is therefore smaller in these scenarios and of order 250 GeV.

As we further increase the stop masses, a maximum sensitivity bound for $m_{\tilde{t}_1}$ can be observed. This bound depends on the chosen chargino mass and the considered λ scenario and is rather independent of the LSP mass as long as it is light enough, that is for $m_{\widetilde{\chi}_1^0} \lesssim 150$ GeV.

To better understand the parameter dependence, we chose to show results in the $m_{\tilde{t}_1}$–$m_{\widetilde{\chi}_1^\pm}$–plane for a fixed, light LSP mass of 100 GeV in Fig. 6.13. We explicitly draw the previously discussed threshold lines for $\tilde{t}_1 \to b\widetilde{\chi}_1^\pm$ and $\tilde{t}_1 \to t\widetilde{\chi}_{2/3}^0$ and it can be seen that they can have an important impact on the sensitivity of the experimental analyses to the stop mass: Within λ_L, the upper limit on $m_{\tilde{t}_1}$ is almost constant at ≈ 700 GeV for charginos above the $t\widetilde{\chi}_{2/3}^0$ threshold. This corresponds to similar limits from simplified $\tilde{t} \to t\widetilde{\chi}_1^0$ topologies as in Refs. [202, 322]. The limit gets slightly weaker if the threshold is passed, dropping by at most 50 GeV as soon as `bC` signal regions dominate the limit. In Figs. C.5, C.7 and C.9 we show the branching ratio distributions in the same plane and the same LSP mass as the results in Fig. 6.13. One observes that the mass values in our spectrum are such that the above behaviour coincides with the threshold for $\tilde{b} \to t\widetilde{\chi}^\pm$, which also explains why the `bC`-like signal regions become important within this region of parameter space.

As long as the higgsinos do not appear in the squark decay chains, λ_S returns similar limits as the λ_L scenario, for the same reasons discussed in the previous section. However, within this model one observes a sizable weakening of the limits as soon as the intermediate chargino and NLSP higgsino decays open kinematically. Interestingly, the latter has a particularly negative impact on the result, as the experimental analyses seem to be only weakly sensitive to parameter regions in λ_S where $\tilde{t}_1 \to t\widetilde{\chi}_{2/3}$ is kinematically allowed. As discussed in Section 6.2.1, it is this decay chain which yields NMSSM-specific features in the final state topology: the decay of the higgsino NLSPs into the singlino LSP should create a sizable excess of $h/H/A_1 \to \bar{b}b$ final states. It seems, however, that none of the many distinct final states within the numerous analyses that `CheckMATE` contains is sufficiently sensitive to this topology. Thus, the existing `bC`-like limits are weakened due to reduced branching ratios after passing the NLSP higgsino threshold.

We therefore conclude that not only can many limits on natural NMSSM scenarios be derived from very similar topologies in natural MSSM studies, but we also find that regions of parameter space which produce NMSSM-exclusive final state features are not sufficiently covered by existing studies. Therefore, only weak limits on the NMSSM can be set within this region of parameter space which suffer from branching-ratio penalties.

6.5 Conclusion

In this study we explored the natural NMSSM to determine how the additional singlino can effect the LHC searches compared to the more studied MSSM case. To do this we explored a number of different scenarios, mostly examining the difference between a small-λ case where the LSP is dominantly a singlino and the large-λ case where the LSP can contain a substantial higgsino component. We also studied in detail the differences which occur when the gluino is light enough such that it dominates the SUSY production cross-sections and what happens when the gluino is pushed to a mass where LHC production rates are too small.

We found that, when constructing a realistic phenomenological model, the NMSSM-specific decay chains via intermediate heavy neutralinos often create an MSSM-like topology, $\tilde{q}_3 \to q_3\widetilde{\chi}_1^0$ which can be preceded by $\tilde{g} \to \tilde{q}_3 q_3$ if the gluino is light. If the branching ratio to these decay

chains are large, the limits very closely follow those often studied as simplified models in the MSSM. However, the branching ratio depends on the size of the NMSSM-coupling λ. If it is large, all neutralinos have a sizable higgsino fraction and direct decays into the lightest neutralino are significant. However, in case of small λ, the coupling of the squarks to the LSP is made small since it has a large singlino content. Therefore decays via intermediate charged and neutral higgsinos are prefered if kinematically allowed which lengthens the decay chains seen. In addition, since different decay modes may be competing with similar branching ratios, asymmetric decay chains can often occur.

These longer decay chains can lead to weaker LHC bounds for two particular reasons. First of all, the ATLAS searches have more focussed of the MSSM specific signatures and consequently not been designed with these final states in mind. Secondly, the longer decay chains lead to a higher final state particle multiplicity but with each individual particle carrying smaller p_T. In addition the same effect reduces the final state E_T^{miss} as observed in other studies with more complicated decay topologies e.g. Ref. [328]. On the other hand, additional final states, namely jets and leptons, can improve the sensitivity even though the invisible transverse momentum is reduced. Therefore an important conclusion of this study is that it is not obvious if the efficiency is smaller or larger in a particular NMSSM scenario simply by looking at the spectrum and decays. Instead it is crucial to test the model against a large number of searches covering various final state topologies.

Within this study we do test a large variety of different analyses but still only use one signal region to define the overall limit. In the models with extended and asymmetric decay chains where we observe a weakening of the LHC limits), we expect the signal to populate a more varied number of signal regions than if the model predicted a single dominating decay chain. Therefore it may be expected that a combination of the sensitivities across all analyses can significantly enhance the limits. This is in fact a future `CheckMATE` feature in current development which promises to significantly improve results for models with various simultaneous decay scenarios like the one we discussed within this chapter.

CHAPTER 7

R-Parity Violation and Light Neutralinos at SHiP and the LHC

In Section 2.4.3 we discussed the role of R-parity violating (RPV) operators in the supersymmetric extension of the Standard Model and how these can allow for the decay of the LSP, the lightest supersymmetric particle. We furthermore discussed how this can open MeV neutralino mass windows which due to cosmological bounds would not be allowed in supersymmetric scenarios where the neutralino LSP is stable. Lastly, we briefly mentioned the generally strong constraints from proton decay and flavour violating observables and how these typically predict the coupling constants of R-parity violating operators — if they at all exist — to be small.

Within this chapter, we focus on the LQD operator in Eq. (2.100), i.e.

$$\mathcal{W}_{LQD} = \sum_{i,a,b=1}^{3} \lambda'_{iab}\left(\widehat{L}_i \cdot \widehat{Q}_a\right)\widehat{D}^c_b. \tag{7.1}$$

We discuss the experimental sensitivity of a new proposed experiment called SHiP (Search for Hidden Particles) to R-parity violating supersymmetry with a long lived light neutralino which decays via this operator. We start with a summary of the individual experimental status of light neutralino searches and R-parity bounds in Section 7.1 before we briefly discuss the SHiP setup and the target signature in Section 7.2. This signature involves interactions of the neutralino with Standard Model mesons and leptons and in Section 7.3 we derive the operators which mediate these interations in general for all possible LQD couplings. Afterwards, in Section 7.4, we specify requirements on the production and decay modes in order to expect SHiP to be sensitive and explain our general numerical methods in Section 7.5. As these conditions paired with the general solutions of LQD induced meson-neutralino-lepton interactions yield a plethora of possible scenarios, we focus on some illustrative benchmark cases in Section 7.6 for which we discuss individual results as well as their applicability to related scenarios we did not analyse explicitly. To show how SHiP competes with existing experiments, we perform a crude analogous sensitivity study of the LHC for two of the chosen benchmark cases in Section 7.7.

The results of this study have already been published for one benchmark case in the SHiP physics case report in Ref. [329] and for a larger set of operators in a separate publication in Ref. [330]. Compared to these references, this chapter provides a larger introductory overview regarding existing experimental limits, however besides minor cosmetic changes the actual analysis is unchanged. Hence, Section 7.2 and beyond draw heavily from Ref. [330].

7.1 Experimental Situation

7.1.1 Light Neutralinos in *R*-Parity Conserved Supersymmetry at Colliders

To understand the difficulty to find light neutralinos at colliders, let us start the discussion under the assumption that R-parity is conserved. We already discussed some limits on supersymmetric particle masses derived from LHC results in Chapter 6. If all supersymmetric particles had comparable masses, strongly coloured particles, i.e. squarks and gluinos, would have the largest cross section (see e.g. Ref. [162]) and thus out of all SUSY particles would be expected to be produced at the highest abundance. These are then expected to produce SUSY decay chains which in most phenomenological SUSY models end with the lightest neutralino as the stable LSP in R-parity conserving supersymmetry (see our discussion in Section 2.4.3). Searches for these decay chains, which typically expect a significant amount of missing transverse momentum, then yield combined limits in the potentially high-dimensional mass plane spanned by the produced coloured SUSY particle, the neutralino LSP and all intermediate particles in the SUSY spectrum. Clearly, if the mass of the first is set high enough such that the production cross section falls below the inverse of the integrated luminosity of the experiment, no BSM events are expected in the first place and thus no limits on the neutralino LSP can be set. We encountered this effect in the results of the natural NMSSM scenario in Section 6.4.2, where a massless neutralino could not be constrained if the gluino had mass beyond 1.5 TeV and the naturally light third generation squarks were heavier than about 700 GeV.

In such a scenario, even though the corresponding production cross sections are small, some sensitivity can be expected through direct production of charginos and neutralinos [331]. However again the bounds on $m_{\widetilde{\chi}_1^0}$ critically depend on the mass of the produced mother particle. Only direct pair production of $\widetilde{\chi}_1^0$ could be used to bound the neutralino mass independently of the remaining SUSY spectrum by for example looking for monojet signatures in $pp \to \chi_1^0\chi_1^0 j$ [91]. However, to be truly independent from the remaining SUSY spectrum the production of such a neutralino can only occur via Standard Model s-channel $Z^{(*)}$ and $h^{(*)}$-boson exchange. Since a very light neutralino should be mostly $\widetilde{B}$, c.f. Section 2.4.3, it does not couple to Z or h at tree level and thus generally the production cross section for these neutralinos is expected to be very small. For the same reason, measurements of the Z-boson width [265] or the invisible Higgs branching ratio (see our discussion in Section 5.2.1) do not constrain Bino-like light neutralinos either.

If the neutralino has sub-GeV mass — which in an R-parity conserving scenario automatically means it must have sub-eV mass according to our discussion in Section 2.4.3 — another production scenario could be thought of via new decays of Standard Model particles. For example, see e.g. Ref. [332], pairs of $\widetilde{\chi}_1^0$ can be produced via decays of e.g. π, K or B mesons. Unfortunately, the maximal possible branching ratios within R-parity conserving MSSM are typically very small. Also, since mesons at colliders are typically produced in association with large hadronic activity, it might be extremely hard to identify such a new partially invisible meson decay.

Hence, from the collider perspective, nearly massless neutralinos in an R-parity conserving setup do not render a problem with existing bounds as long as the remaining SUSY spectrum is beyond the TeV scale and thus invisible. This generally holds for collider neutralino searches and thus also applies to analogous limits from LEP [333] and the Tevatron [334].

7.1.2 Motivation for Searches with Broken *R*-Parity

If R-parity is broken by any of the operators in Eq. (2.100) with a sufficiently large coupling constant, the neutralino is not stable any more on collider scales and thus the above standard signatures which include missing tranverse momentum often become invalid. Instead, searches target events with high final-state multiplicity (for an extensive review, see Ref. [335]) or displaced vertices for neutralinos with $\mathcal{O}$(mm) lifetimes (see exemplary searches at CMS [336] and ATLAS [337]). This can affect mass limits derived from stable neutralino searches. However, if the production rate still depends on an abundantly created mother particle, these limits can still easily be avoided if the remaining SUSY spectrum is set to sufficiently high values[1].

In the special case of very light neutralinos, the consideration of rare meson decays as mentioned above in Section 7.1.1 turns out to be more promising in an R-parity violating scenario thanks to the following reasons:

1. If the neutralino is unstable on cosmological scales, the corresponding mass bounds in Eq. (2.98) are avoided and the neutralino can have mass of similar order of Standard Model mesons, i.e. $\mathcal{O}$(few hundred MeV).

2. Through R-parity violation, meson decays can produce single neutralinos whereas R-parity conservation required them to be produced in pairs. This increases the phase space and the kinematic range for decays to be possible.

3. The new R-parity violating coupling can contribute to the meson branching ratio into the neutralino and hence increase the overall $\widetilde{\chi}_1^0$ production rate sizably.

4. Not only can mesons decay into neutralinos but also neutralino decays into mesons are possible which opens new interesting experimental channels.

It is the combination of all these arguments which motivates the search for neutralinos at a long-baseline experiment as we propose it here, as it is only the presence of R-parity violation which allows for a long-lived neutralino with $\mathcal{O}$(GeV) mass which can be abundantly produced via Standard Model meson decays.

7.1.3 General Bounds on *R*-parity Violating Couplings

In Section 2.4.3 we briefly mentioned the constraints which can be put on R-parity violating operators by low-energy experiments. We now follow with a more complete list of existing bounds on various operators, most importantly those on the couplings λ'_{iab} which we analyse within this thesis. Exhaustive summaries of exiting bounds on individual and products of couplings can be found in Refs. [96, 338, 339]. In the following summary we make use the explanations and results in Ref. [96, 339] and refer to this source and references therein for more details on calculations and used observables.

Numerical bounds on λ' couplings which we use in our study are summarised in Table 7.1. We briefly explain the respective experimental observables which are responsible for these bounds:

[1] It should be mentioned at this point that strictly speaking the neutralino signatures via meson decay rates discussed in this chapter are also not truly independent of the remaining SUSY spectrum either. We derive effective operators by integrating out heavy sfermons from the spectrum which results in decay rates that strongly depend on the sfermion mass $m_{\tilde{f}}$. However, it will turn out that our expected bounds are sensitive to multi-TeV sfermion masses which are significantly beyond direct collider production reaches.

CKM unitarity: Couplings λ' which lead to an effective $(\bar{u}\gamma^\mu P_L d)\cdot(\bar{e}\gamma_\mu P_L \nu)$ operator[2] contribute to the Standard Model Fermi interaction and thus change the predicted value of the CKM matrix element V^{ud}_{CKM} (c.f. Eq. (2.18)). The unitarity of V_{CKM} paired with the unchanged values for V^{us}_{CKM} and V^{ub}_{CKM} can then be translated into bounds on λ'.

leptonic π decay rates: Any contribution of a coupling λ' to the low-energy operator $(\bar{u}\gamma^\mu P_L d)\cdot(\bar{\mu}\gamma_\mu P_L \nu)$ changes the ratio R_π of the pion branching ratios into electrons and muons.

τ-to-π decay rates: Analogously to R_π, a change of the effective operator $(\bar{d}\gamma^\mu P_L u)\cdot(\bar{\nu}\gamma_\mu P_L \tau)$ affects the predicted ratio of $\text{Br}(\tau^- \to \pi^- \nu)$ and $\text{Br}(\pi^- \to \mu^- \overline{\nu})$.

***D* decay rates:** Again very similar to R_π, a change of the effective operators $(\bar{d}\gamma^\mu P_L c)\cdot(\bar{\nu}\gamma_\mu P_L e)$ or $(\bar{s}\gamma^\mu P_L c)\cdot(\bar{\nu}\gamma_\mu P_L e)$ affects the relative branching ratios of D and D_s mesons into kaons and muons or electrons, respectively.

Cs atomic charge: Due to the parity violating nature of weak interactions, the mediation of Z bosons between electrons and nucleus in an atom leads to a small perturbation and thus a misalignment of energy and parity eigenstates. This can be measured by e.g. measuring the transition rate of equal-parity energy eigenstates (in the unperturbed basis) by applying an external electric field for which such a transition would be forbidden if parity was conserved. From this measurement one can induce the weak charge Q_W which is directly related to vector-axial current interactions of type $(\bar{e}\gamma^\mu\gamma^5 e)(\bar{q}\gamma_\mu q)$ between electrons and valence quarks. Any BSM operator contributing to the latter hence changes the prediction of the former and since Q_W of the cesium atom is measured to a good precision, tight bounds on these BSM operators can be derived.

ν_μ deep inelastic scattering: BSM contributions to effective operators $(\bar{\nu_\mu}\gamma^\mu P_L d)\cdot(\bar{d}\gamma^\mu P_L \nu)$ affect the predicted rates for muon-neutrino induced deep inelastic scattering $\nu_\mu + p \to \nu_\mu + X$.

$K - \overline{K}$ mixing: Higher order box diagrams with sfermions and $W^\pm$ bosons can give sizable contributions to $K - \overline{K}$ mixing via operatos of type $(\bar{s}\gamma^5 d)(\bar{d}\gamma^5 s)$.

$K \to \pi\nu\bar{\nu}$: The rate of this decay is strongly suppressed in the Standard Model due to the absence of tree-level flavour changing neutral currents (c.f. Section 2.1.3). It can however easily be enhanced in R-parity violating supersymmetry via sfermion mediation.

Note that all these constraints originate from low energy effective operators resulting from integrating out heavy scalar fermions (see also below in Section 7.3.1) and thus depend on the mass of the respectively heavy sfermion. Also, some combinations of operators are more constrained than individual operators as the presence of two couplings might open new low energy interactions. We quoted bounds on those combinations in Table 7.1 which surpass bounds on the respective individual couplings.

[2] Throughout this chapter, if we talk about neutrinos or antineutrinos whose flavour is irrelevant for the discussion, we simply refer to them via $\nu, \overline{\nu}$.

Coupling	Upper Limit	Constraint
λ'_{112}	0.03 $(m_{\tilde{s}_R}/100\,\text{GeV})$	CKM unitarity + leptonic π decay rates
λ'_{212}	0.06 $(m_{\tilde{s}_R}/100\,\text{GeV})$	leptonic π decay rates
λ'_{121}	0.2 $(m_{\tilde{d}_R}/100\,\text{GeV})$	D decay rates
λ'_{221}	0.1 $(m_{\tilde{d}_R}/100\,\text{GeV})$	D decay rates
λ'_{122}	0.2 $(m_{\tilde{s}_R}/100\,\text{GeV})$	D decay rates
λ'_{222}	0.1 $(m_{\tilde{s}_R}/100\,\text{GeV})$	D decay rates
λ'_{131}	0.03 $(m_{\tilde{t}_L}/100\,\text{GeV})$	Cs atomic charge
λ'_{231}	0.18 $(m_{\tilde{b}_L}/100\,\text{GeV})$	ν_μ deep inelastic scattering
λ'_{312}	0.06 $(m_{\tilde{s}_R}/100\,\text{GeV})$	τ-to-π decay rates
λ'_{313}	0.06 $(m_{\tilde{b}_R}/100\,\text{GeV})$	τ-to-π decay rates
$\sqrt{\lambda'_{121}\lambda'_{112}}$	$3\cdot10^{-5}$ $(m_{\tilde{\nu}_L}/100\,\text{GeV})$	$K-\overline{K}$ mixing
$\sqrt{\lambda'_{122}\lambda'_{112}}$	$4.7\cdot10^{-3}$ $(m_{\tilde{s}_R}/100\,\text{GeV})$	$K\to\pi\nu\bar{\nu}$
$\sqrt{\lambda'_{131}\lambda'_{112}}$	$4.7\cdot10^{-3}$ $(m_{\tilde{e}_L}/100\,\text{GeV})$	$K-\overline{K}$ mixing

Table 7.1: Summary of bounds on those λ'_{iab} coupling which are used within this work. All bounds on single operators are taken from Ref. [339], except for λ'_{231} which is taken from Ref. [96] as there is no bound quoted in Ref. [339]. Bounds on operator products are also taken from Ref. [96].

7.2 Light Neutralinos at SHiP

7.2.1 The SHiP Setup

We present some details of the SHiP setup that are relevant to our analysis. According to the SHiP proposal in Ref. [340], the plan is to employ the 400 GeV proton beam at CERN in the fixed-target mode. This yields a center-of-mass energy of roughly 27 GeV, sufficient to produce D and B mesons. Over the five year lifetime of the experiment a total of $2\cdot10^{20}$ protons on target are foreseen. Such a large event yield is expected to be achievable by e.g. a hybrid target consisting of tungsten and titanium-zirconium doped molybdenum alloy.

A major motivation for the SHiP experiment is to observe new, weakly-interacting particles with long lifetimes. The SHiP physics case report [329] lists various interesting physics scenarios beyond the Standard Model including the Higgs Portal which we encountered in Chapter 5, the NMSSM which we discussed in Section 2.5 or the R-parity violating MSSM we present here. The respectively predicted long-lived particles could be produced via proton-target-collisions and propagate for finite distances of the order tens of meters before decaying back into Standard Model pairs. For that purpose, a decay volume is located 68.8 m behind the target. It has a cylindrical shape with a total length of 60 m, however with the first 5 m dedicated for background suppression vetoes. Furthermore, the decay region has an elliptic face front with semi-axes 5 m and 2.5 m. We sketch this setup later in Fig. 7.2. A spectrometer and a calorimeter system positioned behind the decay volume can identify the visible final state particles that are potentially produced when a hidden particle decays.

SHiP is not only designed to search for BSM physics. Due to the high expected number of $D_S^\pm$ mesons, see our results in Table 7.4 below, $\mathcal{O}(10^{15})$ tau neutrinos are expected to be

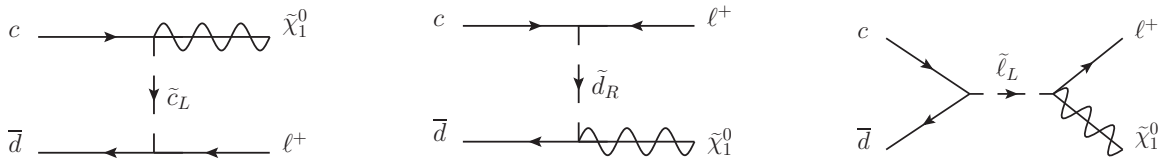

Figure 7.1: Relevant Feynman diagrams for $D^+ \to \tilde{\chi}_1^0 + \ell^+$. For the interpretation of diagrams with broken fermion flow due to charge-conjugated fermions and Majorana neutralinos, see e.g. Ref. [343].

produced after five years of operation via decays $D_s^\pm \to \tau^\pm \nu_\tau$ and the subsequent prompt decay of the tau lepton. A special tau neutrino detector is planned to be positioned before the above mentioned decay chamber. Its target material is designed such that it maximises the neutrino charged current cross section and approximately 10,000 interactions with an average energy of 60 GeV are expected. With such a large expected event rate, SHiP is expected to be the first experiment which can observe, study and distinguish the properties of tau neutrinos and tau antineutrinos which previous physics programs, i.e. the `DONUT` [341] and the `Opera` [342] experiments, were yet unable to do due to their limited statistics.

7.2.2 Production and Decay of Neutralinos via *R*-Parity Violation

A sensitivity study of a long baseline experiment to R-parity violating long lived neutralino decays has already been performed for the NuTeV experiment in Ref. [344]. In agreement with our argumentation above, it has been shown here that pair production of neutralinos has a too small cross section. Instead, a much higher sensitivity is expected if Standard Model mesons which are produced at very high rates can decay to the neutralino LSP and a neutral or charged lepton l via the LQD operator in Eq. (7.1), i.e.

$$\begin{aligned} pp &\to M + X, \\ M &\to \tilde{\chi}_1^0 + l. \end{aligned} \tag{7.2}$$

At SHiP energies, with a 400 GeV proton beam we expect high production rates for charmed mesons and somewhat lower rates for B-mesons. For example, as we discuss below, about 4.8×10^{16} $D^\pm$-mesons are expected to be produced over the lifetime of SHiP. For a nonvanishing λ'_{i12} these could then decay into the neutralino plus a lepton, i.e.

$$D^+ \to \tilde{\chi}_1^0 + \ell_i^+, \; i = 1, 2\,. \tag{7.3}$$

via the Feynman diagrams given in Fig. 7.1. In this specific example the light neutralino can decay via the same R-parity violating operator:

$$\tilde{\chi}_1^0 \to (\nu\, K_{S/L}^0;\, \bar{\nu}\, \bar{K}_{S/L}^0)\,. \tag{7.4}$$

Both sets of decays are possible, as the neutralino is a Majorana fermion. For small values of the coupling λ'_{i21} and given that the neutralino must be lighter than the D^+ meson, the neutralino lifetime can be long enough to decay downstream in the SHiP detector.

As mentioned in the introduction, this particular scenario has already been used as a simple benchmark scenario in Ref. [329] and subsequently was updated and extended in Ref. [330]. Shortly before our extended study was completed, Ref. [345] had appeared which discusses

the SHiP sensitivity to a benchmark case with production via B mesons, as we discuss it here as well, and another benchmark case with neutralinos decaying via a nonvanishing LLE opererator[3].

7.3 Effective Lepton-Neutralino-Meson Interactions

In this section, we discuss the R-parity violating effective interactions between a meson, a lepton, and a neutralino. These interactions are relevant for both the production and the decay of the neutralino and are necessary to determine the possible signatures at SHiP, as in Eqs. (7.3) and (7.4). As discussed, we focus on the LQD operator in Eq. (7.1).

7.3.1 Derivation of Interaction Operators

Effective Couplings

From the single superpotential term in Eq. (7.1) we can derive the interaction Lagrangian $\mathcal{L}_{\mathcal{W}}$ as in Eq. (2.64). Using projection operators to write everything in terms of four-component Dirac spinors, see our discussion below Eq. (2.15), we find the following set of Yukawa-like operators:

$$\begin{aligned}\mathcal{L} \supset \sum_{i,a,b=1}^{3} \lambda'_{iab}\Big[&(\overline{\nu_i^c} P_L d_a)\widetilde{d}^*_{R,b} + (\overline{d_b} P_L \nu^i)\widetilde{d}_{L,a} + (\overline{d_b} P_L d_a)\widetilde{\nu}_{L,i}\Big] \\ &-\lambda'_{iab}\Big[(\overline{u_a^c} P_L \ell^i)\widetilde{d}^*_{R,b} + (\overline{d_b} P_L u_a)\widetilde{\ell}_{L,i} + (\overline{d_b} P_L \ell^i)\widetilde{u}_{L,a}\Big] + \text{h.c.}\ . \end{aligned} \tag{7.5}$$

The dominant contribution to the R-parity violating decay of a meson typically proceeds at tree-level via operators associated with the Feynman diagrams as shown in Fig. 7.1. Thus we also need the standard supersymmetric fermion-sfermion-neutralino vertices. We get these by first diagonalising the neutralino mass matrix in Eq. (2.95) and then rotating the gaugino interactions derived from Eq. (2.62) as well as the higgsino interactions derived from the superpotential Yukawa terms and Eq. (2.64) into the mass eigenbasis. As we consider a dominantly bino LSP neutralino, from Eq. (2.62) it follows that $\widetilde{\chi}_1^0$ only couples fermions and sfermions of the same representation. We further assume that the mixing patterns are aligned in the corresponding sfermion and fermion sectors [346]. The relevant interactions are then given as

$$\begin{aligned}\mathcal{L} \supset \sum_{i,a,b=1}^{3} &g_{\tilde{u}_{L,a}}(\overline{\widetilde{\chi}_1^0} P_L u_a)\widetilde{u}^*_{L,a} + g_{\tilde{d}_{L,a}}(\overline{\widetilde{\chi}_1^0} P_L d_a)\widetilde{d}^*_{L,a} + g_{\tilde{\ell}_{L,i}}(\overline{\widetilde{\chi}_1^0} P_L \ell_i)\widetilde{\ell}^*_{L,i} \\ &+g_{\tilde{\nu}_{L,i}}(\overline{\widetilde{\chi}_1^0} P_L \nu_i)\widetilde{\nu}^*_{L,i} \quad + g^*_{\tilde{d}_{R,b}}(\overline{d}_b P_L \widetilde{\chi}_1^0)\widetilde{d}_{R,b} + \text{h.c.} \end{aligned} \tag{7.6}$$

with the following coupling constants g_X which for pure bino interactions turn out to be family independent [57]:

$$g_{\tilde{\ell}_{L,i}} = g_{\tilde{\ell}_L} = +\frac{g_L}{\sqrt{2}} \tan\theta_W, \tag{7.7}$$

[3] Unfortunately, the authors of Ref. [345] blindly copied our intermediate formulae and results from Ref. [329] including all mathematical and conceptual mistakes. Of course, these errors were corrected for our extended version in Ref. [330] and for this thesis.

$$g_{\tilde{\nu}_{L,i}} = g_{\tilde{\nu}_L} = +\frac{g_L}{\sqrt{2}} \tan\theta_W, \tag{7.8}$$

$$g_{\tilde{u}_{L,a}} = g_{\tilde{u}_L} = -\frac{g_L}{3\sqrt{2}} \tan\theta_W, \tag{7.9}$$

$$g_{\tilde{d}_{L,a}} = g_{\tilde{d}_L} = +\frac{5g_L}{3\sqrt{2}} \tan\theta_W, \tag{7.10}$$

$$g_{\tilde{d}_{R,b}} = g_{\tilde{d}_R} = -\frac{2g_L}{3\sqrt{2}} \tan\theta_W. \tag{7.11}$$

Note that our results can straightforwardly be generalised to non-Bino neutralinos and/or flavour-non-diagonal interactions by determining the respective mixing matrices and using the results in e.g. Ref. [57] to update the above formulae.

We assume that the sfermion masses are significantly larger than the momentum exchange of the process in which case they can be integrated out from the low energy theory. In general, a Lagrangian of the form

$$\mathcal{L} = \bar{\psi}_1 \Gamma \psi_2 X + \bar{\chi}_1 \widetilde{\Gamma} \chi_2 X + \text{h.c.} \tag{7.12}$$

with a complex scalar X and fermions $\psi_{1/2}, \chi_{1,2}$ coupled via arbitrary Dirac operators $\Gamma, \widetilde{\Gamma}$, yields (see e.g. Ref. [347])

$$\mathcal{L}_{\text{eff}} = \frac{1}{m_X^2} (|F_X|)^2 \tag{7.13}$$

with

$$F_X \equiv \frac{\partial \mathcal{L}}{\partial X} = \bar{\psi}_1 \Gamma \psi_2 + \bar{\chi}_1 \widetilde{\Gamma} \chi_2, \tag{7.14}$$

and m_X being the mass of X. The resulting low-energy effective four-fermion Lagrangian which describes both the production and decay of the neutralino then reads

$$\begin{aligned}\mathcal{L} \supset \sum_{i,a,b=1}^{3} \lambda'_{iab} \Bigg[& \frac{g^*_{\tilde{d}_{R,b}}}{m^2_{\tilde{d}_{R,b}}} (\bar{d}_b P_L \widetilde{\chi}_1^0)(\overline{\nu_i^c} P_L d_a) - \frac{g^*_{\tilde{d}_{R,b}}}{m^2_{\tilde{d}_{R,b}}} (\bar{d}_b P_L \widetilde{\chi}_1^0)(\overline{u_a^c} P_L \ell_i) + \frac{g_{\tilde{d}_{L,a}}}{m^2_{\tilde{d}_{L,a}}} (\overline{\widetilde{\chi}_1^0} P_L d_a)(\overline{d_b} P_L \nu_i) \\ & - \frac{g_{\tilde{u}_{L,a}}}{m^2_{\tilde{u}_{L,a}}} (\overline{\widetilde{\chi}_1^0} P_L u_a)(\overline{d_b} P_L \ell_i) + \frac{g_{\tilde{\nu}_{L,i}}}{m^2_{\tilde{\nu}_{L,i}}} (\overline{\widetilde{\chi}_1^0} P_L \nu_i)(\overline{d_b} P_L d_a) - \frac{g_{\tilde{\ell}_{L,i}}}{m^2_{\tilde{\ell}_{L,i}}} (\overline{\widetilde{\chi}_1^0} P_L \ell_i)(\overline{d_b} P_L u_a) \Bigg] + \text{h.c.}\end{aligned} \tag{7.15}$$

We have omitted the terms involving pairs of neutralinos, which are most likely not relevant at SHiP, see Ref. [332]. Similarly, we have dropped interactions involving four SM fermions, see Ref. [338].

Using chiral Fierz identities [348], one can rearrange the four-fermion interactions in Eq. (7.15) such that each term factorizes in a neutralino-lepton current and a quark-bilinear. For general four-component spinors $\psi_{1,2}$, $\eta_{1,2}$ we can write

$$\begin{aligned}(\bar{\psi}_1 P_L \eta_2)(\bar{\eta}_1 P_L \psi_2) = & -\frac{1}{2}(\bar{\psi}_1 P_L \psi_2)(\bar{\eta}_1 P_L \eta_2) - \frac{1}{4}(\bar{\psi}_1 \sigma^{\mu\nu} \psi_2)(\bar{\eta}_1 \sigma_{\mu\nu} \eta_2) \\ & + \frac{i}{8} \epsilon^{\mu\nu\rho\sigma} (\bar{\psi}_1 \sigma_{\mu\nu} \psi_2)(\bar{\eta}_1 \sigma_{\rho\sigma} \eta_2),\end{aligned} \tag{7.16}$$

$$(\bar{\psi}_1 P_R \eta_2)(\bar{\eta}_1 P_R \psi_2) = -\frac{1}{2}(\bar{\psi}_1 P_R \psi_2)(\bar{\eta}_1 P_R \eta_2) - \frac{1}{4}(\bar{\psi}_1 \sigma^{\mu\nu} \psi_2)(\bar{\eta}_1 \sigma_{\mu\nu} \eta_2) - \frac{i}{8}\epsilon^{\mu\nu\rho\sigma}(\bar{\psi}_1 \sigma_{\mu\nu} \psi_2)(\bar{\eta}_1 \sigma_{\rho\sigma} \eta_2), \tag{7.17}$$

with $\sigma^{\mu\nu} \equiv i/2\,[\gamma^\mu, \gamma^\nu]$ and $\epsilon^{0123} = 1$. Making use of these identities and applying $\overline{\psi^c} P_{L/R} \eta = \overline{\eta^c} P_{L/R} \psi$ in combination with the Majorana identity $\chi^c = \chi$ for the neutralino, Eq. (7.15) can be written as the sum of the following four interactions:

$$(\overline{\widetilde{\chi}^0} P_L \nu_i)(\overline{d_b} P_L d_a) \times \underbrace{\lambda'_{iab}\Big(\frac{g_{\tilde{\nu}_L}}{m^2_{\tilde{\nu}_{L,i}}} - \frac{1}{2}\frac{g_{\tilde{d}_L}}{m^2_{\tilde{d}_{L,a}}} - \frac{1}{2}\frac{g^*_{\tilde{d}_R}}{m^2_{\tilde{d}_{R,b}}}\Big)}_{\equiv G^{S,\nu}_{iab}}, \tag{7.18}$$

$$(\overline{\widetilde{\chi}^0} P_L \ell_i)(\overline{d_b} P_L u_a) \times \underbrace{\lambda'_{iab}\Big(\frac{1}{2}\frac{g_{\tilde{u}_L}}{m^2_{\tilde{u}_{L,a}}} + \frac{1}{2}\frac{g^*_{\tilde{d}_R}}{m^2_{\tilde{d}_{R,b}}} - \frac{g_{\tilde{\ell}_L}}{m^2_{\tilde{\ell}_{L,i}}}\Big)}_{\equiv G^{S,\ell}_{iab}}, \tag{7.19}$$

$$(\overline{\widetilde{\chi}^0} \sigma^{\mu\nu} \nu_i)(\overline{d_b} \sigma^{\rho\sigma} d_a) \times \underbrace{\lambda'_{iab}\Big(\frac{g_{\tilde{d}_L}}{4m^2_{\tilde{d}_{L,a}}} + \frac{g^*_{\tilde{d}_R}}{4m^2_{\tilde{d}_{R,b}}}\Big)}_{\equiv G^{T,\nu}_{iab}} \Big(g_{\mu\rho} g_{\nu\sigma} - \frac{i\epsilon_{\mu\nu\rho\sigma}}{2}\Big), \tag{7.20}$$

$$(\overline{\widetilde{\chi}^0} \sigma^{\mu\nu} \ell_i)(\overline{d_b} \sigma^{\rho\sigma} u_a) \times \underbrace{\lambda'_{iab}\Big(\frac{g_{\tilde{u}_L}}{4m^2_{\tilde{u}_{L,a}}} + \frac{g^*_{\tilde{d}_R}}{4m^2_{\tilde{d}_{R,b}}}\Big)}_{\equiv G^{T,\ell}_{iab}} \Big(g_{\mu\rho} g_{\nu\sigma} - \frac{i\epsilon_{\mu\nu\rho\sigma}}{2}\Big), \tag{7.21}$$

and their hermitean conjugates.

Quark-Meson Currents

For pseudoscalar mesons composed of anti-quarks $\bar{q}_1$ and quarks q_2, we can connect the quark bilinear vector currents with external meson fields by defining pseudoscalar meson decay constants f_M

$$\langle 0|\bar{q}_1 \gamma^\mu \gamma^5 q_2|M(p)\rangle \equiv i p^\mu f_M, \tag{7.22}$$

where $|M(p)\rangle$ denotes a pseudoscalar meson M with momentum p and quark content $\bar{q}_1 q_2$. By dotting with the momentum operator $\hat{p}_\mu$ from the left and using the low energy approximation $p^i \ll p^0 = \text{mass}$, we can easily relate Eq. (7.22) to the pseudoscalar current

$$\langle 0|\bar{q}_1 \gamma^5 q_2|M(p_M)\rangle = i\frac{m^2_M}{m_{q_1} + m_{q_2}} f_M \equiv f^S_M, \tag{7.23}$$

which can be applied to Eqs. (7.18) and (7.19). Here, m_M, m_{q_1} and m_{q_2} are the masses of the meson M and the quarks q_1, q_2, respectively.

The tensor structure in Eqs. (7.20) and (7.21) can never lead to a purely leptonic processes such as $M \to \widetilde{\chi}^0 + \ell_i$ or $\widetilde{\chi}^0 \to M + \ell_i$. The reason is that a pseudoscalar meson only has its momentum as a Lorentz-vector degree of freedom. Hence, no antisymmetric tensor combination can be formulated and thus the matrix element is trivially zero. Hence, for pseudoscalar mesons tensor currents can only contribute to higher multiplicity processes such as $M \to \widetilde{\chi}^0 + l_i + M'$, with a lighter meson M'. These however are phase space suppressed by two to three orders of magnitude in the decay widths. Thus, the can be neglected compared to the accompanying pseudoscalar current in Eqs. (7.18) and (7.19).

Vector mesons, however, have two intrinsic Lorentz vectors, their momentum p^μ and spin polarization ϵ^μ. The decay constant of a vector meson M^* with mass m_{M^*}, can be defined as (see e.g. Ref. [349])

$$\langle 0|\bar{q}_1\gamma^\mu q_2|M^*(p,\epsilon)\rangle \equiv f^V_{M^*} m_{M^*}\epsilon^\mu. \tag{7.24}$$

Heavy-quark symmetry relates the respecive vector meson constant $f^V_{M^*}$ and pseudoscalar constants f^V for mesons M which contain a heavy quark, i.e. $f^V_{M^*} \simeq f_M$ [350]. We use this relation for the B and D mesons. For lighter mesons, such as K^* and ϕ, the relation is not accurate and instead we follow Ref. [351] where the vector decay constants are obtained from $M^* \to e^+e^-$ decays.

Similarly we can define the tensor meson constant

$$\langle 0|\bar{q}_1\sigma^{\mu\nu} q_2|M^*(p,\epsilon)\rangle \equiv i f^T_{M^*}(p^\mu_M\epsilon^\nu - p^\nu_M\epsilon^\mu). \tag{7.25}$$

For mesons containing a heavy quark (c or b), heavy-quark symmetry again relates the vector and tensor decay constants $f^T_{M^*} \simeq f^V_{M^*} \simeq f_M$ [352]. Since the tensor decay constants are not known in all cases, we also employ this relation for lighter mesons. The additional uncertainties entering via these simplifying assumptions hardly affect the SHiP sensitivity curves on $\lambda'/m^2_{\widetilde{f}}$. These range over many orders of magnitude and thus an $\mathcal{O}(50\%)$ correction in a decay constant $f^{S,T,V}_{M^{(*)}}$ does not noticeably change the results presented in the figures in Section 7.6.

We list the values of the pseudoscalar and vector decay constants we use in Table 7.3 later in Section 7.6. In general, we find that neutralinos can interact both with pseudoscalar and vector mesons via different but related effective couplings. In the following analysis we therefore consider both meson types and also show how the inclusion of the latter affects the overall sensitivity.

As a side remark, we want to mention that potentially fine-tuned models with non-degenerate sfermion masses could lead to a complete cancellation of the individual contributions in Eqs. (7.18) and (7.19). No sensitivity would be expected in such a scenario if only pseudoscalar mesons were considered in the analysis. However, for a nonzero RPV coupling the effective operators in Eqs. (7.18) to (7.21) can not all vanish simultaneously. We hence safely use the simplifying assumption of completely mass degenerate sfermions which is allowed due to our consideration of vector mesons.

7.3.2 Possible Decay Modes

From Eqs. (7.18) to (7.21), a single $\lambda'_{iab}(\widehat{L}_i \cdot \widehat{Q}_a)\widehat{D}^c_b$ operator leads to interactions with charged pseudoscalar or charged vector mesons M^+_{ab} of flavour content $(u_a\overline{d_b})$ as well as neutral mesons M^0_{ab} with quark composition $d_a\overline{d_b}$, and their respective charge conjugated equivalents. If $m_{\widetilde{\chi}^0_1} <$

$m_M - m_{l_i}$, the operator opens a decay channel of the meson into the neutralino plus lepton l_i. For example, $M^\pm \to \widetilde{\chi}_1^0 \ell^\pm$, or $M^0 \to \widetilde{\chi}_1^0 \nu$, $\bar{M}^0 \to \widetilde{\chi}_1^0 \bar{\nu}$. Such processes serve as the initial neutralino production mechanism here. In addition, for $m_{\widetilde{\chi}_1^0} > m_M + m_{l_i}$ the neutralino can decay via $\widetilde{\chi}_1^0 \to M^+ \ell^-, M^- \ell^+$ or $\widetilde{\chi}_1^0 \to M^0 \nu, \bar{M}^0 \bar{\nu}$. Such decays are necessary to produce an observable final state in the SHiP detector.

From the structure of the operators in Eqs. (7.18) to (7.21), the definition of the effective couplings and the meson structure constants in Eqs. (7.23) to (7.25), we obtain the following unpolarized decay widths:

$$\Gamma(M_{ab} \to \widetilde{\chi}_1^0 l_i) = \frac{\lambda^{\frac{1}{2}}(m_{M_{ab}}^2, m_{\widetilde{\chi}_1^0}^2, m_{l_i}^2)}{64\pi m_{M_{ab}}^3} |G_{iab}^{S,f}|^2 (f_{M_{ab}}^S)^2 (m_{M_{ab}}^2 - m_{\widetilde{\chi}_1^0}^2 - m_{l_i}^2), \tag{7.26}$$

$$\Gamma(M_{ab}^* \to \widetilde{\chi}_1^0 l_i) = \frac{\lambda^{\frac{1}{2}}(m_{M_{ab}^*}^2, m_{\widetilde{\chi}_1^0}^2, m_{l_i}^2)}{3\pi m_{M_{ab}^*}^3} |G_{iab}^{T,f}|^2 (f_{M_{ab}^*}^T)^2 \times \left[m_{M_{ab}^*}^2 (m_{M_{ab}^*}^2 + m_{\widetilde{\chi}_1^0}^2 + m_{l_i}^2) - 2(m_{\widetilde{\chi}_1^0}^2 - m_{l_i}^2)^2 \right], \tag{7.27}$$

$$\Gamma(\widetilde{\chi}_1^0 \to M_{ab} l_i) = \frac{\lambda^{\frac{1}{2}}(m_{\widetilde{\chi}_1^0}^2, m_{M_{ab}}^2, m_{l_i}^2)}{128\pi m_{\widetilde{\chi}_1^0}^3} |G_{iab}^{S,f}|^2 (f_{M_{ab}}^S)^2 (m_{\widetilde{\chi}_1^0}^2 + m_{l_i}^2 - m_{M_{ab}}^2), \tag{7.28}$$

$$\Gamma(\widetilde{\chi}_1^0 \to M_{ab}^* l_i) = \frac{\lambda^{\frac{1}{2}}(m_{\widetilde{\chi}_1^0}^2, m_{M_{ab}^*}^2, m_{l_i}^2)}{2\pi m_{\widetilde{\chi}_1^0}^3} |G_{iab}^{T,f}|^2 (f_{M_{ab}^*}^T)^2 \times \left[2(m_{\widetilde{\chi}_1^0}^2 - m_{l_i}^2)^2 - m_{M_{ab}^*}^2 (m_{M_{ab}^*}^2 + m_{\widetilde{\chi}_1^0}^2 + m_{l_i}^2) \right]. \tag{7.29}$$

Here, l_i either denotes $\ell_i^\pm$ or ν_i, depending on whether M_{ab} is charged or neutral. The phase space function $\lambda^{\frac{1}{2}}(x,y,z) \equiv \sqrt{x^2+y^2+z^2-2xy-2xz-2yz}$ is propotional to the momentum of the daughter particles in the mother's rest frame. The coefficients G are defined in Eqs. (7.18) to (7.21). For each of the above decays there exists a charge-conjugated process with identical decay width. In Table 7.2 we list the relevant mesons M_{ab} that participate in each interaction for given quark family indices a, b

For light neutral pseudoscalar mesons, mass and flavour eigenstates do not coincide. For our studies this is only relevant for the $\bar{K}_{L,S}^0$, η, and η' mesons as we take ϕ to be a pure $(s\bar{s})$ state. For the former, we neglect any $\mathcal{CP}$-violation and define the mass eigenstates $|K_{L/S}\rangle \equiv (|K_0\rangle \pm |\bar{K}_0\rangle)/\sqrt{2}$, where $|K_0\rangle$ and $|\bar{K}_0\rangle$ are flavor eigenstates $(d\bar{s})$ and $(s\bar{d})$, respectively. We can then read off the decay constants from

$$\langle 0|\bar{s}\gamma^\mu\gamma^5 d|K_L^0(p)\rangle = + \langle 0|\bar{d}\gamma^\mu\gamma^5 s|K_L^0(p)\rangle = \frac{ip^\mu f_K}{\sqrt{2}}, \tag{7.30}$$

$$\langle 0|\bar{s}\gamma^\mu\gamma^5 d|K_S^0(p)\rangle = - \langle 0|\bar{d}\gamma^\mu\gamma^5 s|K_S^0(p)\rangle = \frac{ip^\mu f_K}{\sqrt{2}}, \tag{7.31}$$

where f_K is the decay constant of the charged kaon as defined in Eq. (7.22).

For η and η' we consider mixing between the η^0 and η^8 flavor states. We are only interested in the $(\bar{s}s)$ content of these mesons. We follow Refs. [332, 353] and define

$$\langle 0|\bar{s}\gamma^\mu\gamma^5 s|\{\eta,\, \eta'\}(p)\rangle = ip^\mu f_{\{\eta,\eta'\}}^{\bar{s}s}\,, \tag{7.32}$$

Coupling	Which ($\bar{q}q$)	Relevant Mesons	Coupling	Which ($\bar{q}q$)	Relevant Mesons
λ'_{i11}	$(u\bar{d})$	π^+, ρ^+	λ'_{i22}	$(c\bar{s})$	D_s^+, D_s^{*+}
	$(d\bar{d})$	$\pi^0, \eta, \eta', \rho, \omega$		$(s\bar{s})$	η, η', ϕ
λ'_{i12}	$(u\bar{s})$	K^+, K^{*+}	λ'_{i23}	$(c\bar{b})$	B_c^+, B_c^{*+}
	$(d\bar{s})$	K_L^0, K_S^0, K^{*0}		$(s\bar{b})$	B_s^0, B_s^{*0}
λ'_{i13}	$(u\bar{b})$	B^+, B^{*+}	λ'_{i31}	$(b\bar{d})$	B^0, B^{*0}
	$(d\bar{b})$	B^0, B^{*0}	λ'_{i32}	$(s\bar{b})$	B_s^0, B_s^{*0}
λ'_{i21}	$(c\bar{d})$	D^+, D^{*+}	λ'_{i33}	$(b\bar{b})$	η_b, Υ
	$(s\bar{d})$	K_L^0, K_S^0, K^{*0}			

Table 7.2: Bilinear quark currents and resulting list of relevant mesons which can be derived from the R-parity violating operator $\lambda'_{iab}(\widehat{L}_i \cdot \widehat{Q}_a)\widehat{D}_b^c$ by the procedure explained in Section 7.3.1. The lepton index i is irrelevant for the meson-current discussion, however plays a role later in the discussion if kinematically possible decay scenarios.

and give numerical values in Table 7.3. Note that we take all Standard Model meson and lepton masses from Ref. [87].

7.4 Observable Signatures of *R*-Parity Violation

With the predicted decay widths at hand we investigate how and under which circumstances R-parity violation can be observed at the SHiP experiment.

7.4.1 Neutralino Production

Each λ' coupling causes at least one type of meson to decay into a neutralino and another charged or neutral lepton, provided it is kinematically allowed. This process serves as the initial neutralino production mechanism at SHiP in our analysis. Given the number N_M of mesons M produced at SHiP and the lifetime τ_M, the expected number of initially produced neutralinos is given by

$$N_\chi^{\text{prod.}} = \sum_M N_M \cdot \Gamma(M \to \tilde{\chi}_1^0 l) \cdot \tau_M. \tag{7.33}$$

As apparent from the previous section, for each operator there are both pseudoscalar and vector mesons which can produce neutralinos. However, the lifetimes of a pseudoscalar and the corresponding vector meson of the same quark composition differ by many orders of magnitude. As an example, for the lightest charged charm meson, $D^\pm$, and its vector resonance partner, $D^{*\pm}$, one finds $\tau_{D^{*\pm}}/\tau_{D^\pm} \approx 8 \times 10^{-9}$ [87]. Similar ratios appear for kaons and even though the lifetime of vector B-mesons is yet unknown there is no reason to expect largely different behaviour.

For the RPV decay widths, however, one finds that $\Gamma(D^{*\pm} \to \tilde{\chi}_1^0 \ell^\pm)/\Gamma(D^\pm \to \tilde{\chi}_1^0 \ell^\pm)$ depends mainly on the ratio of masses and of the effective operator couplings G_T/G_S. Thus, it is hardly larger than 2 orders of magnitude unless one chooses a very peculiar setup of fine-tuned

Decay Constant	Value	Refs.	Decay Constant	Value	Refs.
$f_\eta^{\bar{s}s}$	−142 MeV	[332, 353]	f_D, $f_{D^\star}^V$	205 MeV	[87]
$f_{\eta'}^{\bar{s}s}$	38 MeV	[332, 353]	f_{D_s}, $f_{D_s^\star}^V$	259 MeV	[87]
f_ϕ^V	230 MeV	[351]	f_B	191 MeV	[87]
f_K	156 MeV	[87]	f_{B_s}	228 MeV	[354]
$f_{K^*}^V$	230 MeV	[351]			

Table 7.3: Values of the pseudoscalar and vector decay constants that are used in the various benchmark scenarios. Definitions of the constants are given in Eqs. (7.22) to (7.24). Tensor decay constants are chosen to be equal to the pseudoscalar decay constants.

parameters. As the expected number of initial mesons, N_M and N_{M^*}, will also be of roughly the same order, we conclude that if both $M \to \widetilde{\chi}_1^0 f$ and $M^* \to \widetilde{\chi}_1^0 f$ are kinematically allowed, the contribution from vector meson decays is completely negligible.

In the small mass range $m_M < m_{\widetilde{\chi}_1^0} < m_{M^*}$ it might only be the vector mesons that can produce neutralinos in the first place, but by the above arguments and from the results below we expect the neutralino event rates to be far too small to be observable in this very limited mass window. We therefore ignore any neutralino production via vector meson decays in the following study.

7.4.2 Neutralino Decay

For the neutralinos to be observable, a sufficiently high fraction must decay within the decay chamber of the SHiP experiment. By summing the widths $\Gamma(\widetilde{\chi}_1^0 \to Mf)$ of all allowed channels for a given operator, we can derive the proper lifetime of a neutralino given the parameters of the RPV supersymmetric model. Given the kinematical distributions of neutralinos produced via meson decay and knowing the geometry of the decay chamber, we can find the average probability $\langle P[\widetilde{\chi}_1^0 \text{ in d.r.}]\rangle$ of a neutralino decaying inside the detectable region. This is explained in more detail below.

A neutralino decaying inside the decay chamber is a necessary, but not a sufficient condition, as the final state particles have to be observed and traced back to an invisibly decaying new particle. For a charged final state, e.g. K^+e^-, one can measure the trajectory of both particles, measure their momenta and presumably identify the neutralino decay vertex. For a neutral final state, e.g. $K_L^0\nu$, one loses information on both tracks and the momentum of the second particle. We expect that these are hard to be linked to the decay of a neutralino. Thus we only count neutralinos that decay into charged final state particles. The final number of observed neutralinos is then

$$N_{\widetilde{\chi}_1^0}^{\text{obs.}} = N_{\widetilde{\chi}_1^0}^{\text{prod.}} \cdot \langle P[\widetilde{\chi}_1^0 \text{ in d.r.}]\rangle \cdot \text{Br}(\widetilde{\chi}_1^0 \to \text{charged})\,. \tag{7.34}$$

We should note that if we compare Eq. (7.40) with our general collider event formula in Eq. (3.1), one realises that we did not take into account the final state efficiency ϵ, i.e. the probability that a signal event would actually be counted by the detector according to the applied cuts. Also, our estimate for the acceptance $\mathcal{A}$ only requires the neutralino to decay inside the decay chamber but did not take into account the finite probability that the decay products actually

hit the detector. These factors do affect the expected number of observed events, however as signal and the very few expected background events e.g. from initially produced K_L^0 should be very well distinguishable, we hardly expect that the proper consideration of these factors changes the event rates by more than a factor of 2. In fact, since the exact details of e.g. energy thresholds in the detector are now known, a precise result could anyway not be calculated at this stage. In any event, as becomes apparent in our resuls below, such a relatively small change in event rates would barely be visible in our sensitivity curves which ranges over many orders of magnitude in the expected number of events.

With the above considerations, we thus demand the following conditions for observable neutralino decays via LQD operators at SHiP:

1. A pseudoscalar meson M with $m_M > m_{\widetilde{\chi}_1^0}$ must have a non-vanishing decay rate into neutralinos.

2. The neutralino must have a non-vanishing decay rate into another charged meson $M'^{\pm}$ with $m_{M'^{\pm}} < m_{\widetilde{\chi}_1^0} < m_M$.

With these conditions, it is practically impossible for SHiP to observe R-Parity violation if only one λ'_{iab} coupling is nonzero: Table 7.2 shows which operator leads to which sets of mesons that can decay into the neutralino or the neutralino can decay into. The only operator related to both a pseudoscalar meson M and a charged meson $M'^{\pm}$ with $m_M > m_{M'^{\pm}}$ is λ'_{112}, which might be observable via the chain

$$K_{L/S}^0 \to \widetilde{\chi}_1^0 \nu, \qquad \widetilde{\chi}_1^0 \to K^{\pm} \ell^{\mp} \,. \tag{7.35}$$

However, as $|m_{K^{\pm}} - m_{K_{L/S}^0}| \approx 4$ MeV, the testable range of neutralino masses is extremely limited and the expected energies of the final state particles are so small that the decays would be very challenging to observe.

Thus we require two different operators $\lambda'_{iab}, \lambda'_{jcd} \neq 0$, with iab and jcd such that the decays fulfill the above requirements. This necessary extension leads to a plethora of possible combinations. In Section 7.6 we restrict ourselves to an interesting subset of benchmark scenarios.

7.5 Simulation of RPV Scenarios

Eqs. (7.33) and (7.34) tell us how to estimate the number of observable neutralino decays $N_{\widetilde{\chi}_1^0}^{\text{obs}}$ for any given operator combination and parameter values. The total widths and branching ratios into charged final states can be calculated from the general width formulae, Eqs. (7.26) to (7.29). We next describe the numerical tools we use to estimate N_M and $\langle P[\widetilde{\chi}_1^0 \text{ in d.r.}]\rangle$.

To get a reliable estimate on the kinematics of the initially produced mesons at SHiP, as well as the resulting neutralinos after their decay, we use `Pythia 8.175` [147]. In scenarios with initial charm (bottom) mesons we use the `HardQCD:hardccbar` (`HardQCD:hardbbbar`) matrix element calculator within `Pythia`, which includes the partonic processes $q\bar{q}, gg \to c\bar{c}\,(b\bar{b})$ and select the specific meson type for each benchmark scenario. According to the original[4] SHiP proposal in Ref. [355], the number of $c\bar{c}$ events after 5 years of operation is expected to be

[4] By the time this project was completed, the updated physics case report in Ref. [329] had not been published yet.

Variable	Description	Numerical Value	Source
$N_{c\bar{c}}$	Number of initially produced $c\bar{c}$ events	9×10^{16}	Ref. [355]
$\sigma_{b\bar{b}}/\sigma_{c\bar{c}}$	Ratio of production cross sections	2.1×10^{-4}	`Pythia 8` [147]
$n_{D^\pm}^{c\bar{c}}$	produced $D^\pm$ mesons per $c\bar{c}$ event	0.53	`Pythia 8` [147]
$n_{D_s^\pm}^{c\bar{c}}$	produced $D_s^\pm$ mesons per $c\bar{c}$ event	0.074	`Pythia 8` [147]
$n_{B^\pm}^{b\bar{b}}$	produced $B^\pm$ mesons per $b\bar{b}$ event	0.83	`Pythia 8` [147]
$n_{B^0}^{b\bar{b}}$	produced B^0 mesons per $b\bar{b}$ event	0.80	`Pythia 8` [147]
$n_{B_s^0}^{b\bar{b}}$	produced B_s^0 mesons per $b\bar{b}$ event	0.14	`Pythia 8` [147]

Table 7.4: Numerical values used to estimate the number N_M in Eq. (7.38). Except for $N_{\bar{c}c}$, which is taken from [355], all numbers are evaluated by simulating 1M events of each `HardQCD` type in `Pythia 8`.

$N_{c\bar{c}} = 9 \times 10^{16}$. By simulating 1M events of type $c\bar{c}$, we can use `Pythia` to find the average number of produced charm mesons per $c\bar{c}$ event, i.e.

$$n_D^{c\bar{c}} \equiv N_D / N_{c\bar{c}}, \quad \text{with} \quad D \in \{D^\pm, D_s\}\,. \tag{7.36}$$

Note that N_D considers both D mesons which originate from hadronisation of a c quark as well as those produced from the immediate decay of heavy resonances, e.g. $(D^*)^\pm \to D^\pm \pi^0$. The analogous simulation of $b\bar{b}$ events gives the respective number for bottom mesons:

$$n_B^{b\bar{b}} \equiv N_B / N_{b\bar{b}}, \quad \text{with} \quad B \in \{B^0, B^\pm, B_s^0\}\,. \tag{7.37}$$

The total number of expected $b\bar{b}$ events is taken by scaling the known number for $c\bar{c}$ events by the ratio of total cross sections determined by `Pythia`, i.e. $N_{b\bar{b}} = N_{c\bar{c}} \times \sigma_{b\bar{b}}/\sigma_{c\bar{c}}$. We therefore combine

$$N_M = N_{c\bar{c}} \cdot \begin{cases} n_M^{c\bar{c}} & \text{for charm mesons} \\ n_M^{b\bar{b}} \cdot \sigma_{b\bar{b}}/\sigma_{c\bar{c}} & \text{for bottom mesons} \end{cases} \tag{7.38}$$

and list the numerical values in Table 7.4. Note that the number of $D^\pm$ mesons per $c\bar{c}$ event differs from the number of $B^\pm$ per $b\bar{b}$ event. This is mainly caused by the fact that $c\bar{c}$ and $b\bar{b}$ hadronise with same probabilities to the pseudoscalar ground state $D^\pm, B^\pm$ and the corresponding vector resonances $D^{*\pm}, B^{*\pm}$. Whilst the $D^{*\pm}$ decays at the rate of 1:2 into $D^+\pi^0$ and $D^-\pi^+$, the $B^{*\pm}$ has a nearly 100 % branching ratio into $B^\pm\gamma$ as the mass splitting between vector resonance and pseudoscalar ground state is smaller than the pion masses. This results in $n_{D^\pm}^{c\bar{c}} < n_{B^\pm}^{b\bar{b}}$ as shown in Table 7.4.

For each benchmark scenario, we simulate 20,000 events of the correct `HardQCD` type and — to increase statistics — set the branching ratio $\mathrm{Br}(M \to \widetilde{\chi}_1^0 f)$ to 100 %. We then scale the final numbers accordingly in our results. As the decaying mesons are scalar particles, the momentum of the neutralino is chosen to be uniformly distributed in the rest frame of the decaying meson. We then sum over all such produced neutralinos and determine the average probability, i.e. for all possible neutralino momenta, that an arbitrary neutralino decays within the SHiP detector. Given the four-vector of the ith simulated neutralino $(\widetilde{\chi}_1^0)_i$ in spherical

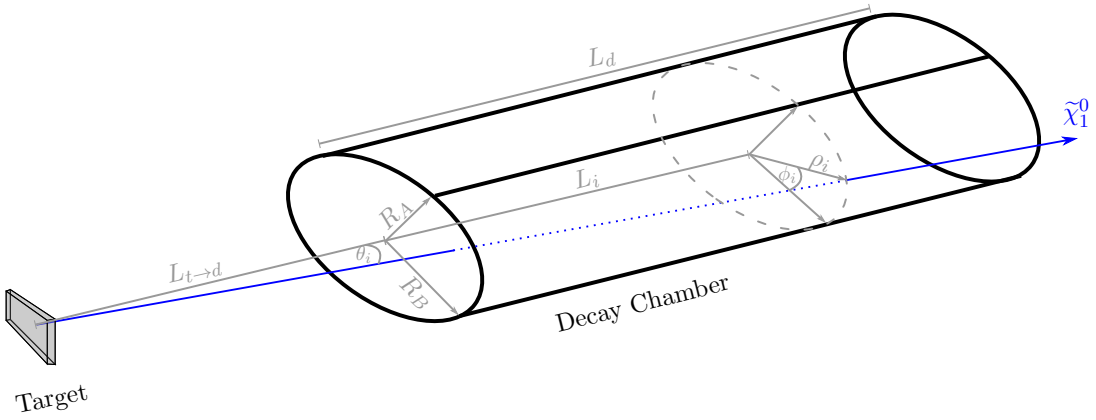

Figure 7.2: Schematic overview of the SHiP detector geometry and definition of distances and angles used in text.

coordinates as $(E_i, p_i^z, \theta_i, \phi_i)$ and the distances and angles as defined in Fig. 7.2, the average probability for N neutralinos in a given sample generated by a Monte Carlo program is evaluated as

$$\langle P[\tilde{\chi}_1^0 \text{ in d.r.}]\rangle = \frac{1}{N}\sum_{i=1}^{N} P[(\tilde{\chi}_1^0)_i \text{ in d.r.}], \tag{7.39}$$

$$P[(\tilde{\chi}_1^0)_i \text{ in d.r.}] = e^{-L_{t\to d}/\lambda_i^z}\cdot\left(1-e^{-L_i/\lambda_i^z}\right). \tag{7.40}$$

Here, λ_i^z denotes the mean decay length of the neutralino in the lab frame which is given by

$$\lambda_i^z = \beta_i^z\gamma_i/\Gamma_{\text{tot}}(\tilde{\chi}_1^0), \tag{7.41}$$

$$\beta_i^z = p_i^z/E_i, \tag{7.42}$$

$$\gamma_i = E_i/m_{\tilde{\chi}_1^0}. \tag{7.43}$$

β_i^z is the z-component of the relativistic velocity of $(\tilde{\chi}_1^0)_i$, γ_i the corresponding Lorentz boost factor. $\Gamma_{\text{tot}}(\tilde{\chi}_1^0)$ is the total decay width of the neutralino LSP, which only depends on the model parameters and not on the kinematics of an individual candidate $(\tilde{\chi}_1^0)_i$. L_i denotes the distance in z-direction a neutralino can travel inside the decay chamber before leaving it in radial direction. It can be determined as, see also Fig. 7.2,

$$L_i = \begin{cases} 0 & \text{if } \rho_i\cot\theta_i < L_{t\to d}, \\ L_d & \text{if } \rho_i\cot\theta_i > L_{t\to d}+L_d, \\ \rho_i\cot\theta_i - L_{t\to d} & \text{else,} \end{cases} \tag{7.44}$$

where

$$\rho_i = R_A R_B/\sqrt{(R_B\cos\phi_i)^2+(R_A\sin\phi_i)^2} \tag{7.45}$$

is the radius of the ellipsis in the direction ϕ_i. θ_i is the angle between the flight direction of the neutralino and the central axis of the detector; the polar angle, ϕ_i, is the azimuthal angle of the neutralino momentum 3-vector. R_A denotes the semi-minor axis, and R_B the semi-major axis of the elliptical face of the detector. $L_{t\to d}$ denotes the distance from the target to the front of the detector. L_d denotes the length of the detector along the central axis. As explained in Section 7.2.1, we use the numerical values $L_{t\to d} = 68.8\,\mathrm{m}, L_d = 55\,\mathrm{m}, R_A = 2.5\,\mathrm{m}$ and $R_B = 5\,\mathrm{m}$.

7.6 Results for Various Benchmark Scenarios

In Table 7.2 we have listed the twenty-seven operators λ'_{iab} together with the corresponding mesons they couple to. For a fixed lepton flavor there are 36 possible combinations for production and decay of the neutralinos, if we assume distinct operators. The number of possibilities exceeds 100 if one in addition tests all possible values for the lepton flavor indices. It is clear that we can not investigate all of these cases in detail. In order to analyze the sensitivity at SHiP, we have thus focussed on a subset which we propose as, hopefully representative, benchmark scenarios.

In choosing the benchmark scenarios, we took the following points into consideration. For the sensitivity, to first order, it does not matter if we consider electrons or muons. We thus restrict ourselves to electrons[5]. We have one benchmark with final state taus, as their considerably larger mass affects the accessible decay phase space and the respective total widths.

The meson production rates can differ substantially. Thus we consider various scenarios where the neutralinos are produced via neutral or charged D- or B-mesons. To estimate the production rates we use `Pythia`, as discussed above. We do not consider the production of neutralinos via $\lambda'_{i11}, \lambda'_{i12}$ as the production of the corresponding light mesons are not well simulated in forward direction with `Pythia`. For kinematic reasons, we restrict the final state mesons in the neutralino decays to K and D mesons. We also do not consider decays into pions and the associated vector resonances, as we expect sizable deviations from our approximations. However, from the results of the benchmark scenarios discussed below, an estimate for pion final states can be derived easily, by letting the neutralino mass range down to the pion mass of about 135 MeV, instead of the kaon mass. The pion and kaon decay constants are related by $SU(3)$ flavor symmetry. Of course, a neutralino decay into pions requires turning on the coupling λ'_{i11} where $i = 1, 2$. Note that in this case it does matter if $i = 2$ as now $m_\mu \simeq m_\pi$.

To be precise we consider the following benchmark cases.

7.6.1 Benchmark Scenario 1

We begin with scenarios where the neutralino is produced via the RPV decay of a D meson and subsequently decays into a kaon plus lepton. We turn on two RPV couplings λ'_{121} and λ'_{112}. Neutralino production then occurs via the decay $D^\pm \to \widetilde{\chi}^0_1 + e^\pm$ with a branching ratio nearly proportional to $(\lambda'_{121})^2$. The same coupling also leads to neutralino decay via the process $\widetilde{\chi}^0_1 \to (K^0_L, K^0_S, K^{*0}) + \nu$ which contains no charged particles in the final state and will therefore be difficult to observe. However, these decays do impact the neutralino lifetime. The relevant information is summarized in Table 7.5.

[5] Although the existing bounds on λ'_{2jk} are typically weaker than on λ'_{1jk} and we can have tighter bounds on coupling products with same lepton index i, see e.g. Table 7.1

Property	Value	Comments
λ'_P	λ'_{121}	
λ'_D	λ'_{112}	
M_{produced}	$D^{\pm}$	
$M^{\pm}_{\text{decay}}\ell^{\mp}$	$K^{\pm}e^{\mp}, K^{*\pm}e^{\mp}$	
M^{0}_{decay} via λ'_P	K^0_L, K^0_S, K^{*0}	
M^{0}_{decay} via λ'_D	K^0_L, K^0_S, K^{*0}	
applicable to	$\lambda'_P = \lambda'_{i21}, \lambda'_D = \lambda'_{j12}$	• $i, j \neq 3$ • for $i = 2$, upper kinematic bounds on $m_{\widetilde{\chi}^0_1}$ shift by m_μ to the left • for $j = 2$, lower kinematic bounds on $m_{\widetilde{\chi}^0_1}$ shift by m_μ to the right
	$\lambda'_P = \lambda'_{i21}, \lambda'_D = \lambda'_{j21}$	• $i, j \neq 3$ • for $i = 2$, upper kinematic bounds on $m_{\widetilde{\chi}^0_1}$ shift by m_μ to the left • only applicable if neutral final state can be observed

Table 7.5: Features of benchmark scenario 1. λ'_P, λ'_D define the λ'_{iab} coupling responsible for production and decay of the neutralino, respectively. The meson produced during the fixed target collision M_{produced} then decays into the neutralino via λ'_P, which then decays into the observable charged final states $M^{\pm}_{\text{decay}}\ell^{\mp}$ via λ'_D. In addition, decays into neutrinos and neutral mesons M^0_{decay} are typically induced in addition by λ'_P and λ'_D which decrease the neutralino lifetime and reduces the branching ratio into observable final states. In the "applicable to" section we list λ' combinations which lead to very similar results as those shown in Section 7.6.1, see also the in-text discussion.

Because we have turned on the coupling λ'_{112} the neutralino can furthermore decay via $\widetilde{\chi}^0_1 \to (K^{\pm}, K^{*\pm}) + e^{\mp}$, which is possible to detect at SHiP. This coupling also leads to the same invisible decay to neutral kaons and neutrinos as λ'_{121}. The invisible decays are important to include in the computation.

Taking the bounds listed in Table 7.1 into consideration, one finds that this setup with its nonvanishing $\lambda'_{121}\lambda'_{112}$ can be very tighly constrained by Kaon mixing. However, the Kaon mixing bound depends on the mass $m_{\tilde{\nu}_L}$ of the left-chiral sneutrino, while our effective interactions responsible for the more important visible charged final states in Eqs. (7.18) to (7.21) are independent of this mass. Hence, if sfermion masses are hierarchical, e.g. if sleptons turn out to be much heavier than squarks, the Kaon bound would be avoided while our results would be almost unchanged.

We now present our results. The expected number of events depends on three independent parameters: $\lambda'_{121}/m^2_{\tilde{f}}$, $\lambda'_{112}/m^2_{\tilde{f}}$, and the neutralino mass $m_{\widetilde{\chi}^0_1}$. We find it convenient to present our results in two different ways. At first, we assume the RPV coupling constants to be equal, $\lambda'_{121} = \lambda'_{112} \equiv \lambda'$. In Fig. 7.3a we show the number of expected visible neutralino decays in the SHiP detector as event rate iso-curves which are functions of $\lambda'/m^2_{\tilde{f}}$ and $m_{\widetilde{\chi}^0_1}$. The bright blue area bounded by a thick solid line shows the expected maximum sensitivity curve for the SHiP experiment. This area in parameter space gives rise to ≥ 3 neutralino decays within the

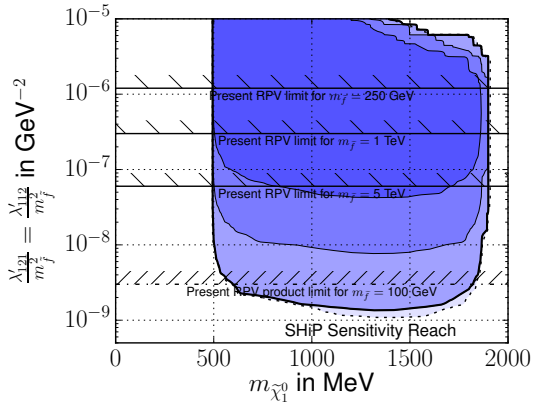

(a) Expected sensitivity bound with $\lambda_P = \lambda_D$. The maximum sensitivity reach, corresponding to ≥ 3 events, is shown in bright blue, with a solid curve edge. The blue area corresponds to $\geq 3 \cdot 10^3$ events and dark blue to $\geq 3 \cdot 10^6$ events. The dashed curve extending just below the light blue region denotes the extended sensitivity if the neutral mesons from neutralino decays are also visible.

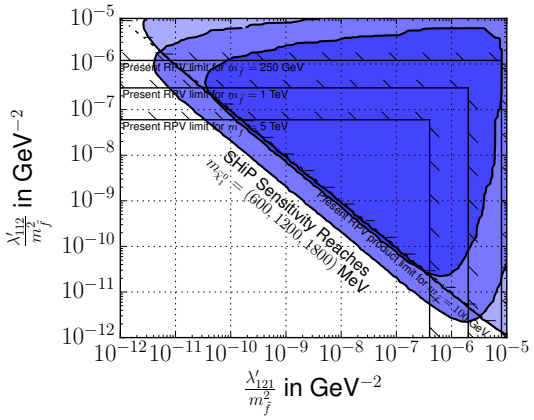

(b) Expected sensitivity bound, ≥ 3 events, as a function of the two independent RPV couplings for three fixed neutralino masses: 600 MeV (bright blue), 1200 MeV (blue), 1800 MeV (dark blue). For the x-axis we always choose the coupling responsible for the production of the neutralinos, here $\lambda'_{121}/m^2_{\tilde{f}}$. For the y-axis we choose the coupling responsible for the decay of the neutralinos, here $\lambda'_{112}/m^2_{\tilde{f}}$.

Figure 7.3: SHiP sensitivity curves for benchmark scenario 1. In both figures, straight hatched lines correspond to the existing limits on the RPV couplings as listed in Section 7.1.3, for three different sfermion masses: 250 GeV, 1 TeV and 5 TeV. We also show the respective product bound on $\lambda'_{121}\lambda'_{112}$ with a dot-dashed line and a sfermion mass of 100 GeV. Note that the dependence on the sfermion mass is identical for both types of bounds, such that it is sufficient to show the product operator bound for a single choice of $m_{\tilde{f}}$.

detector into charged final state particles for $2 \cdot 10^{20}$ protons-on-target expected in 5 years of operation. As no Standard Model background is expected for this search, this expected event yield would be sufficient to — if not observed — exclude the respective parameter combination.

The corresponding expected meson production rates are listed in Section 7.5. To show how the event rate increases with $\lambda'/m^2_{\tilde{f}}$ and $m_{\tilde{\chi}^0_1}$, we also show areas for $\geq 3 \cdot 10^3$ (blue) and $\geq 3 \cdot 10^6$ (dark blue) observable decays. The horizontal hashed lines depict existing bounds on single operators and operator products for various values of the sfermion mass $m_{\tilde{f}}$, cf. Section 7.1.3.

We see that if the SUSY setup is such that the Kaon bound holds, it cannot be challenged by SHiP for reasonable sfermion masses. However, if this bound does not apply, see our discussion above, the SHiP experiment can improve the current bounds on single $\lambda'/m^2_{\tilde{f}}$ couplings by one to three orders of magnitude depending on $m_{\tilde{f}}$. The kinematically accessible range for $m_{\tilde{\chi}^0_1}$ is dictated by the requirements that the neutralino must be lighter than the D-meson, yielding an upper bound, while at the same time being heavier than the K-meson, thus giving a lower bound. We find that the discovery region is mostly independent of $m_{\tilde{\chi}^0_1}$, i.e. the lower solid curve edge of the discovery range is fairly flat, as long as the mass lies within this kinematically

Property	Value	Comments
λ'_P	λ'_{122}	
λ'_D	λ'_{112}	
M_{produced}	$D_S^{\pm}$	
$M^{\pm}_{\text{decay}}\ell^{\mp}$	$K^{\pm}e^{\mp}, K^{*\pm}e^{\mp}$	
M^0_{decay} via λ'_P	η, η', ϕ	
M^0_{decay} via λ'_D	K^0_L, K^0_S, K^{*0}	
applicable to	$\lambda'_P = \lambda'_{i22}, \lambda'_D = \lambda'_{j12}$	• $i, j \neq 3$ • for $i = 2$, upper kinematic bounds on $m_{\widetilde{\chi}^0_1}$ shift by m_μ to the left • for $j = 2$, lower kinematic bounds on $m_{\widetilde{\chi}^0_1}$ shift by m_μ to the right
	$\lambda'_P = \lambda'_{i22}, \lambda'_D \in \left\{\lambda'_{j21}, \lambda'_{j22}\right\}$	• $i, j \neq 3$ • for $i = 2$, upper kinematic bounds on $m_{\widetilde{\chi}^0_1}$ shift by m_μ to the left • only applicable if neutral final state can be observed

Table 7.6: Features of benchmark scenario 2.

allowed range between 500 and 1900 MeV.

The additional small lighter shaded region marked by the dashed line indicates the extended sensitivity if the SHiP detector could detect neutral kaons in the final state, as well. In this particular scenario, this barely affects the exclusion contours because the branching ratios to visible and invisible final states are roughly the same. However, as we see below, in other scenarios the difference can be more substantial.

If $\lambda'/m^2_{\tilde{f}}$ becomes larger than $10^{-5}\,\text{GeV}^{-2}$, the neutralinos decay too fast, in fact mostly before reaching the detector. We note that this parameter region is subject to large numerical uncertainties in our Monte Carlo simulation approach, and as such the exclusion lines show fluctuations with no underlying physical cause.

In Fig. 7.3b we remove the restriction that the couplings λ'_{121} and λ'_{112} are equal. Instead, we present the SHiP sensitivity depending on the separate couplings for three representative values of $m_{\widetilde{\chi}^0_1}$. We choose a light mass close to the lower kinematic threshold (600 MeV, bright blue), a heavy one close to the higher kinematic threshold (1800 MeV, dark blue) and one halfway between the other two (1200 MeV, blue). In the same manner as before, existing limits on the two couplings are plotted for three representative values of $m_{\tilde{f}}$ and also the product limit is drawn. Again we see that the contours are fairly insensitive to the neutralino mass. In all cases, SHiP probes a new region of parameter space even for 5 TeV sfermion masses if the Kaon bound is avoided. The shape of the sensitivity regions are due to *both* couplings defining the neutralino lifetime, but only λ'_{121} leads to the production and only λ'_{112} to the *observable* decay of the neutralinos. To avoid confusion, let us call the couplings λ'_P and λ'_D respectively in the following discussion. If $\lambda'_P/m^2_{\tilde{f}}$ becomes too small, too few neutralinos are produced in the first place. This leads to an overall minimum requirement on $\lambda'_P/m^2_{\tilde{f}}$.

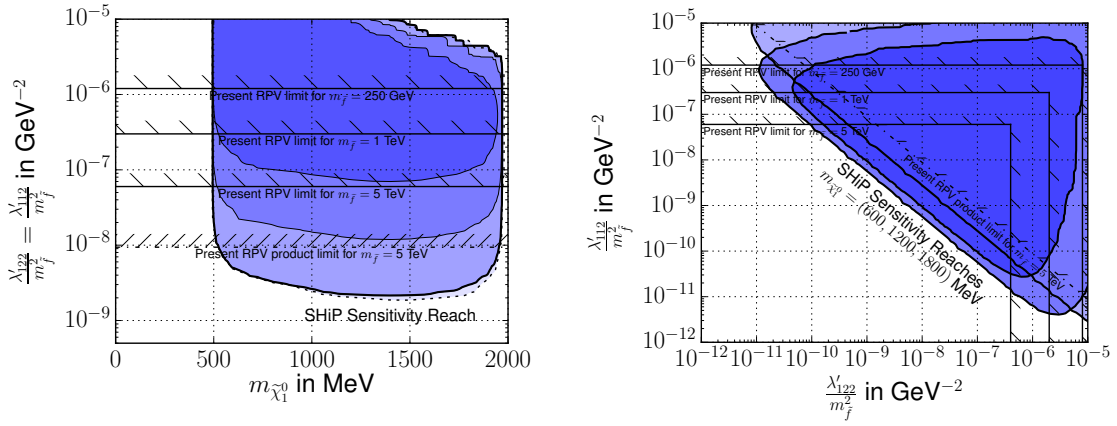

(a) (b)

Figure 7.4: Search sensitivity for benchmark scenario 2. The labelling is as in Fig. 7.3, except for the couplings λ'_{112}, λ'_{122}. Also, as the product operator bound is not as severe as in benchmark case 1, we now chose to show it for the case of $m_{\tilde{f}} = 5\,\text{TeV}$.

For increasing $\lambda'_P/m^2_{\tilde{f}}$, more neutralinos are produced and thus the allowed neutralino lifetime to observe three events at SHiP can be reached for increasingly larger ranges of $\lambda'_D/m^2_{\tilde{f}}$. As before, too small/large couplings lead to too many neutralinos decaying after/before the detector. Furthermore, smaller λ'_D/λ'_P ratios lead to more invisibly decaying neutralinos. In Fig. 7.3b this corresponds to the slanted edge running from the upper left-hand corner to the lower right-hand corner.

Once $\lambda'_P/m^2_{\tilde{f}}$ becomes too large, the lifetime induced by this operator is already too small and neutralinos decay mostly before reaching the detector, regardless of $\lambda'_D/m^2_{\tilde{f}}$. This explains the sensitivity limitations on the right edge of Fig. 7.3b.

This benchmark can easily be translated to arbitrary cases with $\lambda'_P = \lambda'_{i21}$ and/or $\lambda_D = \lambda'_{j12}$. Note that for $i = 2$, neutralinos are produced via $D^\pm \to \tilde{\chi}_1^0 + \mu^\pm$ and the extra muon would shift the upper kinematical limit of all regions in Fig. 7.3 by $m_\mu \approx 100\,\text{MeV}$ to the left. Analogously, the case $j = 2$ would move the lower kinematical limit of all but the shaded regions by the same amount to the right. Within this scenario, the cases $i = 3$ and/or $j = 3$ would not be observable as there would not be enough phase space to produce a τ lepton. Note that the corresponding single operator limits from low energy constraints are typically weaker for muons (see e.g. Ref. [96]) and the Kaon bound does not apply if $i \neq j$.

If SHiP is sensitive also to neutral final states, the above results also apply to the cases with $\lambda_D = \lambda'_{j21}$, again with $i, j \neq 3$. The sensitivity curve in this case would be very similar to the shaded region in Fig. 7.3a. The case $j = 2$ would not lead to a kinematic shift here as the neutralino would decay into the nearly massless muon neutrino which does not reduce the available phase space.

7.6.2 Benchmark Scenario 2

This is similar to the previous benchmark, except the production of the neutralinos is via D_s mesons. The observable charged final states are the same. There are however further invisible neutral final states, which are kinematically accessible: $(\eta, \eta', \phi) + (\nu, \bar{\nu})$. The details of this benchmark scenario are summarized in Table 7.6.

Property	Value	Comments
λ'_P	λ'_{131}	
λ'_D	λ'_{112}	
M_{produced}	$B^0, \bar{B}^0$	
$M^{\pm}_{\text{decay}}\ell^{\mp}$	$K^{\pm}e^{\mp}, K^{*\pm}e^{\mp}$	
M^0_{decay} via λ'_P	none	
M^0_{decay} via λ'_D	K^0_L, K^0_S, K^{*0}	
applicable to	$\lambda'_P = \lambda'_{i31}, \lambda'_D = \lambda'_{j12}$	• for $j = 2/3$, lower kinematic bounds on $m_{\tilde{\chi}^0_1}$ shift by m_μ/m_τ to the right

Table 7.7: Features of benchmark scenario 3.

The results for the SHiP sensitivity are presented in Fig. 7.4. The reach is extended to higher neutralino masses, as $M_{D_s} > M_D$. The lower edge is still given by $m_{\tilde{\chi}^0_1} \approx M_K$. The sensitivity in $\lambda'/m^2_{\tilde{f}}$ is slightly weaker for two reasons. First, the production rate D_s mesons is lower than $D^{\pm}$ mesons, see Table 7.4. Second, the neutralino branching ratio to an observable charged final state is smaller. Correspondingly the sensitivity is enhanced more in this scenario if neutral mesons are observable at SHiP, shown by the dashed line in the bottom of Fig. 7.4b.

Note that for the sake of uniformity, we again show bounds on single as well as product of operators, even though in this particular case they both depend scale with $m_{\tilde{s}_R}$ and therefore there is no case where the product bound could be evaded but the single operator bound would still apply. Contrarilty to the previous case, SHiP can even compete with product operator bounds for considerably heavy sfermion masses. With the same comments as for benchmark scenario 1, the analysis described here applies to the cases with $\lambda_D = \lambda'_{j12}, \lambda'_{j21}, \lambda'_{j22}$, with the last two only being possible if neutral final states are observable.

7.6.3 Benchmark Scenario 3

In this scenario the neutralino production proceeds via neutral B mesons. The decay of the neutralino via the coupling λ'_{112} leads to charged K-mesons and electrons, which are readily visible. The coupling λ'_{112} also leads to neutral neutralino decays to K^0 mesons and neutrinos. There are no additional kinematically accessible invisible neutralino decay modes through the coupling λ'_{131}. This information is summarized in Table 7.7.

The results of the simulation in this scenario are presented in Fig. 7.5. The kinematically accessible neutralino mass range is $M_{K^{\pm}} < m_{\tilde{\chi}^0_1} < M_{B^0}$. This is reflected in the shape of the sensitivity region in Fig. 7.5a, which is cut off on the left at a neutralino mass of about 500 MeV and on the right just under 5.3 GeV. In the top-right corner, where $\lambda'/m^2_{\tilde{f}}$ and $m_{\tilde{\chi}^0_1}$ are large, the neutralino lifetime becomes very short. The neutralinos then overwhelmingly decay before the detector. Since so few neutralinos reach the detector, we are here probing the extreme tail of the exponential decay distribution. Consequently, the top-right part of the curve is jagged, due to lack of statistics in this regime. The lower curve slopes downward left to right, much more so than in Figs. 7.3a and 7.4a. This effect is due to the presence of the final-state vector mesons K^{*0}, which are more important for the heavier neutralinos,

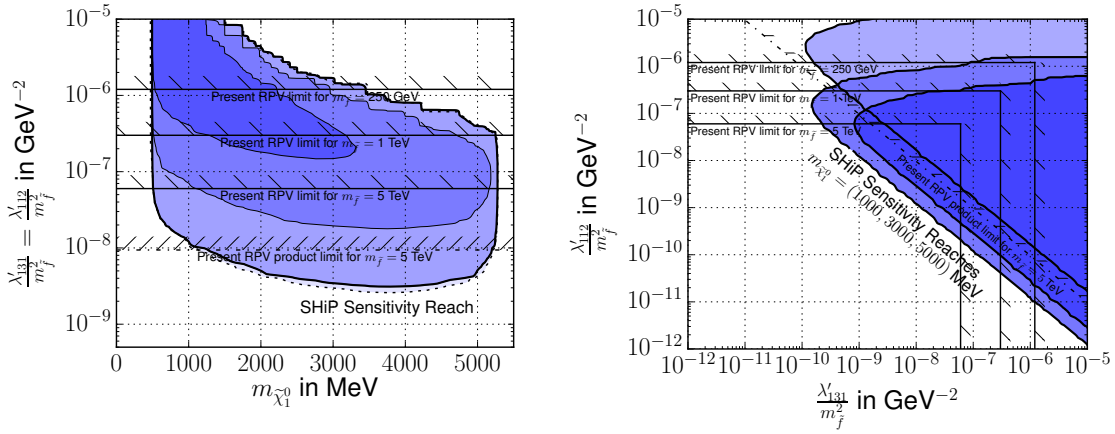

(a) (b)

Figure 7.5: Search sensitivity for benchmark scenario 3. The labelling is as in Fig. 7.3, except for the couplings λ'_{112}, λ'_{131}. Also in b) the neutralino masses are 1000 MeV (light blue), 3000 MeV (blue), and 5000 MeV (dark blue). Note that the x-axis range for figure a) has been changed compared to previous cases, as the initial state B meson allows for a larger kinematical reach.

accessible in B-meson decays. This is discussed in more detail in Section 7.6.6, below. The added sensitivity due to possible neutral final states is marginal, as the branching ratios are comparable. As can be seen from the numbers in Table 7.4, the B-meson production rate is roughly four orders of magnitude smaller than the D-meson production rate. As the neutralino production is proportional to $(\lambda'/m^2_{\tilde{f}})^2$, the curves in Fig. 7.5b are shifted by almost two orders of magnitude to the right, compared to the corresponding results, e.g. Fig. 7.3b, of the previous benchmark scenarios. The new sensitivity reach of SHiP is thus smaller here. However, since λ'_{131} does not induce any invisible decays of the neutralino, the sensitivity regions in Fig. 7.5b are not bounded on the right, in contrast to analogous regions of previous scenarios. Increasing $\lambda'_{131}/m^2_{\tilde{f}}$ then always leads to an increased number of expected neutralinos and hence always improves the sensitivity to $\lambda'_{112}/m^2_{\tilde{f}}$. We note that Fig. 7.5b has the same characteristic shape as 6 in Ref. [344]. Interestingly, even though the B meson production rate is considerably smaller than the D production rate of the previous two benchmark scenarios, SHiP is still expected to significantly improve on the existing λ' bounds listed in Table 7.1.

Analogously to the previous cases, the decay operator can be changed to λ'_{j12}. The phase space is suficient now to also allow for $i, j = 3$. Note that the lepton index i does not affect the upper kinematic bound for $m_{\tilde{\chi}^0_1}$ in the decay $B^0 \to \nu_i \tilde{\chi}^0_1$ whereas j shifts the lower bounds to the right. The particular effect of τ leptons in the decay chain is analysed in more detail within benchmark scenario 5.

7.6.4 Benchmark Scenario 4

In this scenario the neutralinos are also produced via B-mesons and the coupling λ'_{131}. However, now the decay is into D mesons via the coupling λ'_{121}. There are kinematically accessible invisible decays to neutral K mesons and neutrinos via λ'_{121}. This is summarized in Table 7.8. Note that there is no product limit on this operator combination such that existing limits come only from independent bounds on λ'_{131} and λ'_{121}.

Property	Value	Comments
λ'_P	λ'_{131}	
λ'_D	λ'_{121}	
M_{produced}	$B^0, \bar{B}^0$	
$M^{\pm}_{\text{decay}}\ell^{\mp}$	$D^{\pm}e^{\mp}, D^{*\pm}e^{\mp}$	
M^0_{decay} via λ'_P	none	
M^0_{decay} via λ'_D	K^0_L, K^0_S, K^{*0}	
applicable to	$\lambda'_P = \lambda'_{i31}, \lambda'_D \in \{\lambda'_{j21}, \lambda'_{j22}\}$	• $j \neq 3$ • for $j = 2$, lower kinematic bounds on $m_{\widetilde{\chi}^0_1}$ shift by m_μ to the right

Table 7.8: Features of benchmark scenario 4.

The results of the simulation for this scenario are displayed in Fig. 7.6. In the left panel, we show the search sensitivity as a function of the neutralino mass and of a common coupling $\lambda'_{113}/m^2_{\tilde{f}} = \lambda'_{112}/m^2_{\tilde{f}} \equiv \lambda'/m^2_{\tilde{f}}$. The mass sensitivity range is again mainly fixed kinematically: $M_D < m_{\widetilde{\chi}^0_1} < M_B$, which is narrower than in Fig. 7.5 due to the larger D-meson mass.

When allowing for neutral final states the sensitivity is dramatically increased to lower neutralino masses, corresponding to the kinematic range $M_K < m_{\widetilde{\chi}^0_1} < M_B$. This is shown in Fig. 7.6a by the very light blue region bounded by the dashed line.

In Fig. 7.6b the sensitivity range is similar to Fig. 7.5b, as it is dominated by B-meson production. The differences in the curves are mainly due to the different neutralino masses that are considered: 2000 MeV (light blue), 3500 MeV (blue), and 5000 MeV (dark blue).

We can extend this analysis to cases with $\lambda_D = \lambda'_{j21}, \lambda'_{j22}$, where in the latter the decay takes place via D_s mesons which have little effect on the kinematically available phase space. Note that j cannot be 3 here since the mass splitting of B and D mesons is below the tau lepton mass threshold.

7.6.5 Benchmark Scenario 5

Here the production goes via B-mesons and the coupling λ'_{313}. We thus consider the third generation lepton index. The features of this benchmark scenario are summarized in Fig. 7.7. It comes with two possible production modes for neutralinos, i.e.

$$B^{\pm} \to \widetilde{\chi}^0_1 \tau^{\pm} \,. \tag{7.46}$$

$$B^0 \to \widetilde{\chi}^0_1 \nu \,. \tag{7.47}$$

Therefore the charged $B^{\pm}$ meson can only contribute for the restricted neutralino mass range $m_{\widetilde{\chi}^0_1} < M_B - m_\tau$. The corresponding B^0-meson decay has neutrinos in the final state and is thus allowed for the larger range $m_{\widetilde{\chi}^0_1} < M_B$. In Fig. 7.7a this leads to a kink in the solid curves surrounding the sensitivity regions at $m_{\widetilde{\chi}^0_1} = M_B - m_\tau$. The region corresponding to $\geq 10^6$ events is also cut off to higher neutralino masses compared to Fig. 7.6a.

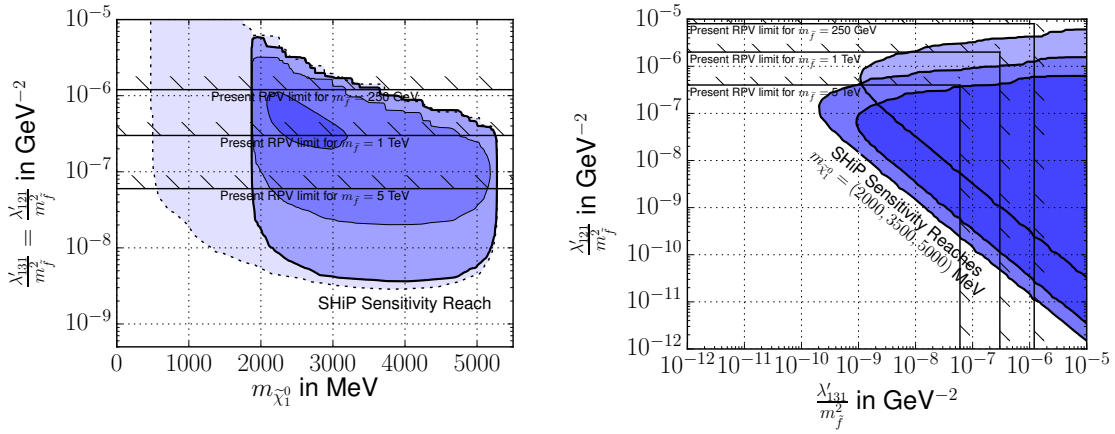

(a) (b)

Figure 7.6: Search sensitivity for benchmark scenario 4. The labelling is as in Fig. 7.3 except for the couplings λ'_{131}, λ'_{121}. Also in (b) the neutralino masses are 2000 MeV (light blue), 3500 MeV (blue), and 5000 MeV (dark blue) and there are no bounds on coupling products.

The neutralino decay proceeds via the coupling λ'_{312}.

$$\widetilde{\chi}^0_1 \to K^{\pm} + \tau^{\mp} \,. \tag{7.48}$$

Thus the visible final states involve charged K-mesons *and* tau leptons, which might be difficult to detect but which we for now do not treat differently than other charged final state particles before. This decay also requires $m_{\widetilde{\chi}^0_1} > M_K + m_\tau \simeq 2300\,\text{MeV}$ which explains the cutoff on the left of the blue regions in Fig. 7.7a.

There are possible additional neutral final states involving neutral K-mesons and neutrinos and *no* tau lepton. When these are included the sensitivity reach is dramatically extended to lower neutralino masses as can be seen in Fig. 7.7a, just as in Fig. 7.6a.

Fig. 7.7b shows the sensitivity region as a function of the two now independent couplings $\lambda'_{313}/m^2_{\tilde{f}}$ and $\lambda'_{312}/m^2_{\tilde{f}}$ for the three neutralino masses 2750 MeV (light blue), 3750 MeV (blue), and 5000 MeV (dark blue). These are slightly modified compared to Scenario 4, because of the tau mass, leading to slightly different curves.

As denoted in the bottom part of Table 7.8, the results of this benchmark case paired with the results from scenario 3 and 4 can be combined to cover various combinations, including production via B^0 or $B^{\pm}$ mesond and decays into K, D, D_S with and without τ leptons. These scenarios will mainly differ with respect to the kinematic ranges of accessible values for $m_{\widetilde{\chi}^0_1}$. One can also easily extend to the cases with λ_P being λ'_{i32} or λ'_{i23} by considering the production via B_s mesons. As can be seen from Table 7.4, B_s production is suppressed compared to B-meson production by roughly a factor $n^{b\bar{b}}_{B^0}/n^{b\bar{b}}_{B^0_s} \approx 0.18$. The sensitivity to the coupling $\lambda'/m^2_{\tilde{f}}$ is reduced by roughly a factor $\sqrt[4]{0.18} \approx 0.65$.

7.6.6 Relevance of Vector Mesons

As discussed at the end of Section 7.3.1, the inclusion of vector mesons in the final state lead to complementary dependence on SUSY paramaters. In addition, the final state vector mesons lead

Property	Value	Comments
λ'_P	λ'_{313}	
λ'_D	λ'_{312}	
M_{produced}	$B^0, \bar{B}^0, (B^\pm\tau^\mp)$	• $B^\pm$ only if $m_{\tilde{\chi}_1^0} < m_{B^\pm} - m_{\tau^\mp}$
$M^\pm_{\text{decay}}\ell^\mp$	$K^\pm\tau^\mp, K^{*\pm}\tau^\mp$	
M^0_{decay} via λ'_P	none	
M^0_{decay} via λ'_D	K^0_L, K^0_S, K^{*0}	
applicable to	$\lambda'_P = \lambda'_{i13}, \lambda'_D = \lambda'_{j12}$	• Thresholds depend on choice of $i, j = 1, 2, 3$
	$\lambda'_P = \lambda'_{i13}, \lambda'_D \in \{\lambda'_{j21}, \lambda'_{j22}\}$	• Thresholds depend on choice of $i = 1, 2, 3, j = 1, 2$ • As in benchmark case 4, decays to D mesons affect lower kinematic range
	$\lambda'_P = \lambda'_{i31}, \lambda'_D$ as above	• no contribution from $B^\pm$ • Thresholds depend on choice of $i, j = 1, 2, 3$ and if decays go via K or D
	$\lambda'_P \in \{\lambda'_{i32}, \lambda'_{i23}\}, \lambda'_D$ as above	• Production via B^0_s, see $n^{b\bar{b}}_{B^0_s}$ in Table 7.4 • Thresholds depend on choice of $i, j = 1, 2, 3$ and if decays go via K or D

Table 7.9: Features of benchmark scenario 5.

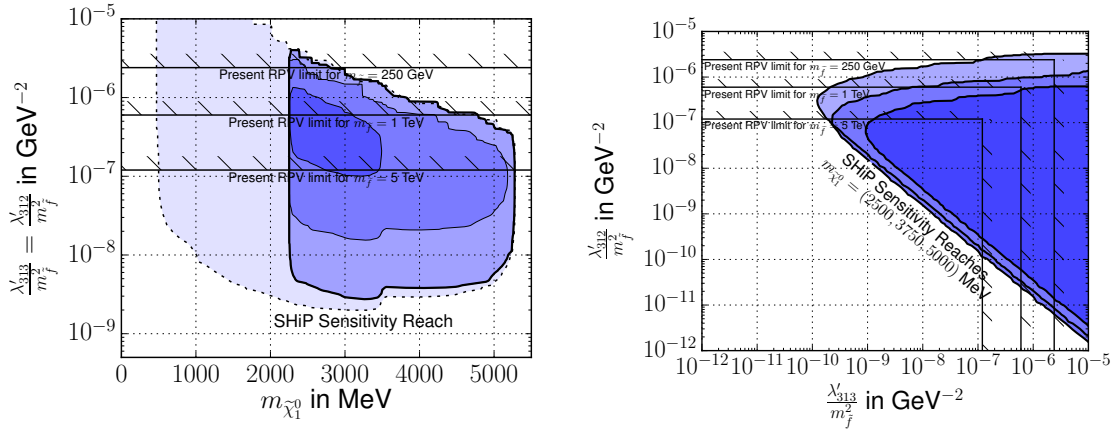

(a) (b)

Figure 7.7: Search sensitivity for benchmark scenario 5. The labelling is as in Fig. 7.3 except for the couplings λ'_{313}, λ'_{312}. Also in (b) the neutralino masses are 2750 MeV (light blue), 3750 MeV (blue), and 5000 MeV (dark blue).

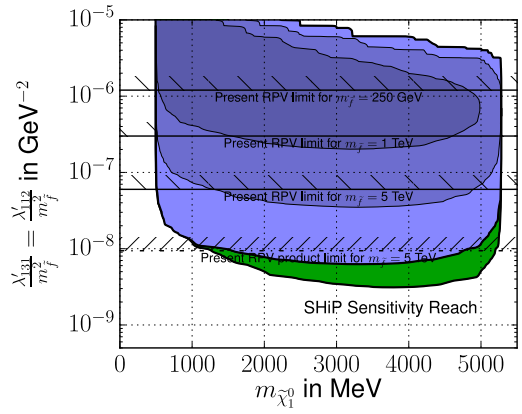

Figure 7.8: Sensitivity curve for enchmark Scenario 3 if decays into vector mesons are ignored. The green region shows the sensitivity curve including vector mesons which corresponds to the "SHiP Sensitivity Reach" of Fig. 7.5a

.

to an interesting kinematical enhancement of the neutralino decay width. This enhancement can be understood from the decay width formulæ in Eqs. (7.28) and (7.29). When $m_{\tilde{\chi}^0_1} \gg m_M$, where m_M is the mass of the final state meson, the decay to scalar mesons is proportional to

$$(f_M^S)^2 m^2_{\tilde{\chi}^0_1} \simeq f_M^2 m_M^2 m^2_{\tilde{\chi}^0_1}, \tag{7.49}$$

whereas the decay to vector mesons is proportional to

$$(f_M^T)^2 m^4_{\tilde{\chi}^0_1} \simeq f_M^2 m^4_{\tilde{\chi}^0_1}. \tag{7.50}$$

The decay into vector mesons is thus enhanced by roughly a factor

$$\frac{\Gamma(\tilde{\chi}^0_1 \to \text{ vector })}{\Gamma(\tilde{\chi}^0_1 \to \text{ pseudoscalar })} \approx \frac{m^2_{\tilde{\chi}^0_1}}{m_M^2} \gg 1. \tag{7.51}$$

This is mainly relevant for cases such as our benchmark scenario 3, where neutralino production occurs via B-meson decays. Then the neutralino can be significantly heavier than the final-state meson, here the kaon. To illustrate the enhancement, in Fig. 7.8, we repeat the analysis for benchmark scenario 3, but exclude final state vector mesons. The sensitivity contour of the same analysis including vector mesons is shown by the green shaded area. This region is identical to the sensitivity area shown in Fig. 7.6a. We show it again here to make the difference between the two cases easier to see. The inclusion of vector mesons is barely visible for neutralino masses smaller than 1 GeV, but the enhancement is clearly visible in the 2-5 GeV mass range.

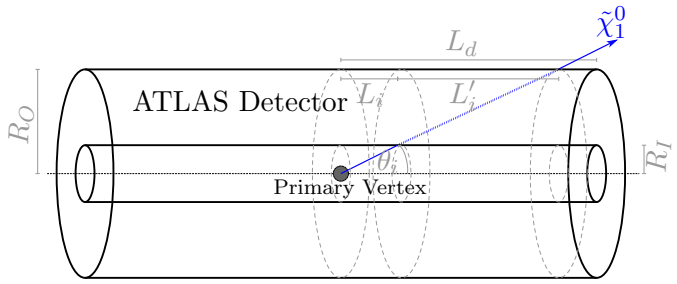

Figure 7.9: Schematic overview of the ATLAS detector geometry and definition of distances and angles used in text.

7.7 LHC Estimate

As we have seen, the sensitivity at SHiP in the production coupling results from an interplay between the length scales of the target- detector-distance $L_{t\to d}$, the length of the detector L_d, the meson production rate N_M, the boost γ_i of the neutralinos and their azimuthal angle θ_i. The LHC operates at much higher energies in the center-of-mass frame and the detectors are built right at the collision points. Thus all the above parameters change and we would expect a different sensitivity when comparing to SHiP[6]. To estimate the net result of these effects, we briefly discuss the sensitivity for our scenarios at the LHC here.

To allow for an easy comparison, we consider two example cases which correspond to our earlier discussed benchmark scenarios 1 and 5. These involve the observable decay chains

$$D^\pm \to \tilde{\chi}_1^0 e^\pm, \quad \tilde{\chi}_1^0 \to e^\pm K^\mp \quad \text{via } \lambda'_{121}, \lambda'_{112}, \tag{7.52}$$

$$B^\pm/B^0 \to \tilde{\chi}_1^0 \tau^\pm/\nu, \quad \tilde{\chi}_1^0 \to \tau^\pm K^\mp \quad \text{via } \lambda'_{313}, \lambda'_{312}. \tag{7.53}$$

To compare like with like, we estimate the neutralino event rates analogously to Section 7.5: we simulate these scenarios using `Pythia 8.175` and find a production cross section for $c\bar{c}$ at 14 TeV of $6\cdot 10^{12}$ fb and $\sigma_{b\bar{b}}/\sigma_{c\bar{c}} = 8.6\times 10^{-3}$. We consider an integrated luminosity of 250 fb^{-1}, which roughly corresponds to the expected value for a high-energy LHC running for 5 years — the same time period as we considered for SHiP. We determine the other parameters of interest as in Section 7.5 and list them in Table 7.10.

As an example we consider the ATLAS detector setup as sketched in Fig. 7.9. Here we assume the detectable region to approximately range from $R_I = 0.0505$ m, the beginning of the inner detector, to $R_O = 11$ m, the end of the muon chambers. The detector has cylindrical shape with a total length of $2L_D = 43$ m. The probability for the neutralino to decay within this range is then, similarly to Eq. (7.40),

$$P[(\tilde{\chi}_1^0)_i \text{ in d.r.}] = e^{-L_i/\lambda_i^z}\cdot(1-e^{-L_i'/\lambda_i^z}), \tag{7.54}$$

$$L_i \equiv \min(L_d, |R_I/\tan\theta_i|), \tag{7.55}$$

$$L_i' \equiv \min(L_d, |R_O/\tan\theta_i|) - L_i, \tag{7.56}$$

with angles and distances defined in Fig. 7.9 and λ_i^z as defined in Eq. (7.41). In similar manner as for SHiP, we use `Pythia` to simulate 20,000 events, force all mesons of the right type to

[6] We thank Jesse Thaler for drawing our attention to this point. See also Ref. [356] on a related discussion on dark photons.

Variable	Description	Numerical Value	Source
$N_{c\bar{c}}$	Number of initially produced $c\bar{c}$ events	1.5×10^{15}	`Pythia 8` [147]
$\sigma_{b\bar{b}}/\sigma_{c\bar{c}}$	Ratio of production cross sections	8.6×10^{-3}	`Pythia 8` [147]
$n^{c\bar{c}}_{D^\pm}$	produced $D^\pm$ mesons per $c\bar{c}$ event	0.59	`Pythia 8` [147]
$n^{b\bar{b}}_{B^\pm}$	produced $B^\pm$ mesons per $b\bar{b}$ event	0.87	`Pythia 8` [147]
$n^{b\bar{b}}_{B^0}$	produced B^0 mesons per $b\bar{b}$ event	0.87	`Pythia 8` [147]

Table 7.10: Numerical values used to estimate the number N_M in (Eq. (7.38)) for the LHC with $\sqrt{s} =$ 14 TeV and an integrated luminosity of 250 fb^{-1}. All numbers are evaluated by simulating 1M events of each `HardQCD` type in `Pythia`.

decay into neutralinos and average the results for $P[(\widetilde{\chi}^0_1)_i$ in d.r.] over all these Monte-Carlo neutralinos to find the overall probability that an LHC-produced neutralino decays inside the detectable region of the ATLAS detector. The number of observable neutralino decays is then determined by considering the RPV branching ratio of the initially produced mesons and the branching ratio of neutralinos into charged final states, according to Eqs. (7.33) and (7.34).

The expected sensitivity regions are shown in Fig. 7.10. For easy comparison we show the same information as in their corresponding SHiPs analogues Figs. 7.6a and 7.7a and focus on the 3 event threshold which would be required for a significant observation. We restrict the discussion to the $m_{\tilde{\chi}^0_1}$–$\lambda'/m^2_{\tilde{f}}$–plane as the limits in the $\lambda'_{\text{prod.}}/m^2_{\tilde{f}}$–$\lambda'_{\text{dec.}}/m^2_{\tilde{f}}$–plane can be easily deduced.

For both scenarios, the structure of the plots do not largely differ between ATLAS and SHiP. The testable kinematic regions are obviously identical for the same scenario and it is only the required value for $\lambda'/m^2_{\tilde{f}}$ to observe enough neutralino decays which changes. At SHiP we found that the expected sensitivity quickly drops if the neutralinos decay too promptly, that is before they reach the decay chamber at roughly 70 m behind the target. This resulted in an upper limit on the couplings SHiP would be sensitive to. However, as the detectable region at ATLAS already starts at $\mathcal{O}$(cm) distances from the primary vertex, this upper limit is pushed to higher values.

Comparing the results for scenario 1, Figs. 7.6a and 7.10a, we find that LHC has a comparable but still by a factor 2 weaker expected sensitivity on $\lambda'/m^2_{\tilde{f}}$ than the expected value from SHiP. From comparing the respective values for $N_{c\bar{c}}$ in Tables 7.10 and 7.10, one expects SHiP to produce almost 100 times more neutralinos than the LHC in a comparable time frame. This is partially compensated by the effect that neutralinos which are produced at large angles θ can be observed at the almost spherical ATLAS detector but miss the decay chamber at SHiP.

Furthermore, the boost distribution of the two experiments largely differ. The fixed target setup of SHiP causes most produced mesons to have a large boost which is inherited by the daughter neutralinos they decay into. Contrarily, the center-of-mass collision for the LHC will lead to most mesons to be produced at rest. We show the boost distribution of the neutralinos we get with `Pythia` in Fig. 7.11. For SHiP, the distribution shows an expectation value of $\langle\gamma\rangle \approx 30$ and a maximum probability for $\gamma_{\text{max}} \approx 7.5$. This leads to an increased lifetime in the lab frame which reduces the detection probability if $c\tau_\chi$ is larger than the size of the detector, see e.g. Eq. (7.40).

The large center-of-mass energy of the LHC leads to an even larger *average* boost, $\langle\gamma\rangle \approx 55$,

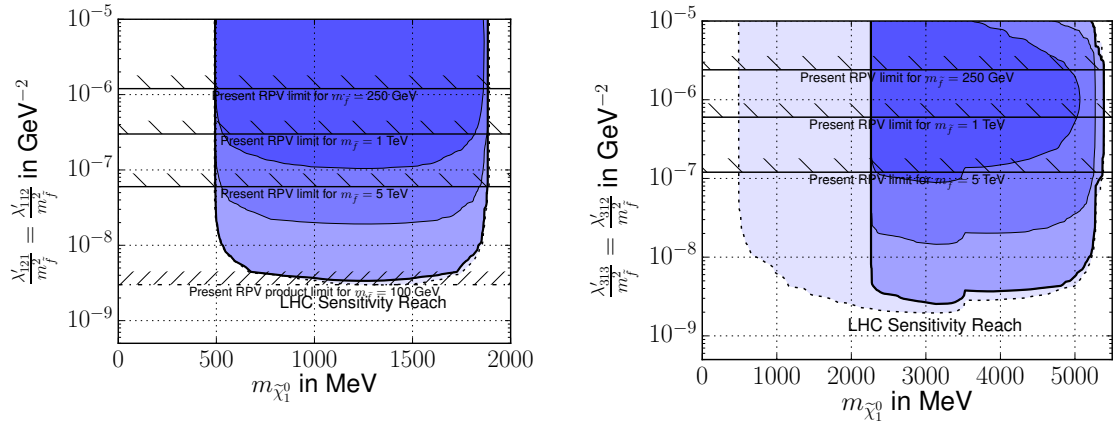

(a) Benchmark Scenario 1

(b) Benchmark Scenario 5

Figure 7.10: Expected LHC search sensitivities. The labelling is as in Figs. 7.3 and 7.7.

which however has a larger spread, resulting in many neutralinos with boost of $\mathcal{O}(1)$ and a few with boost $\mathcal{O}(1000)$. As shown in Fig. 7.11, the peak of the boost distribution for the LHC is located at $\gamma = 2.5$ and the resulting large fraction of unboosted neutralinos improve the overall probability to observe a decay within ATLAS.

Combining the above effects, we find that $\langle P[\widetilde{\chi}^0_1 \text{ in d.r.}]\rangle$ at ATLAS is greater by a factor 4 than at SHiP. Taking into account the much larger meson production yield of SHiP, it is expected to observe approximately 25 times more events than ATLAS, leading to an improved sensitivity on the coupling of $\sqrt[4]{25} \approx 2.2$.

For scenario 5, we compare Figs. 7.7a and 7.10b and interestingly find very comparable expected sensitivities. All the effects discussed for the previous scenario equally apply here and lead to approximately similar results. Therefore one would still expect SHiP to observe roughly 25 times more decays. However, this scenario requires B-mesons to be initially produced. The larger center-of-mass energy at LHC leads to an increased relative production yield $\sigma_{b\bar{b}}/\sigma_{c\bar{c}}$ of approximately 40 (see Tables 7.4 and 7.10). This results in a roughly 60 % larger overall expected event rate at the LHC, which however is a negligible improvement when translated into a limit on $\lambda'/m^2_{\tilde{f}}$.

It is clear that the results we show can just serve as a very approximate comparison. As we do not know the efficiency with which SHiP would be able to detect a neutralino decay and distinguish it from Standard Model, we did not take it into account for our LHC discussion either. However, it can be expected that the final state efficiencies for the two experiments differ significantly, most likely with a significant penalty on the ATLAS side. SHiP will be specifically designed to observe rare decays of new, long-lived particles. It can therefore be expected that the neutralino decays will have a large probability to actually be measured by the detector. The ATLAS detector, however, is not designed for this purpose. The combined efficiencies to trigger on the event, to reconstruct the final state particles, to identify the significantly displaced vertex and to distinguish it from Standard Model mesons decays will most likely lead to a significant reduction of the final event yield, potentially by orders of magnitude. Still, we find it an interesting observation that when just considering the geometry of the setup, the meson production yield and the expected kinematics of the neutralinos, SHiP and ATLAS

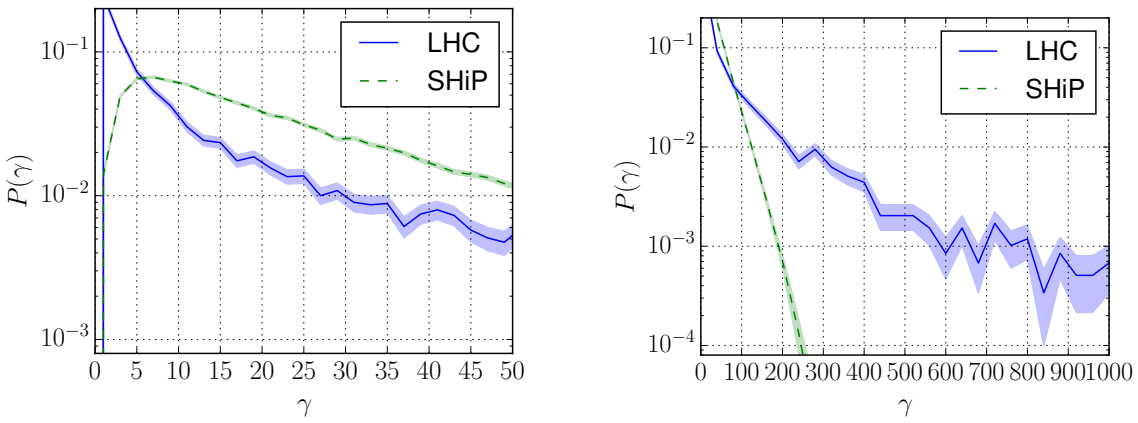

Figure 7.11: Boost distribution for neutralinos produced at a $\sqrt{s} = 14$ TeV LHC and at SHiP, determined with `Pythia`. We show the same results for two different choices of axis scaling. Fluctuations due to limited Monte Carlo statistics are denoted by respectively colored 1σ errorbands.

seem to have comparable sensitivity to the discussed decay scenario. Thus we conclude that the final state reconstruction efficiency will play a crucial role in determining the importance of the SHiP experiment with regards to the search for light neutralinos.

7.8 Summary

In this work we have studied the sensitivity of the proposed SHiP experiment to the R-parity violating production and decay of neutralinos whose masses lie in the range of $0.5 - 5$ GeV. As discussed in Section 2.4.3, a neutralino in this mass range is only allowed if R-parity is violated. We have focused on the semi-leptonic R-parity violating LQD operators but our work is easily extended to the purely leptonic case LLE. The basic idea pursued in this work is that a small fraction of the D and B mesons produced in the SHiP experiment, can potentially decay into a neutralino plus lepton. Because the R-parity violating couplings are expected to be small, the neutralino can have a sufficiently long lifetime to travel a distance of 63.8 m to the ShiP detector where it can subsequently decay into a, presumably detectable, meson-lepton pair.

For neutralinos in the mass-range of $0.5 - 5$ GeV, the SHiP experiment is sensitive to several combinations of R-parity violating couplings. In general, the number of neutralino decays in the SHiP detector is proportional to $(\lambda'_{iab}\lambda'_{jcd})^2/m^8_{\tilde{f}}$, where i, j denote the lepton generation indices and a, b, c, d the quark generation indices. We have classified benchmark scenarios for different combinations of the generation indices i, j, a, b, c, d. Although many different combinations of couplings exist, we have argued that most of them can be captured in this relatively small set of benchmark scenarios. We highlight here a number of conclusions and caveats of our findings.

- We find no feasible scenario where SHiP is sensitive to only a single λ'_{iab} coupling. The main obstacle for such a scenario is that the final state decay products will consist of a neutrino and a neutral meson from which it is difficult to reconstruct the neutralino decay. An example of such a scenario would be a nonzero λ'_{i21} coupling, which would lead to the production and decay channels $D^{\pm} \to \widetilde{\chi}^0_1 + l^{\pm}_i$ and $\widetilde{\chi}^0_1 \to K_{S,L} + \nu$. In order to get an observable final state we thus always require two distinct nonzero λ' couplings. We have found, however, that including the invisible final states is mandatory as they influence

the neutralino lifetime.

- That being said, we have shown that the SHiP experiment has the potential to significantly improve the constraints on various combinations of R-parity violating couplings. This is clearly illustrated in the figures in Section 7.6. For instance, constraints on $\lambda'_{112}/m^2_{\tilde{f}}$ can be strengthened by one to three orders of magnitude (see Fig. 7.3), depending on the sfermion mass. Similar improvements are found for third generation couplings such as $\lambda'_{131}\lambda'_{121}/m^4_{\tilde{f}}$. We have presented sensitivity curves for each of the benchmark scenarios: $[\lambda'_{121}, \lambda'_{112}]$, $[\lambda'_{122}, \lambda'_{112}]$, $[\lambda'_{131}, \lambda'_{112}]$, $[\lambda'_{131}, \lambda'_{121}]$, $[\lambda'_{313}, \lambda'_{312}]$. These curves can be used to estimate the sensitivity of the SHiP experiment to various combinations of R-parity violating interactions, as outlined in the text.

- We have focused on neutralino production via the decay of B and D mesons. Very light neutralinos could be produced in kaon decays and be detected by their subsequent decay into pionic final states. We have not included this in this work as the production of light mesons is not well simulated in the forward direction with `Pythia`. Such an extended study would extend the sensitivity to the neutralino mass range $0.1 - 0.5$ GeV. Similarly, including neutralino production in the decays of $\bar{b}b$ mesons would give a sensitivity to λ'_{i33} and to higher-mass neutralinos.

- We have found that including vector mesons in the final state leads to an enhanced sensitivity to neutralinos at the higher end of the allowed mass range. This enhancement can be understood from the decay-width formula presented in Section 7.3.2 as discussed in Section 7.6.6. In addition, the neutralino decay into vector mesons is proportional to a different combination of SUSY parameters than the corresponding decay into scalar mesons. The processes are therefore complementary.

- Our analysis did not include possible uncertainties arising from hadronic matrix elements. The decay constants used are not in all cases known to high precision. Nevertheless, the SHiP sensitivity curves range over many orders of magnitude and we do not expect that changes in the decay constants drastically change our conclusions.

- We determined the expected sensitivity of the ATLAS detector at a 14 TeV LHC with an integrated luminosity of $250\,\text{fb}^{-1}$. To do a fair comparison, we did not take into account the final state reconstruction efficiency and only determined the expected number of neutralino decays inside the detector region of ATLAS. We found that in scenarios with initially produced D mesons, ATLAS expects roughly 4 % of the number of events expected for SHiP, leading to an expected limit on $\lambda'/m^2_{\tilde{f}}$ which is weaker by roughly a factor of 2. This is caused by a combination of a larger meson flux expected for SHiP and a higher detection probability for long-lived neutralinos at ATLAS. For initially produced B mesons, the expected sensitivities are very similar, as the large LHC energies will produce relatively more b-quarks. It is therefore the final state reconstruction efficiency which will be the decisive factor.

CHAPTER 8

Conclusions and Outlook

We know that the Standard Model of particle physics suffers from many experimental and theoretical inconsistencies. As such it eventually has to be replaced by an improved theory which is able to solve these issues. The more experiments we perform whose outcomes violate the predictions of the Standard Model, the more information we gain about the nature of this new theory. In order to ascend the throne, it needs to be able to reproduce all of the correct predictions of the Standard Model while at the same time accounting for the observational discrepancies.

Primarily, however, this procedure requires discrepancies from the Standard Model to be observed. These were greatly awaited before the Large Hadron Collider was constructed, but unfortunately after the first sets of data have been taken at $\sqrt{s} = 7$ and 8 TeV, no such clear discrepancy was found and thus only constraints on new physics models can be made. Still, the more such constraints are taken into account, the more information one gains about those regions of parameter space which are sensible to consider further and which ones should be discarded. Practically however, it unfortunately becomes increasingly more difficult to simultaneously consider all LHC bounds as more and more results become available.

In this thesis, we discussed the tool `CheckMATE` which aims to provide a tool for the phenomenological community for the above purpose. By externally providing or internally generating simulated event files of a given BSM model, `CheckMATE` automatically applies a detector simulation tuned to well reproduce the accuracy of the ATLAS and CMS detectors. The reconstructed final state objects are then quantified by one or more analyses which determines the predicted number of signal events after a given set of cuts has been applied. After comparing to the respective number of observed and Standard Model expected events quoted by ATLAS or CMS in the corresponding publication, `CheckMATE` determines whether the prediction violates the observation or not. The internal structure of the tool is set up very model independently and thus `CheckMATE` can be used to test a large variety of BSM theories with or without Supersymmetry.

We performed phenomenological studies of three BSM theories which attempt to solve individual problems of the Standard Model. For two scenarios we used `CheckMATE` to do the collider phenomenology, in one case using the numerous implemented analyses to cover a large set of possible final state signatures, and in the other case to easily project an analysis performed at $\sqrt{s} = 8$ TeV to a high luminosity LHC running at its full centre-of-mass energy. The results have been discussed in the extensive summary sections of the respective chapters. In both cases, `CheckMATE` greatly eased the task of performing the collider tests. We merely had to use one of the available event generator tools which was compatible with the respective model of interest, state which analyses we wanted to test, and draw exclusion contours around those parameter points for which `CheckMATE` returned `excluded`.

Let us conclude with some further important aspects of CheckMATE which go beyond those already outlined within this thesis:

CheckMATE as an increasingly time economical tool: CheckMATE has been successfully used by many people outside the collaboration to test their respective models of interest without much effort. Due to the modular nature and the user friendly input routines, the program can easily be extended to new results from the LHC which await us in the near and far future. Especially now that ATLAS and CMS have started publishing more and more studies evaluated with $\sqrt{s} = 13\,\text{TeV}$ data, a tool like CheckMATE becomes increasingly more valuable. This is due to the above quoted problem of taking all available collider limits simultaneously into account which becomes even more complicated now that both results from 8 and 13 TeV are available. Without CheckMATE, analyses from both datasets would have to be filtered by hand for new studies which supersede analogous results from earlier analyses and vice versa old studies which have not yet been updated with new data. As there is however practically no disadvantage in simply considering all CheckMATE analyses at the same time, the above effort is easily avoided by making use of this tool.

CheckMATE as an analysis preservation tool: The era of the LHC has just started and already now, proper ways for a long-term conservation of LHC results even beyond its lifetime are discussed within the particle physics community, most recently in Ref. [357]. Here, a joint accord between phenomenologists and experimentalists is envisaged which ensures that no valuable information gets lost within the vast amount of individual publications which not always contain all required information in an unambigous way. A recasting framework like CheckMATE can be of great help in this regard as it necessarily needs to translate any implemented publication in a common, internal format already. As hopefully could be shown in this thesis, CheckMATE stores the required analysis information in a human readable form. Also, since any implemented analysis needs to pass a proper validation procedure before it can be made public, CheckMATE puts the completeness and unambiguity of the respective analysis publications to the test. The experimental collaborations therefore also profit from such a recasting tool as it can — and indeed did — find errors in these documents.

CheckMATE as a signal discovery tool: Throughout this thesis, CheckMATE was mainly advertised as a model exclusion tool. This might be in agreement with Popper's philosophy of science as outlined in the introductory chapter, however it states a rather pessimistic point of view that LHC results can only be used to identify incorrect models. It should be kept in mind though that as soon as a significant deviation from Standard Model predictions is found, CheckMATE can be used to exclude those models, first and foremost the Standard Model itself, which *falsely predict the absence of a signal*. This will hopefully only keep a small set of still viable particle physics models and might bring us much closer to the ultimate goal of selecting the one theory which replaces the Standard Model.

Still, as outlined in the introduction it is not only the predictability but also the falsifiability which is relevant for the formulation of a proper scientific theory. As such, before any such model can be claimed as the successor of the Standard Model, it must clearly still be tested for their compatibility with all the results of earlier analysis channels which were accurately predicted by the Standard Model[1]. With a tool like CheckMATE, this task can be performed

[1] In the wave of excitement about the recent $\approx 2\sigma$ global deviation of the measured diphoton invariant mass

almost immediately, as the overall structure of the program stays exactly the same and it is only the statistical evaluation methods which have to be adapted.

We should therefore continue updating `CheckMATE` with all the Standard Model compatible results, not in spite that we eagerly await signs of new physics to be seen, but because of it!

spectrum from Standard Model predictions [170], this supposedly obvious detail of proper scientific research seems to be easily overlooked.

Appendix

APPENDIX A

Additional Information for Chapter 3

A.1 Integrated Luminosity L

The instantaneous luminosity $\mathcal{L}$ is a purely experimental quantity which relates the event rate $\mathcal{R}$ for a given scattering process to the total cross section σ of that same process

$$\mathcal{L}(t) = \frac{\mathcal{R}_{pp\to X}(t)}{\sigma_{pp\to X}}. \tag{A.1}$$

Through fluctuations in the experimental setup, the event rate and $\mathcal{L}$ are functions of time. As we are interested in the total amount of events $N = \int \mathrm{d}t\ \mathcal{R}(t)$ after a certain time interval, it is the integrated luminosity $L = \int \mathrm{d}t\ \mathcal{L}(t)$ which is more interesting for our purposes; given L, a theoretically determined cross section can be translated into physical number of final state events.

For the frequent collision of proton bunches, as it is the case for the LHC, the luminosity can be evaluated geometrically from the total amount of bunches n_b, the amount of protons $n_{1/2}$ per bunch, the revolution frequency f_r and the spatial widths $\sigma_{x/y}$ of the Gaussianly spread proton beams as [360]

$$\mathcal{L}(t) = \frac{n_b f_r n_1 n_2}{2\pi\sigma_x\sigma_y}(t). \tag{A.2}$$

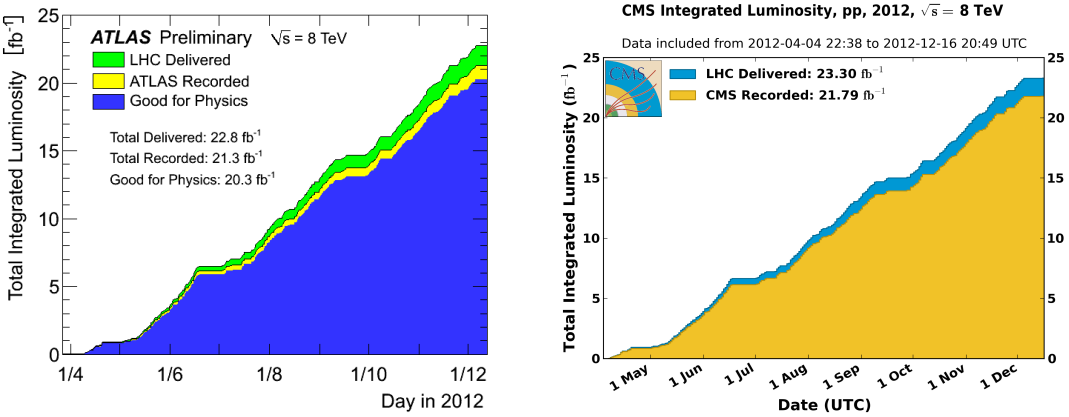

(a) ATLAS [358] (b) CMS [359]

Figure A.1: Cumulative luminosity versus day delivered to and recorded by the two multipurpose LHC experiments during stable beams and for p-p collisions at 8 TeV centre-of-mass energy in 2012.

With f_r, n_b, n_1 and n_2 being known beam parameters, the luminosity $\mathcal{L}(t)$ for a given beam setup can be determined by gradually changing the beam separation to determine its profile and fit $\sigma_{x/y}$, commonly known as *van der Meer scan* [361]. Then, with $\mathcal{L}(T_{\text{cal}})$ being known for a given beam setup, the time independent total visible cross section σ_{vis} of the detector around the collision area can be determined by measuring the event rate $\mathcal{R}_{\text{vis}}(T_{\text{cal}})$ inside the detectors and using Eq. (A.1). With σ_{vis} as a time-independent calibration constant, the luminosity can be re-evaluated at any time t from measuring the respective event rate $\mathcal{R}(t)$. More information about luminosity measurements at ATLAS and CMS can be found in e.g. [362, 363].

In most of the analyses performed within this work, the final datasets of the $\sqrt{s} = 8\,\text{TeV}$ run from ATLAS and CMS are used. In Fig. A.1, we show the cumulative luminosities for both experiments during this run. These final datasets correspond to an integrated luminosity of roughly 20 fb^{-1}.

A.2 Statistical Evaluation Revised

Within the main text, we gave the prescription to calculate CL_S in a scenario with a measurement of a counting experiment yielding N events, a fixed background expectation B and a fixed signal expectation S. Realistically, these two numbers are never known exactly, but rather within uncertainties $S \pm \Delta S$ and $B \pm \Delta B$. The errors are caused by systematic uncertainties from experimental error sources, approximations within the theoretical calculation and propagated errors from using physical quantities which have uncertainties by themselves. In addition, the finite sample size of the Monte-Carlo approach leads to a statistical uncertainty of the result. In the following, we assume that all these error sources can be combined into a single error ΔX. The algorithm, however, can be straightforwardly adapted to independent error sources ΔX_i.

Contrarily to the original calculation, we therefore now assume that we do not know the background for certain but that repeated evaluations would result in different values $B_{\text{unc.}}$ according to a probability density $P(B_{\text{unc.}}|B, \Delta_B)$. It is common practice to redefine $B_{\text{unc.}} = B_{\text{unc.}}(\theta)$ in terms of a dimensionless nuisance parameter θ, which is distributed according to a density function $P(\theta|\tilde{\theta})$ where $\tilde{\theta}$ is the *a priori* most probable value.

In the following, we choose $B_{\text{unc.}}(\theta) = B \exp(\theta \Delta B/B)$ and θ to be Gaussianly distributed according to $P(\theta|\tilde{\theta}) \propto \exp(-(\theta - \tilde{\theta})^2/2)$. With this choice of parameters, the *a priori* value for $\tilde{\theta}$ is 0. For small $\Delta B/B_0$, this *lognormal distribution* will lead to a Gaussianly disributed B_{unc} around B with width ΔB. However, for very large uncertainties it prevents $B(\theta)$ from turning to unphysical negative values. Following the same approach for $S(\theta)$ and assigning independent uncertainties to both yields the following extended likelihood[1].

$$\mathcal{L}(N, \tilde{\theta}_S, \tilde{\theta}_B|\mu, \theta_B, \theta_S) = \left(\frac{1}{N!}\left[\lambda(\mu, \theta_B, \theta_S)\right]^N e^{-\lambda(\mu,\theta_B,\theta_S)}\right) \cdot \left(e^{-\frac{(\tilde{\theta}_B - \theta_B)^2}{2}}\right) \cdot \left(e^{-\frac{(\tilde{\theta}_S - \theta_S)^2}{2}}\right), \quad \text{(A.3)}$$

$$\lambda(\theta_B, \theta_S) = \mu S e^{\left(\frac{\Delta S}{S}\theta_S\right)} + B e^{\left(\frac{\Delta B}{B}\theta_B\right)}. \quad \text{(A.4)}$$

Note that we have introduced the signal strength modifier μ, which will prove more convenient in distinguishing signal and background hypotheses for varying $S_{\text{unc}}(\theta_S)$.

[1] Note that we can safely ignore normalisation factors for the Gaussian distributions as they will not contribute to the likelihood ratio.

There are different approaches to incorporate the unknown nuisance parameters θ_B, θ_S into the test statistic. A standard approach is the usage of the *Profile Likelihood Ratio* defined as

$$q_\mu(N, \tilde{\theta}_S, \tilde{\theta}_B) \equiv -2 \log \left(\frac{\mathcal{L}(N, \tilde{\theta}_S, \tilde{\theta}_B | \mu, \hat{\theta}_S^\mu, \hat{\theta}_B^\mu)}{\mathcal{L}(N, \tilde{\theta}_S, \tilde{\theta}_B | \hat{\mu}, \hat{\theta}_S, \hat{\theta}_B)} \right). \tag{A.5}$$

Here, $\hat{\mu} \in [0, \mu], \hat{\theta}_S, \hat{\theta}_B$ is the combination of all three parameters which maximises $\mathcal{L}$, whereas $\hat{\theta}_S^\mu, \hat{\theta}_B^\mu$ are the values which maximise $\mathcal{L}(\mu)$ for fixed μ. Again, $q_\mu(N, \tilde{\theta}_S, \tilde{\theta}_B)$ becomes larger for less compatibility of observation and null hypothesis and the reason to take the ratio with the global maximum is to use a test statistics which becomes χ^2-distributed for large event rates. Note that even for our rather simple statistical setup, the denominator can but the numerator cannot be evaluated analytically. As such, numerical routines are necessary for the evaluation of the test statistic.

The motivation behind the evaluation of CL_{S+B}, CL_B and CL_S is the same as before. However, the appearance of nuisance parameters renders the calculation slightly more complicated: If the hypothesis $\mu = 1$ was true, according to the likelihood the most compatible values for the nuisance parameters θ_S, θ_B with respect to the observed value N would be their best fit values $\hat{\theta}_S^{\mu=1}$, $\hat{\theta}_B^{\mu=1}$. If we thus *a posteriori* assume these were the true values, when hypothetically redoing the experiment we expect the number of events N' to be Poisson distributed according to $\lambda(\mu = 1, \hat{\theta}_S^{\mu=1}, \hat{\theta}_B^{\mu=1})$. Furthermore, a similarly hypothetically repeated evaluation of B_{unc} and S_{unc} should yield different best-guess nuisance parameters $\tilde{\theta}'_S, \tilde{\theta}'_B$ each time, which however are expected to be Gaussian distributed around the allegedly true values $\theta_S^{\mu=1}, \theta_B^{\mu=1}$. Therefore the chances in the infinite repetition limit of observing an at least as bad test statistic as the observed one would be

$$\begin{aligned} CL_{S+B} = \sum_{N'=0}^{\infty} \int_{-\infty}^{\infty} \mathrm{d}\tilde{\theta}'_S \int_{-\infty}^{\infty} \mathrm{d}\tilde{\theta}'_B \; \Theta\Big(q_S(N', \tilde{\theta}'_S, \tilde{\theta}'_B) - q_S(N, \tilde{\theta}_S, \tilde{\theta}_B)\Big) \times \\ \mathrm{Poiss}(N' | \lambda(\mu = 1, \hat{\theta}_S^{\mu=1}, \hat{\theta}_B^{\mu=1}) \cdot \mathrm{Gauss}(\tilde{\theta}'_S | \hat{\theta}_S^{\mu=1}) \cdot \mathrm{Gauss}(\tilde{\theta}'_B | \hat{\theta}_B^{\mu=1}). \end{aligned} \tag{A.6}$$

Analogously we can argue the evaluation for the alternative $\mu = 0$ hypothesis

$$\begin{aligned} 1 - CL_B = \sum_{N'=0}^{\infty} \int_{-\infty}^{\infty} \mathrm{d}\tilde{\theta}'_S \int_{-\infty}^{\infty} \mathrm{d}\tilde{\theta}'_B \; \Theta\Big(q_S(N', \tilde{\theta}'_S, \tilde{\theta}'_B) - q_S(N, \tilde{\theta}_S, \tilde{\theta}_B)\Big) \times \\ \mathrm{Poiss}(N' | \lambda(\mu = 0, \hat{\theta}_S^{\mu=0}, \hat{\theta}_B^{\mu=0}) \cdot \mathrm{Gauss}(\tilde{\theta}'_S | \hat{\theta}_S^{\mu=0}) \cdot \mathrm{Gauss}(\tilde{\theta}'_B | \hat{\theta}_B^{\mu=0}) \end{aligned} \tag{A.7}$$

Finally, as before, CL_S is the ratio of the two. The above integrals are most conveniently evaluated numerically by generation random numbers $N', \tilde{\theta}'_S$ and $\tilde{\theta}'_B$ according to their Poissonian/Gaussian probability distributions and to count those configurations which yield a larger or equal test statistic as the observed one. This number divided by the total number of generated configurations is then a numerical estimate for CL_X.

The above prescription can easily be extended to arbitrary many independent nuisance paramaters by simply extending the likelihood and the confidence level integrals by the probability density of each nuisance parameter and still maximising over all parameters for the test statistic. In a multi-bin analysis, each bin contributes with a Poissonian given $N_i, S_i, \Delta S_i, B_i$ and ΔB_i to the likelihood and gets an independent sum in the confidence level evaluation. However, for

finding the global maximum of the likelihood for the test statistic, the signal strength modifier μ is global for all bins! Therefore the calculation does not trivially factorise and the pratical evaluation becomes complicated quickly.

APPENDIX B

Additional Information for Chapter 4

B.1 Installing CheckMATE

In this section we give a detailled step-by-step tutorial to install **CheckMATE** and all the required dependencies to reproduce the examples shown in Chapter 4.

The entire package including source codes[1] for all requires tools can be downloaded from

http://checkmate.hepforge.org/private/CheckMATE-Thesis.tar.gz

This `gzip` compressed file can be extracted with the command

Terminal

```
~:  tar -xzf CheckMATE-Thesis.tar.gz
```

This should create a directory which we refer to as `$CMMAIN` in the following. It should contain the following files

Terminal

```
~:  ls $CMMAIN
CheckMATE-2.0.0beta  Delphes-3.2.0X  HepMC-2.6.9  Pythia-8.2.19  ROOT-5.34.36
```

We start with the installation[2]. of the **HepMC** library [160] which is required by **Pythia 8** to generate events in this event format. Here and in the following, we use `[...]` to denote the verbatim output created by the respective commands which we enter. These strongly depend on the system setup which is used. Typically, they should not contain any important information, however should any of the steps fail for an unexpected reason, e.g. a missing library or a

Terminal

```
~:  cd $CMMAIN/HepMC-2.6.9
$CMMAIN/HepMC-2.6.9:  ./configure --with-momentum=GEV --with-length=MM \
  --prefix=$CMMAIN/HepMC-2.6.9/build
[...]
$CMMAIN/HepMC-2.6.9:  make -j4
[...]
$CMMAIN/HepMC-2.6.9:  make install
[...]
```

[1] This tutorial has been tested on a Linux machine running under Ubuntu 16.04. The same source files can be used for other operating systems, however some flags might change or some additional system libraries might be required. We refer to the documentation pages of the respective tools if problems of that kind occur.

[2] Note that the `-j4` flag which we use here improves the compilation speed due to paralellisation into 4 independent processes. The number can be changed in accordance to the number of accessible cores on the computer.

If the installation finished successfully the `build` directory should contain the required libraries and header files which are needed by `Pythia 8`:

Terminal

```
$CMMAIN/HepMC-2.6.9:  ls build
include  lib  share
```

We can continue with the compilation and installation of the `Pythia 8` event generator:

Terminal

```
$CMMAIN/HepMC-2.6.9:  cd $CMMAIN/Pythia-8.2.19
$CMMAIN/Pythia-8.2.19:  ./configure --with-hepmc2=$CMMAIN/HepMC-2.6.9/build \
 --prefix=$CMMAIN/Pythia-8.2.19/build
[..]
$CMMAIN/Pythia-8.2.19:  make -j4
[...]
$CMMAIN/Pythia-8.2.19:  make install
[...]
```

Again, a successful installation prcedure should have filled the `build` directory with the necessary library files

Terminal

```
$CMMAIN/Pythia-8.2.19:  ls build
bin  include  lib  share
```

Next, we have to install the `ROOT` package

Terminal

```
$CMMAIN/Pythia-8.2.19:  cd $CMMAIN/ROOT-5.34.36
$CMMAIN/ROOT-5.34.36:  mkdir build
$CMMAIN/ROOT-5.34.36:  mkdir build/etc
$CMMAIN/ROOT-5.34.36:  ./configure --prefix=$CMMAIN/ROOT-5.34.36/build --disable-fftw3 \
  --enable-minuit2 --etcdir=$CMMAIN/ROOT-5.34.36/build/etc
[...]
$CMMAIN/ROOT-5.34.36:  make -j4
[...]
$CMMAIN/ROOT-5.34.36:  make install
[...]
```

Let us check again if the build directory contains all relevant files

Terminal

```
$CMMAIN/ROOT-5.34.36:   ls build
bin             etc      misc       rmkdepend  version.cxx
CMakeLists.txt  include  Module.mk  share      version_number
dummy.d         lib      package    unix       win
```

In order to build the `Delphes` detector simulation framework, we have to load the above compiled `ROOT` libraries

Terminal

```
$CMMAIN/ROOT-5.34.36:  cd $CMMAIN/Delphes-3.2.0X
$CMMAIN/Delphes-3.2.0X:  source $CMMAIN/ROOT-5.34.36/build/bin/thisroot.sh
$CMMAIN/Delphes-3.2.0X:  ./configure
$CMMAIN/Delphes-3.2.0X:  make -j4
[...]
```

A promising sign of a succesful installation is the presence of the file `libDelphes.so` within the `Delphes` directory.

With all required libraries being ready, we can finally compile the `CheckMATE` framework

Terminal

```
$CMMAIN/Delphes-3.2.0X:  cd $CMMAIN/Delphes-3.2.0X
$CMMAIN/CheckMATE-2.0.0beta:  ./configure --with-hepmc=$CMMAIN/HepMC-2.6.9/build \
  --with-pythia=$CMMAIN/Pythia-8.2.19/build --with-delphes=$CMMAIN/Delphes-3.2.0X \
  --with-rootsys=$CMMAIN/ROOT-5.34.36/build
[...]
 make -j4
[...]
 make install
```

Let us finish this tutorial with a simple test run, using an example spectrum file which is provided with the CheckMATE package. It corresponds to a CMSSM scenario with $\tan\beta = 10, m_0 = 100\,\text{GeV}, m_{1/2} = 250\,\text{GeV}, A_0 = -100\,\text{GeV}$ and positive μ. This results in a spectrum with all SUSY particles having mass in the range 100–600 GeV.

Terminal

```
$CMMAIN/CheckMATE-2.0.0beta/bin:  ./CheckMATE -pyp 'p p > go go' -maxev 100 \
  -slha example_run_cards/auxiliary/testspectrum.slha
[...]
Is this correct? (y/n)  y
[...]
Evaluating Results
Test: Calculation of r = signal/(95%CL limit on signal)
Result:  Excluded
Result for r: 1.15744708205
Analysis: atlas_1405_7875
SR: SR03_a.4jl-
```

Such a SUSY scenario is so constrained by existing LHC searches that even a sample of only 100 Monte-Carlo events is sufficient to exclude it within seconds.

B.2 Full List of CheckMATE Parameters

There exist many optional parameters within CheckMATE which can change the standard behaviour of the code. We already covered some of these in our example in Section 4.2 and want to provide the full list of currently implemented parameters here. One way to provide these is via the input file format which we used in the example. Alternatively, CheckMATE can be set up directly within the command line by adding arbitrary many `-parameter value` pairs after the `./CheckMATE` command. The second alternative is unfortunately only possible for a setup with only one process as only one `-p` command can be provided. If more than one process needs to be analysed at once, one either has to use the input file format or make use of the `add` feature described below.

The exhaustive list of currently implemtented analyses is given in Tables B.1 and B.2. We provide additional information for some of these below:

Analyses: Many analyses are already embedded into the CheckMATE framework, see also Section 4.4. The following possible specifications for `X` are allowed o specify which of these CheckMATE should be taken into account.

- `-a atlas_1404_2500` tests only analysis `atlas_1404_2500`
- `-a 8TeV` tests all implemented analyses which correspond to $\sqrt{s} = 8\,\text{TeV}$. This is the standard value if `-a` is not specified. Alternative values are `7TeV`, `13TeV` and `14TeV`.

Parameter Card	Terminal	Description
	General Options	
`Name: X`	`-n X`	Gives name `X` to the run which specifies output directory.
`Analyses: X`	`-a X`	States which analysis/es X should be applied on the processed event files, see text.
`SLHAFile: X`	`-slha X`	Use `SLHA` file X. Mandatory if event generation via `Pythia 8` is set up.
`InvisiblePIDs: X`	`-invpids X`	BSM Monte Carlo Particle IDs [140] which are invisible for the detector, see text.
`QuietMode: B`	`-q`	No terminal output is produced. Automatically sets `-sp`.
`SkipParamCheck: B`	`-sp`	Skip startup parameter check.
`SkipAnalysis: B`	`-sa`	Skip analysis step. Requires `-wp8` or `-wd`.
`SkipPythia: B`	`-spy`	Only if `.lhe` are provided. These are not showered by `Pythia 8` but instead directly processed via `Delphes`.
`SkipEvaluation: B`	`-se`	Skips evaluation step.
`RandomSeed: X`	`-rs X`	Chooses fixed seed `X` for random number generator to render output deterministic.
	Options related to output	
`WritePythiaEvents: B`	`-wp8`	Write `.hepmc` files produced by `Pythia 8` on disk.
`WriteDelphesEvents: B`	`-wd`	Write `.root` files produced by `Delphes` on disk.
`EventResult-FileColumns: X`	`-erfc X`	Sets columns which are stored in event-wise result files, see text
`ProcessResult-FileColumns: X`	`-prfc X`	Sets columns which are stored in process-wise result files, see text
`TotalResult-FileColumns: X`	`-tefc X`	Sets columns in `TotalResults.txt` after evaluation, see text.
`BestPerAnalysisResult-FileColumns: X`	`-bpaefc X`	Sets columns in `BestPerAnalysis.txt` after evaluation, see text.
`OutputDirectory: X`	`-od X`	Specifies directory in which the results should be stored.
`OutputExists: X`	`-oe X`	Speficy what to do if output directory already exists. `overwrite` will delete existing output and overwrite it with the new results. `add` will add the current results to the old ones, see text.

Table B.1: Summary of all parameters which can be set within `CheckMATE`, either via the parameter card introduced in Section 4.2 or as command line input `./CheckMATE -X -Y ...`. Occasional dash symbols (-) in the first column only indicate that a command is split in two lines to reduce the column width and are *not* part of the keyword.

Parameter Card	Terminal	Description
	Options related to statistical evaluation	
FullCLs: B	-cls	Evaluate full observed and expected CLs for all signal regions and use it for exclusion test.
BestCLs: X	-bcls X	As above but only for the X signal regions with highest rexpcons value.
Likelihood: B	-likeli	Evaluate likelihood for all signal regions using the MC-approach and sum all tested signal regions, see text.
Likelihood-RootMethod: B	-likelirm	Evaluate likelihood for each signal region using the As above using a faster method.
EffTab: B	-eff_tab	Creates efficiency tables for every signal region in each analysis run.
Process wise options		
[X]	-p X	Sets up a process with name X..
MaxEvents: X	-maxev X	Defines the number of generated events if Pythia 8 is used for generation. If events are provided, simulation stops when either the end of the event file or MaxEvents is reached.
XSect: X	-xs X	Sets the cross section for the given process including unit. *Must* be provided for .hepmc and .root input and *can* be provided to overwrite Pythia 8 results used otherwise.
XSectErr: X	-xse X	Sets the systematic cross section error for the given process including unit which can be %.
KFactor: X	-kf X	Sets the K-factor to multiply the cross section with.
Events: X	-ev X	Sets the .hepmc, .hep, .lhe or .root event files which are to be analysed for the given process.
Pythia8Process: X	-pyp X	Specifies the SUSY process to be generated by Pythia 8, see text.
Pythia8Card: X	-pyc X	Specifies the .in input card used by Pythia 8

Table B.2: Continuation of Table B.1.

- `-a atlas&8TeV` tests all implemented atlas analyses of the given center of mass energy. Similarly for `cms`.

Any of the above specifiers can be combined via simple separation with commas, e.g. `-a cms&8TeV, atlas_1404_2500` tests all 8 TeV CMS analyses and the single ATLAS analysis `atlas_1404_2500`. All analyses combined this way *must* correspond to the same center-of-mass energy, otherwise `CheckMATE` aborts.

Invisible PIDs: Physics beyond the Standard Model, especially if it is linked to the dark matter problem explained in Section 2.1.5, often predicts the existence of one or more stable, light particles which hardly interact with ordinary matter. Typical examples are the lightest neutralino in Supersymmetry, c.f. Section 2.4.3, or the hidden sector particles in a portal model, c.f. Section 2.2. Whilst `Delphes` automatically identifies all neutral MSSM SUSY particles, other BSM particles have to be explicitly declared as invisible as they otherwise are considered as exotic hadrons which deposit their energy into the hadronic calorimeter. As an example, a Higgs Portal model with a stable second scalar would require the setting `Invisible PIDs: 35`.

Result file columns: As stated in the example section, the content of the result files is adaptable such that more intermediate results are stored. By setting the corresponding `ResultFileColumns` parameter to `a,b,d,...` the corresponding file(s) are set to contain respective information a, b, c. `EventResultFileColumns` and `ProcessResultFileColumns` can be taken out of the following set:

`'analysis', 'sr', 'totalmcevents', 'totalnormevents', 'totalsumofweights', 'totalsumofweights2', 'signalsumofweights', 'signalsumofweights2', 'signalnormevents', 'signal_err_stat', 'signal_err_sys', 'signal_err_tot'`. The names are mostly self-explanatory; `total` refers to the full input sample whereas `signal` corresponds to the events which pass the respective signal region cuts. `weights2` corresponds to squared weights which are important to calculate the statistical uncertainty properly. `normevents` correspond to the physical number of events after normalising to the provided cross section and the analysis' respective integrated luminosity.

`TotalResultFileColumns` and `BestSignalRegionResultFileColumns` can in addition use the following columns

`'obs', 'bkg', 'bkgerr', 'eff', 'eff_err_stat', 'eff_err_sys' 'eff_err_tot', 's95obs', 's95exp', 'robs', 'robscons', 'robsconssysonly', 'rexp', 'rexpcons', 'rexpconssysonly', 'clsobs', 'clsobs_err', 'clsexp', 'clsexp_err', 'likelihood'` which are all self-explanatory. Note that CL_S and likelihood related columns are set to -1 unless the calculation of the respective quantity is enabled via the corresponding flag, see Table B.2.

`add` mode: After a `CheckMATE` run is completed, the user might realise that the events which were processed were insufficient. For example, the size of the tested Monte-Carlo samples might be too small to find the number S with good enough statistical precision. Alternatively, it might happen that *a posteriori* it becomes apparent that other processes need to be taken into account which were expected to be negligible before `CheckMATE` was run. For those cases, `CheckMATE` allows for new results to be added to old ones. To do so, `CheckMATE` has to be set up with the same name and the same output directory as

the original run. During the initialisation step it then explicitly asks the user if the new results are supposed to replace or to be added to the existing ones. If the second option is chosen, the original CheckMATE settings are restored from the earlier run, all events in the current setup file are processed and properly added to the ones of the first run. This procedure can be repeated arbitrary many times.

Likelihood: Instead of exclusion tests, CheckMATE can also be used for model fits by calculating the likelihood ratios for all signal regions which test the compatibility of a given model with the observered results. A formulae for a simplified LHC profile likelihood ratios without nuisance parameters is given in Eq. (3.12) in Section 3.3.3. CheckMATE uses the full version including ΔB and ΔS as nuisance parameters in Eq. (A.5) of Appendix A.2. In the final results, CheckMATE sums the likelihood ratios over all signal regions and returns this value to the user. Analysing the behavious of this quantity under change of model parameters can be used to find best fit points and the corresponding confidence intervals, see e.g. Ref. [364].

Pythia8Process: The production of pairs of SUSY particles in the MSSM is a standard benchmark scenario used in many LHC analyses to test the sensitivity of a given model. This is why CheckMATE provides the possibility to easily set up the generation of these processes by making use of the Pythia8Process keyword. Possible values for this parameter are p p > X, with X being any of the following:

go go **or** go go**:** Gluino pair production

go sq **or** go sq **:** Gluino-squark and Gluino-antisquark associated production

sq sq **:** Squark-antisquark production

t1 t1 **:** pair production of the lightest stop

3gen**':** pair production of stops and sbottoms

sq sq**:** squark pair production

ewsusy**:** pair production of neutrainos, charginos and neutralino-chargino associated production

allsusy**:** all of the above

Note that "squark" always corresponds to the squarks of the first two generations in the above explanations. To simulate any other process or any combination of the above, an explicit Pythia 8 .in file has to be provided.

B.3 CheckMATE Detector Tunings

In this section we provide some more quantitative details on the detector tunings qualitatively discussed in Chapter 4.

B.3.1 Lepton Kinematic Smearing

The energy measurement of electrons in the calorimeter and the momentum measurement of muons in the muon chambers typically leads to an uncertainty in the reconstructed kinematic value. This can be approximated by a Gaussian smearing of the true Monte Carlo value with

$\lvert\eta\rvert$ range	$A(\eta)$	$B(\eta)$	$\lvert\eta\rvert$ range	$A(\eta)$	$B(\eta)$	$\lvert\eta\rvert$ range	$A(\eta)$	$B(\eta)$
$[0.0, 0.1]$	0.094	0.012	$[0.1, 0.2]$	0.096	0.012	$[0.2, 0.3]$	0.096	0.012
$[0.3, 0.4]$	0.100	0.012	$[0.4, 0.5]$	0.107	0.012	$[0.5, 0.6]$	0.115	0.012
$[0.6, 0.7]$	0.125	0.012	$[0.7, 0.8]$	0.136	0.012	$[0.8, 0.9]$	0.150	0.012
$[0.9, 1.0]$	0.161	0.012	$[1.0, 1.1]$	0.172	0.012	$[1.1, 1.2]$	0.180	0.012
$[1.2, 1.3]$	0.194	0.012	$[1.3, 1.37]$	0.211	0.012	$[1.37, 1.6]$	0.221	0.018
$[1.6, 1.7]$	0.192	0.018	$[1.7, 1.8]$	0.184	0.018	$[1.8, 1.9]$	0.166	0.018
$[1.9, 2.0]$	0.162	0.018	$[2.0, 2.1]$	0.160	0.018	$[2.1, 2.2]$	0.168	0.018
$[2.2, 2.3]$	0.167	0.018	$[2.3, 2.4]$	0.167	0.018	else	0.167	0.018

Table B.3: Parameters for the position dependent energy resoltion function for electrons in Eq. (B.1).

an energy- and position-dependent width σ. For electrons, the smearing function for σ_E has been determined from combining information in Refs. [189, 365]:

$$\left.\frac{\sigma_E}{E}\right|_{\text{electrons}} = \sqrt{\left(\frac{A(\eta)}{\sqrt{E}}\right)^2 + B^2(\eta)}, \tag{B.1}$$

with $A(\eta), B(\eta)$ given in Table B.3 and E in units of GeV.

For muons[3], momentum resolution information in Ref. [191] was extended to higher scales by a shape fit to results from ATLAS Z' searches in Ref. [192]. This renders the result slightly more complicated:

$$\left.\frac{\sigma_{p_T}}{p_T}\right|_{\text{muon}} = \begin{cases} \epsilon\sqrt{\frac{A_1(\eta)}{p_T^2} + B_1(\eta) + C_1(\eta)\cdot p_T^2} + (1-\epsilon)\sqrt{\frac{A_2(\eta)}{p_T^2} + B_2(\eta) + C_2(\eta)\cdot p_T^2} & \text{if } p_T \leq 100 \\ A'(\eta) + B'(\eta)\cdot p_T & \text{else} \end{cases} \tag{B.2}$$

with $\epsilon = 0.776$, p_T in units of GeV and the remaining parameters as in Table B.4.

B.3.2 Electron Efficiencies

The efficiencies for electron objects to be reconstructed as such are combined from the individually measured reconstruction and identification efficiency, for which the latter distinguishes between two kinds of electrons: 'medium' and 'tight'[4]. The reconstruction efficiency does not show any significant dependence on the candidate's momentum but mostly on the pseudorapidity, as can be seen in Fig. B.2a. Conversely, the identification efficiency for medium electrons mostly depends on the transverse energy of the electron, as shown in Fig. B.2b, and insignificantly on its position. The total efficiency is given as the product of the two contributions and

[3] The momentum resoluton formula for muons was determined and implemented by Florian Jetter.

[4] The 'loose' electron efficiency for identifying a truth-level electron is estimated by implementing a weak calorimeter isolation that mimics the ATLAS reconstruction. We require that within a cone size $dR < 0.2$ around the electron, at least 80% of energy deposition is due to the electron.

$\lvert\eta\rvert$ range	$A_1(\eta)$	$B_1(\eta)$	$C_1(\eta)$	$A_2(\eta)$	$B_2(\eta)$	$C_2(\eta)$
$[0, 1.05]$	1.63×10^{-2}	3.98×10^{-5}	2.05×10^{-8}	1.39×10^{-5}	1.16×10^{-5}	1.04×10^{-11}
$[1.05, 2.0]$	1.60×10^{-6}	1.04×10^{-4}	8.44×10^{-8}	1.03×10^{-3}	3.50×10^{-4}	1.92×10^{-10}
else	4.14×10^{-5}	4.71×10^{-5}	7.37×10^{-9}	1.29×10^{-4}	2.90×10^{-4}	1.27×10^{-12}

$\lvert\eta\rvert$ range	$A'(\eta)$	$B'(\eta)$
$[0, 1.05]$	-1.94×10^{-2}	3.23×10^{-4}
$[1.05, 2.0]$	-3.75×10^{-3}	3.18×10^{-4}
else	-1.42×10^{-2}	2.66×10^{-4}

Table B.4: Parameters for the position dependent momentum resolution function for muons in Eq. (B.2).

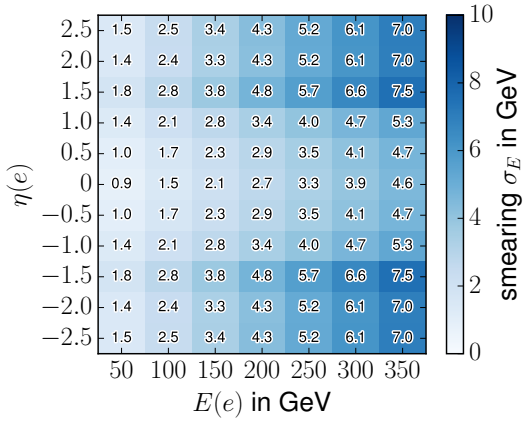

(a) Discretised version of continuous 2D function used for smearing electron energies.

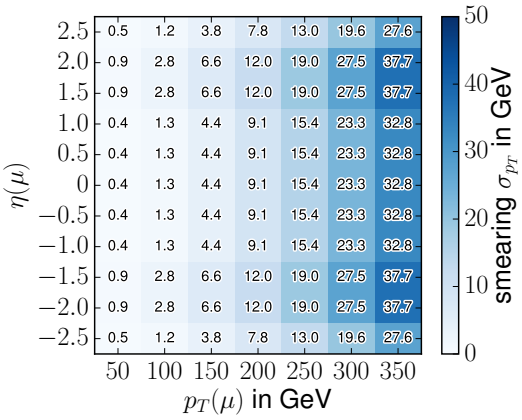

(b) Discretised version of continuous 2D function used for smearing muon momenta.

can be seen in a representative two-dimensional grid in Fig. B.3a.

For 'tight' electrons, there exist measurements for both the pseudorapidity and the p_T dependence of the identification efficiency individually, for which the corresponding other variable has been integrated over (see Fig. B.2c and Fig. B.2d). We normalise the pseudorapidity dependent function to an average value of unity and use as the overall identification efficiency the absolute efficiency with respect to p_T, multiplied by the renormalised efficiency with respect to pseudorapidity. Combining this with the reconstruction efficiency described before leads to the total efficiency distribution shown in Fig. B.3b.

The following functional behaviour for the efficiencies is used (p_T in GeV):

$$\begin{aligned}\epsilon_{\text{rec}}(\eta) = 0.987 &+ (1.28 \times 10^{-2})\eta^2 - (1.76 \times 10^{-2})\eta^4 \\ &+ (5.21 \times 10^{-3})\eta^6 - (4.49 \times 10^{-4})\eta^8,\end{aligned} \tag{B.3}$$

$$\epsilon_{\text{id, medium}}(p_T) = \begin{cases} 0.767 + \dfrac{0.151}{1 + \mathrm{e}^{-0.145 \cdot (p_T - 29.1)}} & \text{if } p_T < 80, \\ 0.946 & \text{if } p_T \geq 80, \end{cases} \tag{B.4}$$

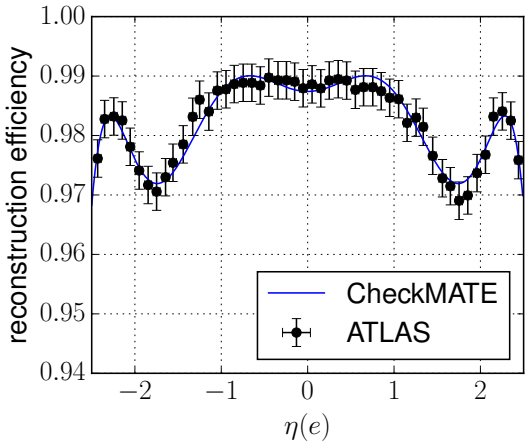

(a) Efficiency for the reconstruction of an electron object inside the calorimeter taken from Ref. [193].

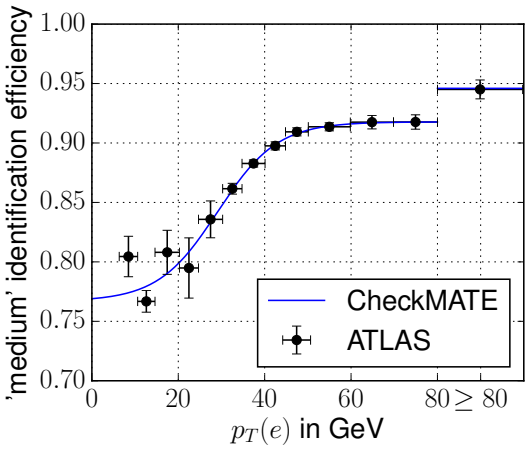

(b) Identification efficiency for 'medium' electrons taken from Ref. [193].

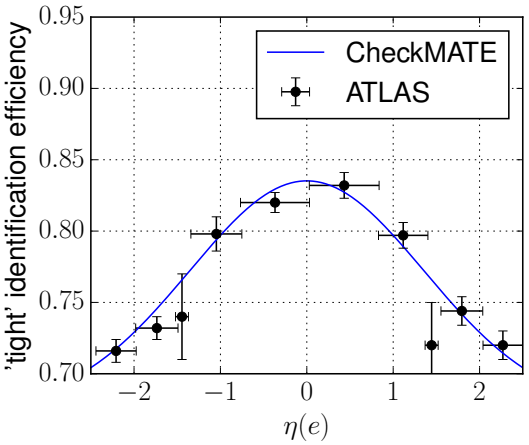

(c) Identification efficiency for 'tight' electrons as a function of the candidate's pseudorapidity fitted to Ref. [189].

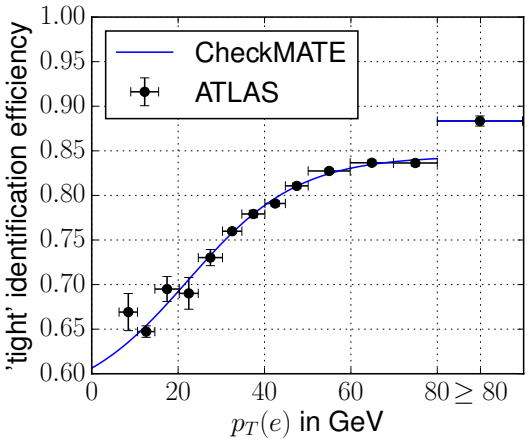

(d) Identification efficiency for 'tight' electrons as a function of the candidate's p_T, taken from Ref [193].

Figure B.2: Electron efficiency distributions used in `CheckMATE`. The functions that have been used to fit the data are given in Eqs. (B.3) to (B.6). For the tight identification efficiency, `CheckMATE` uses the absolute value from the p_T dependent efficiency shown in d), and multiplies it with the η dependent efficiency in c) normalised to an average value of 1.

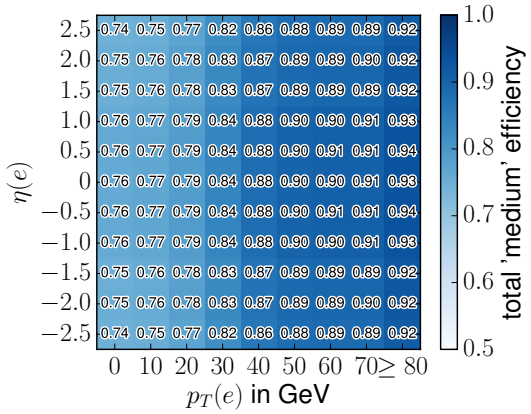

(a) Discretised version of continuous 2D efficiency map for 'medium' ATLAS electrons.

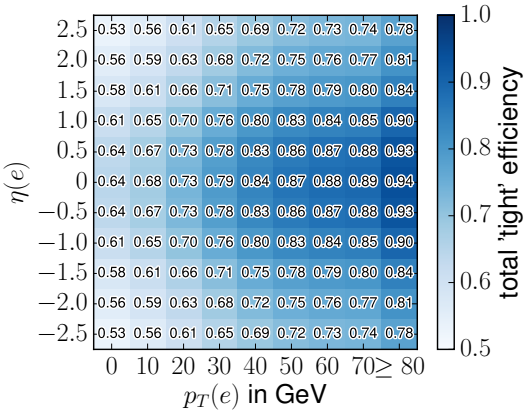

(b) Discretised version of continuous 2D efficiency map for 'tight' ATLAS electrons.

Figure B.3: Total efficiency map with respect to pseudorapidity and energy. This discretised version is only meant for illustrative purposes; `CheckMATE` uses the full functional behaviour as shown in Eqs. (B.3) to (B.6).

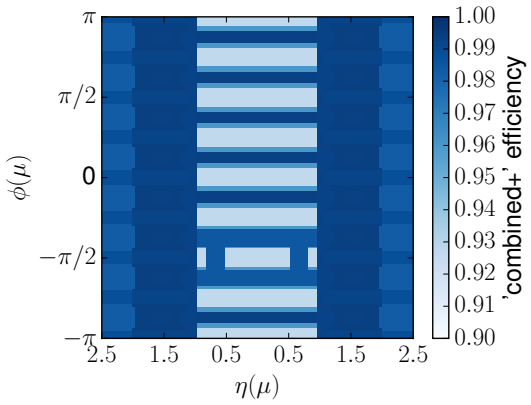

(a) Discrete 2D efficiency map for 'combined plus' ATLAS muons

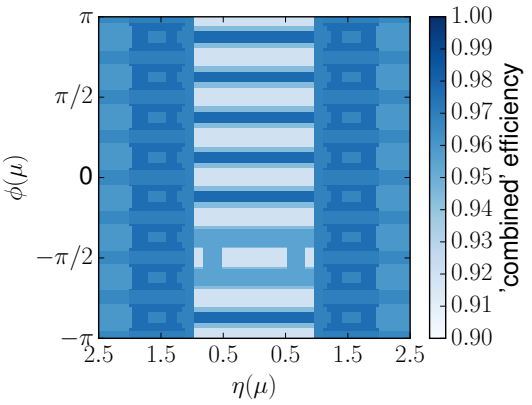

(b) Combined Muons

Figure B.4: Discrete 2D efficiency map for 'combined' ATLAS muons

$$\epsilon_{\text{id, tight}}(p_T) = \begin{cases} 0.565 + \dfrac{0.279}{1 + \mathrm{e}^{-0.0786 \cdot (p_T - 22.3)}} & \text{if } p_T < 80, \\ 0.883 & \text{if } p_T \geq 80, \end{cases} \tag{B.5}$$

$$\epsilon^{\text{normalised}}_{\text{id, tight}}(\eta) = \frac{0.675 + 0.160 \cdot e^{-(\eta/1.92)^2}}{0.777}. \tag{B.6}$$

B.3.3 Muon Efficiencies

For muons, the main effect which has to be taken into account is the efficiency to reconstruct an object in the muon chambers and to associate it to a track in the inner detector region. There exist two main quality criteria for this reconstruction, namely 'combined' which requires both

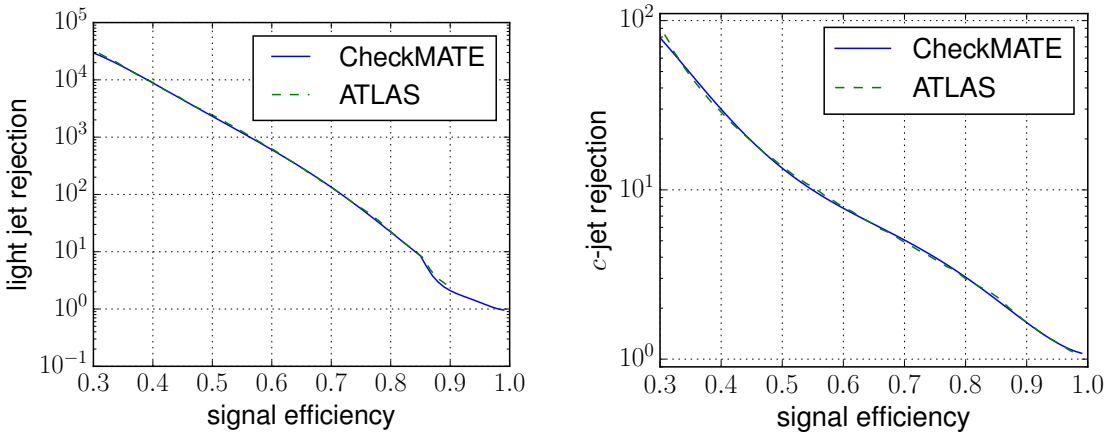

(a) b-tag ROC curve. Rejection considers jets from light quarks only.

(b) b-tag ROC curve. Rejection considers jets from c quarks only.

Figure B.5: ROC curves for the dependence of the background rejection for jets with different quark contents on the chosen signal efficiency working point of the b-tagger. Tagging information is taken from Ref. [198]

a track in the inner detector and muon chambers and 'segment tagged' which only requires a track in the muon chamber) The latter is usually used in combination with the first to maximise the muon efficiency and is hence called 'combined+segment tagged', or 'combined plus'.

The muon chambers in ATLAS consist of different components, which each have a different reconstruction probability, mainly caused by different types and quantities of material and the geometry inside the full detector. In `CheckMATE`, we parametrised a detector-component map in the η–ϕ plane and associate a particular efficiency to each detector type. The resulting two-dimensional grid[5] is shown in Fig. B.4.

B.3.4 *b*-Tagger

The quality of algorithms that try to filter jets containing b-quarks from others is determined by two main quantities. The signal efficiency describes the probability to assign a tag to a jet that actually contains a b-quark, whereas the background efficiency is a measure for the relative amount of jets that are tagged even though they did not originate from a bottom quark. Since the background efficiency is usually small, it is common to use the *rejection* instead, i.e. the inverse of the background efficiency,. Also, one usually distinguishes between rejections against jets with charm–content and other jets that only contain light quarks, as the first are harder to distinguish from the signal.

Since the rejection gets weaker with increasing signal efficiency, one has to find a balance between signal quantity and signal purity, which depends crucially on the details of the respective analysis. For this purpose, one uses the ROC (Receiver Operation Characteristic) curve that describes the relation between these two quantities. We show the ROC curves for light-jet

[5] We refrain from showing the functional description of the full map inside the main text, as the fine and irregular segmentation leads to a hard-to-read 21×53 matrix. The matrix can be found within the `CheckMATE` example code in `CheckMATE-2.0.0beta/tools/fritz/src/analysishandler/AnalysisHandlerATLAS_8TeV.cc`, line 931.

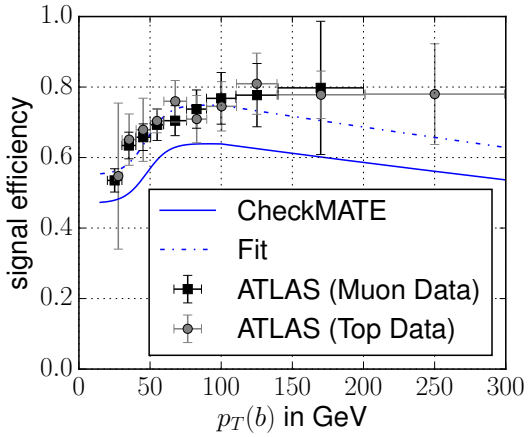

(a) p_T dependence of signal efficiencies for b–tagging for a working point efficiency of 70 %, determined by downscaling (see text) the combined information of two different search channels for [197, 198]

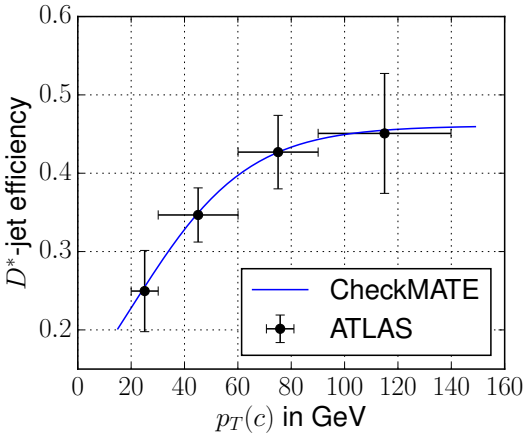

(b) p_T dependence of b–tagging background efficiency of jets containing D^* mesons for a working point efficiency of 70 %, determined from Ref. [197]. The inclusive efficiency on c–jets is assumed to be 40 % of this D^* efficiency.

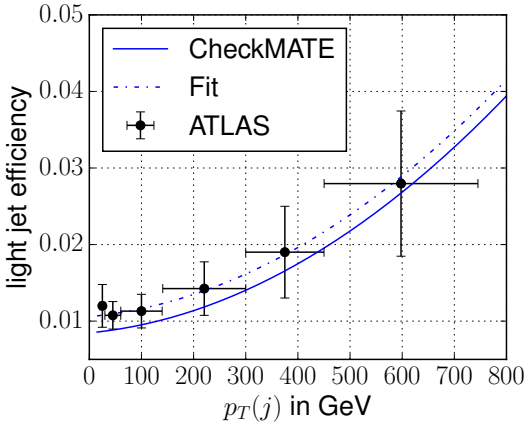

(c) b–tagging efficiency of jets containing light quarks for a working point efficiency of 70 % and $|\eta| < 1.3$, see Ref. [196]

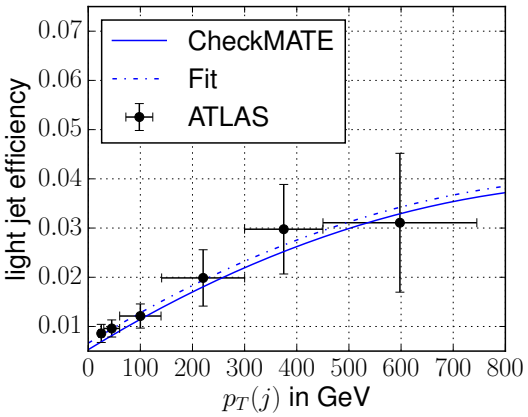

(d) same as Fig. 4.3e for $1.3 \leq |\eta| < 2.5$

Figure B.6

rejection and c-jet rejection separately in Fig. B.5 and internally parametrise these as follows:

$$\log_{10}\left[\bar{r}_{\text{light}}(\bar{\epsilon}_S)\right] = \begin{cases} 52.8 \cdot (\bar{\epsilon}_S - 4.045 \cdot \bar{\epsilon}_S^2 + 7.17 \cdot \bar{\epsilon}_S^3 - 6.14 \cdot \bar{\epsilon}_S^4 + 2.01 \cdot \bar{\epsilon}_S^5) & \text{if } \bar{\epsilon}_S < 0.87, \\ -75.4 \cdot (\bar{\epsilon}_S - 1.07)^3 & \text{if } \bar{\epsilon}_S \geq 0.87, \end{cases} \tag{B.7}$$

$$\log_{10}\left[\bar{r}_c(\bar{\epsilon}_S)\right] = 29.3 \cdot (\bar{\epsilon}_S - 4.572 \cdot \bar{\epsilon}_S^2 + 8.496 \cdot \bar{\epsilon}_S^3 - 7.253 \cdot \bar{\epsilon}_S^4 + 2.33 \cdot \bar{\epsilon}_S^5). \tag{B.8}$$

Given a particular working point on the ROC curve, i.e. a specific chosen signal efficiency $\bar{\epsilon}_S$ and the corresponding background rejections $\bar{r}_{\text{light/c}}$, the actual tagging probabilities depend on the transverse momentum of the considered object. These have been measured individually

for signal–, light-quark– and D^* meson[6] jets and we show the results in Fig. B.6.

For the signal efficiency, we use two different data sets as they have different sensitivities at low and high energies (see Fig. B.6a). In order to agree with the cutflows of various analyses that require b-tagging, a reduction in the overall normalisation by 15% has been applied. In addition, the significant decrease of the signal efficiency at large energies has been manually added in order to get better agreement with experimental results.

Furthermore, the light quark jet rejection has been measured for two different η regions, which we adapt in our parametrisations. We also perform a reduction in the light-quark tagging rates (20%) in order to better agree with experimental cutflows.

Since the p_T dependent distributions are given for a particular working point $\bar{\epsilon}_S = 0.7$, we linearly rescale the functions to the given chosen signal efficiency $\bar{\epsilon}_S$, or the corresponding background efficiency given by the ROC curves (p_T in GeV):

$$\epsilon_S(p_T) = \frac{\bar{\epsilon}_S \cdot 0.85}{0.7}\left(0.552 + \frac{0.210}{1+\mathrm{e}^{-0.123\cdot(p_T-47.6)}}\right)\frac{0.7+0.05\cdot\mathrm{e}^{-\frac{p_T}{308}}}{0.75} \times \begin{cases} 1 & \text{if } p_T \leq 100, \\ 1-7\times10^{-4}\cdot(p_T-100) & \text{if } p_T > 100, \end{cases} \tag{B.9}$$

$$\epsilon_{\text{light}}(p_T,\eta) = \frac{\bar{r}_{\text{light}}(0.7)\times 0.8}{\bar{r}_{\text{light}}(\bar{\epsilon}_S)} \times \begin{cases} 1.06\times10^{-2} + (6.47\times10^{-6})p_T^2 + (4.03\times10^{-8})p_T^4 & \text{if } |\eta|<1.3, \\ 6.61\times10^{-3} + (6.49\times10^{-5})p_T^2 - (3.12\times10^{-8})p_T^4 & \text{if } 1.3\leq|\eta|<2.5, \end{cases} \tag{B.10}$$

$$\epsilon_c(p_T) = \frac{\bar{r}_c(0.7)\cdot 0.4}{\bar{r}_c(\bar{\epsilon}_S)}\cdot\frac{0.461}{1+\mathrm{e}^{-0.0464\cdot(p_T-20.4)}}. \tag{B.11}$$

B.3.5 Tau–Tagger

Analogously to the tagging of jets containing b-quarks, there exist algorithms to distinguish jets that originated from a hadronically decaying τ lepton from those that originated from quarks or gluons. Due to charge conservation, the τ lepton can only decay into an odd number of charged objects — mostly into 1 or 3 — called prongs. Since the structures of the resulting jets look rather different, identification algorithms usually differentiate between these two cases and hence there are individual efficiencies for each. The efficiency determined for 3-prong objects are applied to all jets with more than one reconstructed and associated track and called *multiprong*. This accounts for the fact that there is a nonvanishing probability for one of the tracks in a 3-prong decay to not be reconstructed.

We show the efficiencies for signal and background with respect to the momentum of the jet candidate in Fig. B.8. Again, three common efficiency working points — 'loose, 'medium' and 'tight' — are used in most analyses, and we show results for each of the three. The functional descriptions of the data points are shown in Eqs. (B.12) and (B.13), with the corresponding numerical values listed in Tables B.5a and B.5b. For background and 3–prong jets, these are

[6] The tagging probability for jets containing D^* mesons is roughly 2 times better than for 'normal' c-quarks. Using the cutflows from various analyses we have tuned this parameter to 0.4 to be in agreement with the ATLAS results.

the final efficiency functions CheckMATE uses. Note that these efficiencies do not depend on η, but $|\eta| < 2.5$ is always implied to fall within the angular coverage of the tracking detectors.

In addition to QCD jets, there is a second type of background which has to be taken into account: Electrons, which have been reconstructed as jets, can resemble 1-prong tau decays and need a separate tagging algorithm, which has been specifically tuned to reject these electron jets[7]. Efficiencies with respect to this algorithm depend on both transverse momentum and pseudorapidity as shown in Figs. B.7e and B.7f. We follow the same approach as for the electron efficiencies, i.e. we take the absolute value from the momentum dependent efficiency distribution and multiply with the pseudorapidity distribution normalised to an average efficiency value of 1. The corresponding functions are shown in Eqs. (B.14) and (B.15) and Tables B.5c and B.5d. We show a final combination of these with the 1-prong signal efficiency from before in Figs. B.8a to B.8c for each of the three working points (p_T in GeV):

$$\epsilon_{\mathrm{S}}(p_T) = \epsilon_0 + A_1 p_T^{\alpha} e^{-\lambda_1 p_T^{\beta}} + A_2 \left\{ \begin{array}{ll} (p_T - 80)^2 e^{-\lambda_2 (p_T - 80)} & \text{if } p_T < 80 + \frac{2}{\lambda_2}, \\ \frac{4}{\lambda_2^2} e^{-2} & \text{if } p_T \geq 80 + \frac{2}{\lambda_2}, \end{array} \right\} + A_3 \left\{ \begin{array}{ll} \frac{\sin(\omega(p_T - 15) + \phi)}{p_T^{\gamma}} & \text{if } p_T < 105, \\ \frac{\sin(90\omega + \phi)}{105^{\gamma}} & \text{if } p_T \geq 105, \end{array} \right\} \tag{B.12}$$

$$\epsilon_{\mathrm{B}}(p_T) = \left\{ \begin{array}{ll} A_1 \mathrm{e}^{-\lambda_1 p_T} + m \cdot p_T & \text{if } p_T < 80, \\ A_2 \left(1 - \frac{1}{1 + e^{\lambda_2 (p_T - p_T^0)}} \right) & \text{if } p_T \geq 80, \end{array} \right\} \tag{B.13}$$

$$\epsilon_{\mathrm{S}}^{\text{el. veto}}(p_T) = \left\{ \begin{array}{ll} \epsilon_0 + \frac{k}{1 + e^{\lambda \cdot (p_T - p_T^0)}} & \text{if } p_T \leq 80, \\ -m \cdot p_T + n & \text{if } p_T > 80, \end{array} \right. \tag{B.14}$$

$$\epsilon_{\mathrm{S}}^{\mathrm{1p(norm)}}(\eta) = \frac{1}{\langle \epsilon \rangle} \left(\epsilon_0 - A_1 \mathrm{e}^{-\frac{(|\eta| - 1.2)^2}{\sigma_1^2}} + A_2 \mathrm{e}^{-\frac{(|\eta| - 1.2)^2}{\sigma_2^2}} - A_3 \frac{\sin(\eta)}{\eta} \mathrm{e}^{-\frac{\eta^2}{\sigma_3^2}} + A_4 \eta^2 \mathrm{e}^{-\frac{\eta^2}{\sigma_4^2}} \right). \tag{B.15}$$

[7] We only consider the impact on the signal efficiencies of this algorithm. In particular, we did not implement a specific mistagging efficiency for electrons. With the given Delphes code structure, any electron that fails the identification efficiency cut will be counted as a jet. Then, it will be tagged according to the corresponding background efficiency in Eq. (B.13)

	ϵ_0	A_1	α	λ_1	β	$A_2/10^{-5}$	λ_2	A_3	ω	ϕ	γ
1,l	0.0223	−2.55	1.16	0.427	0.846	2.14	0.670	100	0.0974	2.34	2.04
1,m	0.0223	−2.69	1.23	0.483	0.791	3.46	0.586	100	0.0997	2.23	1.91
1,t	0.0292	−2.78	1.17	0.377	0.799	6.17	0.388	100	0.101	2.16	1.79
m,l	0.0192	−6.44	0.143	0.106	1.08	4.22	0.594	99.6	0.0958	2.09	1.92
m,m	0.0191	−2.32	0.924	0.233	0.940	5.00	0.510	100	0.0950	2.18	1.86
m,t	0.0212	−2.29	0.671	0.104	1.096	6.30	0.324	100	0.0971	2.09	1.78

(a) Parameters corresponding to Eq. (B.12) for both 1-prong (1) and multiprong (m) candidates and different signal working points 'loose' (l), 'medium' (m), 'tight' (t).

	A_1	λ_1	m	A_2	λ_2	p_T^0
1,l	0.717	7.89×10^{-2}	1.82×10^{-3}	0.106	9.73×10^{-2}	64.3
1,m	0.301	7.20×10^{-2}	9.35×10^{-4}	6.27×10^{-2}	1.44×10^{-2}	20.0
1,t	0.117	7.42×10^{-2}	3.59×10^{-4}	1.92×10^{-2}	2.47×10^{-2}	46.8
m,l	0.265	8.27×10^{-2}	2.26×10^{-4}	1.24×10^{-2}	2.28×10^{-2}	4.08
m,m	0.154	8.32×10^{-2}	1.36×10^{-4}	9.06×10^{-3}	1.19×10^{-2}	20.0
m,t	5.79×10^{-2}	8.80×10^{-2}	4.08×10^{-5}	3.14×10^{-3}	1.73×10^{-2}	78.9

(b) Parameters corresponding to Eq. (B.13) for the same combinations as Table B.5a.

	ϵ_0	A_1	σ_1	A_2	σ_2	A_3	σ_3	A_4	σ_4
l	0.94	0.875	0.294	0.886	0.286	-2.68×10^{-2}	1.16	4.19×10^{-3}	10.9
m	0.91	0.283	0.303	0.309	0.256	3.46×10^{-2}	0.113	-7.96×10^{-2}	1.25
t	0.84	0.472	0.304	0.503	0.258	5.94×10^{-2}	0.102	-8.51×10^{-2}	1.42

(c) Parameters corresponding to Eq. (B.14) for different working points but 1-prong only.

	$\langle\epsilon\rangle$	ϵ_0	k	λ	p_T^0	m	n
l	0.956	0.928	3.54×10^{-2}	0.0994	55.1	5.52×10^{-5}	0.966
m	0.878	0.833	6.13×10^{-2}	0.0922	57.8	1.90×10^{-4}	0.893
t	0.789	0.738	7.06×10^{-2}	0.140	61.4	2.59×10^{-4}	0.812

(d) Parameters corresponding to Eq. (B.15) for the same combinations as Table B.5c.

Table B.5

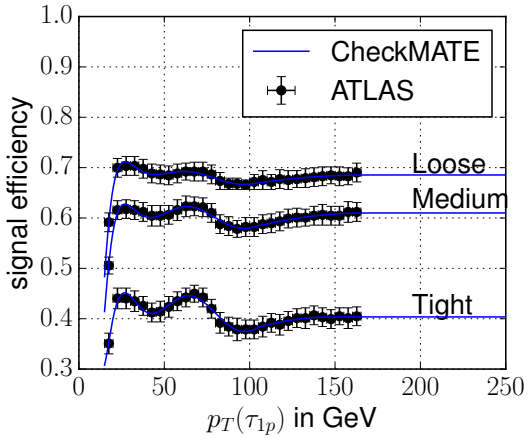

(a) τ-tagging efficiencies of the main identification algorithm for 1-prong τ candidates.

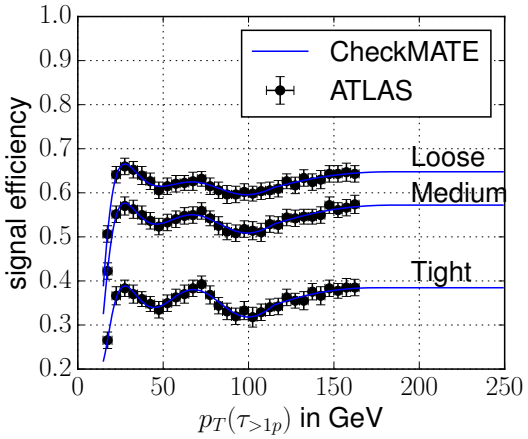

(b) τ-tagging efficiencies for multiprong τ candidates

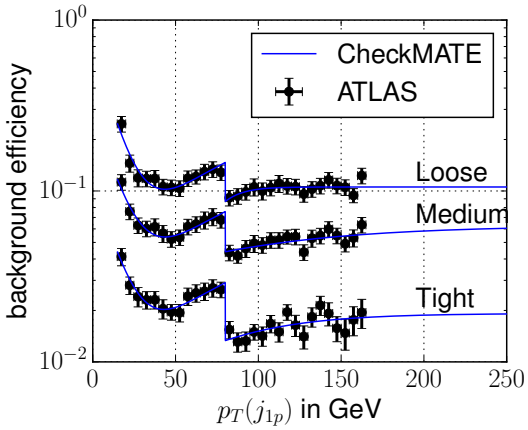

(c) τ-tagging background efficiencies for 1-prong jets

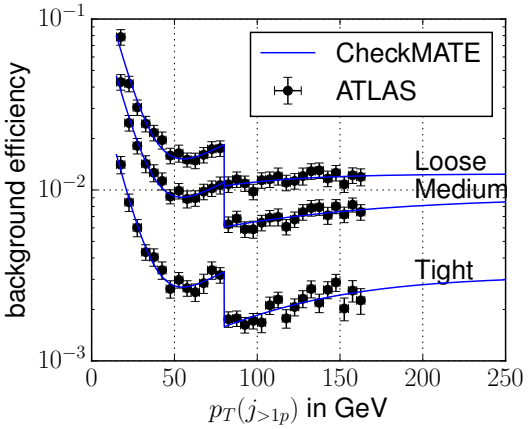

(d) τ-tagging background efficiencies for 3-prong jets

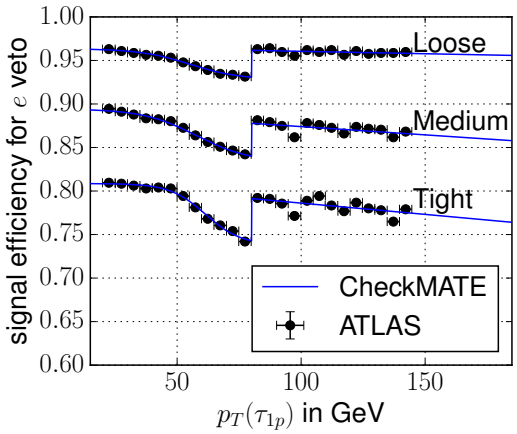

(e) Signal efficiency with respect to the candidate's transverse momentum for the electron-veto of 1-prong τ candidates.

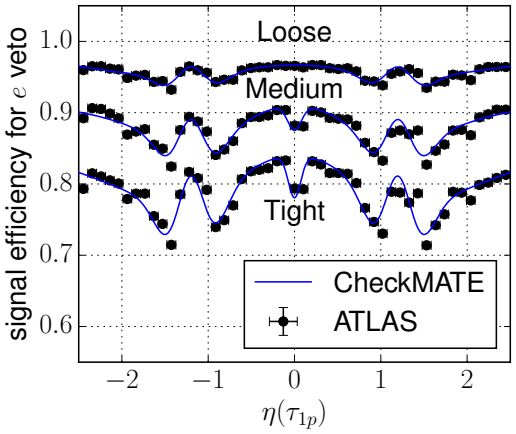

(f) Signal efficiency with respect to the candidate's pseudorapidity for the electron-veto of 1-prong τ candidates.

Figure B.7: Signal efficiencies used for the tau–tagging discrimination against electrons [366]. These only affect 1–prong candidates, but differ between the different considered working points. Explicit functions for the CheckMATE parametrisations are shown in Eqs. (B.14) and (B.15).

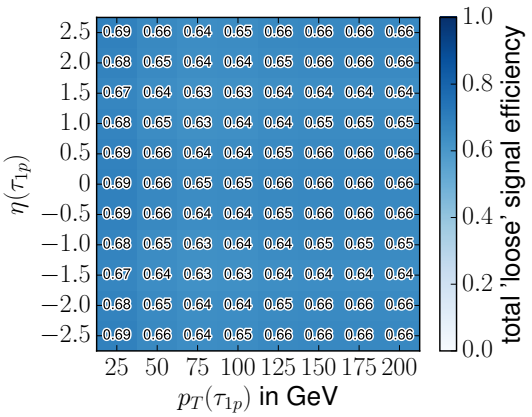

(a) 'loose' τ-tagging efficiency for 1-prong τ candidates.

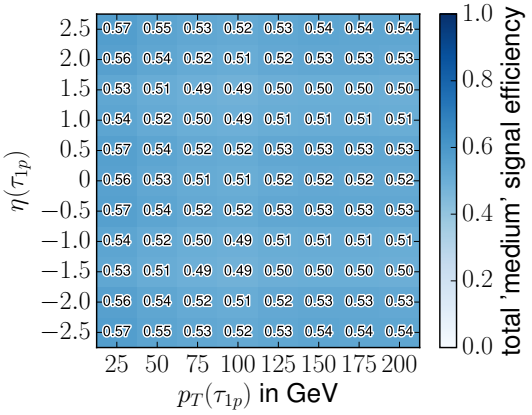

(b) 'medium' τ-tagging efficiency for 1-prong τ candidates.

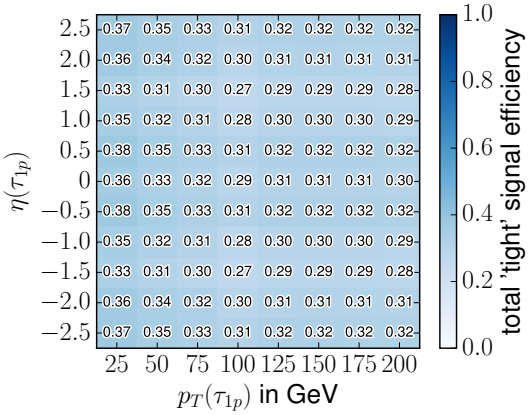

(c) 'tight' τ-tagging efficiency for 1-prong τ candidates.

Figure B.8: Total signal 1-prong efficiencies for 1-prong signal candidates, combining the contributions from rejections against QCD jets and electrons.

APPENDIX C

Additional Information for Chapter 6

C.1 Distributions for the Natural NMSSM Scan

C.1.1 Mass Distributions

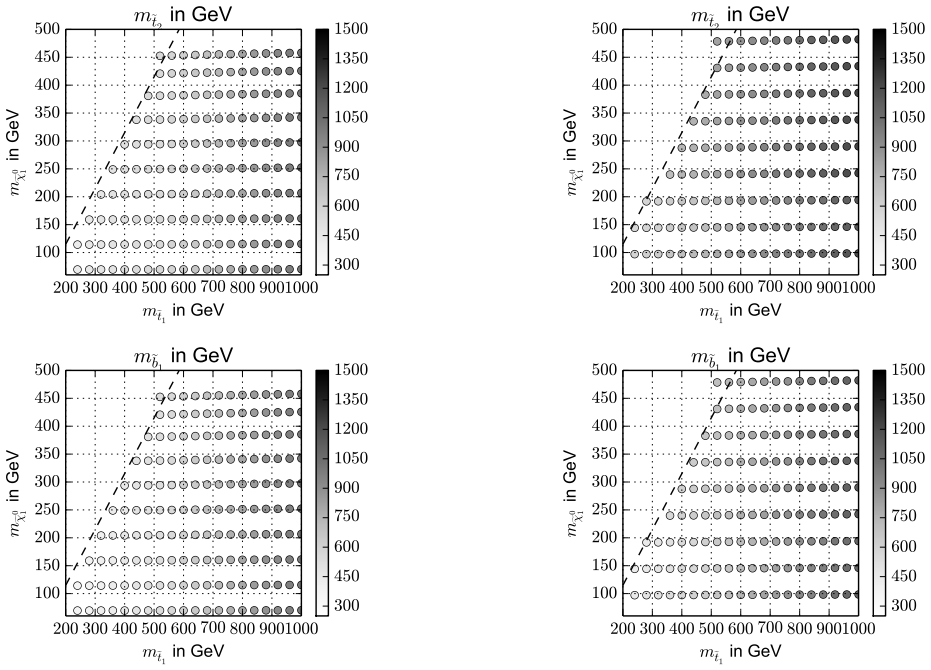

Figure C.1: Mass of the heavier stop and the lighter sbottom (which is very degenerate with the heavier sbottom) for a decoupled gluino and $m_{\widetilde{\chi}_1^\pm} = 500$ GeV. Left: λ_L. Right: λ_S

C.1.2 Cross Section Distributions

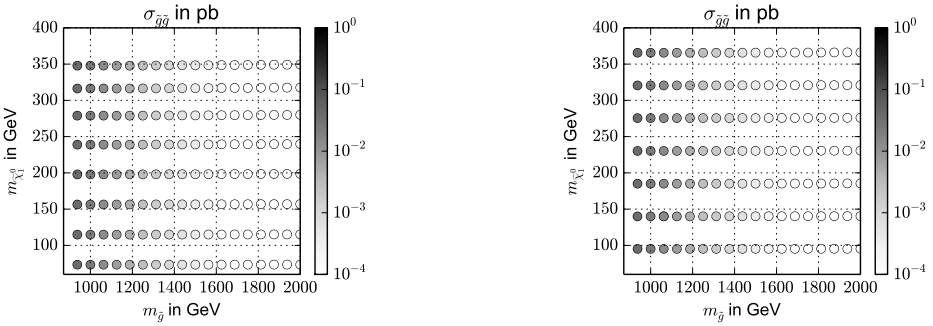

Figure C.2: Total production cross section for gluinos, using $m_{\tilde{t}_1} = 500$ GeV, $m_{\tilde{\chi}_1^\pm} = 400$ GeV. Left: λ_L. Right: λ_S.

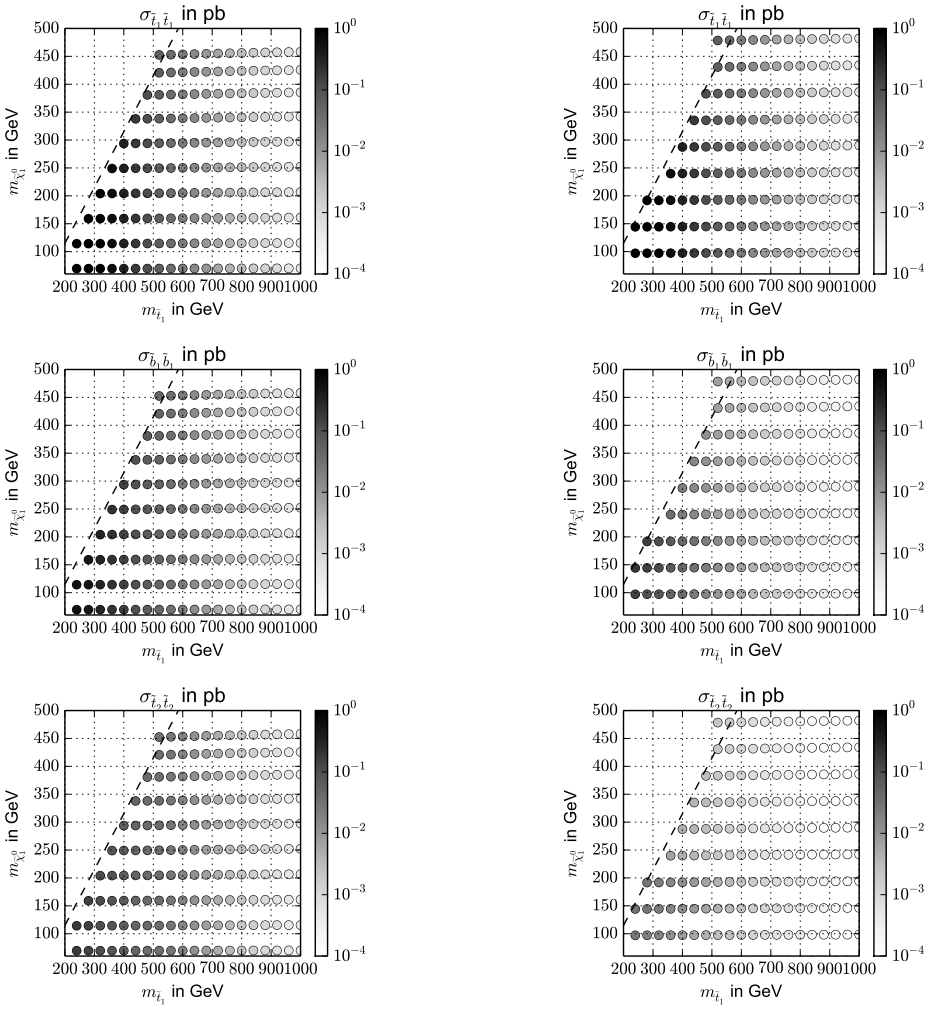

Figure C.3: Total production cross section for the third generation squarks for a decoupled gluino and $m_{\tilde{\chi}_1^\pm} = 500$ GeV. Left: λ_L. Right: λ_S

C.1.3 $\widetilde{t}_1$ Branching Ratio Distributions

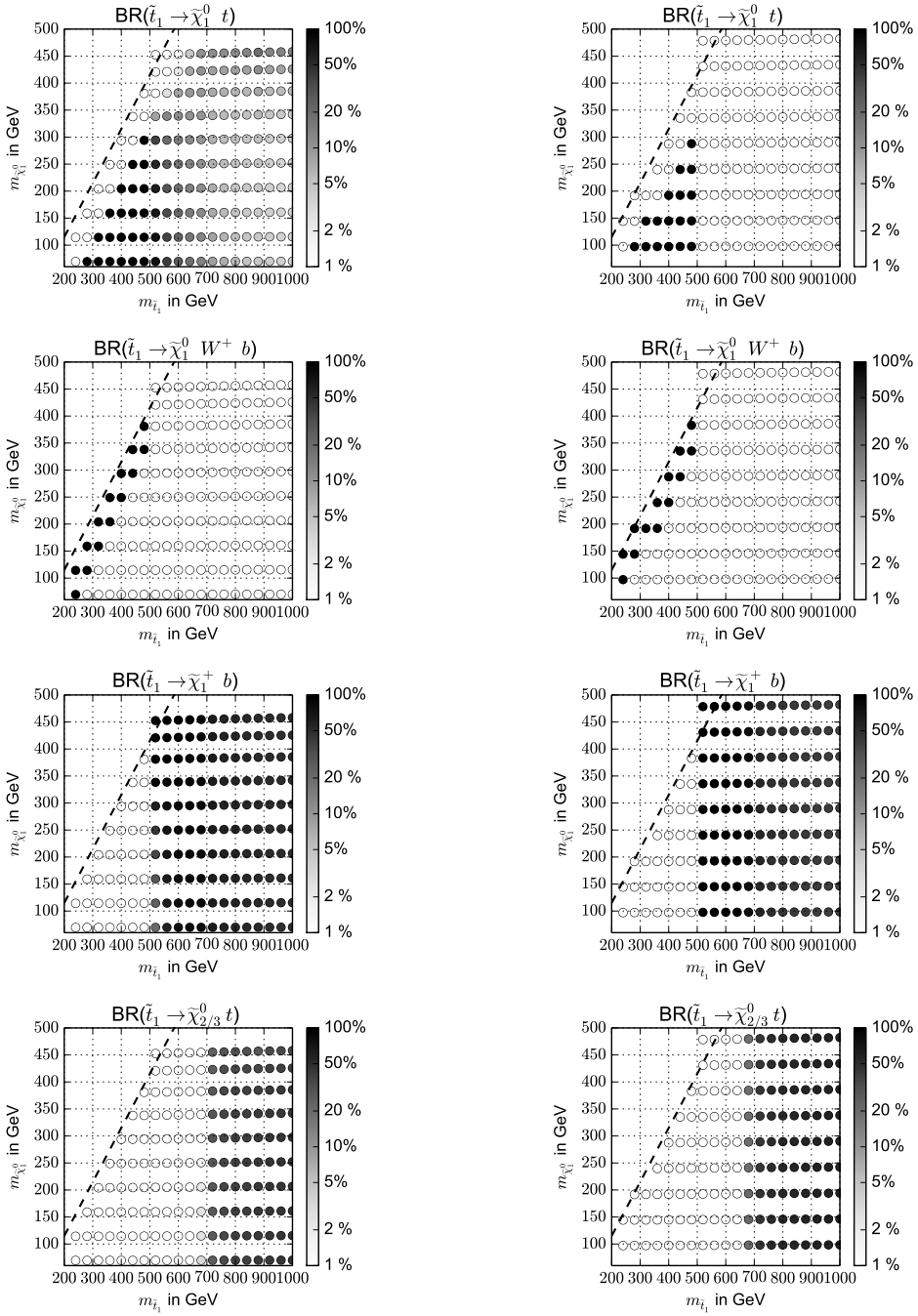

Figure C.4: Most significant branching ratios of the lightest stop into the the singlino LSP, the higgsino NLSPs and the chargino for a decoupled gluino and $m_{\widetilde{\chi}_1^\pm} = 500$ GeV. Left: λ_L. Right: λ_S

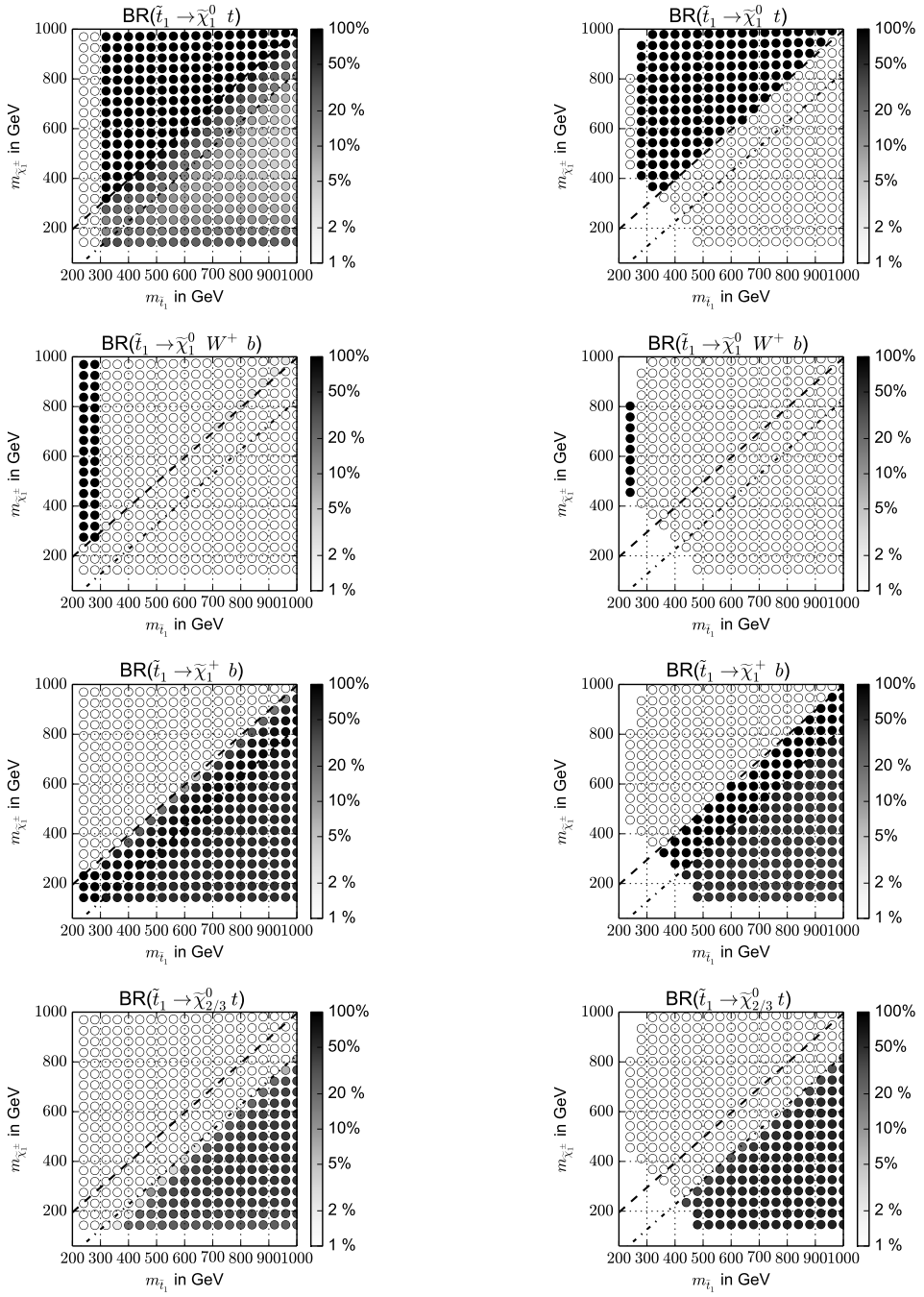

Figure C.5: Most significant branching ratios of the lightest stop into the the singlino LSP, the higgsino NLSPs and the chargino for a decoupled gluino and $m_{\widetilde{\chi}_1^0} = 100$ GeV. Left: λ_L. Right: λ_S

C.1.4 $\widetilde{b}_{1/2}$ Branching Ratio Distributions

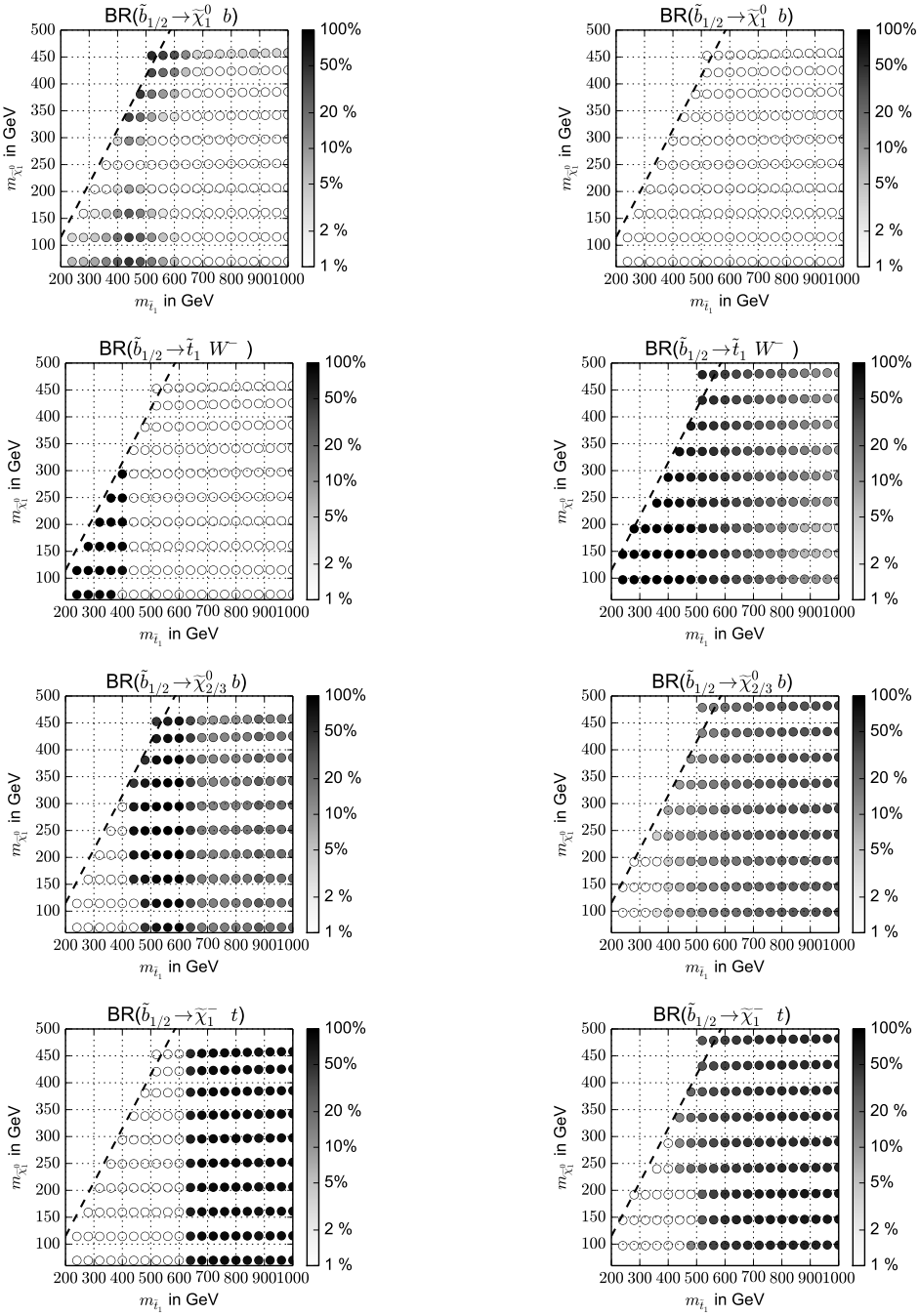

Figure C.6: Most significant branching ratios of the (mostly degenerate) sbottoms into the the lightest stop, the higgsino NLSPs and the chargino for a decoupled gluino and $m_{\widetilde{\chi}_1^\pm} = 500$ GeV. Left: λ_L. Right: λ_S

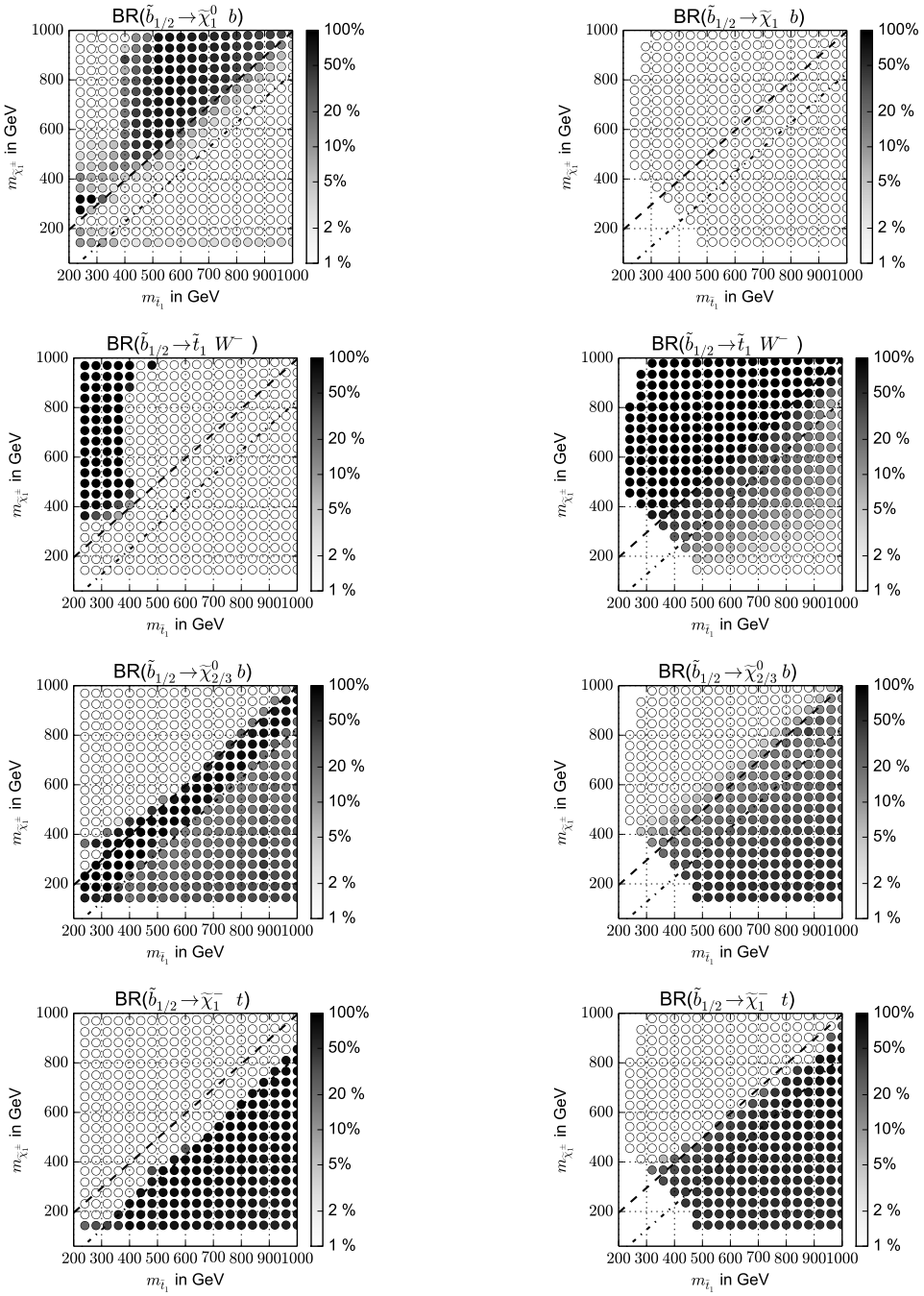

Figure C.7: Most significant branching ratios of the (mostly degenerate) sbottoms into the the lightest stop, the higgsino NLSPs and the chargino for a decoupled gluino and $m_{\widetilde{\chi}_1^0} = 100$ GeV. Left: λ_L. Right: λ_S

C.1.5 $\widetilde{t}_2$ Branching Ratio Distributions

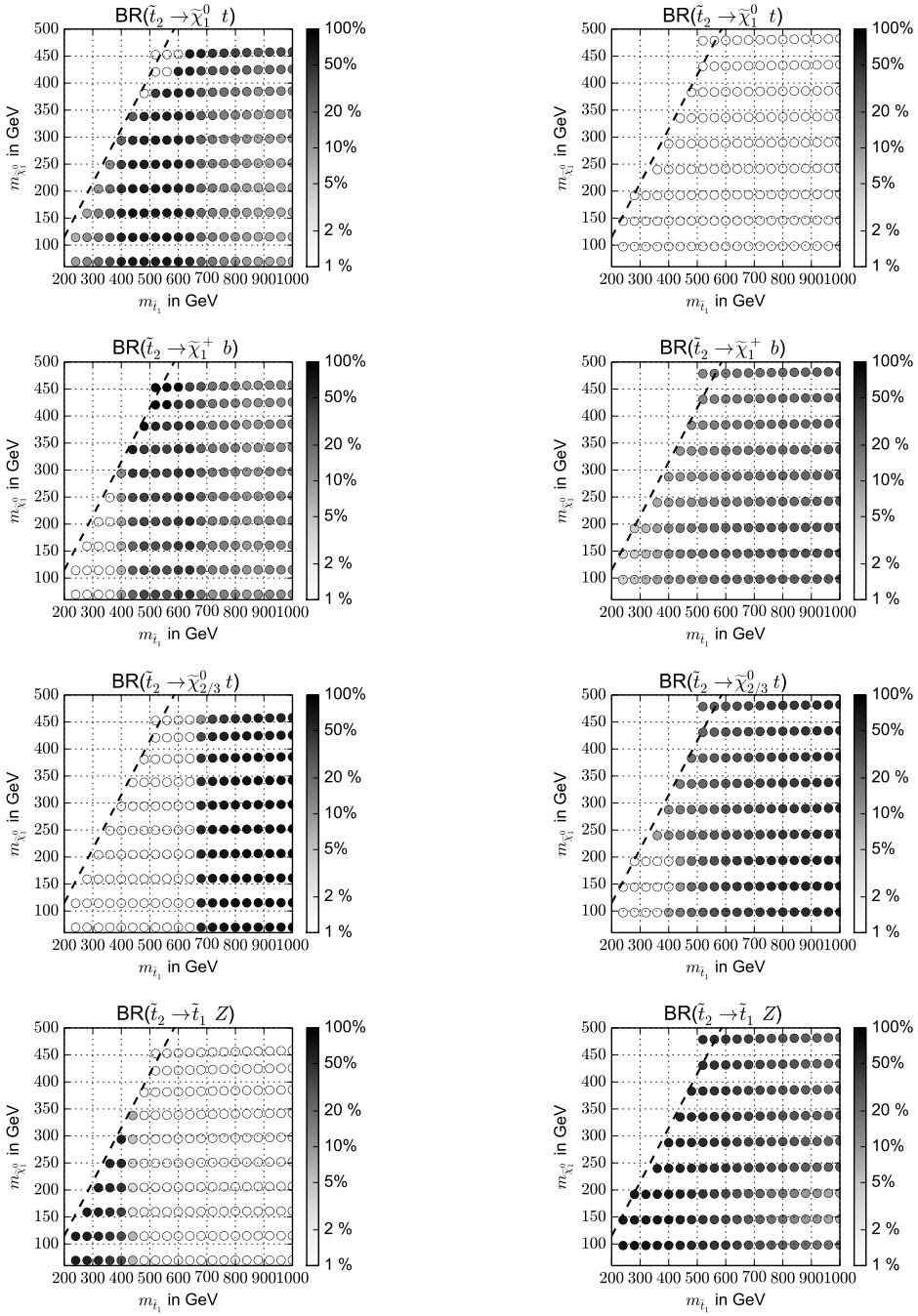

Figure C.8: Most significant branching ratios of the heavier stop into the the singlino LSP, the higgsino NLSPs and the chargino for a decoupled gluino and $m_{\widetilde{\chi}_1^\pm} = 500$ GeV. Left: λ_L. Right: λ_S

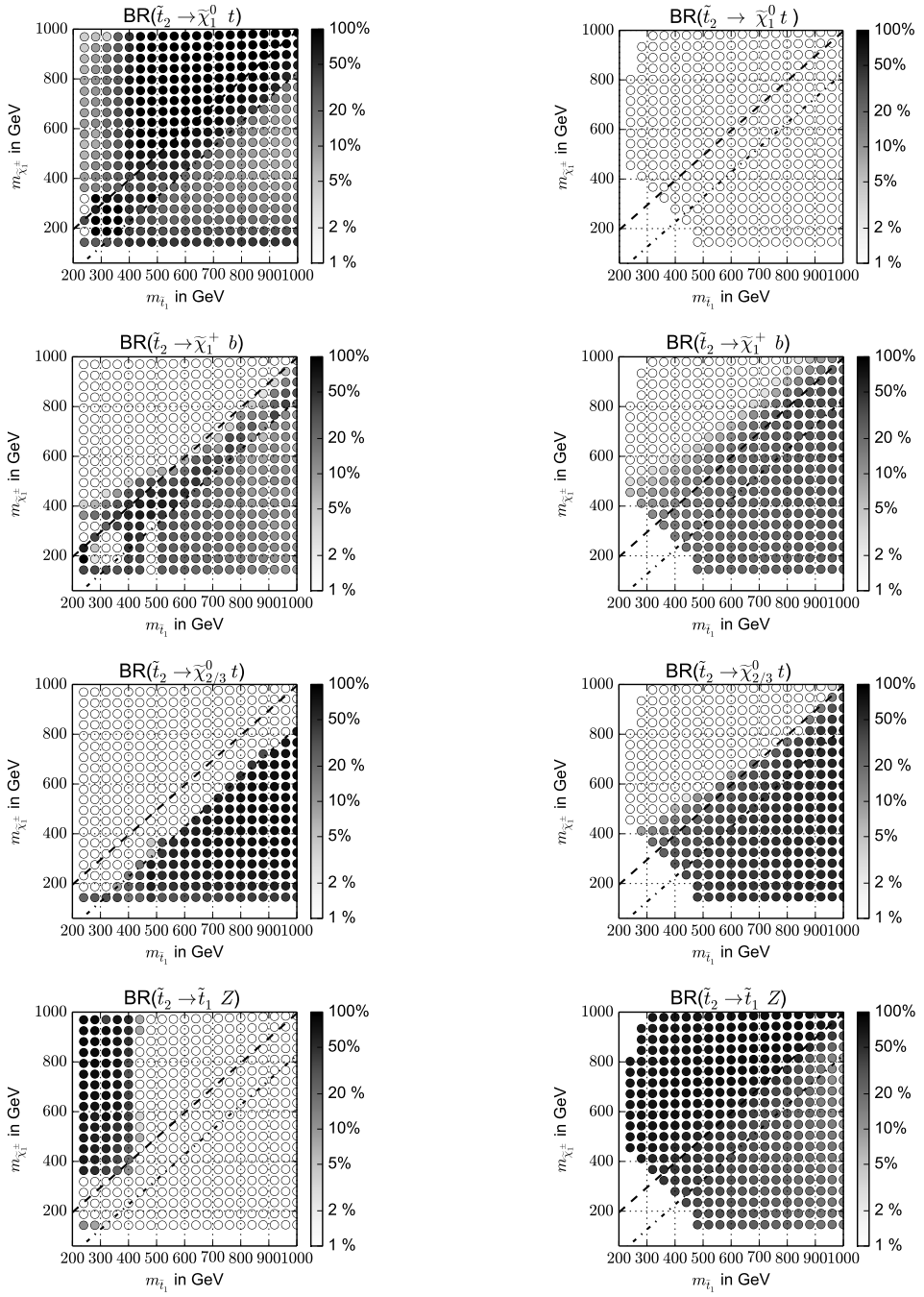

Figure C.9: Most significant branching ratios of the heavier stop into the the singlino LSP, the higgsino NLSPs and the chargino for a decoupled gluino and $m_{\widetilde{\chi}_1^0} = 100$ GeV. Left: λ_L. Right: λ_S

C.1.6 $\widetilde{\chi}^0_{2/3}$ Branching Ratio Distributions

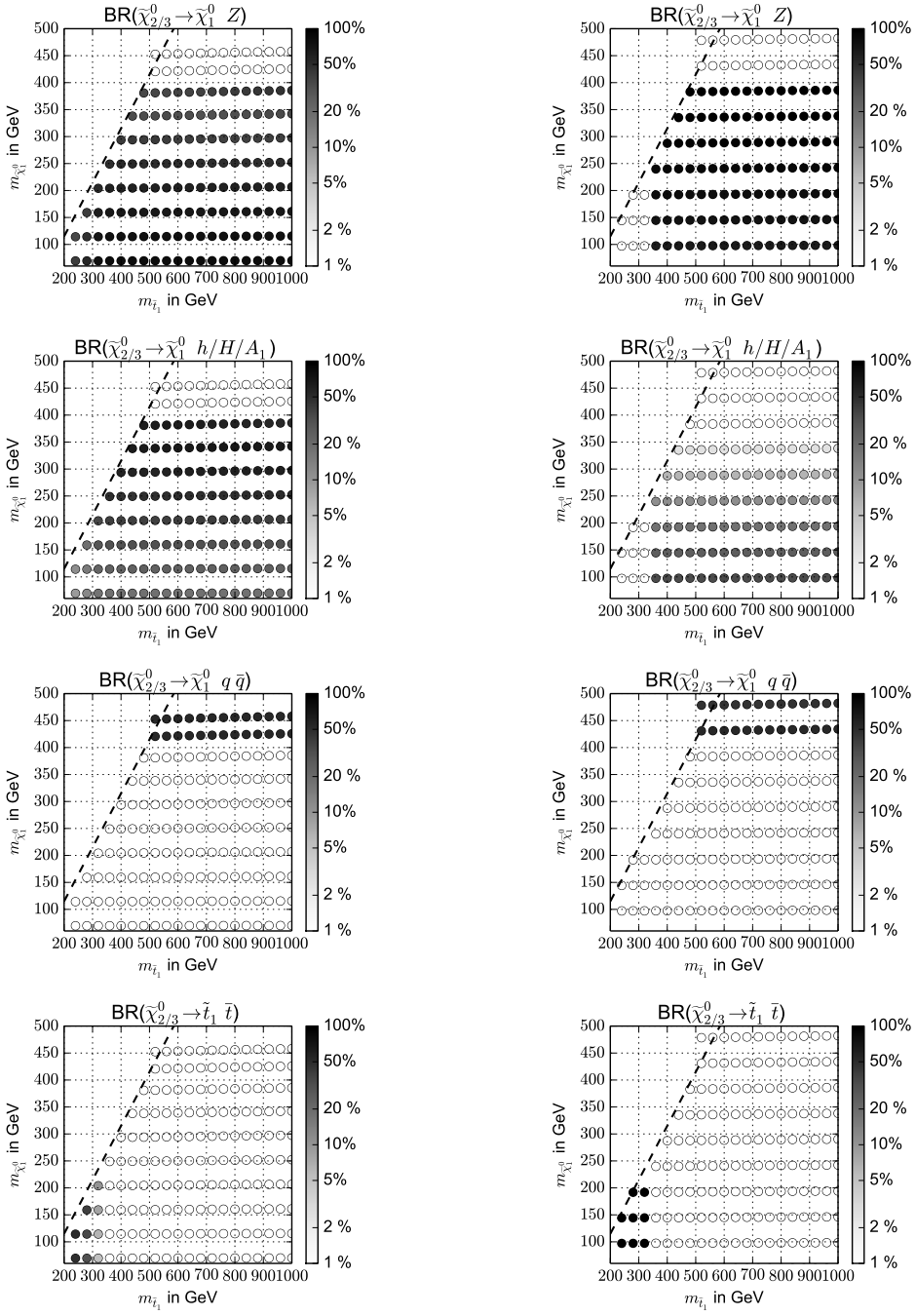

Figure C.10: Most significant branching ratios of the higgsino-like neutralinos for a decoupled gluino and $m_{\widetilde{\chi}^\pm_1} = 500$ GeV. Left: λ_L. Right: λ_S.

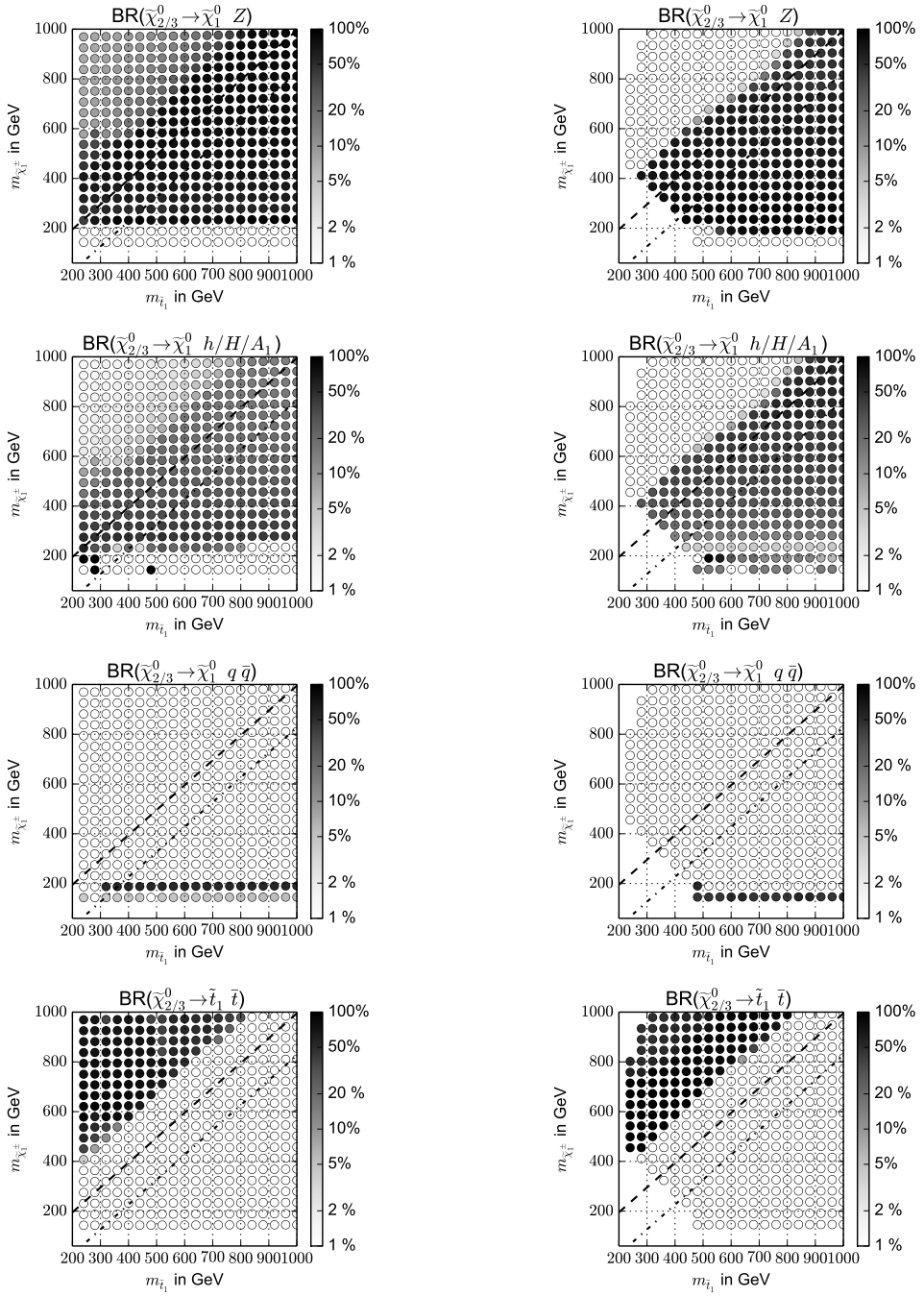

Figure C.11: Most significant branching ratios of the higgsino-like neutralinos for a decoupled gluino and $m_{\tilde{\chi}^0_1} = 100$ GeV. Left: λ_L. Right: λ_S

APPENDIX C

Bibliography

[1] K. Popper, *The Logic of Scientific Discovery*, ISSR library, Routledge, 2002.

[2] D. Hume, *An Enquiry Concerning Human Understanding*, Dover philosophical classics, Dover Publications, 2004.

[3] J. J. Thomson, *The existence of bodies smaller than atoms*, Proc. Roy. Inst **16** (1901) 138–150.

[4] C. D. Anderson, *The Positive Electron*, Phys. Rev. **43** (6 1933) 491–494.

[5] M. Gell-Mann and Y. Ne'eman, *The eightfold way*, Prog.Theoret.Phys. (Kyoto) **27** (1962) 949–966.

[6] S. Weinberg, *A Model of Leptons*, Phys. Rev. Lett. **19** (21 1967) 1264–1266

S. L. Glashow, *Partial-symmetries of weak interactions*, Nuclear Physics **22**.4 (1961) 579–588

A. Salam and J. Ward, *Electromagnetic and weak interactions*, Physics Letters **13**.2 (1964) 168–171.

[7] F. Englert and R. Brout, *Broken Symmetry and the Mass of Gauge Vector Mesons*, Phys. Rev. Lett. **13** (9 1964) 321–323

P. W. Higgs, *Broken Symmetries and the Masses of Gauge Bosons*, Phys. Rev. Lett. **13** (16 1964) 508–509

G. S. Guralnik, C. R. Hagen and T. W. B. Kibble, *Global Conservation Laws and Massless Particles*, Phys. Rev. Lett. **13** (20 1964) 585–587.

[8] D. J. Gross and F. Wilczek, *Ultraviolet behavior of non-abelian gauge theories*, Physical Review Letters **30**.26 (1973) 1343

H. D. Politzer, *Reliable perturbative results for strong interactions?*, Physical Review Letters **30**.26 (1973) 1346

H. Fritzsch, M. Gell-Mann and H. Leutwyler, *Advantages of the color octet gluon picture*, Physics Letters B **47**.4 (1973) 365–368.

[9] D. Ross and M. Veltman, *Neutral currents and the Higgs mechanism*, Nuclear Physics B **95**.1 (1975) 135–147.

[10] J. E. Kim et al., *A theoretical and experimental review of the weak neutral current: a determination of its structure and limits on deviations from the minimal* $\mathrm{SU}(2)_L \times \mathrm{U}(1)$ *electroweak theory*, Rev. Mod. Phys. **53** (2 1981) 211–252.

[11] G. Aad et al., *Observation of a new particle in the search for the Standard Model Higgs boson with the ATLAS detector at the LHC*, Phys. Lett. **B716** (2012) 1–29, arXiv: 1207.7214 [hep-ex].

[12] S. Chatrchyan et al., *Observation of a new boson at a mass of 125 GeV with the CMS experiment at the LHC*, Phys. Lett. **B716** (2012) 30–61, arXiv: 1207.7235 [hep-ex].

[13] B. W. Lee, C. Quigg and H. B. Thacker, *Weak interactions at very high energies: The role of the Higgs-boson mass*, Phys. Rev. D **16** (5 1977) 1519–1531.

[14] G. L. Kane et al., *Study of constrained minimal supersymmetry*, Phys. Rev. D **49** (11 1994) 6173–6210.

[15] J. Ellis et al., *Supersymmetric dark matter in light of {WMAP}*, Physics Letters B **565** (2003) 176–182.

[16] O. Buchmueller et al., *Likelihood Functions for Supersymmetric Observables in Frequentist Analyses of the CMSSM and NUHM1*, Eur. Phys. J. **C64** (2009) 391–415, arXiv: 0907.5568 [hep-ph].

[17] O. Buchmueller et al., *The CMSSM and NUHM1 after LHC Run 1*, Eur. Phys. J. **C74**.6 (2014) 2922, arXiv: 1312.5250 [hep-ph].

[18] P. Bechtle et al., *Killing the cMSSM softly*, Eur. Phys. J. **C76**.2 (2016) 96, arXiv: 1508.05951 [hep-ph].

[19] H. K. Dreiner, H. E. Haber and S. P. Martin, *Two-component spinor techniques and Feynman rules for quantum field theory and supersymmetry*, Phys.Rept. **494** (2010) 1–196, arXiv: hep-ph/0812.1594 [hep-ph].

[20] T. D. Lee and C. N. Yang, *Question of Parity Conservation in Weak Interactions*, Phys. Rev. **104** (1 1956) 254–258.

[21] C. S. Wu et al., *Experimental Test of Parity Conservation in Beta Decay*, Phys. Rev. **105** (4 1957) 1413–1415.

[22] C. Q. Geng and R. E. Marshak, *Uniqueness of Quark and Lepton Representations in the Standard Model From the Anomalies Viewpoint*, Phys. Rev. **D39** (1989) 693.

[23] R. Crewther et al., *Chiral estimate of the electric dipole moment of the neutron in quantum chromodynamics*, Physics Letters B **88**.1 (1979) 123–127.

[24] F. Abe et al., *Observation of Top Quark Production in $\overline{p}p$ Collisions with the Collider Detector at Fermilab*, Phys. Rev. Lett. **74** (14 1995) 2626–2631.

[25] G. Arnison et al., *Experimental Observation of Lepton Pairs of Invariant Mass Around 95-GeV/c**2 at the CERN SPS Collider*, Phys. Lett. **B126** (1983) 398–410.

[26] G. Hooft, *Renormalizable Lagrangians for massive Yang-Mills fields*, Nuclear Physics B **35**.1 (1971) 167–188.

[27] S. Weinberg, *Physical Processes in a Convergent Theory of the Weak and Electromagnetic Interactions*, Phys. Rev. Lett. **27** (24 1971) 1688–1691.

[28] J. Goldstone, *Field theories with 'Superconductor' solutions*, Il Nuovo Cimento (1955-1965) **19**.1 (1961) 154–164.

[29] A. S. Goldhaber and M. M. Nieto, *Photon and graviton mass limits*, Rev. Mod. Phys. **82** (1 2010) 939–979.

[30] T. Nakano and K. Nishijima, *Charge Independence for V-particles*, Progress of Theoretical Physics **10** (1953) 581–582.

[31] S. L. Glashow, J. Iliopoulos and L. Maiani, *Weak Interactions with Lepton-Hadron Symmetry*, Phys. Rev. D **2** (7 1970) 1285–1292.

[32] A. V. Artamonov et al., *New Measurement of the $K^+ \to \pi^+ \nu\overline{\nu}$ Branching Ratio*, Phys. Rev. Lett. **101** (19 2008) 191802.

[33] N. Cabibbo, *Unitary Symmetry and Leptonic Decays*, Phys. Rev. Lett. **10** (12 1963) 531–533

M. Kobayashi and T. Maskawa, *CP-Violation in the Renormalizable Theory of Weak Interaction*, Progress of Theoretical Physics **49**.2 (1973) 652–657.

[34] J. C. Romao and J. P. Silva, *A resource for signs and Feynman diagrams of the Standard Model*, Int. J. Mod. Phys. **A27** (2012) 1230025, arXiv: 1209.6213 [hep-ph].

[35] V. Takhistov et al., *Search for Nucleon and Dinucleon Decays with an Invisible Particle and a Charged Lepton in the Final State at the Super-Kamiokande Experiment*, Phys. Rev. Lett. **115**.12 (2015) 121803, arXiv: 1508.05530 [hep-ex].

[36] S. M. Bilenky, S. T. Petcov and B. Pontecorvo, *Lepton Mixing, mu –¿ e + gamma Decay and Neutrino Oscillations*, Phys. Lett. **B67** (1977) 309.

[37] J. Adam et al., *New Constraint on the Existence of the $\mu^+ \to e^+\gamma$ Decay*, Phys. Rev. Lett. **110** (20 2013) 201801.

[38] G. 't Hooft, *Symmetry Breaking through Bell-Jackiw Anomalies*, Phys. Rev. Lett. **37** (1 1976) 8–11.

[39] L. F. Abbott and M. B. Wise, *Effective Hamiltonian for nucleon decay*, Phys. Rev. D **22** (9 1980) 2208–2212.

[40] R. Davis, D. S. Harmer and K. C. Hoffman, *Search for Neutrinos from the Sun*, Physical Review Letters **20** (1968) 1205–1209

Y. Fukuda et al., *Evidence for Oscillation of Atmospheric Neutrinos*, Phys. Rev. Lett. **81** (8 1998) 1562–1567

J. K. Ahn et al., *Observation of Reactor Electron Antineutrinos Disappearance in the RENO Experiment*, Phys. Rev. Lett. **108** (19 2012) 191802.

[41] T. Blum et al., *The Muon (g-2) Theory Value: Present and Future* (2013), arXiv: 1311.2198 [hep-ph].

[42] G. W. Bennett et al., *Final Report of the Muon E821 Anomalous Magnetic Moment Measurement at BNL*, Phys. Rev. **D73** (2006) 072003, arXiv: hep-ex/0602035 [hep-ex].

[43] P. Huet and E. Sather, *Electroweak baryogenesis and standard model CP violation*, Phys. Rev. **D51** (1995) 379–394, arXiv: hep-ph/9404302 [hep-ph]

M. Gavela et al.,
Standard model CP-violation and baryon asymmetry (II). Finite temperature,
Nuclear Physics B **430**.2 (1994) 382–426.

[44] D. Wallace, *The Quantization of gravity: An Introduction* (2000),
arXiv: gr-qc/0004005 [gr-qc].

[45] J. H. Oort, *The force exerted by the stellar system in the direction perpendicular to the galactic plane and some related problems*, Bull. Astrom. Inst. Neth. **6** (1932) 249.

[46] P. A. R. Ade et al., *Planck 2015 results. XIII. Cosmological parameters* (2015),
arXiv: 1502.01589 [astro-ph.CO].

[47] M. Drees and G. Gerbier, *Mini-Review of Dark Matter: 2012* (2012),
arXiv: 1204.2373 [hep-ph].

[48] E. Kolb and M. Turner, *The Early Universe*, Frontiers in physics,
Westview Press, 1994.

[49] B. W. Lee and S. Weinberg, *Cosmological Lower Bound on Heavy Neutrino Masses*,
Phys. Rev. Lett. **39** (1977) 165–168.

[50] G. Steigman, *Neutrinos And Big Bang Nucleosynthesis*,
Adv. High Energy Phys. **2012** (2012) 268321, arXiv: 1208.0032 [hep-ph].

[51] S. D. M. White, C. S. Frenk and M. Davis,
Clustering in a neutrino-dominated universe, ApJ **274** (1983) L1–L5.

[52] J. R. Primack, "Dark matter and structure formation",
Midrasha Mathematicae in Jerusalem: Winter School in Dynamical Systems Jerusalem, Israel, January 12-17, 1997, 1997, arXiv: astro-ph/9707285 [astro-ph].

[53] R. Cowsik and J. McClelland, *An Upper Limit on the Neutrino Rest Mass*,
Phys. Rev. Lett. **29** (1972) 669–670.

[54] G. Aad et al., *Combined Measurement of the Higgs Boson Mass in pp Collisions at $\sqrt{s} = 7$ and 8 TeV with the ATLAS and CMS Experiments*,
Phys. Rev. Lett. **114** (19 2015) 191803.

[55] E. Gildener, *Gauge Symmetry Hierarchies*, Phys. Rev. **D14** (1976) 1667.

[56] M. Veltman, *The Infrared - Ultraviolet Connection*, Acta Phys. Polon. **B12** (1981) 437.

[57] M. Drees, R. Godbole and P. Roy, *Theory and phenomenology of Sparticles: an account of four-dimensional N=1 supersymmetry in high-energy physics*,
Singapore: World Scientific, 2004.

[58] C. Bollini and J. Giambiagi,
Dimensional renorinalization: The number of dimensions as a regularizing parameter,
Il Nuovo Cimento B (1971-1996) **12**.1 (1972) 20–26

G. '. Hooft and M. Veltman, *Regularization and renormalization of gauge fields*,
Nuclear Physics B **44**.1 (1972) 189–213.

[59] G. Passarino and M. Veltman,
One-loop corrections for e+ e- annihilation into μ+ μ- in the Weinberg model,
Nuclear Physics B **160**.1 (1979) 151–207.

[60] W. Siegel, *Supersymmetric dimensional regularization via dimensional reduction*, Physics Letters B **84**.2 (1979) 193–196.

[61] J. C. Romao, *Modern Techniques for One-Loop Calculations*, 2004, URL: http://porthos.ist.utl.pt/Public/textos/one-loop.pdf.

[62] V. Silveira and A. Zee, *SCALAR PHANTOMS*, Phys. Lett. **B161** (1985) 136.

[63] P. Nath et al., *The Hunt for New Physics at the Large Hadron Collider*, Nucl. Phys. Proc. Suppl. **200-202** (2010) 185–417, arXiv: 1001.2693 [hep-ph]

Y. Cui and U. of Michigan, *Phenomenology of Hidden Sector Physics*, University of Michigan, 2008.

[64] B. Holdom, *Two U(1)'s and Epsilon Charge Shifts*, Phys. Lett. **B166** (1986) 196.

[65] A. Aranda and C. D. Carone, *Orthogonal U(1) ' s, proton stability and extra dimensions*, Phys. Rev. **D63** (2001) 075012, arXiv: hep-ph/0012092 [hep-ph].

[66] E. J. Chun, J.-C. Park and S. Scopel, *Dark matter and a new gauge boson through kinetic mixing*, JHEP **02** (2011) 100, arXiv: 1011.3300 [hep-ph].

[67] J. Erler and P.Langacker, *Review of Particle Physics — 10. Electroweak Model and Constraints on New Physics*, Chin. Phys. **C38** (2014) 090001.

[68] J. Wess and B. Zumino, *Supergauge Transformations in Four-Dimensions*, Nucl. Phys. **B70** (1974) 39–50.

[69] H. P. Nilles, *Supersymmetry, Supergravity and Particle Physics*, Phys.Rept. **110** (1984) 1–162.

[70] S. P. Martin, *A Supersymmetry primer* (1997), arXiv: hep-ph/9709356 [hep-ph].

[71] D. J. H. Chung et al., *The Soft supersymmetry breaking Lagrangian: Theory and applications*, Phys. Rept. **407** (2005) 1–203, arXiv: hep-ph/0312378 [hep-ph].

[72] L. Girardello and M. Grisaru, *Soft breaking of supersymmetry*, Nuclear Physics B **194**.1 (1982) 65–76.

[73] P. Fayet and J. Iliopoulos, *Spontaneously broken supergauge symmetries and goldstone spinors*, Physics Letters B **51**.5 (1974) 461–464.

[74] M. Srednicki, *Generalized O'Raifeartaigh models coupled to N=1 supergravity*, Physics Letters B **122**.3 (1983) 243–246.

[75] E. A. Paschos, *Diagonal neutral currents*, Phys. Rev. D **15** (7 1977) 1966–1972

S. L. Glashow and S. Weinberg, *Natural conservation laws for neutral currents*, Phys. Rev. D **15** (7 1977) 1958–1965.

[76] J. Rosiek, *Complete set of Feynman rules for the MSSM: Erratum* (1995), arXiv: hep-ph/9511250 [hep-ph].

[77] J. F. Gunion et al., *The Higgs Hunter's Guide*, Front. Phys. **80** (2000) 1–448.

[78] H. E. Haber, "Challenges for nonminimal Higgs searches at future colliders", *Perspectives for electroweak interactions in e+ e- collisions. Proceedings, Ringberg Workshop, Tegernsee, Germany, February 5-8, 1995*, 1995, arXiv: hep-ph/9505240 [hep-ph].

[79] K. Inoue et al., *Low Energy Parameters and Particle Masses in a Supersymmetric Grand Unified Model*, Progress of Theoretical Physics **67**.6 (1982) 1889–1898.

[80] P. Draper and H. Rzehak, *A Review of Higgs Mass Calculations in Supersymmetric Models*, Phys. Rept. **619** (2016) 1–24, arXiv: 1601.01890 [hep-ph].

[81] S. Heinemeyer, W. Hollik and G. Weiglein, *The Mass of the lightest MSSM Higgs boson: A Compact analytical expression at the two loop level*, Phys. Lett. **B455** (1999) 179–191, arXiv: hep-ph/9903404 [hep-ph].

[82] M. Papucci, J. T. Ruderman and A. Weiler, *Natural SUSY Endures*, JHEP **1209** (2012) 035, arXiv: 1110.6926 [hep-ph].

[83] R. Barbieri and A. Strumia, "The 'LEP paradox'", *4th Rencontres du Vietnam: Physics at Extreme Energies (Particle Physics and Astrophysics) Hanoi, Vietnam, July 19-25, 2000*, 2000, arXiv: hep-ph/0007265 [hep-ph].

[84] H. K. Dreiner et al., *Mass Bounds on a Very Light Neutralino*, Eur. Phys. J. **C62** (2009) 547–572, arXiv: hep-ph/0901.3485 [hep-ph].

[85] L. S. W. Group et al., *ALEPH, DELPHI, L3 and OPAL experiments*, notes LEPSUSYWG/01-03.1 and LEPSUSYWG/02-04.1 (2001).

[86] H. K. Dreiner et al., *Supernovae and light neutralinos: SN1987A bounds on supersymmetry revisited*, Phys. Rev. **D68** (2003) 055004, arXiv: hep-ph/0304289 [hep-ph].

[87] K. A. Olive et al., *Review of Particle Physics*, Chin. Phys. **C38** (2014) 090001.

[88] C. F. Berger et al., *Supersymmetry Without Prejudice*, JHEP **02** (2009) 023, arXiv: 0812.0980 [hep-ph].

[89] G. R. Farrar and P. Fayet, *Phenomenology of the Production, Decay, and Detection of New Hadronic States Associated with Supersymmetry*, Phys. Lett. **B76** (1978) 575–579.

[90] G. Jungman, M. Kamionkowski and K. Griest, *Supersymmetric dark matter*, Phys. Rept. **267** (1996) 195–373, arXiv: hep-ph/9506380 [hep-ph].

[91] G. Bélanger et al., *LHC constraints on light neutralino dark matter in the MSSM*, Phys. Lett. **B726** (2013) 773–780, arXiv: 1308.3735 [hep-ph]

L. Calibbi et al., *Cornering light Neutralino Dark Matter at the LHC*, JHEP **10** (2013) 132, arXiv: 1307.4119.

[92] J. M. Lindert, F. D. Steffen and M. K. Trenkel, *Direct stau production at hadron colliders in cosmologically motivated scenarios*, JHEP **08** (2011) 151, arXiv: 1106.4005 [hep-ph].

[93] L. Calibbi et al., *LHC Tests of Light Neutralino Dark Matter without Light Sfermions* (2014), arXiv: 1410.5730 [hep-ph].

[94] H. K. Dreiner, *An Introduction to explicit R-parity violation* (1997), arXiv: hep-ph/9707435 [hep-ph].

[95] S. Davidson and J. R. Ellis, *Basis independent measures of R-parity violation*, Phys. Lett. **B390** (1997) 210–220, arXiv: hep-ph/9609451 [hep-ph].

[96] B. Allanach, A. Dedes and H. K. Dreiner, *Bounds on R-parity violating couplings at the weak scale and at the GUT scale*, Phys. Rev. **D60** (1999) 075014, arXiv: hep-ph/9906209 [hep-ph].

[97] L. E. Ibanez and G. G. Ross, *Discrete gauge symmetry anomalies*, Phys. Lett. **B260** (1991) 291–295.

[98] H. K. Dreiner, C. Luhn and M. Thormeier, *What is the discrete gauge symmetry of the MSSM?*, Phys. Rev. **D73** (2006) 075007, arXiv: hep-ph/0512163 [hep-ph].

[99] L. J. Hall and M. Suzuki, *Explicit R-parity breaking in supersymmetric models*, Nuclear Physics B **231**.3 (1984) 419–444.

[100] A. Vilenkin, *Cosmic strings and domain walls*, Physics Reports **121**.5 (1985) 263–315.

[101] D. Baumann, "Inflation", *Physics of the large and the small, TASI 09, proceedings of the Theoretical Advanced Study Institute in Elementary Particle Physics, Boulder, Colorado, USA, 1-26 June 2009*, 2011 523–686, arXiv: 0907.5424 [hep-th].

[102] U. Ellwanger, *Nonrenormalizable interactions from supergravity, quantum corrections and effective low energy theories*, Physics Letters B **133**.3 (1983) 187–191.

[103] U. Ellwanger, C. Hugonie and A. M. Teixeira, *The Next-to-Minimal Supersymmetric Standard Model*, Phys. Rept. **496** (2010) 1–77, arXiv: 0910.1785 [hep-ph].

[104] S. A. Abel, S. Sarkar and P. L. White, *On the cosmological domain wall problem for the minimally extended supersymmetric standard model*, Nuclear Physics B **454** (1995) 663–681, eprint: hep-ph/9506359.

[105] M. Drees, *Supersymmetric models with extended Higgs sector*, International Journal of Modern Physics A **04**.14 (1989) 3635–3651, eprint: http://www.worldscientific.com/doi/pdf/10.1142/S0217751X89001448.

[106] U. Ellwanger, M. Rausch de Traubenberg and C. A. Savoy, *Phenomenology of supersymmetric models with a singlet*, Nucl. Phys. **B492** (1997) 21–50, arXiv: hep-ph/9611251 [hep-ph].

[107] D. M. Pierce et al., *Precision corrections in the minimal supersymmetric standard model*, Nucl. Phys. **B491** (1997) 3–67, arXiv: hep-ph/9606211 [hep-ph].

[108] S. F. King and P. L. White, *Resolving the constrained minimal and next-to-minimal supersymmetric standard models*, Phys. Rev. **D52** (1995) 4183–4216, arXiv: hep-ph/9505326 [hep-ph].

[109] M. D. Goodsell, K. Nickel and F. Staub, *Two-loop corrections to the Higgs masses in the NMSSM*, Phys. Rev. **D91** (2015) 035021, arXiv: 1411.4665 [hep-ph].

[110] F. Staub et al., *Higgs mass predictions of public NMSSM spectrum generators* (2015), arXiv: 1507.05093 [hep-ph].

[111] U. Ellwanger, J. F. Gunion and C. Hugonie, *NMHDECAY: A Fortran code for the Higgs masses, couplings and decay widths in the NMSSM*, JHEP **02** (2005) 066, arXiv: hep-ph/0406215 [hep-ph]

U. Ellwanger and C. Hugonie, *NMHDECAY 2.0: An Updated program for sparticle masses, Higgs masses, couplings and decay widths in the NMSSM*, Comput. Phys. Commun. **175** (2006) 290–303, arXiv: hep-ph/0508022 [hep-ph]

U. Ellwanger and C. Hugonie, *NMSPEC: A Fortran code for the sparticle and Higgs masses in the NMSSM with GUT scale boundary conditions*, Comput. Phys. Commun. **177** (2007) 399–407, arXiv: hep-ph/0612134 [hep-ph]

D. Das, U. Ellwanger and A. M. Teixeira, *NMSDECAY: A Fortran Code for Supersymmetric Particle Decays in the Next-to-Minimal Supersymmetric Standard Model*, Comput. Phys. Commun. **183** (2012) 774–779, arXiv: 1106.5633 [hep-ph]

M. Muhlleitner, A. Djouadi and Y. Mambrini, *SDECAY: A Fortran code for the decays of the supersymmetric particles in the MSSM*, Comput. Phys. Commun. **168** (2005) 46–70, arXiv: hep-ph/0311167 [hep-ph].

[112] K. Matchev, "Physics Beyond the Standard Model at Colliders", *TASI 2014 - Journeys Through the Precision Frontier: Amplitudes for Colliders*, ed. by F. P. Lance Dixon, Singapore: World Scientific Publishing Co. Pte. Ltd., 2016, chap. 9 391–417.

[113] A. Buckley et al., *General-purpose event generators for LHC physics*, Phys. Rept. **504** (2011) 145–233, arXiv: 1101.2599 [hep-ph].

[114] P. Nason and P. Skands, *Review of Particle Physics — 40. Monte Carlo Event Generators*, Chin. Phys. **C38** (2014) 090001.

[115] R. Ellis, W. Stirling and B. Webber, *QCD and Collider Physics*, Cambridge Monographs on Particle Physics, Nuclear Physics and Cosmology, Cambridge University Press, 2003.

[116] E. Fermi, *Versuch einer Theorie der β-Strahlen. I*, Zeitschrift für Physik **88**.3 () 161–177.

[117] A. V. Semenov, *LanHEP: A Package for automatic generation of Feynman rules in gauge models* (1996), arXiv: hep-ph/9608488 [hep-ph]

A. V. Semenov, *LanHEP: A Package for automatic generation of Feynman rules in field theory. Version 2.0* (2002), arXiv: hep-ph/0208011 [hep-ph]

A. Semenov, *LanHEP: A Package for the automatic generation of Feynman rules in field theory. Version 3.0*, Comput. Phys. Commun. **180** (2009) 431–454, arXiv: 0805.0555 [hep-ph]

A. Semenov, *LanHEP - a package for automatic generation of Feynman rules from the Lagrangian. Updated version 3.2* (2014), arXiv: 1412.5016 [physics.comp-ph].

[118] N. D. Christensen and C. Duhr, *FeynRules – Feynman rules made easy*, Computer Physics Communications **180**.9 (2009) 1614–1641

A. Alloul et al., *FeynRules 2.0 - A complete toolbox for tree-level phenomenology* (2013), arXiv: 1310.1921 [hep-ph].

[119] F. Staub, *SARAH* (2008), arXiv: 0806.0538 [hep-ph]

F. Staub, *From Superpotential to Model Files for FeynArts and CalcHep/CompHep*, Comput. Phys. Commun. **181** (2010) 1077–1086, arXiv: 0909.2863 [hep-ph]

F. Staub, *Automatic Calculation of supersymmetric Renormalization Group Equations and Self Energies*, Comput. Phys. Commun. **182** (2011) 808–833, arXiv: 1002.0840 [hep-ph]

F. Staub, *SARAH 3.2: Dirac Gauginos, UFO output, and more*, Comput. Phys. Commun. **184** (2013) 1792–1809, arXiv: 1207.0906 [hep-ph]

F. Staub, *SARAH 4: A tool for (not only SUSY) model builders* (2013), arXiv: 1309.7223 [hep-ph].

[120] C. Degrande et al., *{UFO} – The Universal FeynRules Output*, Computer Physics Communications **183**.6 (2012) 1201–1214.

[121] P. Z. Skands et al., *SUSY Les Houches accord: Interfacing SUSY spectrum calculators, decay packages, and event generators*, JHEP **0407** (2004) 036, arXiv: hep-ph/0311123 [hep-ph]

B. Allanach et al., *SUSY Les Houches Accord 2*, Comput.Phys.Commun. **180** (2009) 8–25, arXiv: 0801.0045 [hep-ph].

[122] H. Georgi and S. L. Glashow, *Unity of All Elementary-Particle Forces*, Phys. Rev. Lett. **32** (8 1974) 438–441.

[123] A. H. Chamseddine, R. Arnowitt and P. Nath, *Locally supersymmetric grand unification*, Physical Review Letters **49** (1982) 970–974.

[124] W. Porod, *SPheno, a program for calculating supersymmetric spectra, SUSY particle decays and SUSY particle production at e+ e- colliders*, Comput. Phys. Commun. **153** (2003) 275–315, arXiv: hep-ph/0301101 [hep-ph]

W. Porod and F. Staub, *SPheno 3.1: Extensions including flavour, CP-phases and models beyond the MSSM*, Comput. Phys. Commun. **183** (2012) 2458–2469, arXiv: 1104.1573 [hep-ph].

[125] B. C. Allanach, *SOFTSUSY: a program for calculating supersymmetric spectra*, Comput. Phys. Commun. **143** (2002) 305–331, arXiv: hep-ph/0104145 [hep-ph]

B. C. Allanach et al., *Next-to-Minimal SOFTSUSY*, Comput. Phys. Commun. **185** (2014) 2322–2339, arXiv: 1311.7659 [hep-ph]

B. Allanach and M. Bernhardt, *Including R-parity violation in the numerical computation of the spectrum of the minimal supersymmetric standard model: SOFTSUSY*, Comput.Phys.Commun. **181** (2010) 232–245, arXiv: 0903.1805 [hep-ph]

B. C. Allanach, C. H. Kom and M. Hanussek, *Computation of Neutrino Masses in R-parity Violating Supersymmetry: SOFTSUSY3.2*, Comput. Phys. Commun. **183** (2012) 785–793, arXiv: 1109.3735 [hep-ph]

B. C. Allanach, A. Bednyakov and R. Ruiz de Austri, *Higher order corrections and unification in the minimal supersymmetric standard model: SOFTSUSY3.5*, Comput. Phys. Commun. **189** (2015) 192–206, arXiv: 1407.6130 [hep-ph].

[126] H. Baer et al., "Simulating Supersymmetry with ISAJET 7.0 / ISASUSY 1.0", *Workshop on Physics at Current Accelerators and the Supercollider Argonne, Illinois, June 2-5, 1993*, 1993, arXiv: hep-ph/9305342 [hep-ph].

[127] A. Djouadi, J.-L. Kneur and G. Moultaka, *SuSpect: A Fortran code for the supersymmetric and Higgs particle spectrum in the MSSM*, Comput. Phys. Commun. **176** (2007) 426–455, arXiv: hep-ph/0211331 [hep-ph].

[128] Graeme Watt, [Online; accessed January 15, 2016], URL: https://mstwpdf.hepforge.org/plots/mstw2008lo68cl_allpdfs.png.

[129] A. D. Martin et al., *Parton distributions for the LHC*, Eur. Phys. J. **C63** (2009) 189–285, arXiv: 0901.0002 [hep-ph].

[130] R. Placakyte, "Parton Distribution Functions", *Proceedings, 31st International Conference on Physics in collisions (PIC 2011)*, 2011, arXiv: 1111.5452 [hep-ph].

[131] Y. L. Dokshitser, *Calculation of structure functions of deep-inelastic scattering and e+ e-annihilation by perturbation theory in quantum chromodynamics*, Soviet Journal of Experimental and Theoretical Physics **46** (1977) 641

V. N. Gribov and L. N. Lipatov, *Deep inelastic e p scattering in perturbation theory*, Sov. J. Nucl. Phys. **15** (1972) 438–450, [Yad. Fiz.15,781(1972)]

G. Altarelli and G. Parisi, *Asymptotic Freedom in Parton Language*, Nucl. Phys. **B126** (1977) 298.

[132] J. Pumplin et al., *New generation of parton distributions with uncertainties from global QCD analysis*, JHEP **07** (2002) 012, arXiv: hep-ph/0201195 [hep-ph]

S. Dulat et al., *The CT14 Global Analysis of Quantum Chromodynamics* (2015), arXiv: 1506.07443 [hep-ph].

[133] F. D. Aaron et al., *Combined Measurement and QCD Analysis of the Inclusive e+- p Scattering Cross Sections at HERA*, JHEP **01** (2010) 109, arXiv: 0911.0884 [hep-ex].

[134] A. Buckley et al., *LHAPDF6: parton density access in the LHC precision era*, Eur. Phys. J. **C75** (2015) 132, arXiv: 1412.7420 [hep-ph].

[135] H. K. Dreiner and T. Stefaniak, *Bounds on R-parity Violation from Resonant Slepton Production at the LHC*, Phys. Rev. **D86** (2012) 055010, arXiv: 1201.5014 [hep-ph].

[136] S. Dimopoulos et al., *Cross-Sections for Lepton and Baryon Number Violating Processes from Supersymmetry at p anti-p Colliders*, Phys. Rev. **D41** (1990) 2099.

[137] H. K. Dreiner et al., *Supersymmetric NLO QCD corrections to resonant slepton production and signals at the Tevatron and the CERN LHC*, Phys. Rev. **D75** (2007) 035003, arXiv: hep-ph/0611195 [hep-ph].

[138] The ATLAS Collaboration,
Dependence on ATLAS ETMiss resolution on different sources of transverse energy,
[Online; accessed January 27, 2016], 2011, URL: https://atlas.web.cern.ch/Atlas/GROUPS/PHYSICS/PAPERS/PERF-2011-07/fig_16d.png.

[139] A. Papaefstathiou, *How-to: Write a parton-level Monte Carlo event generator* (2014), arXiv: 1412.4677 [hep-ph].

[140] Particle Data Group, Revised by Lynn Garren, Ian Knowles, Torbjorn Sjostrand, and Tom Trippe, *Monte Carlo Particle Numbering Scheme*,
[Online; accessed March 12, 2016],
URL: http://pdg.lbl.gov/mc_particle_id_contents.html.

[141] J. Alwall et al., *A Standard format for Les Houches event files*,
Comput. Phys. Commun. **176** (2007) 300–304, arXiv: hep-ph/0609017 [hep-ph]

E. Boos et al., "Generic user process interface for event generators",
Physics at TeV colliders. Proceedings, Euro Summer School, Les Houches, France, May 21-June 1, 2001, 2001, arXiv: hep-ph/0109068 [hep-ph].

[142] J. Alwall et al., *The automated computation of tree-level and next-to-leading order differential cross sections, and their matching to parton shower simulations*,
JHEP **1407** (2014) 079, arXiv: 1405.0301 [hep-ph].

[143] W. Kilian, T. Ohl and J. Reuter,
WHIZARD: Simulating Multi-Particle Processes at LHC and ILC,
Eur. Phys. J. **C71** (2011) 1742, arXiv: 0708.4233 [hep-ph]

M. Moretti, T. Ohl and J. Reuter, *O'Mega: An Optimizing matrix element generator* (2001), arXiv: hep-ph/0102195 [hep-ph].

[144] A. Belyaev, N. D. Christensen and A. Pukhov,
CalcHEP 3.4 for collider physics within and beyond the Standard Model,
Comput.Phys.Commun. **184** (2013) 1729–1769, arXiv: 1207.6082 [hep-ph].

[145] G. Corcella et al., *HERWIG 6.5 release note* (2002), arXiv: hep-ph/0210213 [hep-ph]

M. Bahr et al., *Herwig++ Physics and Manual*, Eur.Phys.J. **C58** (2008) 639–707,
arXiv: 0803.0883 [hep-ph]

J. Bellm et al., *Herwig 7.0 / Herwig++ 3.0 Release Note* (2015),
arXiv: 1512.01178 [hep-ph].

[146] T. Gleisberg et al., *Event generation with SHERPA 1.1*, JHEP **0902** (2009) 007,
arXiv: 0811.4622 [hep-ph].

[147] T. Sjöstrand, S. Mrenna and P. Skands, *PYTHIA 6.4 physics and manual*,
Journal of High Energy Physics **2006**.05 (2006) 026

T. Sjostrand, S. Mrenna and P. Z. Skands, *PYTHIA 6.4 Physics and Manual*,
JHEP **0605** (2006) 026, arXiv: hep-ph/0603175 [hep-ph]

T. Sjostrand, S. Mrenna and P. Z. Skands, *A Brief Introduction to PYTHIA 8.1*,
Comput.Phys.Commun. **178** (2008) 852–867, arXiv: 0710.3820 [hep-ph]

T. Sjöstrand et al., *An Introduction to PYTHIA 8.2*,
Comput. Phys. Commun. **191** (2015) 159–177, arXiv: 1410.3012 [hep-ph].

[148] The Pythia 8 Collaboration, *PYTHIA 8 Online Documentation*, [Online; accessed May 12, 2016], URL: http://home.thep.lu.se/~torbjorn/pythia82html/Welcome.html.

[149] N. Nakanishi, *General Theory of Infrared Divergence*, Progress of Theoretical Physics **19**.2 (1958) 159–168, eprint: http://ptp.oxfordjournals.org/content/19/2/159.full.pdf+html

T. D. Lee and M. Nauenberg, *Degenerate Systems and Mass Singularities*, Phys. Rev. **133** (1964) B1549–B1562

T. Kinoshita, *Mass singularities of Feynman amplitudes*, J. Math. Phys. **3** (1962) 650–677.

[150] G. C. Fox and S. Wolfram, *A Model for Parton Showers in QCD*, Nucl. Phys. **B168** (1980) 285.

[151] P. Nason, *A New method for combining NLO QCD with shower Monte Carlo algorithms*, JHEP **11** (2004) 040, arXiv: hep-ph/0409146 [hep-ph].

[152] G. Marchesini and B. Webber, *Monte Carlo simulation of general hard processes with coherent {QCD} radiation*, Nuclear Physics B **310**.3–4 (1988) 461–526

T. Sjostrand, *A Model for Initial State Parton Showers*, Phys. Lett. **B157** (1985) 321.

[153] Mangano, Michelangelo L., *The so-called MLM prescription for ME/PS matching.* [Online; accessed January 27, 2016], 2002, URL: http://www-cpd.fnal.gov/personal/mrenna/tuning/nov2002/mlm.pdf.gz

M. L. Mangano et al., *Matching matrix elements and shower evolution for top-quark production in hadronic collisions*, JHEP **01** (2007) 013, arXiv: hep-ph/0611129 [hep-ph].

[154] S. Catani et al., *QCD matrix elements + parton showers*, JHEP **11** (2001) 063, arXiv: hep-ph/0109231 [hep-ph]

L. Lonnblad, *Correcting the color dipole cascade model with fixed order matrix elements*, JHEP **05** (2002) 046, arXiv: hep-ph/0112284 [hep-ph].

[155] J. Alwall, S. de Visscher and F. Maltoni, *QCD radiation in the production of heavy colored particles at the LHC*, JHEP **02** (2009) 017, arXiv: 0810.5350 [hep-ph].

[156] E. C. Poggio, H. R. Quinn and S. Weinberg, *Smearing method in the quark model*, Phys. Rev. D **13** (7 1976) 1958–1968

M. A. Shifman, "Quark hadron duality", *Proceedings, 8th International Symposium on Heavy Flavor Physics (Heavy Flavors 8)*, [hf8/013(2000)], 2000, arXiv: hep-ph/0009131 [hep-ph].

[157] B. Andersson et al., *Parton Fragmentation and String Dynamics*, Phys. Rept. **97** (1983) 31–145.

[158] D. Amati and G. Veneziano, *Preconfinement as a property of perturbative QCD*, Physics Letters B **83**.1 (1979) 87–92

A. Bassetto, M. Ciafaloni and G. Marchesini,
Color Singlet Distributions and Mass Damping in Perturbative QCD,
Phys. Lett. **B83** (1979) 207.

[159] Lynn Garren, *StdHep 4.09, Monte Carlo Standardization at FNAL*,
[Online; accessed February 23, 2016], URL: http://uscms-docdb.fnal.gov/cgi-bin/RetrieveFile?docid=903&filename=stdhep_409_manual.ps&version=10.

[160] M. Dobbs and J. B. Hansen,
The HepMC C++ Monte Carlo event record for high energy physics,
Computer Physics Communications **134**.1 (2001) 41–46.

[161] The FeynRules Collaboration,
FeynRules models to be used for NLO calculations with aMC@NLO,
[Online; accessed June 02, 2016],
URL: http://feynrules.irmp.ucl.ac.be/wiki/NLOModels.

[162] W. Beenakker et al., *Squark and gluino production at hadron colliders*,
Nucl. Phys. **B492** (1997) 51–103, arXiv: hep-ph/9610490 [hep-ph]

W. Beenakker et al., *Stop production at hadron colliders*,
Nucl.Phys. **B515** (1998) 3–14, arXiv: hep-ph/9710451 [hep-ph]

W. Beenakker et al.,
The Production of charginos / neutralinos and sleptons at hadron colliders,
Phys.Rev.Lett. **83** (1999) 3780–3783, arXiv: hep-ph/9906298 [hep-ph]

M. Spira, "Higgs and SUSY particle production at hadron colliders",
Supersymmetry and unification of fundamental interactions. Proceedings, 10th International Conference, SUSY'02, Hamburg, Germany, June 17-23, 2002, 2002
217–226, arXiv: hep-ph/0211145 [hep-ph]

T. Plehn, *Measuring the MSSM Lagrangean*, Czech. J. Phys. **55** (2005) B213–B220,
arXiv: hep-ph/0410063 [hep-ph].

[163] W. Beenakker et al., *Squark and gluino production at hadron colliders*,
Nucl. Phys. **B492** (1997) 51–103, arXiv: hep-ph/9610490 [hep-ph]

W. Beenakker et al., *Stop production at hadron colliders*,
Nucl.Phys. **B515** (1998) 3–14, arXiv: hep-ph/9710451 [hep-ph]

A. Kulesza and L. Motyka,
Threshold resummation for squark-antisquark and gluino-pair production at the LHC,
Phys.Rev.Lett. **102** (2009) 111802, arXiv: 0807.2405 [hep-ph]

A. Kulesza and L. Motyka, *Soft gluon resummation for the production of gluino-gluino and squark-antisquark pairs at the LHC*, Phys.Rev. **D80** (2009) 095004,
arXiv: 0905.4749 [hep-ph]

W. Beenakker et al., *Soft-gluon resummation for squark and gluino hadroproduction*,
JHEP **0912** (2009) 041, arXiv: 0909.4418 [hep-ph]

W. Beenakker et al.,
Supersymmetric top and bottom squark production at hadron colliders,
JHEP **1008** (2010) 098, arXiv: 1006.4771 [hep-ph]

W. Beenakker et al., *Squark and Gluino Hadroproduction*, Int.J.Mod.Phys. **A26** (2011) 2637–2664, arXiv: 1105.1110 [hep-ph].

[164] S. Agostinelli et al., *Geant4—a simulation toolkit*, Nuclear Instruments and Methods in Physics Research Section A: Accelerators, Spectrometers, Detectors and Associated Equipment **506**.3 (2003) 250–303

J. Allison et al., *Geant4 developments and applications*, IEEE Trans. Nucl. Sci. **53** (2006) 270.

[165] J. de Favereau et al., *DELPHES 3, A modular framework for fast simulation of a generic collider experiment* (2013), arXiv: 1307.6346 [hep-ex].

[166] A. Giammanco, *The Fast Simulation of the CMS Experiment*, Journal of Physics: Conference Series **513**.2 (2014) 022012.

[167] John Conway, *PGS4 - Pretty Good Simulation of high energy collisions*, [Online; accessed February 22, 2016], URL: http://conway.physics.ucdavis.edu/research/software/pgs/pgs4-general.htm.

[168] M. Cacciari, G. P. Salam and G. Soyez, *FastJet User Manual*, Eur.Phys.J. **C72** (2012) 1896, arXiv: 1111.6097 [hep-ph].

[169] R. Brun and F. Rademakers, *ROOT: An object oriented data analysis framework*, Nucl.Instrum.Meth. **A389** (1997) 81–86.

[170] The CMS Collaboration, *Search for new physics in high mass diphoton events in proton-proton collisions at* $\sqrt{s} = 13$ *TeV*, tech. rep. CMS-PAS-EXO-15-004, CERN, 2015

The ATLAS Collaboration, *Search for resonances decaying to photon pairs in 3.2* fb^{-1} *of pp collisions at* $\sqrt{s} = 13$ *TeV with the ATLAS detector*, tech. rep. ATLAS-CONF-2015-081, CERN, 2015.

[171] G. Aad et al., *Search for direct production of charginos and neutralinos in events with three leptons and missing transverse momentum in* $\sqrt{s} = 8$*TeV pp collisions with the ATLAS detector*, JHEP **1404** (2014) 169, arXiv: 1402.7029 [hep-ex].

[172] A. Buckley et al., *Rivet user manual* (2010), arXiv: 1003.0694 [hep-ph].

[173] Michele Papucci, Kazuki Sakurai, Andreas Weiler, *ATOM — Automatic Test of Models Tool not public by the time this thesis was completed*, [Online; accessed March 2, 2016], URL: https://lpsc.in2p3.fr/Indico/getFile.py/access?contribId=6&resId=0&materialId=slides&confId=1085.

[174] E. Conte, B. Fuks and G. Serret, *MadAnalysis 5, A User-Friendly Framework for Collider Phenomenology*, Comput.Phys.Commun. **184** (2013) 222–256, arXiv: 1206.1599 [hep-ph].

[175] A. L. Read, *Presentation of search results: the CL's technique*, Journal of Physics G: Nuclear and Particle Physics **28**.10 (2002) 2693.

[176] S. S. Wilks, *The Large-Sample Distribution of the Likelihood Ratio for Testing Composite Hypotheses*, Ann. Math. Statist. **9**.1 (1938) 60–62, URL: http://dx.doi.org/10.1214/aoms/1177732360.

[177] The RooStats Collaboration, *RooStats Wiki*, [Online; accessed June 5, 2016], URL: https://twiki.cern.ch/twiki/bin/view/RooStats/WebHome.

[178] M. Drees et al., *CheckMATE: Confronting your Favourite New Physics Model with LHC Data* (2013), arXiv: 1312.2591 [hep-ph].

[179] J. S. Kim et al., *A framework to create customised LHC analyses within CheckMATE* (2015), arXiv: 1503.01123 [hep-ph].

[180] Wikipedia, *Fritz (chess)*, [Online; accessed May 20, 2016], URL: https://en.wikipedia.org/wiki/Fritz_%28chess%29

ChessBase GmbH, *ChessBase*, [Online; accessed May 20, 2016], URL: http://en.chessbase.com/.

[181] Sabine Kraml, *Mini-workshop on recasting ATLAS and CMS new physics searches*, [Online; accessed May 12, 2016], URL: https://lpsc.in2p3.fr/Indico/conferenceDisplay.py?confId=1085.

[182] G. Aad et al., *Summary of the searches for squarks and gluinos using $\sqrt{s} = 8$ TeV pp collisions with the ATLAS experiment at the LHC*, JHEP **10** (2015) 054, arXiv: 1507.05525 [hep-ex].

[183] G. Aad et al., *Search for squarks and gluinos with the ATLAS detector in final states with jets and missing transverse momentum using $\sqrt{s} = 8$ TeV proton–proton collision data*, JHEP **09** (2014) 176, arXiv: 1405.7875 [hep-ex].

[184] The ATLAS Collaboration, *Results on Squark-Gluino-Neutralino Model from 1405.7875*, [Online; accessed May 20, 2016], URL: https://atlas.web.cern.ch/Atlas/GROUPS/PHYSICS/PAPERS/SUSY-2013-02/fig_09.png.

[185] G. Aad et al., *Search for new phenomena in final states with an energetic jet and large missing transverse momentum in pp collisions at $\sqrt{s}$ =8 TeV with the ATLAS detector*, Eur. Phys. J. **C75**.7 (2015) 299, [Erratum: Eur. Phys. J.C75,no.9,408(2015)], arXiv: 1502.01518 [hep-ex].

[186] S. Chatrchyan et al., *Search for supersymmetry in hadronic final states with missing transverse energy using the variables α_T and b-quark multiplicity in pp collisions at $\sqrt{s} = 8$ TeV* (2013), arXiv: 1303.2985 [hep-ex].

[187] A. Salvucci, "Measurement of muon momentum resolution of the ATLAS detector", *European Physical Journal Web of Conferences*, vol. 28, European Physical Journal Web of Conferences, 2012 12039, arXiv: 1201.4704 [physics.ins-det].

[188] The ATLAS Collaboration, *Muon reconstruction efficiency in reprocessed 2010 LHC proton-proton collision data recorded with the ATLAS detector*, tech. rep. ATLAS-CONF-2011-063, CERN, 2011.

[189] G. Aad et al., *Electron performance measurements with the ATLAS detector using the 2010 LHC proton-proton collision data*, Eur.Phys.J. **C72** (2012) 1909, arXiv: 1110.3174 [hep-ex].

[190] G. Aad et al.,
Expected Performance of the ATLAS Experiment - Detector, Trigger and Physics (2009), arXiv: 0901.0512 [hep-ex].

[191] G. Aad et al., *Measurement of the muon reconstruction performance of the ATLAS detector using 2011 and 2012 LHC proton–proton collision data*, Eur. Phys. J. **C74**.11 (2014) 3130, arXiv: 1407.3935 [hep-ex].

[192] G. Aad et al., *Search for high-mass dilepton resonances in pp collisions at $\sqrt{s} = 8$ TeV with the ATLAS detector*, Phys. Rev. **D90**.5 (2014) 052005, arXiv: 1405.4123 [hep-ex].

[193] *Electron Efficiency Measurements for 2012 and 2011 Data*, tech. rep. ATL-COM-PHYS-2013-1287, CERN, 2013.

[194] The ATLAS Collaboration, *Commissioning of the ATLAS high-performance b-tagging algorithms in the 7 TeV collision data*, tech. rep. ATLAS-CONF-2011-102, CERN, 2011.

[195] The ATLAS Collaboration, *b-jet tagging calibration on c-jets containing D^{*+} mesons*, tech. rep. ATLAS-CONF-2012-039, CERN, 2012.

[196] The ATLAS Collaboration,
Measurement of the Mistag Rate with 5 fb^{-1} of Data Collected by the ATLAS Detector, tech. rep. ATLAS-CONF-2012-040, CERN, 2012.

[197] The ATLAS Collaboration, *Measuring the b-tag efficiency in a top-pair sample with 4.7 fb-1 of data from the ATLAS detector*, tech. rep. ATLAS-CONF-2012-097, CERN, 2012.

[198] The ATLAS Collaboration, *Measurement of the b-tag Efficiency in a Sample of Jets Containing Muons with 5 fb-1 of Data from the ATLAS Detector*, tech. rep. ATLAS-CONF-2012-043, CERN, 2012.

[199] The ATLAS Collaboration, *Performance of the Reconstruction and Identification of Hadronic Tau Decays with ATLAS*, tech. rep. ATLAS-CONF-2011-152, CERN, 2011.

[200] G. Aad et al., *Search for direct third-generation squark pair production in final states with missing transverse momentum and two b-jets in $\sqrt{s}$=8 TeV pp collisions with the ATLAS detector* (2013), arXiv: 1308.2631 [hep-ex].

[201] G. Aad et al., *Search for direct top-squark pair production in final states with two leptons in pp collisions at $\sqrt{s}$=8 TeV with the ATLAS detector* (2014), arXiv: 1403.4853 [hep-ex].

[202] G. Aad et al.,
Search for top squark pair production in final states with one isolated lepton, jets, and missing transverse momentum in $\sqrt{s}$ =8 TeV pp collisions with the ATLAS detector, JHEP **1411** (2014) 118, arXiv: 1407.0583 [hep-ex].

[203] The ATLAS Collaboration, *Search for supersymmetry at $\sqrt{s} = 8$ TeV in final states with jets, missing transverse momentum and one isolated lepton*, tech. rep. ATLAS-CONF-2012-104, CERN, 2012.

[204] The ATLAS Collaboration, *Search for New Phenomena in Monojet plus Missing Transverse Momentum Final States using 10fb-1 of pp Collisions at sqrts=8 TeV with the ATLAS detector at the LHC*, tech. rep. ATLAS-CONF-2012-147, CERN, 2012.

[205] *Search for direct production of the top squark in the all-hadronic ttbar + etmiss final state in 21 fb-1 of p-pcollisions at sqrt(s)=8 TeV with the ATLAS detector*, tech. rep. ATLAS-CONF-2013-024, CERN, 2013.

[206] *Search for direct-slepton and direct-chargino production in final states with two opposite-sign leptons, missing transverse momentum and no jets in 20/fb of pp collisions at sqrt(s) = 8 TeV with the ATLAS detector*, tech. rep. ATLAS-CONF-2013-049, CERN, 2013.

[207] The ATLAS Collaboration, *Search for strong production of supersymmetric particles in final states with missing transverse momentum and at least three b-jets using 20.1 fb-1 of pp collisions at sqrt(s) = 8 TeV with the ATLAS Detector.*, tech. rep. ATLAS-CONF-2013-061, CERN, 2013.

[208] The ATLAS Collaboration, *Search for strongly produced supersymmetric particles in decays with two leptons at $\sqrt{s}$ = 8 TeV*, tech. rep. ATLAS-CONF-2013-089, CERN, 2013.

[209] The CMS Collaboration, *Search for new physics in events with same-sign dileptons and jets in pp collisions at 8 TeV*, tech. rep. CMS-PAS-SUS-13-013, 2013.

[210] The CheckMATE Collaboration, *CheckMATE @ Hepforge*, [Online; accessed May 20, 2016], URL: http://checkmate.hepforge.org.

[211] *Search for Supersymmetry at the high luminosity LHC with the ATLAS experiment*, tech. rep. ATL-PHYS-PUB-2014-010, CERN, 2014.

[212] *Prospects for benchmark Supersymmetry searches at the high luminosity LHC with the ATLAS Detector*, tech. rep. ATL-PHYS-PUB-2013-011, CERN, 2013.

[213] G. Aad et al., *Measurement of W^+W^- production in pp collisions at $\sqrt{s} = 7$ TeV with the ATLAS detector and limits on anomalous WWZ and $WW\gamma$ couplings* (2012), arXiv: 1210.2979 [hep-ex].

[214] G. Aad et al., *Search for new phenomena in final states with large jet multiplicities and missing transverse momentum at $\sqrt{s}$=8 TeV proton-proton collisions using the ATLAS experiment*, JHEP **10** (2013) 130, [Erratum: JHEP01,109(2014)], arXiv: 1308.1841 [hep-ex].

[215] G. Aad et al., *Search for direct top squark pair production in events with a Z boson, b-jets and missing transverse momentum in sqrt(s)=8 TeV pp collisions with the ATLAS detector*, Eur. Phys. J. **C74**.6 (2014) 2883, arXiv: 1403.5222 [hep-ex].

[216] G. Aad et al., *Search for direct production of charginos, neutralinos and sleptons in final states with two leptons and missing transverse momentum in pp collisions at $\sqrt{s}$ = 8 TeV with the ATLAS detector* (2014), arXiv: 1403.5294 [hep-ex].

[217] G. Aad et al., *Search for supersymmetry at $\sqrt{s}$=8 TeV in final states with jets and two same-sign leptons or three leptons with the ATLAS detector*, JHEP **06** (2014) 035, arXiv: 1404.2500 [hep-ex].

[218] G. Aad et al., *Search for strong production of supersymmetric particles in final states with missing transverse momentum and at least three b-jets at $\sqrt{s}$= 8 TeV proton-proton collisions with the ATLAS detector*, JHEP **10** (2014) 024, arXiv: 1407.0600 [hep-ex].

[219] G. Aad et al., *Search for pair-produced third-generation squarks decaying via charm quarks or in compressed supersymmetric scenarios in pp collisions at $\sqrt{s} = 8$ TeV with the ATLAS detector*, Phys.Rev. **D90**.5 (2014) 052008, arXiv: 1407.0608 [hep-ex].

[220] G. Aad et al., *Search for new phenomena in events with a photon and missing transverse momentum in pp collisions at $\sqrt{s} = 8$ TeV with the ATLAS detector*, Phys. Rev. **D91**.1 (2015) 012008, [Erratum: Phys. Rev.D92,no.5,059903(2015)], arXiv: 1411.1559 [hep-ex].

[221] G. Aad et al., *Search for supersymmetry in events containing a same-flavour opposite-sign dilepton pair, jets, and large missing transverse momentum in $\sqrt{s} = 8$ TeV pp collisions with the ATLAS detector*, Eur. Phys. J. **C75**.7 (2015) 318, arXiv: 1503.03290 [hep-ex].

[222] G. Aad et al., *ATLAS Run 1 searches for direct pair production of third-generation squarks at the Large Hadron Collider*, Eur. Phys. J. **C75**.10 (2015) 510, [Erratum: Eur. Phys. J.C76,no.3,153(2016)], arXiv: 1506.08616 [hep-ex].

[223] G. Aad et al., *Search for supersymmetry at $\sqrt{s} = 13$ TeV in final states with jets and two same-sign leptons or three leptons with the ATLAS detector*, Eur. Phys. J. **C76**.5 (2016) 259, arXiv: 1602.09058 [hep-ex].

[224] A. Collaboration, *A Measurement of WZ Production in Proton-Proton Collisions at $\sqrt{s} = 8$ TeV with the ATLAS Detector*, tech. rep. ATLAS-CONF-2013-021, ATLAS-COM-CONF-2013-016, 2013.

[225] The ATLAS Collaboration, *Study of the spin properties of the Higgs-like particle in the $H \to WW^{(*)} \to e\nu\mu\nu$ channel with 21 fb^{-1} of $\sqrt{s} = 8$ TeV data collected with the ATLAS detector*, tech. rep. ATLAS-CONF-2013-031, CERN, 2013.

[226] The ATLAS Collaboration, *Search for supersymmetry in events with four or more leptons in 21 fb^{-1} of pp collisions at $\sqrt{s} = 8$ TeV with the ATLAS detector*, tech. rep. ATLAS-CONF-2013-036, CERN, 2013.

[227] The ATLAS Collaboration, *Search for squarks and gluinos in events with isolated leptons, jets and missing transverse momentum at $\sqrt{s} = 8$ TeV with the ATLAS detector*, tech. rep. ATLAS-CONF-2013-062, CERN, 2013.

[228] The ATLAS Collaboration, *Search for the direct pair production of top squarks decaying to a b quark, a tau lepton, and weakly interacting particles, in $\sqrt{s} = 8TeV$ pp collisions using 20 fb^{-1} of ATLAS data*, tech. rep. ATLAS-CONF-2014-014, CERN, 2014.

[229] The ATLAS Collaboration, *Measurement of the W^+W^- production cross section in proton-proton collisions at $\sqrt{s} = 8$ TeV with the ATLAS detector*, tech. rep. ATLAS-CONF-2014-033, CERN, 2014.

[230] The ATLAS Collaboration, *Measurement of spin correlation in top–antitop quark events and search for top squark pair production in proton–proton collisions at $\sqrt{s}$=8 TeV using the ATLAS detector*, tech. rep. ATLAS-CONF-2014-056, CERN, 2014.

[231] The ATLAS Collaboration,
Search for an Invisibly Decaying Higgs Boson Produced via Vector Boson Fusion in pp Collisions at $\sqrt{s} = 8$ TeV using the ATLAS Detector at the LHC,
tech. rep. ATLAS-CONF-2015-004, CERN, 2015.

[232] *Search for squarks and gluinos in final states with jets and missing transverse momentum at $\sqrt{s}$ =13 TeV with the ATLAS detector*,
tech. rep. ATLAS-CONF-2015-062, CERN, 2015.

[233] The ATLAS Collaboration, *Search for pair-production of gluinos decaying via stop and sbottom in events with b-jets and large missing transverse momentum in $\sqrt{s} = 13$ TeV pp collisions with the ATLAS detector*, tech. rep. ATLAS-CONF-2015-067,
CERN, 2015.

[234] *Search for gluinos in events with an isolated lepton, jets and missing transverse momentum at $\sqrt{s}$= 13 TeV with the ATLAS detector*,
tech. rep. ATLAS-CONF-2015-076, CERN, 2015.

[235] S. Chatrchyan et al., *Measurement of W^+W^- and ZZ production cross sections in pp collisions at $\sqrt{s} = 8$ TeV* (2013), arXiv: 1301.4698 [hep-ex].

[236] V. Khachatryan et al., *Searches for electroweak production of charginos, neutralinos, and sleptons decaying to leptons and W, Z, and Higgs bosons in pp collisions at 8 TeV*,
Eur. Phys. J. **C74**.9 (2014) 3036, arXiv: 1405.7570 [hep-ex].

[237] V. Khachatryan et al., *Search for dark matter, extra dimensions, and unparticles in monojet events in proton–proton collisions at $\sqrt{s} = 8$ TeV*,
Eur. Phys. J. **C75**.5 (2015) 235, arXiv: 1408.3583 [hep-ex].

[238] V. Khachatryan et al.,
Search for Physics Beyond the Standard Model in Events with Two Leptons, Jets, and Missing Transverse Momentum in pp Collisions at sqrt(s) = 8 TeV,
JHEP **04** (2015) 124, arXiv: 1502.06031 [hep-ex].

[239] V. Khachatryan et al.,
Search for the production of dark matter in association with top-quark pairs in the single-lepton final state in proton-proton collisions at sqrt(s) = 8 TeV,
JHEP **06** (2015) 121, arXiv: 1504.03198 [hep-ex].

[240] The CMS Collaboration, *Search for physics beyond the standard model in events with two opposite-sign same-flavor leptons, jets, and missing transverse energy in pp collisions at sqrt[s] = 8 TeV*, tech. rep. CMS-PAS-SUS-12-019, CERN, 2014.

[241] The ATLAS Collaboration, *Search for squarks and gluinos with the ATLAS detector in final states with jets and missing transverse momentum and 20.3 fb^{-1} of $\sqrt{s} = 8$ TeV proton-proton collision data*, tech. rep. ATLAS-CONF-2013-047, CERN, 2013.

[242] J. S. Kim, O. Lebedev and D. Schmeier,
Higgsophilic gauge bosons and monojets at the LHC, JHEP **11** (2015) 128,
arXiv: 1507.08673 [hep-ph].

[243] M. Duch, B. Grzadkowski and M. McGarrie,
A stable Higgs portal with vector dark matter, JHEP **09** (2015) 162,
arXiv: 1506.08805 [hep-ph].

[244] V. V. Khoze, C. McCabe and G. Ro,
Higgs vacuum stability from the dark matter portal, JHEP **08** (2014) 026,
arXiv: 1403.4953 [hep-ph].

[245] A. Falkowski, C. Gross and O. Lebedev, *A second Higgs from the Higgs portal*,
JHEP **05** (2015) 057, arXiv: 1502.01361 [hep-ph].

[246] S. Baek et al., *Higgs Portal Vector Dark Matter : Revisited*, JHEP **05** (2013) 036,
arXiv: 1212.2131 [hep-ph].

[247] O. Lebedev and H. M. Lee, *Higgs Portal Inflation*, Eur. Phys. J. **C71** (2011) 1821,
arXiv: 1105.2284 [hep-ph].

[248] K. R. Dienes, C. F. Kolda and J. March-Russell,
Kinetic mixing and the supersymmetric gauge hierarchy,
Nucl. Phys. **B492** (1997) 104–118, arXiv: hep-ph/9610479 [hep-ph].

[249] O. Lebedev, H. M. Lee and Y. Mambrini,
Vector Higgs-portal dark matter and the invisible Higgs,
Phys. Lett. **B707** (2012) 570–576, arXiv: 1111.4482 [hep-ph].

[250] S. Gopalakrishna, S. Jung and J. D. Wells,
Higgs boson decays to four fermions through an abelian hidden sector,
Phys. Rev. **D78** (2008) 055002, arXiv: 0801.3456 [hep-ph].

[251] M. Endo and Y. Takaesu, *Heavy WIMP through Higgs portal at the LHC*,
Phys. Lett. **B743** (2015) 228–234, arXiv: 1407.6882 [hep-ph].

[252] A. Djouadi et al., *Implications of LHC searches for Higgs–portal dark matter*,
Phys. Lett. **B709** (2012) 65–69, arXiv: 1112.3299 [hep-ph].

[253] A. Djouadi et al., *Direct Detection of Higgs-Portal Dark Matter at the LHC*,
Eur. Phys. J. **C73**.6 (2013) 2455, arXiv: 1205.3169 [hep-ph].

[254] The ATLAS and CMS Collaborations, *Measurements of the Higgs boson production and decay rates and constraints on its couplings from a combined ATLAS and CMS analysis of the LHC pp collision data at* $\sqrt{s} = 7$ *and 8 TeV* (2015).

[255] V. Khachatryan et al.,
Precise determination of the mass of the Higgs boson and tests of compatibility of its couplings with the standard model predictions using proton collisions at 7 and 8 TeV,
Eur. Phys. J. **C75**.5 (2015) 212, arXiv: 1412.8662 [hep-ex].

[256] G. Aad et al.,
Measurements of Higgs boson production and couplings in the four-lepton channel in pp collisions at center-of-mass energies of 7 and 8 TeV with the ATLAS detector,
Phys. Rev. **D91**.1 (2015) 012006, arXiv: 1408.5191 [hep-ex].

[257] G. Aad et al., *Measurement of Higgs boson production in the diphoton decay channel in pp collisions at center-of-mass energies of 7 and 8 TeV with the ATLAS detector*,
Phys. Rev. **D90**.11 (2014) 112015, arXiv: 1408.7084 [hep-ex].

[258] G. Aad et al., *Constraints on new phenomena via Higgs boson couplings and invisible decays with the ATLAS detector*, JHEP **11** (2015) 206, arXiv: 1509.00672 [hep-ex].

[259] V. Khachatryan et al., *Search for a Higgs Boson in the Mass Range from 145 to 1000 GeV Decaying to a Pair of W or Z Bosons*, JHEP **10** (2015) 144,
arXiv: 1504.00936 [hep-ex].

[260] G. Aad et al., *Search for an additional, heavy Higgs boson in the $H \to ZZ$ decay channel at $\sqrt{s} = 8$ TeV in pp collision data with the ATLAS detector*, Eur. Phys. J. **C76**.1 (2016) 45, arXiv: 1507.05930 [hep-ex].

[261] G. Aad et al., *Searches for Higgs boson pair production in the $hh \to bb\tau\tau, \gamma\gamma WW^*, \gamma\gamma bb, bbbb$ channels with the ATLAS detector*, Phys. Rev. **D92** (2015) 092004, arXiv: 1509.04670 [hep-ex].

[262] V. Khachatryan et al., *Search for resonant pair production of Higgs bosons decaying to two bottom quark–antiquark pairs in proton–proton collisions at 8 TeV*, Phys. Lett. **B749** (2015) 560–582, arXiv: 1503.04114 [hep-ex]

V. Khachatryan et al., *Searches for a heavy scalar boson H decaying to a pair of 125 GeV Higgs bosons hh or for a heavy pseudoscalar boson A decaying to Zh, in the final states with $h \to \tau\tau$*, Phys. Lett. **B755** (2016) 217–244, arXiv: 1510.01181 [hep-ex]

V. Khachatryan et al., *Search for two Higgs bosons in final states containing two photons and two bottom quarks* (2016), arXiv: 1603.06896 [hep-ex].

[263] J. R. Andersen et al., *Handbook of LHC Higgs Cross Sections: 3. Higgs Properties* (2013), ed. by S. Heinemeyer et al., arXiv: 1307.1347 [hep-ph].

[264] T. Hambye, *Hidden vector dark matter*, JHEP **01** (2009) 028, arXiv: 0811.0172 [hep-ph].

[265] S. Schael et al., *Precision electroweak measurements on the Z resonance*, Phys. Rept. **427** (2006) 257–454, arXiv: hep-ex/0509008 [hep-ex]

J. Beringer et al., *Review of Particle Physics (RPP)*, Phys. Rev. **D86** (2012) 010001

T. E. W. Group, *2012 Update of the Combination of CDF and D0 Results for the Mass of the W Boson* (2012), arXiv: 1204.0042 [hep-ex]

S. Schael et al., *Electroweak Measurements in Electron-Positron Collisions at W-Boson-Pair Energies at LEP*, Phys. Rept. **532** (2013) 119–244, arXiv: 1302.3415 [hep-ex].

[266] Y. Farzan and A. R. Akbarieh, *VDM: A model for Vector Dark Matter*, JCAP **1210** (2012) 026, arXiv: 1207.4272 [hep-ph].

[267] C. Gross, O. Lebedev and Y. Mambrini, *Non-Abelian gauge fields as dark matter*, JHEP **08** (2015) 158, arXiv: 1505.07480 [hep-ph].

[268] A. J. Brennan et al., *Collide and Conquer: Constraints on Simplified Dark Matter Models using Mono-X Collider Searches* (2016), arXiv: 1603.01366 [hep-ph].

[269] C.-H. Chen and T. Nomura, *Searching for Vector Dark Matter by Higgs Portal at the LHC* (2015), arXiv: 1507.00886 [hep-ph].

[270] G. Aad et al., *Search for pair-produced third-generation squarks decaying via charm quarks or in compressed supersymmetric scenarios in pp collisions at $\sqrt{s} = 8$ TeV with the ATLAS detector*, Phys. Rev. D **90** (5 2014) 052008.

[271] The ATLAS Collaboration, *95% CL upper limit on sigma x BR(H -¿ invisible)*, [Online; accessed March 30, 2016], URL: http://atlas.web.cern.ch/Atlas/GROUPS/PHYSICS/PAPERS/EXOT-2013-13/fig_16.png.

[272] H.-L. Lai et al., *New parton distributions for collider physics*, Phys.Rev. **D82** (2010) 074024, arXiv: 1007.2241 [hep-ph].

[273] S. Frixione, P. Nason and G. Ridolfi, *A Positive-weight next-to-leading-order Monte Carlo for heavy flavour hadroproduction*, JHEP **09** (2007) 126, arXiv: 0707.3088 [hep-ph].

[274] M. Czakon and A. Mitov, *Top++: A Program for the Calculation of the Top-Pair Cross-Section at Hadron Colliders*, Comput. Phys. Commun. **185** (2014) 2930, arXiv: 1112.5675 [hep-ph].

[275] P. Nason, *A New method for combining NLO QCD with shower Monte Carlo algorithms*, JHEP **11** (2004) 040, arXiv: hep-ph/0409146 [hep-ph].

[276] S. Frixione, P. Nason and C. Oleari, *Matching NLO QCD computations with Parton Shower simulations: the POWHEG method*, JHEP **11** (2007) 070, arXiv: 0709.2092 [hep-ph].

[277] S. Alioli et al., *A general framework for implementing NLO calculations in shower Monte Carlo programs: the POWHEG BOX*, JHEP **06** (2010) 043, arXiv: 1002.2581 [hep-ph].

[278] E. Bagnaschi et al., *Higgs production via gluon fusion in the POWHEG approach in the SM and in the MSSM*, JHEP **02** (2012) 088, arXiv: 1111.2854 [hep-ph].

[279] P. Nason and C. Oleari, *NLO Higgs boson production via vector-boson fusion matched with shower in POWHEG*, JHEP **02** (2010) 037, arXiv: 0911.5299 [hep-ph].

[280] N. Kauer and C. O'Brien, *Heavy Higgs signal–background interference in $gg \to VV$ in the Standard Model plus real singlet*, Eur. Phys. J. **C75** (2015) 374, arXiv: 1502.04113 [hep-ph].

[281] J. S. Kim, D. Schmeier and J. Tattersall, *Role of the 'N' in the natural NMSSM for the LHC*, Phys. Rev. **D93**.5 (2016) 055018, arXiv: 1510.04871 [hep-ph].

[282] The CMS Collaboration, *Summary of CMS Results in SMS framework*, [Online; accessed April 28, 2016], URL: https://twiki.cern.ch/twiki/bin/view/CMSPublic/SUSYSMSSummaryPlots8TeV.

[283] The ATLAS Collaboration, *ATLAS SUSY searches, 95 percent confidence limits*, [Online; accessed April 28, 2016], URL: https://atlas.web.cern.ch/Atlas/GROUPS/PHYSICS/CombinedSummaryPlots/SUSY/.

[284] H. K. Dreiner, M. Kramer and J. Tattersall, *How low can SUSY go? Matching, monojets and compressed spectra*, Europhys.Lett. **99** (2012) 61001, arXiv: 1207.1613 [hep-ph].

[285] V. Khachatryan et al., *Search for supersymmetry in the multijet and missing transverse momentum final state in pp collisions at 13 TeV*, Submitted to: Phys. Lett. B (2016), arXiv: 1602.06581 [hep-ex].

[286] V. Khachatryan et al., *Search for new physics with the MT2 variable in all-jets final states produced in pp collisions at sqrt(s) = 13 TeV* (2016), arXiv: 1603.04053 [hep-ex].

[287] The ATLAS Collaboration, *Searches for Supersymmetry at the high luminosity LHC with the ATLAS Detector*, tech. rep. ATL-PHYS-PUB-2013-002, CERN, 2013.

[288] The CMS Collaboration, "Projected Performance of an Upgraded CMS Detector at the LHC and HL-LHC: Contribution to the Snowmass Process", *Community Summer Study 2013: Snowmass on the Mississippi (CSS2013) Minneapolis, MN, USA, July 29-August 6, 2013*, 2013, arXiv: 1307.7135.

[289] The CMS Collaboration, *Exclusion limits on gluino and top-squark pair production in natural SUSY scenarios with inclusive razor and exclusive single-lepton searches at 8 TeV.* (2014).

[290] S. Chatrchyan et al., *Search for top-squark pair production in the single-lepton final state in pp collisions at $\sqrt{s}$ = 8 TeV*, Eur.Phys.J. **C73** (2013) 2677, arXiv: 1308.1586 [hep-ex].

[291] The CMS Collaboration, *Search for top squarks decaying to a charm quark and a neutralino in events with a jet and missing transverse momentum* (2014).

[292] K. Rolbiecki and J. Tattersall, *Refining light stop exclusion limits with W^+W^- cross sections* (2015), arXiv: 1505.05523 [hep-ph].

[293] The CMS Collaboration, *Search for direct production of bottom squark pairs* (2014).

[294] The CMS Collaboration, *Search for supersymmetry in pp collisions at sqrt(s) = 8 TeV in events with three leptons and at least one b-tagged jet* (2013).

[295] S. Chatrchyan et al., *Search for new physics in events with same-sign dileptons and jets in pp collisions at $\sqrt{s}$ = 8 TeV*, JHEP **01** (2014) 163, [Erratum: JHEP01,014(2015)], arXiv: 1311.6736.

[296] H. Dreiner, F. Staub and A. Vicente, *General NMSSM signatures at the LHC*, Phys.Rev. **D87**.3 (2013) 035009, arXiv: 1211.6987 [hep-ph].

[297] A. Chakraborty et al., *Probing the NMSSM via Higgs boson signatures from stop cascade decays at the LHC*, Phys. Rev. **D91** (2015) 115018, arXiv: 1503.07592 [hep-ph].

[298] J. Beuria et al., *Two Light Stops in the NMSSM and the LHC* (2015), arXiv: 1505.00604 [hep-ph].

[299] J. Beuria, A. Chatterjee and A. Datta, *Sbottoms of Natural NMSSM at the LHC* (2016), arXiv: 1603.08463 [hep-ph].

[300] T. Cheng et al., *Natural NMSSM confronting with the LHC7-8*, Phys.Rev. **D89**.1 (2014) 015015, arXiv: 1304.3182 [hep-ph].

[301] U. Ellwanger, *Testing the higgsino-singlino sector of the NMSSM with trileptons at the LHC*, JHEP **11** (2013) 108, arXiv: 1309.1665 [hep-ph].

[302] J. S. Kim and T. S. Ray, *The higgsino-singlino world at the large hadron collider*, Eur.Phys.J. **C75** (2015) 40, arXiv: 1405.3700 [hep-ph].

[303] R. Dermisek and J. F. Gunion, *Escaping the large fine tuning and little hierarchy problems in the next to minimal supersymmetric model and h —¿ aa decays*, Phys. Rev. Lett. **95** (2005) 041801, arXiv: hep-ph/0502105 [hep-ph].

[304] R. Dermisek and J. F. Gunion, *The NMSSM Close to the R-symmetry Limit and Naturalness in h —¿ aa Decays for m(a) ¡ 2m(b)*, Phys. Rev. **D75** (2007) 075019, arXiv: hep-ph/0611142 [hep-ph].

[305] R. Dermisek and J. F. Gunion, *The NMSSM Solution to the Fine-Tuning Problem, Precision Electroweak Constraints and the Largest LEP Higgs Event Excess*, Phys. Rev. **D76** (2007) 095006, arXiv: 0705.4387 [hep-ph].

[306] J. F. Gunion, *A Light CP-odd Higgs boson and the muon anomalous magnetic moment*, JHEP **08** (2009) 032, arXiv: 0808.2509 [hep-ph].

[307] F. Domingo, U. Ellwanger and M.-A. Sanchis-Lozano, *Bottomoniom spectroscopy with mixing of eta(b) states and a light CP-odd Higgs*, Phys. Rev. Lett. **103** (2009) 111802, arXiv: 0907.0348 [hep-ph].

[308] C. T. Potter, *Natural NMSSM with a Light Pseudoscalar Higgs and Singlino LSP* (2015), arXiv: 1505.05554 [hep-ph].

[309] G. Moortgat-Pick, S. Porto and K. Rolbiecki, *Neutralinos betray their singlino nature at the ILC*, JHEP **09** (2014) 002, arXiv: 1406.7701 [hep-ph].

[310] U. Ellwanger and A. M. Teixeira, *NMSSM with a singlino LSP: possible challenges for searches for supersymmetry at the LHC*, JHEP **10** (2014) 113, arXiv: 1406.7221 [hep-ph].

[311] U. Ellwanger and A. M. Teixeira, *Excessive Higgs pair production with little MET from squarks and gluinos in the NMSSM*, JHEP **04** (2015) 172, arXiv: 1412.6394 [hep-ph].

[312] M. Masip, R. Munoz-Tapia and A. Pomarol, *Limits on the mass of the lightest Higgs in supersymmetric models*, Phys. Rev. **D57** (1998) R5340, arXiv: hep-ph/9801437 [hep-ph].

[313] S. Kraml and W. Porod, *Sfermion decays into singlets and singlinos in the NMSSM*, Phys. Lett. **B626** (2005) 175–183, arXiv: hep-ph/0507055 [hep-ph].

[314] U. Ellwanger and C. Hugonie, *The Upper bound on the lightest Higgs mass in the NMSSM revisited*, Mod. Phys. Lett. **A22** (2007) 1581–1590, arXiv: hep-ph/0612133 [hep-ph].

[315] U. Ellwanger, C. Hugonie, *NMSSMTools — Tools for the calculation of the Higgs and sparticle spectrum in the NMSSM*, [Online; accessed April 29, 2016], URL: http://www.th.u-psud.fr/NMHDECAY/nmssmtools.html.

[316] P. Bechtle et al., HiggsBounds – 4*: Improved Tests of Extended Higgs Sectors against Exclusion Bounds from LEP, the Tevatron and the LHC*, Eur. Phys. J. **C74**.3 (2014) 2693, arXiv: 1311.0055 [hep-ph].

[317] P. Bechtle et al., *HiggsSignals: Confronting arbitrary Higgs sectors with measurements at the Tevatron and the LHC*, Eur.Phys.J. **C74**.2 (2014) 2711, arXiv: 1305.1933 [hep-ph].

[318] R. Barbieri and G. F. Giudice, *Upper Bounds on Supersymmetric Particle Masses*, Nucl. Phys. **B306** (1988) 63–76.

[319] G. W. Anderson and D. J. Castano, *Measures of fine tuning*, Phys. Lett. **B347** (1995) 300–308, arXiv: hep-ph/9409419 [hep-ph].

[320] H. Baer, V. Barger and D. Mickelson, *How conventional measures overestimate electroweak fine-tuning in supersymmetric theory*, Phys. Rev. **D88**.9 (2013) 095013, arXiv: 1309.2984 [hep-ph].

[321] P. M. Nadolsky et al., *Implications of CTEQ global analysis for collider observables*, Phys. Rev. **D78** (2008) 013004, arXiv: 0802.0007 [hep-ph].

[322] The ATLAS Collaboration, *Search for direct production of the top squark in the all-hadronic ttbar + etmiss final state in 21 fb-1 of p-pcollisions at sqrt(s)=8 TeV with the ATLAS detector* (2013).

[323] The ATLAS collaboration, *Search for strong production of supersymmetric particles in final states with missing transverse momentum and at least three b-jets using 20.1 fb-1 of pp collisions at sqrt(s) = 8 TeV with the ATLAS Detector.* (2013).

[324] The ATLAS collaboration, *Search for squarks and gluinos in events with isolated leptons, jets and missing transverse momentum at* $\sqrt{s} = 8$ *TeV with the ATLAS detector* (2013).

[325] M. Krämer and M. Mühlleitner, *Higher-order QCD corrections to supersymmetric particle production and decay at the LHC*, Nucl. Part. Phys. Proc. **261-262** (2015) 232–245, arXiv: 1501.06655 [hep-ph].

[326] M. Drees, M. Hanussek and J. S. Kim, *Light Stop Searches at the LHC with Monojet Events*, Phys.Rev. **D86** (2012) 035024, arXiv: 1201.5714 [hep-ph].

[327] S. Bornhauser et al., *Light Stop Searches at the LHC in Events with two b-Jets and Missing Energy*, Phys. Rev. **D83** (2011) 035008, arXiv: 1011.5508 [hep-ph].

[328] J. Fan, M. Reece and J. T. Ruderman, *A Stealth Supersymmetry Sampler*, JHEP **07** (2012) 196, arXiv: 1201.4875 [hep-ph].

[329] S. Alekhin et al., *A facility to Search for Hidden Particles at the CERN SPS: the SHiP physics case* (2015), arXiv: 1504.04855 [hep-ph].

[330] J. de Vries, H. K. Dreiner and D. Schmeier, *R-Parity Violation and Light Neutralinos at SHiP and the LHC* (2015), arXiv: 1511.07436 [hep-ph].

[331] V. Khachatryan et al., *Searches for electroweak neutralino and chargino production in channels with Higgs, Z, and W bosons in pp collisions at 8 TeV*, Phys. Rev. D **90**.arXiv:1409.3168. CMS-SUS-14-002. CERN-PH-EP-2014-216 (2014) 092007. 61 p

G. Aad et al., *Search for the electroweak production of supersymmetric particles in $\sqrt{s} = 8$ TeV pp collisions with the ATLAS detector*, Phys. Rev. D **93** (5 2016) 052002.

[332] H. K. Dreiner et al., *Rare meson decays into very light neutralinos*, Phys. Rev. **D80** (2009) 035018, arXiv: 0905.2051 [hep-ph].

[333] G. Abbiendi et al., *Search for chargino and neutralino production at S**(1/2) = 181-GeV - 184-GeV at LEP*, Eur. Phys. J. **C8** (1999) 255–272, arXiv: hep-ex/9809031 [hep-ex]

R. Barate et al., *Search for charginos and neutralinos in e^+e^- collisions at centre-of-mass energies near 183 GeV and constraints on the MSSM parameter space*, Eur. Phys. J. C **11**.CERN-EP-99-014. 2 (1999) 193–216. 48 p.

[334] T. A. Aaltonen et al., *Search for new physics in trilepton events and limits on the associated chargino-neutralino production at CDF*, Phys. Rev. **D90**.1 (2014) 012011, arXiv: 1309.7509 [hep-ex]

S. Abachi et al., *Search for $\tilde{W}_1\tilde{Z}_2$ Production via Trilepton Final States in $p\bar{p}$ Collisions at $\sqrt{s} = 1.8$ TeV*, Phys. Rev. Lett. **76** (13 1996) 2228–2233.

[335] A. Redelbach, *Searches for Prompt R-Parity-Violating Supersymmetry at the LHC* (2015), arXiv: 1512.05956 [hep-ex].

[336] V. Khachatryan et al., *Search for long-lived particles that decay into final states containing two electrons or two muons in proton-proton collisions at $\sqrt{s} = 8$ TeV*, Phys. Rev. **D91**.5 (2015) 052012, arXiv: 1411.6977 [hep-ex].

[337] G. Aad et al., *Search for massive, long-lived particles using multitrack displaced vertices or displaced lepton pairs in pp collisions at $\sqrt{s} = 8$ TeV with the ATLAS detector*, Phys. Rev. D **92** (7 2015) 072004.

[338] V. D. Barger, G. F. Giudice and T. Han, *Some New Aspects of Supersymmetry R-Parity Violating Interactions*, Phys. Rev. **D40** (1989) 2987

G. Bhattacharyya, "A Brief review of R-parity violating couplings", *Beyond the desert 1997: Accelerator and non-accelerator approaches. Proceedings, 1st International Conference on Particle Physics beyond the Standard Model, Tegernsee, Ringberg Castle, Germany, June 8-14, 1997*, 1997, arXiv: hep-ph/9709395 [hep-ph]

R. Barbier et al., *R-parity violating supersymmetry*, Phys.Rept. **420** (2005) 1–202, arXiv: hep-ph/0406039 [hep-ph].

[339] Y. Kao and T. Takeuchi, *Single-Coupling Bounds on R-parity violating Supersymmetry, an update* (2009), arXiv: 0910.4980 [hep-ph].

[340] M. Anelli et al., *A facility to Search for Hidden Particles (SHiP) at the CERN SPS* (2015), arXiv: 1504.04956 [physics.ins-det].

[341] K. Kodama et al., *Observation of tau neutrino interactions*, Phys. Lett. **B504** (2001) 218–224, arXiv: hep-ex/0012035 [hep-ex].

[342] N. Agafonova et al., *Discovery of τ Neutrino Appearance in the CNGS Neutrino Beam with the OPERA Experiment*, Phys. Rev. Lett. **115**.12 (2015) 121802, arXiv: 1507.01417 [hep-ex].

[343] A. Denner et al., *Feynman rules for fermion-number-violating interactions*, Nuclear Physics B **387**.2 (1992) 467–481.

[344] A. Dedes, H. K. Dreiner and P. Richardson, *Attempts at explaining the NuTeV observation of dimuon events*, Phys. Rev. **D65** (2001) 015001, arXiv: hep-ph/0106199 [hep-ph].

[345] D. Gorbunov and I. Timiryasov, *Decaying light particles in the SHiP experiment. II. Signal rate estimates for light neutralinos*, Phys. Rev. **D92**.7 (2015) 075015, arXiv: 1508.01780 [hep-ph].

[346] Y. Nir and N. Seiberg, *Should squarks be degenerate?*, Physics Letters B **309**.3 (1993) 337–343.

[347] N. Haba et al., *A Simple Method of Calculating Effective Operators*, Acta Phys. Polon. **B43** (2012) 405–444, arXiv: 1106.6106 [hep-ph].

[348] C. M. Bouchard, *The Brown Muck of B^0 and B_s^0 Mixing: Beyond the Standard Model* (2011).

[349] D. Becirevic et al., *Coupling of the light vector meson to the vector and to the tensor current*, JHEP **05** (2003) 007, arXiv: hep-lat/0301020 [hep-lat].

[350] N. Isgur and M. B. Wise, *Weak Decays of Heavy Mesons in the Static Quark Approximation*, Phys. Lett. **B232** (1989) 113–117.

[351] H. Dreiner, M. Kramer and B. O'Leary, *Bounds on R-parity violating supersymmetric couplings from leptonic and semi-leptonic meson decays*, Phys.Rev. **D75** (2007) 114016, arXiv: hep-ph/0612278 [hep-ph].

[352] R. Casalbuoni et al., *Phenomenology of heavy meson chiral Lagrangians*, Phys. Rept. **281** (1997) 145–238, arXiv: hep-ph/9605342 [hep-ph].

[353] T. Feldmann, P. Kroll and B. Stech, *Mixing and decay constants of pseudoscalar mesons*, Phys. Rev. **D58** (1998) 114006, arXiv: hep-ph/9802409 [hep-ph].

[354] S. Aoki et al., *Review of lattice results concerning low-energy particle physics*, Eur. Phys. J. **C74** (2014) 2890, arXiv: 1310.8555 [hep-lat].

[355] W. Bonivento et al., *Proposal to Search for Heavy Neutral Leptons at the SPS* (2013), arXiv: 1310.1762 [hep-ex].

[356] P. Ilten et al., *Dark photons from charm mesons at LHCb* (2015), arXiv: 1509.06765 [hep-ph].

[357] G. Brooijmans et al., "Les Houches 2015: Physics at TeV colliders - new physics working group report", *9th Les Houches Workshop on Physics at TeV Colliders (PhysTeV 2015) Les Houches, France, June 1-19, 2015*, 2016, arXiv: 1605.02684 [hep-ph].

[358] The ATLAS Collaboration,
Cumulative luminosity at ATLAS for sqrt(s) = 8 TeV in 2012,
[Online; accessed January 14, 2016], 2012, URL:
https://atlas.web.cern.ch/Atlas/GROUPS/DATAPREPARATION/PublicPlots/2011-2012/Luminosity/intlumivstime2012DQ.png.

[359] The CMS Collaboration,
Cumulative luminosity at ATLAS for sqrt(s) = 8 TeV in 2012,
[Online; accessed January 14, 2016], 2012,
URL: http://cms-service-lumi.web.cern.ch/cms-service-lumi/publicplots/int_lumi_per_day_cumulative_pp_2012.png.

[360] Particle Data Group, Revised by D. A. Edwards and M. J. Syphers,
Accelerator Physics of Colliders, [Online; accessed Jun 06, 2016], URL:
http://pdg.lbl.gov/2015/reviews/rpp2015-rev-accel-phys-colliders.pdf.

[361] S. van der Meer, *Calibration of the effective beam height in the ISR*,
tech. rep. CERN-ISR-PO-68-31. ISR-PO-68-31, CERN, 1968.

[362] G. Aad et al., *Improved luminosity determination in pp collisions at sqrt(s) = 7 TeV using the ATLAS detector at the LHC*, Eur. Phys. J. **C73**.8 (2013) 2518,
arXiv: 1302.4393 [hep-ex].

[363] The CMS Collaboration, *Measurement of CMS Luminosity* (2010).

[364] Particle Data Group, Revised by G. Cowan, *Statistics*, [Online; accessed May 18, 2016],
URL: http://pdg.lbl.gov/2015/reviews/rpp2015-rev-statistics.pdf.

[365] Nebot del Busto, Eduardo, *Electron energy reconstruction in the ATLAS electromagnetic End-Cap calorimeter using calibration hits*,
[Online; accessed Jun 6, 2016], URL: http://www.tdx.cat/handle/10803/280875.

[366] The ATLAS Collaboration, *Identification of the Hadronic Decays of Tau Leptons in 2012 Data with the ATLAS Detector*, tech. rep. ATLAS-CONF-2013-064, CERN, 2013.